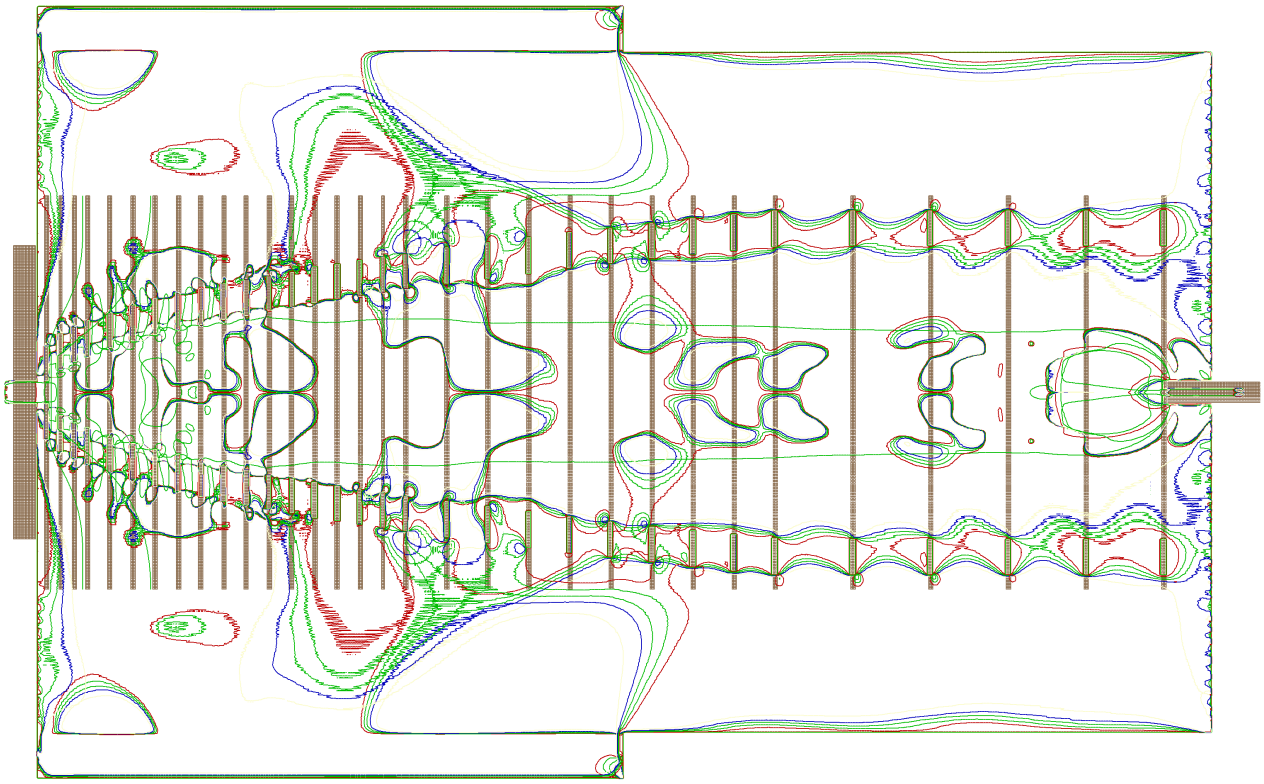


Preparative Mass Spectrometry Instrumentation for Large Native Protein Deposition

Paul Fremdling

Wadham College,
University of Oxford

A thesis submitted for the degree of *Doctor of Philosophy in Physical and Theoretical Chemistry*.

23rd January 2023

Title figure: An artist’s impression of the gas flow field within a parabolic ion funnel.

Acknowledgement

First and foremost, I want to thank Stephan Rauschenbach, my supervisor. He encouraged me to pursue my own, sometimes unconventional approach, no matter if it was about the set-up of the new laboratory at Oxford or ion-optics design. I am grateful for his support at all stages of this doctorate. He has taught me how to develop a mass spectrometer, how to write a scientific text, and even helped when it came to the unpleasant task of cleaning up the laboratory after a waste-water leakage.

Due to the nature of the project, instrument building, more than 50 people have contributed. I do appreciate the work of everyone involved, and ask for forgiveness to those I have forgotten to mention.

Thank you to Tim Esser, without his help it would have been impossible to make the modified instrument so simple to use as it is today. I'm glad for his advice for coding in Lua and Python. His minimal working examples made life a lot easier.

I'm deeply indebted to Laurent for computing the gas flow fields and his patience in explaining the results to me. His thesis was the place to look for an answer when I got stuck with a problem concerning high-pressure ion optics. Julius Reiss had the inspiring idea to totally redesign the ion funnel to improve the hydrodynamic properties. The rewarding discussion with Laurent and Julius were the basis for the insights into the functioning of an ion funnel.

The parts for the modification of the commercial mass spectrometer as well as the entire *'inverted porcupine'* were manufactured at the Max-Planck-Institute for solid state research (MPI-FKF, Stuttgart, European Union). I owe a huge thanks to Artur Küster, who dedicated half a year of his work to the CAD-construction of the *'inverted porcupine'*. It is the merit of Moritz and Luigi, who prepared the laboratory and assembled most of the instrument, that the

prototype of the ‘*inverted porcupine’* works. They, Hannah and Sven were a great company and always made me feel like home when I took a trip to Stuttgart.

A special thanks goes to Ivo Čermák of CGC Instruments (Chemnitz, European Union). He has taught me enthusiastically and with great detail all relevant aspects of RF electronics for ion optics. This knowledge ranged from power switches to cable dimensioning and atmosphere-vacuum electrical feedthrough selection.

I want to thank all so-called support staff who helped me during my time at Oxford University. They are often forgotten but friendly and prompt support made such a big difference for me when we needed a new socket in the lab, a leaking tap fixed or the supply of a chemical was running out. I’d like to thank Ron from facilities, the lab managers Vicky and Andy of the Robinson group, but also Peter from the mechanical workshop. His hands-on course on how to use a turning lathe and how to mill were one of the experiences I liked most during my PhD.

I thank all who proof-read the thesis for their helpful comments. The speedy proofreading Tim H., Nico, Fabien and Cecilia provided was much appreciated to get the thesis across the finish line. Thank you!

I’m incredibly thankful to my friends and family in the European Union and in Reading for the relief, laughter and the unconditional support they provided all along.

Finally, the biggest thanks goes to Henriette. She left out on an opportunity to complete a PhD at a nice place to live together in a town far away from home. I’m so glad for her constant encouragement, academic advice and support.

Summary

Electrospray-ion-beam deposition (ES-IBD) is a preparative mass spectrometry technique which produces highly purified samples of non-volatile molecules adsorbed on a surface. An ES-IBD mass spectrometer (MS) ionises the analyte, transfers it into the gas phase, removes contaminations with a mass filter in vacuum and deposits it with a controlled landing energy onto a substrate. ES-IBD coupled to microscopy can elucidate the structure of biomolecules and their assemblies. In conjunction with scanning tunnelling microscopy, glycan connectivity of oligosaccharides was revealed. For larger molecules, such as native protein complexes, efforts are underway to determine their structure and conformation by coupling ES-IBD to cryo-electron microscopy or low-energy electron holography. However, there are no instruments available dedicated to depositing large, native protein complexes controlled and efficiently. In this thesis, I have modified a commercial MS designed for the analysis of large, native protein complexes (Thermo Scientific™ Q Exactive™ UHMR) for deposition. The modified instrument has adequate beam intensity and good landing energy control. In conjunction with electron microscopy, it was shown that the native shape of protein assemblies is retained after dehydration and deposition. I used an enzymatic assay to quantify the activity of the non-covalent protein complex alcohol dehydrogenase after deposition on a dry surface. Moreover, I developed another instrument for mass- and mobility-filtered deposition of both small and large molecules. Its atmosphere-pressure interface, the ion funnel, is optimised for high transmission and it has a continuous parallel flow ion mobility filter to enable conformation-selected deposition. Radio-frequency power switches with a flexible operation frequency permit to transmit any ion with a mass-to-charge range > 50 Th, in particular heavy ions. The basis for the development of the second MS was the detailed investigation of the transport processes within an ion funnel. I formulate a 4-step ion funnel transmission model underpinned by transmission measurements of a conventional ion funnel and ion trajectory simulations taking into account the gas flow field.

Résumé

Le dépôt par électronébulisation et faisceau d'ions (ES-IBD) est une technique de spectrométrie de masse préparative qui produit des échantillons hautement purifiés de molécules non volatiles adsorbées sur une surface. Un spectromètre de masse ES-IBD ionise l'analyte, le transfère en phase gazeuse, élimine les contaminations avec un filtre de masse sous vide et le dépose avec une énergie d'atterrissage contrôlée sur un substrat. L'ES-IBD couplé à la microscopie peut déterminer la structure des biomolécules et de leurs assemblages. En association avec la microscopie à effet tunnel, les ramifications glycanes des oligosaccharides ont été révélées. Pour les plus grandes molécules, telles que les complexes protéiques natifs, des efforts sont en cours pour déterminer leurs structures et leurs conformations en couplant l'ES-IBD à la cryo-microscopie électronique ou à l'holographie électronique à basse énergie. Cependant, il n'existe pas d'instruments dédiés au dépôt contrôlé et efficace de grands complexes protéiques natifs. Dans cette thèse, nous modifions un MS commercial conçu pour l'analyse de complexes protéiques natifs de grande taille (Thermo Scientific™ Q Exactive™ UHMR) pour le dépôt d'ions. L'instrument modifié a une intensité de faisceau adéquate et un bon contrôle de l'énergie d'atterrissage. En association avec la microscopie électronique, il a été démontré que la forme native des assemblages de protéines est conservée après déshydratation et dépôt. Nous avons utilisé un test enzymatique pour quantifier l'activité du complexe protéique non covalent alcool déshydrogénase après dépôt sur une surface sèche. De plus, nous avons développé un autre instrument pour le dépôt filtré par masse et mobilité de petites et grandes molécules. L'interface atmosphère-pression, l'entonnoir à ions, est optimisé pour une transmission élevée et dispose d'un filtre de mobilité ionique à flux parallèle continu pour permettre le dépôt par conformation. Des commutateurs de puissance à radiofréquence avec une fréquence de fonctionnement flexible permettent de transmettre n'importe quel ion avec un rapport masse/charge > 50 Th, en particulier les ions lourds. La base du développement du

deuxième spectromètre de masse a été l'étude détaillée des processus de transport dans un entonnoir à ions. Nous formulons un modèle de transmission en entonnoir à ions à 4 étapes, étayé par des mesures de transmission d'un entonnoir à ions conventionnel et des simulations de trajectoires d'ions prenant en compte le champ d'écoulement du gaz.

Zusammenfassung

Elektrospray-Ionenstrahl-Deposition (ES-IBD) ist eine präparative Massenspektrometrietechnik, die hochreine Proben von nichtflüchtigen Molekülen erzeugt, die an einer Oberfläche adsorbiert sind. Ein ES-IBD Massenspektrometer ionisiert den Analyten, überführt ihn in die Gasphase, entfernt Verunreinigungen mit einem Massenfilter im Vakuum und deponiert ihn mit einer kontrollierten Landeenergie auf einem Substrat. ES-IBD gekoppelt mit Mikroskopie kann die Struktur von Biomolekülen aufklären. In Verbindung mit Rastertunnelmikroskopie wurde die Verzweigung von Oligosacchariden ermittelt. Bei größeren Molekülen wie nativen Proteinkomplexen wird versucht, ihre Struktur und Konformation durch Kopplung von ES-IBD mit Kryo-Elektronenmikroskopie oder Niederenergie-Elektronenholographie zu bestimmen. Es gibt jedoch keine Instrumente, mit denen große, native Proteinkomplexe kontrolliert und effizient deponiert werden können. In dieser Arbeit habe ich ein kommerzielles Massenspektrometer, das für die Analyse großer, nativer Proteinkomplexe entwickelt wurde (Thermo Scientific™ Q Exactive™ UHMR), für die Deposition von Ionen modifiziert. Das modifizierte Gerät verfügt über eine angemessene Stahlintensität und eine gute Kontrolle der Landeenergie. In Verbindung mit Elektronenmikroskopie konnte gezeigt werden, dass die native Form der Proteinkomplexe nach Dehydrierung und Deposition erhalten blieb. Mit Hilfe eines enzymatischen Assays konnte ich die Aktivität des nicht-kovalenten Proteinkomplexes Alkoholdehydrogenase nach der Deposition auf einer trockenen Oberfläche quantifizieren. Darüber hinaus habe ich ein weiteres Instrument für die massen- und mobilitätsgefilterte De-

position von kleinen und großen Molekülen entwickelt. Dessen Atmosphärendruck-Vakuum Schnittstelle, der Ionentrichter, ist für eine hohe Transmission optimiert und verfügt über einen kontinuierlichen Parallelfluss-Ionenmobilitätsfilter, der eine konformationsselektive Deposition ermöglicht. Hochfrequenz-Leistungsschalter mit flexibler Betriebsfrequenz ermöglichen die Transmission beliebiger Ionen mit einem Masse zu Ladungs-Verhältnis > 50 Th, insbesondere schwerer Ionen. Grundlage für die Entwicklung des zweiten Massenspektrometers war die detaillierte Untersuchung der Transportprozesse innerhalb eines Ionentrichters. Ich stelle ein 4-stufiges Ionentrichter-Transmissionsmodell auf, welches durch Transmissionsmessungen eines konventionellen Ionentrichters und Ionentrajektorien-Simulationen unter Berücksichtigung des Gasströmungsfeldes untermauert wird.

Table of Contents

1. Introduction....12

2. Theory and Methods....19

2.1 The effective potential approximation....20
2.2 Limits of the effective potential approximation....23
2.3 Ion trajectory simulation with gas interaction....29
Gas interaction....31
Limitations of SDS....32
Integration of gas flow field data in SDS....35
2.4 Numerical calculation of the effective potential....35

3. A preparative mass spectrometer to deposit intact large native protein complexes....38

3.1 Abstract....38
3.2 Introduction....39
3.3 Results and Discussion....43
Instrument setup and modification....43
Deposition workflow....44
Beam-energy distribution....45
Transmission....48
Ion-Beam Shape and Control....50
Control of conformation after landing by mass filtering and solution composition....54
Mass-selective preparation of cryo-EM protein samples....56
Retention of enzymatic activity....60
3.4 Conclusion....62
3.5 Methods....63
Mass-filtered electrospray-ion-beam-deposition machine design....63
Deposition workflow....64
Energy width....66
Transmission....66
Ion beam shape analysis and control....67
Spray solution preparation....68
AFM analysis....69
TEM....69
Retention of enzymatic activity....69
3.6 Acknowledgement....72
3.7 Supporting information available....72
3.8 Statement of Authorship....73

4. RF ion funnel transmission....74

4.1 Ion funnel: principle and ion transport parameters....75

Principle:....75
Ion transport parameters:....77
State of the art:....78
Gas Flow questions:....80
Effective Potential questions:....80
4.2 Experimental investigation of a conventional funnel....82
Experimental details and methods....83
Pressure and RF-amplitude dependency....84
Estimation of the space charge limit....87
Variation of input current....89
DC-Gradient variation....91
4.3 Ion trajectory simulations of new ion funnel geometries....94
Pressure:....98
Capillary shape:....103
4.4 Electrode spacing....107
4.5 RF trapping in the final funnel section....109
RF trapping in the existing, conventional funnel....110
RF trapping in the parabolic ion funnel A....114
4.6 How does a conventional ion funnel work?....118
Supersonic expansion:....118
Collisional cooling and confinement:....118
Ion transport....119
Extraction....119
4.7 Outlook: 2-step atmospheric-pressure interface....120
5. A new instrument for mass and mobility filtered deposition....127
5.1 Concept....130
5.2 Atmosphere-vacuum interface for high transmission at low pumping powers....133
Verification of the Hydrodynamic Properties....135
DC Gradient....137
Mechanical construction....138
5.3 Continuous mobility filter....140
High-pass Low-pass Parallel Flow Mobility Filter....142
DC electric field....146
Ion trajectory simulation....150
Implemented design....155
Implemented DC-Gradient....158
Gas velocity calibration....159
5.4 RF power switches....161
5.5 Beam transfer into high vacuum free flight....165
5.6 Current state and outlook....169
6. Conclusion....172

7. Bibliography....176
8. Table of Figures....191
9. Index of Tables....198
10. Acronyms....199
11. Appendix....201
11.1 Limits of the effective potential approximation....201
11.2 SDS integration....202
Lua-script to integrate a numerical gas flow field as a Simion potential array....202
11.3 Supporting information: A preparative mass spectrometer to deposit intact large native protein complexes....205
Beam energy....206
Transmission....208
Ion beam size....209
Mass filtering and solution composition....210
TEM....211
ADH activity....212
2D scan scheme....216
11.4 Ion funnel....217
Ion funnel geometries A and D....218
11.5 Using the python script to calculate the effective potential....223
Copy of the python script included in the minimal working example:....225
11.6 Ions used for mobility filter simulation....233
11.7 Step-by-step manual to optimise the voltages for mobility filtering....234
11.8 Ion mobility filter test....235

1. Introduction

Many synthetic and analytical applications require clean precursor materials or samples. For example, molecular beam epitaxy (MBE) is used to grow ordered thin films from multiple ultra-pure chemical elements sublimated in separate effusion cells.[1], [2] The flux and the chemical composition of the thin film growth are controlled.[2] This makes MBE a key process in the fabrication of laser-diodes for CD and DVD players and in the production of transistors.[3], [4] In analytical chemistry, mass spectrometry (MS) ionises molecules from a sample and separates the ions according to their mass-to-charge ratio[5]. Thus, mass spectrometry can identify the chemical composition of the molecules and accurately quantify their amounts.[5] Mass spectrometry often cannot directly analyse heterogeneous samples. These samples are, for example, complex mixtures directly taken from biological tissue[6], [7] or sludge from a waste-water treatment plant.[8], [9] Such samples require a clean-up or purification step prior to analysis.[6], [8]–[10]

Separation techniques, such as liquid-phase chromatography[11, p. 793], extraction[12] and precipitation[13] have been developed to obtain clean samples and precursor materials. They are commonly used to purify compound mixtures. This happens both on a small scale for later analysis and on a preparative scale to produce precursor materials in the agrochemical sector[14], [15], clean up wastewater[16], [17] and remove contaminations to obtain white food-grade sugar[18]. However, none of these techniques can separate atomic isotopes because most physico-chemical properties do not differ between isotopes.[19] Hence, at the beginning of the 1940s, scientists within the Manhattan project tried to separate Uranium 235 from Uranium 238 to gain fissionable material for a nuclear bomb.[20] They built the first large-scale preparative mass spectrometer.[20] A preparative mass spectrometer can differentiate between ionised ^{235}U and ^{238}U isotopes because the ions have a different mass-to-charge-ratio.

In this early mass spectrometer, a vacuum arc ion source generated high currents of uranium ions.[20] The ^{235}U and ^{238}U isotope ions were then separated with a magnetic sector.[21]

The vacuum arc ion can only ionise metals.[22] To ionise larger molecules, current analytical mass spectrometers predominantly use electrospray ionisation (ESI).[23] An ESI source consists of a conductive capillary attached to a high-voltage power supply and an atmosphere-vacuum interface.[24] The capillary contains the dissolved analyte molecule.[24] A high electric field ($\approx 10^6$ $V \cdot m^{-1}$) between the tip of the capillary and the atmosphere-vacuum interface produces a spray of small, charged droplets.[25] These droplets evolve to multiply charged ions in the gas phase.[25] In contrast to earlier ionisation techniques[26], [27], the electrospray ionisation is soft and does not induce fragmentation.[28] It readily ionises a wide range of analytes – from small molecules[29] to particles with molecular masses in the giga-Dalton range[30]. ESI has opened mass spectrometry to the analysis of large biological molecules because it produces multiply-charged ions softly.[24] The multiple charges on a macromolecule reduce the mass-to-charge ratio of the ion within a range common mass spectrometers can transmit.[28]

Prior to the advent of electrospray ionisation, preparative mass spectrometry used different fragmenting ionisation sources.[27], [31] Today, the prevalent preparative mass spectrometry technique is electrospray ion beam deposition (ES-IBD).[32]–[38] In ES-IBD, molecules are ionised in an electrospray ion source and then transferred into the gas phase (Figure 1). After the transfer into the gas-phase, the ions are transported into vacuum and get mass-analysed. The ion beam is mass-to-charge-ratio filtered. Finally, a monitored number of ions are deposited with a controlled landing energy onto a suitable substrate. The key ES-IBD characteristics mass-to-charge ratio filtering, selectable landing energy and ion amount monitoring yield controlled, reproducible deposition results.

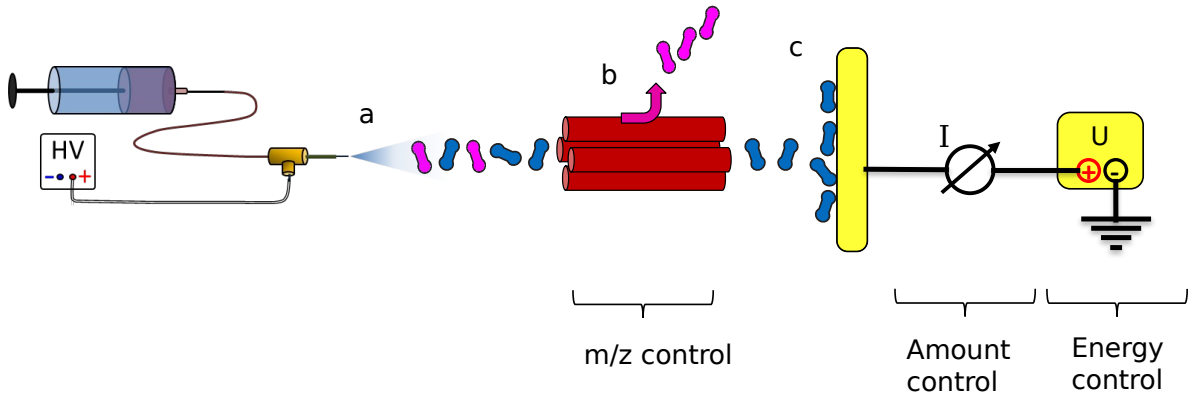


Figure 1: Principle of Electrospray ion beam deposition (ES-IBD). Process steps: a) Electrospray ionisation and transfer into the gas phase. b) Mass-to-charge filtering in vacuum. c) Energy- and amount-controlled deposition onto a substrate.

The energy of the ions (beam energy) and the potential of the sample define the collision energy. The term "soft landing" describes ES-IBD at lower collision energies, whereas "reactive landing" implies higher collision energies. “Reactive landing” can also be used if the collision results in formation of a covalent bond to the surface[39] or to describe an intrinsically reactive combination of a molecular ion and a surface[38], [40]. To monitor the deposited amount, an ammeter measures the ion beam current on the sample. The charge of the deposited ions is proportional to the deposited amount, usually given in the unit pAh (1 pAh = $3.6 \cdot 10^{-9}$ C = $2.2 \cdot 10^{10}$ *e*).[39]

The high-purity of the ion beam is of particular importance to produce samples for scanning probe microscopy (SPM). SPM can image individual atoms[41] and even molecules[42] with atomic resolution. Due to the high resolution, SPM detects any dirt or impurities on a sample. Moreover, SPM-based single-molecule imaging works best in ultra-high-vacuum conditions. [43] This is to avoid that a layer of adsorbate covers the molecules of interest, as SPM is insensitive to buried surfaces.[43] Some molecules, such as sugars, are so non-volatile that they decompose at lower temperatures than their expected sublimation/boiling point.[44] Hence, it is not possible to transfer such a non-volatile molecule from solution onto a clean surface with conventional physical vapour deposition techniques, even under high vacuum conditions.

Here, ES-IBD with its mass-selected ion beam can help. It produces sample surface coated with non-volatile molecules for imaging with little or no contaminations. For example, this was used in combination with scanning probe microscopy to reveal the molecular structure of branched oligosaccharides[45], fabricate 2D peptide molecular nanostructures[46] and inform about conformations of small biomolecules on metal surfaces.[47], [48]

ES-IBD also produces high-purity surfaces of a single analyte, for example, to study parasitic reactions which occur in battery electrodes.[49] Finally, it is the only technique capable of preparing high-purity samples of protein complexes for low-energy electron holography (LEEH), the single-particle microscopy method that allows imaging of highly flexible proteins in their individual conformations.[36], [50]

Beyond the preparative application, it enables studying of non-thermally induced chemical reactions inaccessible with other techniques.[38], [51] Either the ion-surface collision (reactive landing)[51] or ion-gas collisions[38] provide the activation energy.

The lack of readily available instrumentation has hampered the wide-spread application of ES-IBD. Currently, there are no commercial ES-IBD instruments, and only a few academic prototypes. Especially for the deposition of large protein complexes, the current equipment is inadequate.

But why is there an interest to deposit large native protein complexes with ES-IBD?
The three-dimensional structure determines the biological function of a protein.[52] To obtain the structure of a large protein, structural biologists traditionally used X-ray crystallography.[53] More recently, cryo-electron microscopy (Cryo-EM) complements X-ray crystallography.[53] Cryo-EM is of special interest for large biomolecules which are difficult to crystallise, such as membrane proteins.[54] Human membrane proteins are involved in ion transport, metabolism, enzymatic processes and signal transduction.[54] This makes them an im-

portant target for small-molecule drugs.[54], [55] Structural information from Cryo-EM can help to speed up the design of these drugs.[56]

Cryo-EM allows to obtain structural data of large proteins with near-atomic resolution.[57] Proteins consist of light atoms, mainly carbon, hydrogen, nitrogen and oxygen. These light atoms interact only weakly with the electron beam.[57] The resulting electron micrograph contains only low contrast, high noise 2-D protections of the different conformations of the protein.[57] These are called “particles”. They are identified and sorted according to their composition, configuration, conformation and orientation into 2-D classes.[57] To access high-resolution structural data, the information from thousands of particles within the same composition and configuration has to be computationally averaged.[57] The more heterogeneous (broken particles, denatured conformations, impurities…) the sample, the more tedious the classification is.[57] Sample heterogeneity can reduce resolution or even prevent successful 3D reconstruction.[57]

Currently, the structural biologist drop-casts the dissolved protein sample onto an EM-grid, blots away excess solution and drops the entire grid into liquid ethane.[57] This embeds the proteins into a thin layer of vitreous ice, which spans the holes of the EM-grid.[57], [58] However, the drop-casting sample preparation has significant problems: During this process proteins can denature due to interaction with the air water-interface, the water-substrate interface, whilst blotting or during the plunge-freezing.[59]–[62] Moreover, the drop-casting has no selectivity: All contaminations, agents necessary to stabilise the protein (complex) in solution, aggregated or damaged protein will be present on the EM-grid. Therefore, a complementary, more selective sample preparation technique is necessary. A possible alternative is ES-IBD.

Large protein complexes can be fragile biomolecules, and their structural integrity has to be maintained from the electrospray source to the deposited sample. This requires to combine ES-IBD with ‘native mass spectrometry’. For analytical applications, the term ‘native mass spectrometry’ describes a set of conditions to analyse intact large biomolecules.[63] These conditions include non-denaturing solvents, gentle electrospray source conditions and careful transport in the vacuum stages of the mass spectrometer.[64]–[66] Native ESI mass spectrometry retains most non-covalent interactions within a protein complex, such as shape, fold and subunit stoichiometry.[64]–[66] However, academic instrument developments have focused on preparative mass spectrometers mainly for small and medium-sized ions, which tolerate harsher treatment.[27], [31], [33]–[35], [37], [67]–[69] Consequently, these instruments show limited performance and capabilities for native mass spectrometry. In particular, the formation and conditioning of the beam and the gentle transmission are not guaranteed.

To fill this gap, I have, together with others, converted a proven commercial native MS platform for deposition. Commercial analytical mass spectrometers are optimised to obtain high-resolution mass spectra.[70] To record such a mass spectrum, relatively few ions are necessary ($< 10^5$). Thus, the beam intensity of analytical instruments is often insufficient for ES-IBD. Furthermore, the workflow implemented in the control software is suited only for analytical mass spectrometry measurements.

In chapter 3 I and others present the modifications for deposition, including those to reach higher currents with the commercial instrument. I and others characterise the beam energy and ion current of the instrument. I and others demonstrate the retention of a globular conformation after the deposition of native proteins with scanning probe microscopy and cryo electron microscopy (Cryo-EM). Finally, I use an enzymatic assay to test if a non-covalent protein complex can retain enzymatic activity after deposition and rehydration.

While the modified commercial mass spectrometer is capable of native mass spectrometry, it has two drawbacks: It transmits only medium- and large-sized ions such as heavy native protein complexes. On top of the limited transmission range, it does not provide any information about the conformation of the deposited molecules. Consequently, an instrument which combines a high mass-to-charge range with a well-defined high-intensity ion beam is required. It should provide information about the analyte's ion mobility. Preferably, it should offer the ability to select ions with a specific mobility prior to deposition.

For this purpose, I developed a preparative mass spectrometer which can handle both small and heavy ions at high ion beam intensity. It is equipped with a novel continuous ion mobility filter for conformation-selected deposition. Chapter 5 discusses the principle design considerations and simulations of the ion transmission.

Finally, I look into a problem which already the Manhattan project scientists had to deal with on their preparative mass spectrometer: The transmission efficiency of ions from the source to the sample.[20], [21] Specifically, I investigate the transmission performance of the ion funnel, a key component in the atmosphere-vacuum interface of an ES-IBD device. Chapter 4 contains experimental transmission measurements and computer simulations to understand the processes within the funnel.

2. Theory and Methods

An ion optic can move the ion beam through a mass spectrometer either with electric or magnetic fields. Whilst early mass spectrometers relied on magnetic fields[20], [71], instruments using electric fields are now common. Electric fields can be static or time-dependent. As it is not possible to trap an ion with electrostatic fields[72, p. 3], mass spectrometers use both static and time-dependent, inhomogeneous electric fields to move and trap ions in their ion optics.

Two radio-frequency (RF) voltages applied to alternating electrodes create the inhomogeneous electric field.[72, p. 31] The two RF voltages are 180° out of phase, so the voltage on one set of electrodes is $V_0 \cdot \cos(\Omega t)$, and on the other $-V_0 \cdot \cos(\Omega t)$.[72, p. 31] V_0 is the RF amplitude, Ω the angular frequency and t the time. Figure 2 shows typical RF ion optics.

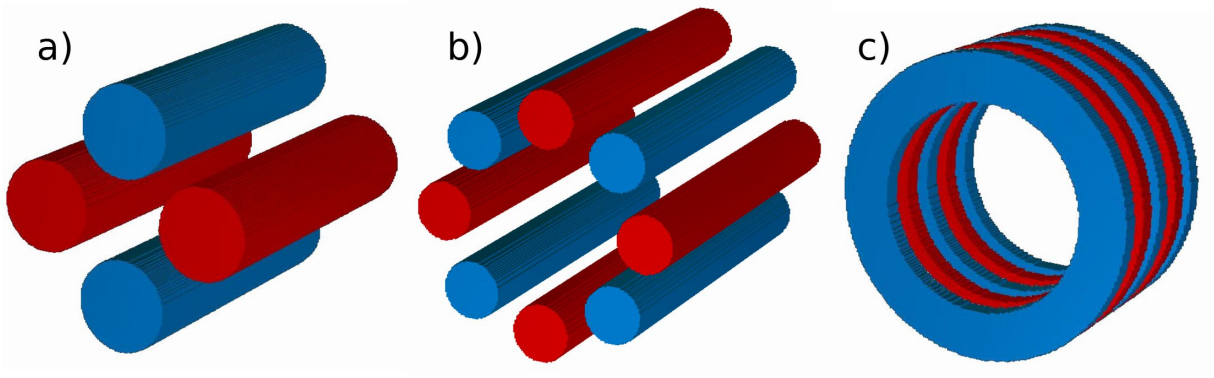


Figure 2: Common RF ion optics. a) Quadrupole b) Octupole c) Stacked-ring ion guide. The blue and red colour of the electrodes symbolise the two RF phases.

Blue and red colour electrodes mark electrodes of different RF phases. The quadrupole (Figure 2a) and octupole (Figure 2b) are linear multipoles. The number of electrodes in a linear multipole is a multiple of two.[73] In contrast to linear ion multipoles, in the stacked-ring ion guide (SRIG), the RF phase of the electrodes alternates along the ion path (Figure 2c). The quadrupole, octupole and the SRIG can transport ions of a wide mass-to-charge range through a mass spectrometer (ion guides). They create inhomogeneous electric fields, which confine

the ions at different radial locations (see also section 4.1). With additional differential DC voltages applied to the RF electrode pairs, the quadrupole can also mass-to-charge filter an ion beam.[74, p. 38]

There are several methods available for calculating the trajectory of an ion in an ion optic. In some special ion optics geometries, such as the quadrupole or the quadrupole-based Paul trap[73], an exact analytical expression describes the ion's trajectory. For more complex ion optics geometries, no exact analytical solution exists because the equation of motion is a non-linear differential equation.[72, p. 5] To solve this problem, the forces of the electric field and the resulting movement on an ion can be calculated in very small time steps. The ion trajectory calculation software Simion uses this approach (see section 2.3). Alternatively, the effective potential approximation is a tool to describe the movement of an ion in high vacuum. It approximates the ion trajectory in a time-dependant field via a time-independent effective potential.[72]

In this chapter I introduce the effective potential approximation, discuss its limits in gas-filled ion optics, and provide an overview of Simion ion trajectory simulation with gas interaction.

2.1 The effective potential approximation

An ion moves in an electric field in high vacuum. The field has two components: The electrostatic field $\vec{E}_s(r)$ (DC field) and the time-dependant, oscillating field $\vec{E_{0,RF}}(\vec{r})\cdot\cos(\Omega t+\delta)$ (RF-field). $\vec{E_{0,RF}}(r)$ is the amplitude of the oscillating field, Ω the angular frequency, t the time and δ a phase. The electric field vector at any point of the field can be numerically calculated from the Laplace equation (see section 2.3). The equation of motion of the ion in this field is[72, p. 10]:

$$m\vec{a} = q\vec{E_{0,RF}}(\vec{r})\cos(\Omega t + \delta) + q\vec{E}_s(\vec{r}) \tag{2.1}$$

where m is the mass of the ion, $\vec{a}$ its acceleration and q its charge. This is a differential equation. The full derivation of an approximative solution is beyond the scope of this work. Instead, the main ideas are briefly outlined. For more information, refer to Gerlich 1992, which contains a detailed derivation of a solution[72], or Wester 2009 for a summary[73].

For the initial steps, the electrostatic field and phase δ is set to zero. The motion of the ion can be considered to have two components: a smooth drift term $\vec{R}_0(t)$ and a rapid oscillating motion, the secular motion $\vec{R}_1(t)$ (Figure 3a): [72, p. 10]

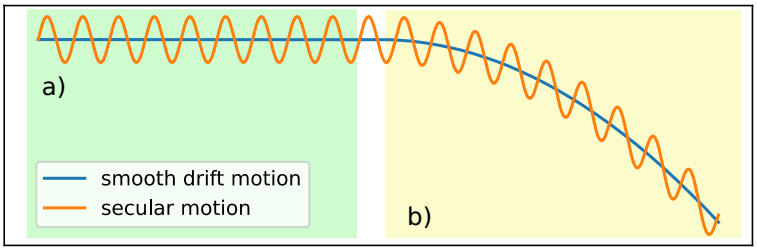


Figure 3: Rapid oscillating motion, the secular motion, in an RF field leads to a smooth drift motion. a) In an homogenous electric field, the smooth drift motion follows a straight line. b) In an inhomogeneous RF field, the secular motion influences the trajectory of an ion.

Under these assumptions, the trajectory of an ion in a homogenous, time-dependant electric field is:[72, p. 10]

$$\vec{r}(t) = \vec{R}_0(t) - \vec{\alpha}(t)\cos(\Omega t) \tag{2.2}$$

$\vec{\alpha}$ is the amplitude vector of the secular motion. This is the starting point for further derivation. This derivation is similar to an integration of the trajectory over several oscillation periods of the secular motion. It simplifies the equation of motion. To this end, the electric field is considered to vary smoothly as a function of the coordinate $\vec{r}$.[72, p. 12] Equation 2.2 is inserted into the general equation of motion (equation 2.1). With additional assumptions, such

as that the amplitude of the secular motion at a specific place does not change with time,[72, p. 12] it is possible to obtain the differential equation for the average motion in a time-dependant electric field:[75]

$$m\vec{a}=\frac{1}{4}\cdot\frac{-q^2}{m\Omega^2}\nabla(\vec{E}_0(\vec{r})\cdot\vec{E}_0(\vec{r})) \tag{2.3}$$

Note that the resulting electric field $\vec{E}_0(\vec{r})$ is time-independent. To generate a force changing the smooth drift motion of the ion, the gradient $\nabla(\vec{E}_0(\vec{r})\cdot\vec{E}_0(\vec{r}))$ must not be zero. Hence, only an inhomogeneous oscillating field changes the smooth drift motion of the ion (see Figure 3b).

If the ion moves in a combination of an oscillating and an electrostatic electric field and we consider $\vec{F}=m\vec{a}$, we obtain the equation for the effective or average force. For better readability, the dependence of $\vec{E}_0$ and $\vec{E}_s$ on the position $\vec{r}$ are omitted: [72, pp. 10–13]

$$\vec{F_{eff}}(\vec{R}_0)=\frac{1}{4}\cdot\frac{-q^2}{m\Omega^2}\nabla(\vec{E}_0\cdot\vec{E}_0)+q\cdot\vec{E}_s \tag{2.4}$$

This equation of motion allows to calculate the trajectory of an ion. The trajectory calculation is simplified because there is no need to calculate every step of the secular (rapidly oscillating) motion.

To move an ion in the effective force field from a point A to a point B requires energy. The work *ΔE* equals the integral of the force field along the path between A and B:

$$\Delta E=\int_A^B \vec{F_{eff}}\cdot(\vec{dr}) \tag{2.5}$$

If I consider that point A is on a grounded electrode, I get a measure for the potential energy of any ion within an RF ion optic, the effective potential *V**:

$$\Delta E = \int_0^B \vec{F_{eff}} \cdot (\vec{dr}) = V^* \tag{2.6}$$

The effective potential *V**, a time-independent scalar field, is an energy:[72, p. 13]

$$V^*(\vec{R_0}) = \frac{1}{4} \cdot \frac{q^2}{m\Omega^2} (\vec{E_0} \cdot \vec{E_0}) + q\,\Phi_s \tag{2.7}$$

Φ_s is the electrostatic potential at the position $\vec{R_0}$. The unit of the effective potential is e.g. Joule.

The effective force field is the gradient of the effective potential field *V**:[72, p. 13]

$$\vec{F_{eff}} = -\nabla V^* \tag{2.8}$$

Thus, the effective force field is assumed to be conservative: The value of the line-integral between two points A and B is independent of the path between them. Regardless of the path along which an ion travels from A to B, its kinetic and potential energy will be converted without losses or gains.[72, p. 13]

Therefore, A 3D visualisation of the effective potential of an ion optic is similar to a mountain landscape. Maxima mark regions which only high-kinetic energy ions can reach. Low-kinetic energy ions move along valleys. If a depression is surrounded by hills or mountains in all directions, it represents an ion trap. Hence, the effective potential allows humans to understand and predict ion trajectories without complex calculations.

2.2 Limits of the effective potential approximation

The effective potential approximation has a limited validity. As previously noted, one of the assumptions was that the amplitude of the secular (rapidly oscillating) motion does not change over time. If the RF frequency Ω is low or the amplitude $\vec{E_{0,RF}}$ of the RF field is high for the ion at a specific position, the ion's secular motion amplitude will rapidly increase. Its oscilla-

tion builds up, energy is transferred from the secular motion to the slow drift motion and the ion ends up colliding into an electrode or leaves the ion optic.[73]

To identify critical regions in an RF optics, Teloy and Gerlich introduced the stability parameter η , the adiabaticity: [72, p. 19], [75]

$$\eta = \frac{2q}{m\Omega^2} |\nabla |\vec{E}_0|| \tag{2.9}$$

If η is smaller or equal to 0.3 in the region of interest, the trajectory of an ion with mass m and charge q is stable.[72, p. 20], [76] For η = 0.3 … 0.5, the trajectories can still be stable, whereas the trajectories are unstable when η exceeds 0.5 in high vacuum.[72, pp. 20–21]

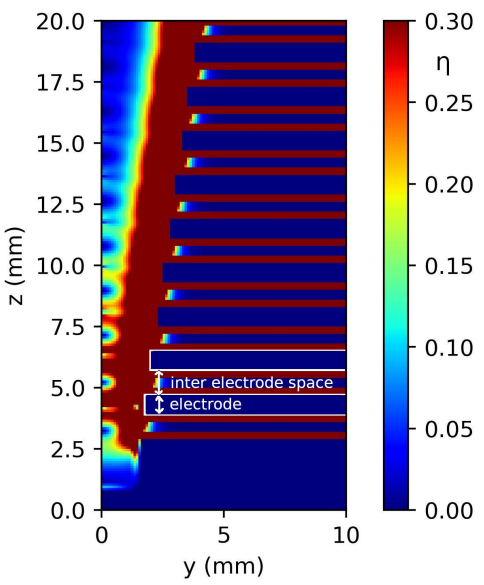


Figure 4: Adiabaticity parameter for the central plane of a gas-filled ion optic, an ion funnel. Typical operation parameters v_{RF} = 1 MHz, V_{RF} = 60 V, m = 443 u and q = 1 e (Rhodamine B). y = 0 is a symmetry plane.

The situation is different if there is gas present in the ion optic. The adiabaticity parameter η can exceed 0.3 in large areas at a pressure of 1 mbar (Figure 4).

However, the ion trajectories remain stable due to the damping caused by the gas interaction (see Chapter 4).

Unfortunately, the effective potential does not accurately describe the energy landscape in a gas-filled ion optic. [77], [78] The friction a molecule experiences when moving between two points in a gas causes the line-integral to depend on the path. Therefore, the effective force field at high gas pressures is not conservative any more.

Bernier 2020 introduced a correction factor c_{gas} to take into account the deviation of the effective electric force in a gas filled ion optic from the ideal, high-vacuum case:[78, p. 90]

$$c_{gas} = \frac{\vec{F}_{eff,gas}}{\vec{F}_{eff,vac}} = \frac{\tau_p^2 \Omega^2}{1 + \tau_p^2 \Omega^2} \tag{2.10}$$

c_{gas} allows to calculate the effective force in gas-filled ion optics. The particle response time τ_p is a measure for the inertia of an ion in such a gas-filled ion optic. Specifically, of an ion drifting at constant electric field in high pressure conditions. It describes how quickly it reacts to a change in gas velocity:[79] (in Supporting Information)

$$\tau_p = \frac{m_{ion} K}{q_{ion}} = \frac{m_{ion}}{q_{ion}} \cdot K_0 \cdot \frac{p_0}{p} \cdot \frac{T}{T_0} \tag{2.11}$$

q_{ion} is the ion charge, m_{ion} the ion mass. Heavier, low-charged ions have longer τ_p than small molecules. K is the ion mobility. K is indirect proportional to the pressure. Hence, τ_p is indirect proportional to pressure, too. τ_{p0} is the particle response time at standard pressure $p_0 = 10^5\,\mathrm{Pa} = 1000\,\mathrm{mbar}$ and standard temperature $T_0 = 273.15\,\mathrm{K}$, K_0 the mobility at these conditions.[80]

At atmospheric pressure c_{gas} tends to 0 – the RF field is less effective. In high vacuum (pressure → 0) c_{gas} tends to 1. Consequently, a transitional pressure range exists, in which the uncorrected effective potential approximation can still yield good order-of-magnitude estimates.

To find the extent of this transitional pressure range, I calculated the correction factor c_{gas} for four probe ions (listed in Table 1) at typical RF operation frequencies (Figure 5) and performed ion trajectory simulations. (see below).

*Table 1: Mass-to-charge ratio, particle response time at standard pressure and critical pressure the effective potential approximation for four probe ions. * denotes calculated values*

Molecule	**m/z (ue^{-1})**	**K_0 ($10^{-4}\,m^2V^{-1}s^{-1}$)**	**τ_{p0} ($10^{-9}s$) ***	**$p_{f,crit}$ (mbar) ***	**$p_{V^*,crit}$ (mbar)**
Hexamethoxyphosphazene (1+)	322.05	1.41 [81]*	0.47	0.7	0.3
Rhodamine B cation (1+)	443.57	0.89 [82]	0.41	0.6	No data
Apomyoglobin (8+)	2119	0.80 [83] [a]	1.76	1.1	2.7
GroEL (+67)	≈11955	0.66 [84]*	8.19	5.1	68

The correction factor c_{gas} remains close to 1 below 0.1 mbar pressure for all probe molecules. For the small organic molecules rhodamine B and hexamethoxyphosphazene, c_{gas} drops to nearly 0 in the low single-digit mbar range. For the large native protein complex ion GroEL, this happens at an-order of magnitude higher pressure. The pressure at which c_{gas} reaches a critical value of 0.95 is defined as $p_{f,crit}$. It is less than 1 mbar for the small organic molecules, 1.1 mbar for the small native protein apomyoglobin, and 5.1 mbar for GroEL (Table 1). I chose $c_{gas} = 0.95$ as critical value, because at lower pressures the effective force deviates less

a Shelimov et al. reported $2.7 \cdot 10^{-4}$ in He, which was divided by 3.4 to get K_0 in N_2. Conversion factor 3.4 according to Matz et. al.[50].

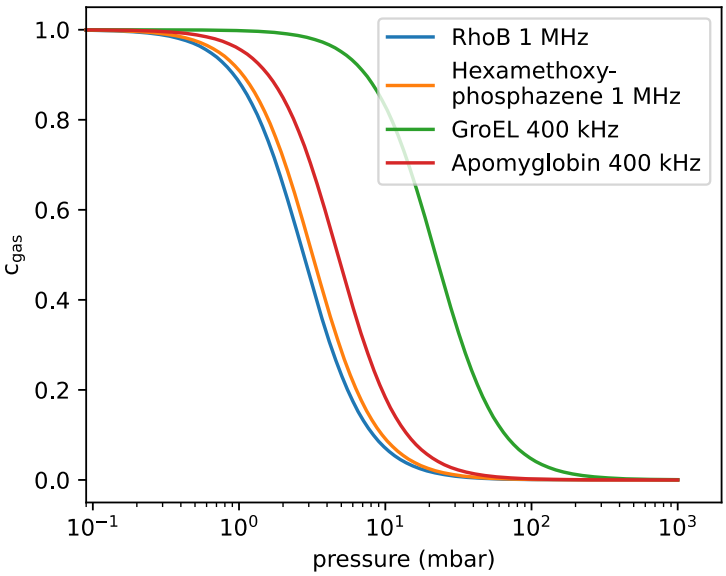


Figure 5: Correction factor for the effective force to account for gas presence according to Bernier 2020. Four probe ions at typical operation conditions are shown.

than 5 % from the ideal vacuum value. Above the $p_{f,crit}$ threshold pressure, the correction factor c_{gas} has to be taken into account to get accurate results of the effective force. Ions in high pressure optics operating below 0.1 mbar, such as collision cells or ion guides, experience the same effective force as in vacuum.

Below the maximum pressure $p_{V^*,crit}$ the effective potential V^* quantitatively describes the energy landscape for a specific ion. In this case, the ion moves like in high vacuum. $p_{V^*,crit}$ is more difficult to define. It depends on the initial kinetic energy of the ion and length of the trajectory in the gas. I performed a simple ion trajectory simulation to obtain an estimation for $p_{V^*,crit}$ for hexamethoxyphosphazene, apomyoglobin and GroEL. My intention was to find the pressure at which the ion still reacts in a similar way as it does in high vacuum. To this end, 80 ions started in the centre of a RF-only gas-filled quadrupole ion guide with 2 mm trap radius. They moved radially towards the rods. In the first simulation, their initial kinetic energy was a third of the quadrupole's radial effective potential barrier. In the second, it was three times V^*. In high vacuum, the ions were confined inside the quadrupole in the first simulation ($E_{kin} = 1/3V^*$) and hit the electrodes in the second ($E_{kin} = 3V^*$). In the next step, I employed the Simion SDS package to simulate a gas. I raised the gas pressure until at least one of the high-energy ions ($E_{kin} = 3V^*$) did not reach the electrode but was confined inside the ion guide. The pressure just below is $p_{V^*,crit}$. For more details, see Figure 59 in the appendix.

The resulting critical pressure $p_{V^*,crit}$ is less than 1 mbar for the small organic molecule hexamethoxyphosphazene and 68 mbar for the large native protein GroEL (Table 1). The simulation revealed that the distance the ions can travel in the field-free gas before they are fully thermalised is the key factor determining $p_{V^*,crit}$. High mass and a comparatively small surface interacting with the gas, the collisional cross section, increase the distance. High initial kinetic increases this distance, too.

Hence, an ion reacts to nearby change in effective potential in a gas-filled ion optic similarly to in high vacuum. If the potential change is far away, it is thermalised before it can reach it. Therefore, the critical pressure $p_{V^*,crit}$ has a characteristic length to which it applies. For the above simulation, this length is 2 mm.
For example, hexamethoxyphosphazene at $p_{V^*,crit}$ = 0.3 mbar reacts still similar to the radial effective trapping potential in a small, longitudinal ion guide, but it will not react to the trapping potential of a narrow, gas-flow limiting aperture at the end of the ion guide.

Even above the critical pressure $p_{V^*,crit}$, the effective potential remains an important tool to understand the way an ion optic functions. Although it cannot accurately model the energy-landscape at high pressure, calculating it helps to analyse ion trajectories and identify possible design flaws. An analogy illustrates the different meanings of the same effective potential values at vacuum or high pressure: In high vacuum, ions experience the effective potential landscape like a free-style skier in an ice-covered halfpipe. No matter which path they choose, they retain their energy. At high pressure, the potential landscape is covered in deep-powder snow. They can only ski if a potential hill is sufficiently steep and stop quickly in flatter areas due to friction. Humans are used to moving with friction over hills and depressions in the landscape, for example when cycling or skiing. Therefore, we can predict the trajectories of an ion in a gas-filled ion optics intuitively on the basis of the effective potential. For us, it is

more difficult to predict trajectories based only on the derivate of the effective potential, the pressure-adapted effective force.

In conclusion, it is possible to use the effective potential approximation in gas-filled ion optics. Stable ion trajectories occur above the adiabaticity limit of 0.3 as a result of the gas damping. Above a critical pressure, which depends on the ion, a correction factor is necessary to calculate the effective force. At any pressure, the effective potential V^* provides a qualitative description of the energy landscape in an ion guide.

2.3 Ion trajectory simulation with gas interaction

The force $\vec{F}$ on a single ion in high vacuum is proportional to the electric field:

$$\vec{F} = q\vec{E} \tag{2.12}$$

To calculate the trajectory of the ion, we need to know the electric field at all points inside an ion optic. The electric field is the negative gradient of the electric potential field V:[85, p. 113]

$$\vec{E}(\vec{r}) = -\nabla V(\vec{r}) = -\left(\frac{\partial V}{\partial x} + \frac{\partial V}{\partial y} + \frac{\partial V}{\partial z}\right) \tag{2.13}$$

Hence, we have to determine the electric potential field V inside the ion optic. This is possible with the Laplace equation:[85, p. 115]

$$\begin{gathered} \nabla^2 V(\vec{r}) = 0 \\ \frac{\partial^2 V}{\partial x^2} + \frac{\partial^2 V}{\partial y^2} + \frac{\partial^2 V}{\partial z^2} = 0 \end{gathered} \tag{2.14}$$

The Laplace equation is partial differential equation which states that the second derivate of the potential field V is zero. The first derivate of V is the electric field (equation 2.13), so it is a solenoidal vector field. Such a vector field has no sources or sinks. Hence, the Laplace equation means that there are no charges in the area it applies to.

To solve the Laplace equation, we need boundary conditions. In ion optics, these are the electrodes. They are good conductors, so all points on their surface are at the same, set electric potential.

The ion trajectory software Simion employs the finite difference method to solve the Laplace equation numerically.[86] The solution of the potential field V is referred to as a "potential array". With the potential array, Simion calculates the electric field and with this, the force on an ion at any point inside the ion optic. This calculation does not take into account the mutual repulsion between two or more ions, the space charge. The electric field calculated by solving the Laplace equation assumes that there are no charges. Therefore, Simion does not model space-charge effects in the potential arrays.

At this point, we are able to calculate the trajectory of an ion in an electrostatic electric field. e.g. by Newton mechanics. In small time-steps, we can calculate the force on the ion and the resulting change in its velocity vector. But what happens if the ion travels in a time-dependent RF electric field? The effective potential approximation yields only correct trajectories in high vacuum. Therefore, we want to use the full time-dependent fields. To this end, we could solve the Laplace equation individually for many time-steps within the oscillation period of the RF field. Fortunately, this is not necessary. The Laplace equation satisfies the superposition principle.[87] Let us assume we have several scalar potential fields V_1, V_2, V_3 etc. All of them are solutions of the Laplace equation, so $\nabla^2 V_j = 0$ applies. Therefore, any linear superposition with the constants a_j

$$V = a_1 V_1 + a_2 V_2 + a_3 V_3 + \ldots \tag{2.15}$$

is also a solution, because:

$$\nabla^2 V = \nabla^2 (a_1 V_1 + a_2 V_2 + a_3 V_3 + \ldots) = a_1 \nabla^2 V_1 + a_2 \nabla^2 V_2 + a_3 \nabla^2 V_3 + \ldots = 0 \tag{2.16}$$

To use the linear superposition principle, Simion solves the Laplace equation for each electrode individually. These solutions are called fast-adjust potential arrays.

To obtain the potential field at a certain time-step in the RF oscillation, Simion scales each potential array to the voltage of the corresponding electrode and adds them together.[86] The scaling approach makes time-resolved trajectory calculation in RF ion optics possible at a low computational cost.

Gas interaction

Two main methods exist to model ion-gas interactions: Individual ion-gas molecule collisions can be calculated with hard-sphere collisions according to the kinetic theory of gas.[88], [89] The hard-sphere model delivers accurate results, but already at 1 mbar pressure, a large native protein ion such as GroEL experiences 10^4 collisions in 1 mm trajectory (Figure 60 in Appendix). Computation times for a single trajectory become very long at high pressure. In this pressure regime, models using Stoke's law deliver faster results.[89], [90] Stoke's law states that the friction force $\vec{F}_d$ a sphere experiences when moving through a viscous fluid is proportional to the drift velocity $\vec{v}_d$. The proportionality constant for an ion drifting in an electrostatic field is the ion mobility K divided by the ion charge q:

$$\vec{v}_d = K\,\vec{E} = \frac{K}{q}\cdot\vec{F}_d \tag{2.17}$$

$\vec{v}_d$ is the steady-state drift velocity and $\vec{E}$ the electric field strength.[91] K is calculated from the ion's collisional cross-section (CCS). CCS values are widely available from ion mobility experiments[92], which measure the drift time an ion needs to travel through a gas-filled ion optic[93].

Viscous motion does not take diffusion into account. Consequently, hybrid models which combine the viscous motion approach with a diffusion model have been developed. Simion's

implementation of such a hybrid model is the statistical diffusion simulation (SDS) package. Briefly, Simion SDS superimposes statistical randomised jumps on the viscous drift motion. [90]

The basis for the randomised jump calculation are five statistical distributions of standardised diffusion lengths obtained with hard-sphere collision simulation. They cover ion-to-background gas ratios from 1 to 10000. They have been calculated for set number of collisions $n_{distribution}$.

For every time step, SDS uses the local pressure and temperature at the ions position to calculate its mean free path λ. With the mean free path, the ion's average thermal speed and the length of the time step, it estimates the number of hard-sphere collisions $n_{expected}$ the ion should have.

Usually, the ion's mass is in between the two standardised diffusion length distributions. Therefore, the values of these two adjacent distributions are interpolated for the ion's mass. A random number generator is used to select a standardised distribution length $r_{jump_distribution}$ from the interpolated distribution. With this information, SDS calculates the jump radius r_{jump}:

$$r_{jump} = \lambda \cdot r_{jump_distibution} \cdot \sqrt{\frac{n_{expected}}{n_{distribution}}} \tag{2.18}$$

Finally, SDS chooses a random direction and adds the diffusion length r_{jump} to the viscous motion.

Limitations of SDS

The main limitation of Simion SDS is that the diffusion models requires at least 10^5 ion-background gas collisions per time step to work correctly.[90] This is not a problem at atmospheric pressure, but becomes critical at low pressure RF simulations. They require short time steps,

e.g. 1/10 of the RF period. A test with SDS at 3 mbar pressure indicated that hexamethoxyphosphazene in a RF ion optic experiences only a few thousand collisions or less per time-step. Furthermore, the ion mass to background gas mass ratio should not exceeded 10000.[90] This means SDS cannot generate correct diffusion jump radii for GroEL, even at atmospheric pressure.

To overcome the SDS limitations, several authors developed new collision models. Poteshin et al. optimised the Simion hard-sphere collision model HS1 code for faster execution and simulated a RF ion optic at atmospheric pressure.[94] Draper et al. coded a complete ion trajectory simulation software. It included a Langevin dynamics model for accurate diffusion simulation of heavy ions.[95] Unfortunately, these new or modified models are either not published or difficult to implement. The development of a new diffusion model would have exceeded the scope of this work.

To assess the error caused by the incorrect diffusion model, I compared the average SDS diffusion length to the estimation according to Pauly et al. 2014.[96, p. S8] To this end, I recorded 38500 SDS diffusion steps for hexamethoxyphosphazene at 3 mbar. Each diffusion step involved at least 10^5 collisions. To suppress diffusion steps with smaller collision numbers, I adapted the SDS program so that it counts the number of collisions predicted per time step and adds them up. It sets the random jump distance to 0 while the sum is smaller than 100000. Once the sum exceeds 100000, it calculates the random jump distance for the sum value. The result was an average random jump distance L_{avg} and an average jump time t_{avg} (total time / number of collision steps). I compared the average random jump distance ($1.6 \cdot 10^{-7}$ m) to the value calculated from the theoretical diffusion coefficient D and the average jump time:

$$\frac{L_{calc}}{L_{avg}} = \frac{\sqrt{D \cdot t_{avg}}}{L_{avg}} \approx 40 \qquad (2.19)$$

SDS with summed collision steps underestimates the diffusion length by a factor of 40 for hexamethoxyphosphazene – that is a dramatic difference. Hence, SDS is not suitable to model diffusion at low vacuum in RF ion optics. The diffusion is wrong in all ion trajectory simulations with SDS in this work.

To avoid absolutely deterministic ion trajectories, I decided to multiply the jump distance with the factor 40. Figure 6 shows the effects for 20 hexamethoxyphosphazene ion trajectories with identical starting conditions.

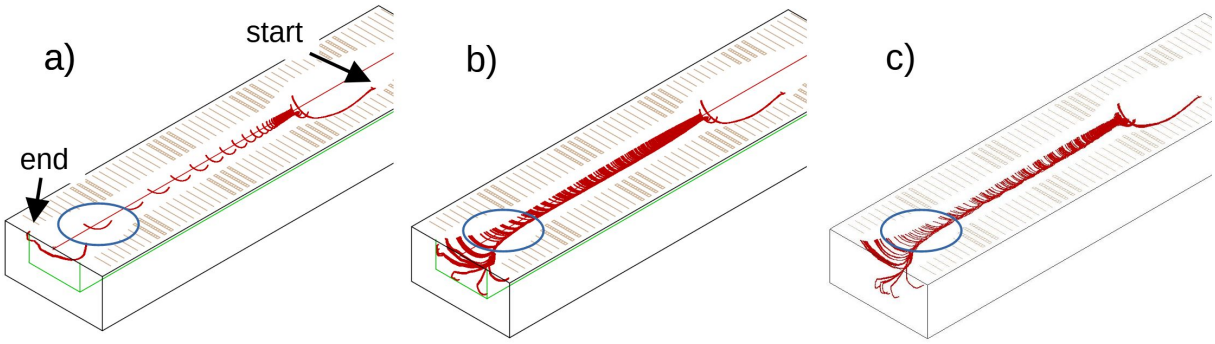


Figure 6: Trajectories of 20 hexamethoxyphosphazene ions at 3 mbar in an RF ion optic. a) SDS with no diffusion: fully deterministic trajectories b) unmodified SDS diffusion, starting conditions do not fully determine trajectories c) at least 10^5 collisions per diffusion step, 40x diffusion length. The difference between the trajectories is well visible in the blue circle.

The random jumping allows the ions to fly through more different regions (see blue circle in Figure 6c) than with the unmodified SDS model (Figure 6b) or no diffusion at all (Figure 6a). Although the random jumping cannot accurately model diffusion, it does avoid deterministic trajectories. This is important to probe all regions of an ion guide in trajectory simulations. I used the modified SDS model (summarised collision steps, 40x diffusion length) in Chapter 5 only. The effects of diffusion on ion trajectories are most important in a stationary background gas,[90] e.g. collision cells or ion traps. The ion optics investigated in this work, an ion funnel and a gas-flow driven mobility filter, do not fall in this category thanks to the high gas velocities inside. Therefore, I focused on the correct integration of gas flow fields (see next section).

In summary, SDS does not model diffusion correctly in low-vacuum RF ion optics. Hence, the simulations in this work combine viscous motion with an arbitrary jumping behaviour to avoid deterministic trajectories.

Integration of gas flow field data in SDS

Simion's SDS package offers two ways to integrate a non-uniform gas flow field. Either an analytical expression describes it, or a numerical flow field is imported as a Simion potential array. I wrote a Lua-script to integrate a numerical 2D flow field as a potential array. The source code is available in section 11.2 in the Appendix. Each gas flow property (p, T, v_x, v_y, v_z) requires its own potential array. I imported the numerical flow field into the Simion optics bench as the .html readme for the Simion 8.1 example "collision_sds" recommends[b]. Simion recognises the radial symmetry of a 2D flow field and uses it for 3D ion trajectory simulation.

I imported either a flow field resulting from computational fluid dynamics calculations (section 4.3) or a flow field defined with an analytical expression by an external python script (sections 4.7 and 5.3).

2.4 Numerical calculation of the effective potential

There are few examples for the numerical calculation of the effective potential V* in literature. Tolmachev et al.[97] and Bernier[78] calculated the effective potential in an ion funnel (for more information on ion funnels, see section 4.1). Fanghänel et al. calculated the effective potential of a Paul trap and a 22-pole trap to optimise their geometries.[98] Tolmachev et al. have not published how they did this calculation. Both Fanghänel et al. and Bernier applied their own method to solve the Laplace equation and used this solution to calculate the effective potential. [78], [99]

b The Simion SDS package .pdf documentation describes an outdated way to integrate numerical flow fields. Refer to the .html readme for the Simion 8.1 example "collision_sds" instead.

For a third person, their approach is difficult to implement. Therefore, I wrote a python script to calculate the effective potential. The python script and a step-by-step manual to use the script are included in section 11.5 in the Appendix. The electronic supplementary material of this thesis contains a minimal working example with all necessary files to calculate and draw the effective potential in a stacked-ring ion guide.

As input, the script uses fast-adjust potential arrays exported from Simion 8.1. For an optic with RF electrodes and a single DC electrode, these solutions of the Laplace equation consist of three files. Each solution array represents the electric potential of all points inside the volume of the ion optics due to a specific electrode group.[100] One is for the RF+ electrode(s), the second for the electric potential due to the RF- electrode(s) and a third for a single DC electrode. The electric potential at any time at a specific point inside the ion optic is a linear combination of the three solutions.

The script can equally use fast-adjust potential arrays with multiple proportional scalable electrodes (.pa+ file). These allow us to define the potential of a single electrode as linear combinations of multiple scalable electrode arrays.[101]

Before the script can read the three fast-adjust potential arrays, they have to be exported to three text files (.patxt). Each line of a text file contains the coordinates and the corresponding potential value in the range 0 to 10000. The script reads these three text files. It subtracts the potential values of the RF- text file from the RF+ text file. The result, a single array, represents the potential values of both the RF+ and RF- electrodes. Then, the script converts this array and the DC one to NumPy arrays. The NumPy arrays are saved for later use. They are much smaller and faster to handle than the original text files because they do not contain the coordinates.

In a second step, the script loads the NumPy files into memory. It scales them to the user-selected RF amplitude and magnitude of the DC coefficient. It calculates the square of the RF electric field $\vec{E}_0 \cdot \vec{E}_0$, and with this the adiabaticity, the RF part of the effective force (left term in equation 2.4) and the RF part of the effective potential (left term in equation 2.7).

Then, it optionally smoothens the RF parts of the effective force and the effective potential. The user can tune the smoothing extent. Usually, the Simion .gem file does not model the tapers and rounded edges present in a real ion optic. This step is important to avoid artefacts due to this simplification at the edges of the electrodes. The DC parts contain much less artefacts at edges because they do not result from a numerical derivation.

After the smoothing step, the DC parts are added to the effective force and potential.

Finally, the script uses the matplotlib package to draw 2D slices of the effective potential, the effective force or the adiabaticity in 2D or 3D. 3D graphs sometimes do not look correct at a certain viewing angle due to limitations of the matplotlib rendering engine.[102] The script can also draw a 1D slice and save it for later use in a separate python script as a NumPy array.

For application examples of the script, please refer to chapters 4 and 5.

3. A preparative mass spectrometer to deposit intact large native protein complexes

This chapter presents the modification of the commercial analytical mass spectrometer and its application for the deposition of large native protein complexes. It is the author's version of the manuscript published in ACS nano.[39] I modified the commercial mass spectrometer, performed all experiments together with Tim K. Esser and developed the adapted enzymatic assay procedure with advice from Bodhisattwa Saha. I wrote the manuscript, with the exception of the section "Mass-selective preparation of cryo-EM protein samples". To ensure the accessibility for users of assistive (screen-reader) technology, the content of the article is set in the normal formatting of this thesis. I integrated the article's bibliography in the thesis' bibliography. The article's supporting information is contained in section 11.3 in the Annex.

Paul Fremdling[a], Tim K. Esser[a,♪], Bodhisattwa Saha[a], Alexander A. Makarov[b,c], Kyle L. Fort[b], Maria Reinhardt-Szyba[b], Joseph Gault[a,♫] and Stephan Rauschenbach[,a,d]*

a: Chemistry Research Laboratory, Department of Chemistry, University of Oxford, 12 Mansfield Road, Oxford OX1 3TA, United Kingdom
b: Thermo Fisher Scientific, Bremen, 28199, Germany
c: Biomolecular Mass Spectrometry and Proteomics, Bijvoet Center for Biomolecular Research and Utrecht Institute for Pharmaceutical Sciences, University of Utrecht, Padualaan 8, 3584 CH Utrecht, The Netherlands
d: Max Planck Institute for Solid State Research, Heisenbergstrasse 1, Stuttgart DE-70569, Germany
♪: Present address: Thermo Fisher Scientific, 1 Boundary Park, Hemel Hempstead, HP2 7GE, United Kingdom
♫: Present address: Vertex Pharmaceuticals, 86-88 Jubilee Avenue, Milton Park, Abingdon, OX14 4RW, United Kingdom
*: E-mail: stephan.rauschenbach@chem.ox.ac.uk

3.1 Abstract

Electrospray ion-beam deposition (ES-IBD) is a versatile tool to study structure and reactivity of molecules from small metal clusters to large protein assemblies. It brings molecules gently

into the gas phase where they can be accurately manipulated and purified, followed by controlled deposition onto various substrates. In combination with imaging techniques, direct structural information of well-defined molecules can be obtained, which is essential to test and interpret results from indirect mass spectrometry techniques.

To date, ion-beam deposition experiments are limited to a small number of custom instruments worldwide, and there are no commercial alternatives. Here we present a module that adds ion-beam deposition capabilities to a popular commercial MS platform (Thermo Scientific™ Q Exactive™ UHMR mass spectrometer). This combination significantly reduces the overhead associated with custom instruments, while benefiting from established high performance and reliability.

We present current performance characteristics including beam intensity, landing-energy control, and deposition spot size for a broad range of molecules. In combination with atomic force microscopy (AFM) and transmission electron microscopy (TEM), we distinguish near-native from unfolded proteins and show retention of native shape of protein assemblies after dehydration and deposition. Further, we use an enzymatic assay to quantify activity of a non-covalent protein complex after deposition on a dry surface. Together, these results indicate a great potential of ES-IBD for applications in structural biology, but also outline the challenges that need to be solved for it to reach its full potential.

3.2 Introduction[c]

Cryogenic electron microscopy (Cryo-EM), low-energy electron holography (LEEH) and scanning probe microscopy (SPM) are complimentary imaging techniques to probe the structure and conformation of biomolecules at sub-nm resolution.[45], [47], [50], [57], [103] Cryo-

c The heading “Introduction” was omitted in the accepted manuscript due to formatting requirements of the journal. Here, it is included for better readability.

EM has evolved into a leading method for high-resolution imaging of biological macromolecules.[104]–[106] LEEH is a low-energy electron, single-particle microscopy method that allows to image highly flexible proteins in their individual conformations.[36] SPM reveals the connectivity of branched oligosaccharides[45] and allows access to the electronic structure of individual molecules.[107], [108]

All three methods require samples produced at highest standard to work optimally. LEEH and high-resolution SPM require ultra-pure, UHV-compatible substrate conditions and greatly profit from chemical purity of the adsorbate.[50] For cryo-EM, the preparation of homogeneous, high-quality samples can be challenging, especially for complex biomolecules. Conventional sample preparation for cryo-EM proceeds through the plunge freezing method, which has been enormously successful, but can be time-consuming and resource-intensive, and homogeneity is limited by solution-based purification techniques.[59], [61], [62], [109]

Electrospray ion beam deposition (ES-IBD) is a preparative mass spectrometry[110], [111] technique, capable of producing highly purified molecular samples for single molecule imaging. It is routinely used for SPM with smaller (bio)molecules[35], [45], [46], [112]–[116] and has been demonstrated also for TEM[117]–[120], LEEH[36], [50], and recently cryo-EM[121], [122]. In contrast to organic molecular beam epitaxy (OMBE),[1], [123] ES-IBD is not limited to small and volatile molecules. In ES-IBD, molecules are ionised in an electrospray ion source, transferred into the gas phase, and mass-analysed in vacuum. Then, the ion beam is mass-to-charge-ratio filtered and deposited with a controlled landing energy onto a suitable substrate. ES-IBD is often referred to as "soft landing" at lower collision energies, or "reactive landing" at higher collision energies or if the collision results in formation of a covalent bond to the surface. It enables reaction pathways inaccessible with other techniques[38], [51] and surface modifications.[124]

In addition to the requirements for ESI mass spectrometry, ES-IBD needs an intense ion beam[33], [96], [112], [125] with well-defined energy distribution, to enable fast sample preparation with controlled landing energy. The width of the beam-energy distribution is crucial, as it defines the collision energy distribution and limits the landing energy range. Reported values for full width at half maximum (FWHM) range from 2 to 10 eV per charge.[32], [51], [112], [113] The beam-energy width determines the minimal landing energy, which can be used without deflecting a significant portion of the ion beam. Narrow beam-energy distributions enable controlled exploration of shallow conformation spaces.[48] A low landing energy per charge is important for highly-charged protein complexes, as their absolute landing energy is proportional to the charge state. For example, the heavy native protein complex ion $GroEL^{+67}$ experiences 670 eV absolute landing energy at a landing energy set to 10 eV per charge.

Likewise, the beam intensity determines the deposition time for a given deposition area and particle density. We use the charge of the deposited ions to quantify the deposited amount, given in the unit pAh (1 pAh = $3.6 \cdot 10^{-9}$ C = $2.2 \cdot 10^{10}$ e). In practice, 5 to 20 pAh are sufficient for imaging.[36], [50], [116], [126] This charge allows to deposit on a several mm^2 large sample with a sub-monolayer coverage that enables imaging of isolated particles. Beam currents of more than 20 pA ensure typical deposition times of less than half an hour, so multiple deposition conditions can be tested in a day. However, precise mass-selection inherently reduces the current available for deposition, since all ions except the selected one are removed from the beam. Finally, an accurate current measurement on the level of 1 pA is needed to achieve reproducible coverage.

For sample preparation of biological macromolecules, the structural integrity of fragile biomolecules has to be maintained for the entire ES-IBD process. Native MS retains covalent and most non-covalent interactions within a protein complex[64]–[66] and can be integrated to

ES-IBD. Nevertheless, it remains unclear to which extent ionisation, liquid-gas-phase-vacuum transfer, and soft landing affect non-covalent interactions and hence the conformation and structure of the protein complexes.

Currently, the barrier to widespread use of ES-IBD is still high and there is no commercial instrument available. Academic instrument developers have designed preparative MS mainly for small and medium size molecule deposition[27], [31], [33], [35], [37], [67]–[69], [113] and only few of these instruments can handle native proteins complexes.[36], [50], [120] To be universally useful for molecular ion-beam deposition, ES-IBD instruments need to be good mass spectrometers, and have a high beam current in addition to the features needed for beam control and deposition.

Commercial, analytical mass spectrometers combine high-resolution mass analysers[70] with a user interface focused on mass spectrometry experiments. However, they have insufficient beam intensity for ES-IBD and lack the flexibility in design and software to integrate deposition as an additional workflow. As a minimum requirement, a native ES-IBD/MS must handle large, low-mass-to-charge-ratio protein ions with a molecular weight of up to a megadalton. Whilst some home-built or converted machines can do this,[32], [36], [50], [122], [127] their mass filter, collisional activation or beam control is severely restricted in comparison to commercial instruments.

Here, we show how to convert a proven, commercial, analytical, native mass spectrometer to a native ES-IBD platform. It has an intense, well-controlled ion beam, which we characterise with current and energy measurements. Three different methods are used to demonstrate that the platform is suitable for near-native deposition: Protein heights observed in SPM images show globular features when preparing samples using native ES-IBD, compared to denatured, conventional MS conditions. Using TEM, we demonstrate the importance of landing energy

control to preserve near-native structural features. Finally, we show that a non-covalent enzymatic complex retains activity after ES-IBD.

3.3 Results and Discussion

Instrument setup and modification

We have converted a Q Exactive UHMR instrument (Thermo Fisher Scientific, Bremen, Germany) into a preparative mass spectrometer by adding a custom-built landing stage downstream of the Higher Energy Collisional Dissociation (HCD) cell. Fig. 7 shows a scheme of the instrument.

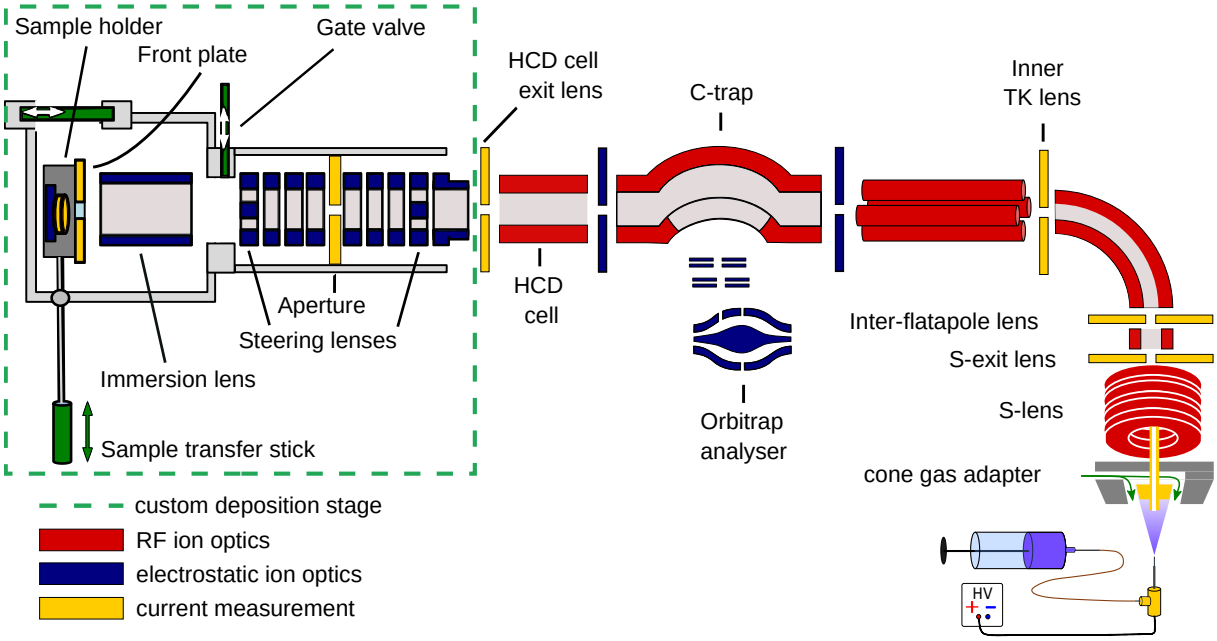


Figure 7: Schematic view of the Q Exactive UHMR mass spectrometer modified for deposition. Custom landing stage to deposit two microscopy samples and measure energy on the left. UHMR with improved source for better transmission on the right.

The added stage contains electrostatic lenses to focus and steer the beam onto a sample holder, containing two sample positions and a retarding grid energy detector (this scheme only shows a single sample in the sample holder).

A sample transfer rod moves the samples in and out of the deposition chamber. That process takes two minutes including pumping and venting. To monitor the beam intensity, the ion current is measured at the landing stage and on apertures throughout the instrument, which was modified to add this capability (yellow elements in Fig. 7). In addition, we have increased the S-exit lens diameter from 1.4 mm to 2.5 mm and added a custom cone gas adapter to increase transmission efficiency and thus achieve shorter deposition times (see Methods).

Deposition workflow

First, we load up to two samples, typically TEM grids or highly oriented pyrolytic graphite (HOPG) substrates, into the sample holder and insert it into the deposition stage. We create an ion beam and check the composition with the Orbitrap mass analyser and set the quadrupole mass filter to select the species required for deposition.

To optimise the beam intensity for deposition, we switch to beam mode. In this mode, the C-trap and the HCD cell guide the ions in a continuous beam, instead of intermittently pulsing the beam into the Orbitrap mass analyser. All direct current (DC) potentials within the Q Exactive UHMR instrument were kept at default values, which minimize activation during transmission from source to the deposition stage (see Fig. 61a). This usually means that potential gradients are as low as possible especially in regions where collisions with the background gas occur.

Next, the beam is steered onto the energy detector. In front of the collector plate that is used to measure the ion current, the detector has a metal grid to apply retarding voltages. Ions with a total energy below their potential energy at the grid cannot reach the detector plate. Hence, we record the ion current at the detector plate as a function of the grid potential to obtain the beam energy.

The difference between the beam energy and the retarding sample potential determines the landing energy. We typically use a range from 2 eV to 100 eV per charge depending on the specific application. For deposition, we finally steer the beam onto the sample and start integrating the detected sample current, to measure when the desired coverage is achieved. During deposition the beam composition is checked periodically using the mass analyser.

Beam-energy distribution

The total energy of the ion beam, its distribution and the sample potential define the collision energy with the surface. The total energy distribution is determined by the potential along the beam path and the interactions of the ions with the background gas. Hence, it can be influenced by the local pressure in the ion optics and by the applied radio-frequency (RF) and DC voltages. The pressure ranges from 0.01 mbar in the HCD cell to high vacuum in the landing stage.

In our instrument, total energy is measured via the retarding grid detector integrated in the sample holder (see Fig. 7 and Methods). We investigated the influence of two distinct sets of potentials on the beam-energy distribution, one with higher and one with lower potential gradients in the landing stage (see Fig. 61b).

For this investigation, we used an ion-beam of denatured and a native bovine serum albumin (BSA). Denatured BSA yields a wide range of charge states between +44 and +15 (1600 to 4500 Th, Fig. 63a, 1 Th = 1 Da·e^{-1}). The native BSA beam contains the monomer as well as undefined, higher-order aggregates. Their mass-to-charge ratio is 3900 (+17, monomer) to 10200 Th (aggregate, Fig. 63b). The detector measures the beam's intensity and the total energy E_{tot}. E_{tot} is the sum of the ion's kinetic[d] E_{kin} and potential energy E_{pot}. E_{kin} only depends on the ion's velocity. Its E_{pot} depends on charge state and position in the electric potential land-

d In the manuscript the word “energy” is missing. Correct is:”E_{tot} is the sum of the ion's kinetic energy E_{kin}...”

scape. The reference for E_{pot} and E_{tot} is electrical ground. Hence, an ion with a negative E_{tot} cannot reach a grounded electrode.

Fig. 8 shows beam-energy distributions measured under different conditions. They are represented as Gaussian fits to the first derivative of the beam current, I, with respect to the grid bias, U_{grid}. The grid potential U_{grid} corresponds to E_{tot}. All measured E_{tot} are negative. Consequently, all ion optics in the landing stage have to shield the ion beam path from the potential of the grounded vacuum chamber. To this end, the ion optics fully enclose the beam path and have a negative potential applied.

The state of the ion, folded or unfolded, as well as the chosen potential landscape influence the E_{tot} mean value and E_{tot} distribution width, in the following given as $E(\Delta E)$. When a lower DC gradient for focusing within the electrostatic lens was applied, the denatured BSA E_{tot} was 9.8(1.1) eV per charge. It is lower by 4 eV per charge and widens by 2.4 eV per charge when choosing a higher gradient instead. Native BSA's E_{tot} follows a similar trend, albeit with a higher E_{tot} mean of -7.9 eV per charge with the lower gradient and -10.2 eV per charge for the higher gradient.

The interplay between local pressure and ion acceleration in the electrostatic lens determines E_{tot}. Ions thermalise in the HCD cell to an E_{tot} of −5 eV per charge, which is defined by the axial DC-potential. From there they enter the electrostatic lenses. Although the pressure rapidly decreases, the ion’s mean free path is significantly shorter than the distance between the HCD exit lens and the next aperture and hence energetic ion-background gas collisions will occur. The ions gain kinetic energy (E_{kin}) between two collisions proportional to the DC gradient (electric field, see figure 61b) along the flight path in the landing stage. The relative loss of kinetic energy per collision depends mainly on the mass of the collision partners, with the absolute loss per collision higher at higher E_{kin}. The randomness of the impact angle between

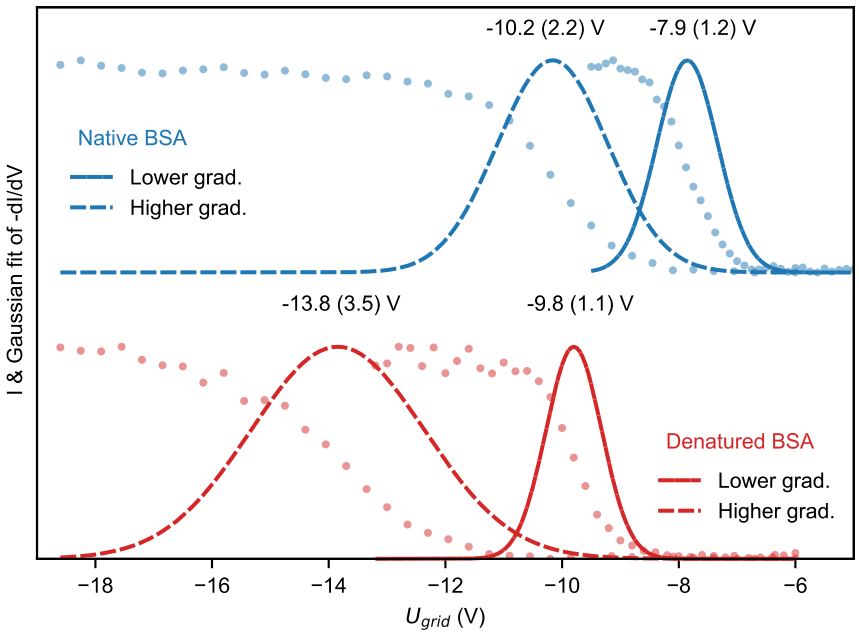


Figure 8: Beam-energy distribution measured for denatured and native BSA ion beams for two different potential gradient settings as shown in Fig. 61b. Dots: Ion current measured as function of the retarding grid potential $I(U_{bias})$. Lines: Gaussian fit for first derivative dI/dU_{bias}, corresponding to the total beam energy per charge (E_{tot}) in eV per charge. FWHM is given in parentheses.

gas and ion causes a distribution in energy loss, which is wider for high E_{kin}. Thus, a high potential gradient causes a large decrease in E_{tot} and widens ΔE_{tot}, the width of the distribution (see SI).

Two factors explain the lower E_{tot} for the denatured protein. First, the number of collisions in the electrostatic lens increases with the unfolded protein's larger collisional cross section. [128] Second, the denatured protein ions' higher charge states raise the overall E_{kin} (for the same value of energy per charge), which leads to higher energy loss in collisions as compared to the low charge state, native ion.

In summary, when transferring an ion beam from high-pressure RF optics into high vacuum, magnitude and distribution of E_{tot} is a function of the DC gradient, background pressure, ion charge, and collision cross section (CCS). For a given type of ion, efficient pumping and a

weak DC gradient ensure a narrow distribution of total beam energy, enabling all ions to land on a substrate downstream with a similar collision energy.

Here, using low gradients, the E_{tot} distribution (FWHM ≤ 1.2 eV per charge) is sharper than previously reported literature values (FWHM ≥ 2.2 eV per charge per charge),[34], [51], [112], [114] pointing to gentle conditions in which gas-phase activation is minimal. Given that the lower gradient conditions also achieved high transmission and good beam focus, we retained them for all other experiments presented here.

Transmission

High transmission is crucial for deposition experiments, since the particle flux directly determines the deposition time for a given coverage and sample surface area. Using a typical analyte concentration of 3 µmol·L^{-1} and assuming a 1 µmol·h^{-1} nano electrospray flow rate with 100 % ionisation efficiency, a 1.2 nA emission current of native BSA (z = 15) would be generated. This emission current is the upper limit estimation for the possible current of a 3 µmol·L^{-1} BSA solution (see SI for details). However, under these conditions we measured initially only 13 pA at the sample position in the Q Exactive UHMR instrument with an unmodified source region. An initial measurement indicated a 1 nA current in the first vacuum chamber (Fig. 9a). This may include ionised solvent and contaminants. There was also a sharp drop in current between the S exit lens and the inter flatapole lens.

To improve the transmission performance, we enlarged the inner diameter of the S-exit lens stepwise from 1.4 to 2.0 and finally to 2.5 mm. With the 2.5 mm opening, the ion current at the sample for large, native proteins doubled to 25 pA and for medium sized, native proteins the current grew more than ten-fold to 170 pA (Fig. 9b). There was no measurable effect for Rhodamine B (RhoB), a relatively small ion with an *m/z* of 443 Th. All currents reported here are routinely reached with fluctuations of up to 80 %, due to emitter performance.

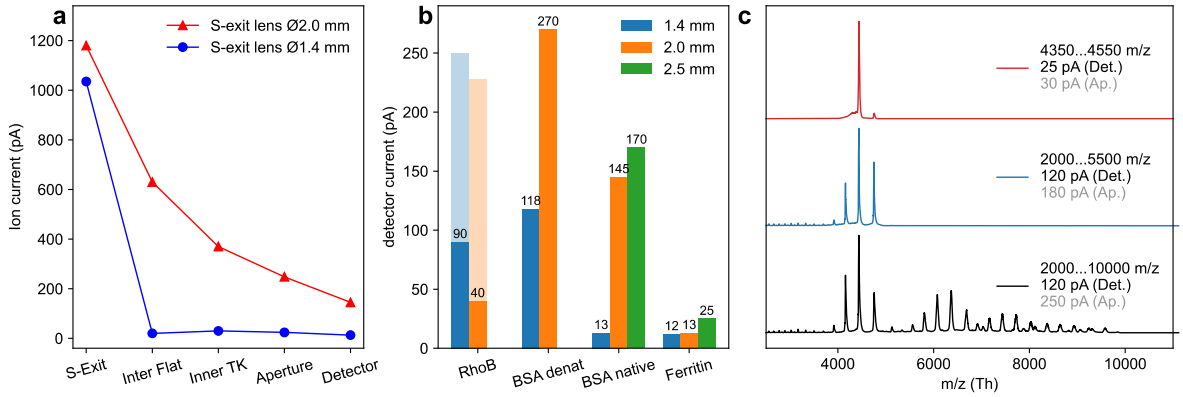


Figure 9: Transmission properties. a) Ion current across the instrument before and after increasing the S-exit-lens diameter, measured at different ion optics. b) Typical ion currents at the energy detector for different S-lens diameters. (Values equivalent to sample currents). Protein ion currents increase with aperture size. RhoB currents don't follow the trend, due to a defocusing effect. Currents on preceding optical element are shown in light colours. c) Native BSA currents on energy detector (Det.) and aperture (Ap.) decrease with the narrowing width of the mass filter window.

The overall transmission is further affected by mass-filtering, where a narrow *m/z*-window not only suppresses contamination, but can also reduce the flux of desired analyte molecules. Fig. 9c illustrates how the width of the mass-filter window affects the native BSA current: Removing higher-order agglomerates has no effect on the sample current (bottom to mid panel). Under the used conditions, the higher-order agglomerates are in the fringe of the ion beam, so they hit the sample holder front plate instead of the sample. It was possible to filter a single charge state whilst retaining a third of the total current.

In contrast to the protein ion currents, RhoB current does not change with increasing S-lens diameters. Likely, a different beam profile as compared to heavy protein ions causes this behaviour. Thanks to its low *m/z*, RhoB experiences a stronger effective potential than high *m/z* protein ions within the S-lens. Thus, it can remain closer to the optical axis, reducing losses at the transfer apertures.

The modifications to increase the ion current are vital for depositing larger molecules. They allow to test several deposition conditions on a single experiment day, where particle densities of 3000 μm^{-2} or more are needed for efficient cryo-EM or SPM. For our applications, this is

usually achieved with a deposited charge of 15 pAh. The modifications lead to a deposition time of approximately 0.5 h for large native protein complexes.

Whilst necessary for preparative MS, our modifications cause the gas flow into the injection flatapole collision cell to become significantly higher. The pressure in the flatapole rises as a consequence and could decrease the in-source-trapping effectiveness.

Ion-Beam Shape and Control

The ability to create a narrowly focused beam is essential to reduce the time needed to achieve the optimal particle density for SPM or TEM. We used three different methods to assess the ion beam profile under typical experimental conditions.

First, we took an ion-beam image of the front plate of our sample holder (see Fig. 10a and Fig. 68). For this, we scanned the beam with the deflection elements in the electrostatic lenses and recorded the current on the front plate. The resulting current image is a convolution of the front plate geometry and the beam shape. Deconvolution revealed a Gaussian-like beam profile (shown in Fig. 10c). A Gaussian fit gives a FWHM of 2.7 mm, only slightly larger than the diameter of the preceding aperture of 2 mm, which the beam typically passes without losses. The observed widening between the last aperture and the front plate is a consequence of the beam-energy distribution and the DC gradient in this section. A weak DC gradient moves the ions slowly in axial direction and gives them more time to expand radially. The beam profile obtained in this way is the profile at the front plate, whereas the samples are located a few mm behind and can be biased at a different potential.

The beam profile is different on the sample, because the potential gradient between front plate and sample can focus the beam (Fig. 10b). We used AFM to determine protein density distribution after ion beam deposition on HOPG and TEM imaging after deposition on a TEM grid.

We typically use 5 mm wide HOPG chips (see Fig. 10e) as substrates for AFM imaging. For the example given here, we deposited 12.5 pAh of GroEL. Multiple AFM images were taken on the graphite sample, distributed along the length and width of the sample. We found that, for the specific DC potentials used in this experiment, most of the surface area was empty and proteins were localized in a small spot near the centre. Surprisingly, we observed a transition from a clean, empty surface to a coverage of more than a monolayer within 250 µm. We estimate the total number of GroEL particles as $4.2 \cdot 10^9$, from the deposited charge and average charge state of +67.

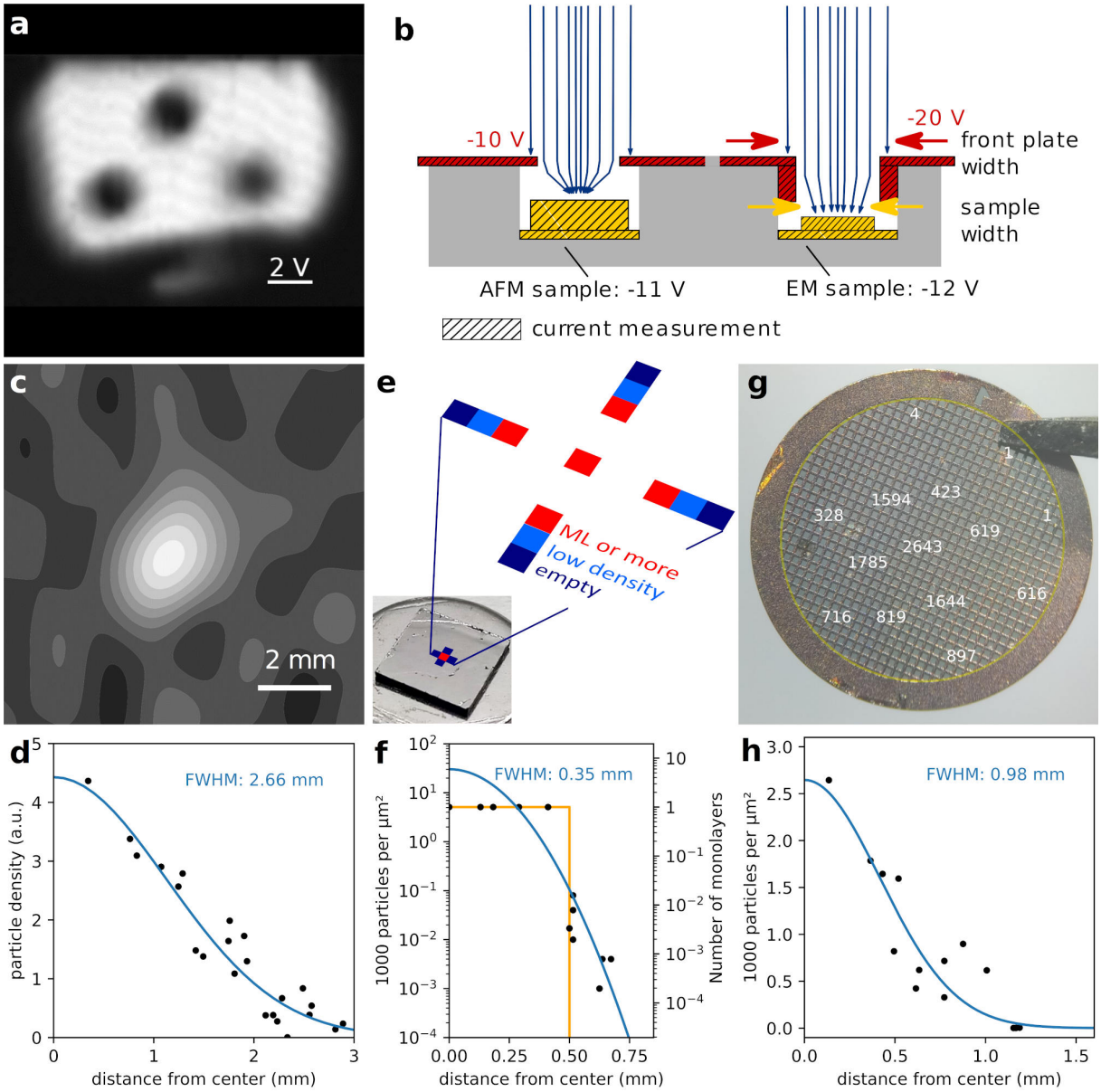


Figure 10: Ion Beam Shape Analysis: a) Ion-beam image of the sample holder front plate. b) Sample holder section view: Different voltages influence focusing. c) Ion-beam shape from deconvolution of a. d) Data points and Gaussian fit of ion-beam intensity distribution. e) HOPG sample used for AFM measurements and protein density distribution in the screened area. f) Measured protein distribution on e (black dots), Gaussian fit (blue), and single monolayer model (orange). g) Amorphous carbon grid used for TEM measurements and protein density distribution in particles per µm². h) Gaussian fit (blue) of density distribution in g. Individual AFM and TEM micrographs are shown in Fig. 64 in the SI.

Because AFM cannot distinguish between single and multiple monolayer coverage, we can only roughly approximate the particle distribution. We fitted our data to two alternative models. A Gaussian fit combines the total particle number with the particle density in the sub-monolayer coverage area. It suggests a deposition spot FWHM of just 350 µm and a coverage

of up to six monolayers at the centre. However, it fails to reproduce the sharp increase in density at the spot's boundary. Alternatively, we assume a monolayer density in the centre (ca. 5000 particles per µm²) with a sharp drop to 0 at .5 mm from the spot centre (orange curve in Fig. 10f). This model overestimates the density at the spot boundary. The real distribution is likely found between these two estimates. As changing position on the sample can be tedious in AFM, other methods with wider field of view or faster change of position would be more appropriate to analyze particle distributions.

Thus, as a third approach, we deposited an apo/holo-ferritin mixture on a TEM grid covered with 3 nm amorphous carbon film (see Fig. 10g) and acquired micrographs at room temperature. The density of holoferritin iron cores was quantified on different grid squares. The resulting distribution is shown in Fig. 10h, together with[e] Gaussian fit. A clear decrease of protein density from the centered maximum to the edges of the grid is observed. The fit gives a FWHM of 1 mm and a total particle count of $2.9 \cdot 10^9$. We can compare this number to the estimate from the total accumulated deposition current of 20 pAh. Using the most abundant apoferritin charge state of +50, this corresponds to $9.0 \cdot 10^9$ particles. We attribute the deviation partially to ambiguity of the charge state, due to the continuous mass to charge distribution of ferritin, caused by the randomness of the mass of the iron cores. Hence, the charge state distribution cannot be measured with ensemble MS techniques. This makes the calculation of the number of landed particles less accurate. In addition, apoferritin, which accounts for 40 % of the total ion-beam intensity, was not detected due to radiation damage.

The different approaches to the measurements of the deposition spot size provide comparable results and show that the ion beam can be focused to reduce the preparation time of high-density protein samples. Differences in the spot size can be understood by the use of two different proteins, DC potentials, and different sample geometry. The AFM sample is thicker,

e Missing article in the manuscript. It should be “...together with a Gaussian fit.”

and thus closer to the front plate. This changes the local electric fields and leads to a different focus. We have observed that the deposition spot size can be tuned most effectively using the DC potential between front plate and sample. The beam can also be defocused to create a more homogeneous distribution across the entire sample. Generally, either full monolayer coverage or few isolated particles can be achieved to optimize the sample for various imaging applications.

The size and shape of the deposition spot measured here is consistent with other observations. Secondary ion mass spectrometry together with infrared reflection absorption spectroscopy showed similar distributions of below- and above-monolayer coverage[68]. Most importantly, the strong influence of the fields directly at the sample suggest that more effective focusing could be achieved with dedicated ion optics installed at this location.

Control of conformation after landing by mass filtering and solution composition

It is established, for example by ion mobility spectrometry, that the three-dimensional (3D) conformation of proteins can be retained to a large degree in native ESI.[129] To study if such a native-like conformation can be retained in our instrument, we soft-landed BSA on HOPG using different solutions and instrument settings.

Fig. 11 shows two mass spectra of BSA. When using a solvent containing 73 % MeOH, 3 % HCOOH (formic acid), and 24 % water and a conventional ESI source, high charge states were observed indicating that the protein is denatured and unfolded. We selected the charge states +40 to +53 with the mass filter for deposition. For a 200 mmol·L^{-1} NH_4Ac solution nano-sprayed at 1.2 kV, much lower charge states between +14 and +17 are observed which indicate folded BSA. We selected only the BSA monomer for deposition.

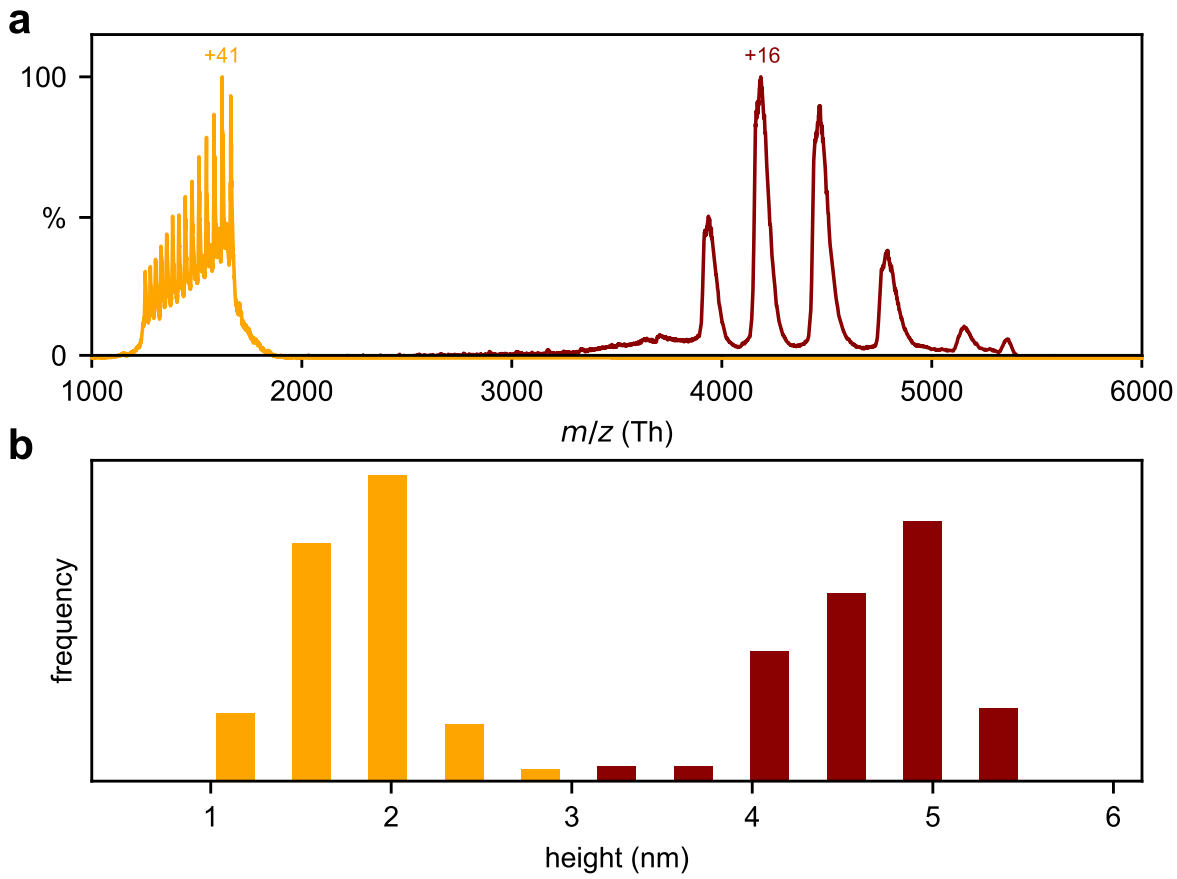


Figure 11: Native BSA (red) and denatured BSA (yellow) mass spectra and height histograms. Spray solution composition: Native 200mM NH_4Ac, denatured 73:24:3 MeOH:H_2O:HCOOH. a) Mass spectra for native (filter window 2000...5000 m/z) and denatured (1250...1700 m/z) BSA. b) Resulting height distribution measured with AFM after soft-landing on HOPG. Native BSA sample size = 47, denatured BSA = 60.

After deposition, AFM images are taken and quantitatively analysed (see methods) to extract the height distribution, which allow an approximation of the shape of the adsorbed proteins. The height distribution is (1.8 ± 0.3) nm for denatured BSA, and (4.7 ± 0.4) nm for native BSA, given as mean ± standard deviation.

Adsorbates originating from highly charged, denatured protein ions appear much flatter than their low-charged native counterparts. This difference in height is consistent with proteins in completely unfolded and globular conformations, respectively. However, it is not possible to directly image the conformation of individual soft-landed proteins in ambient AFM. Firstly, the individual BSA molecules have undergone diffusion limited aggregation[130] on step edges and terraces. Hence, the individual proteins cannot be identified unambiguously

(Fig. 65 and Fig. 66). Secondly, the AFM radius of the tip is too large to resolve the lateral shape of the aggregates. Instead, a convolution of the tip shape and adsorbate shape is measured, but the height is reproduced with great accuracy (< 1 Å).

This result proofs that the ionisation conditions, notably source and solvent, control the conformation of the soft-landed protein on HOPG. The CCS describes the ion conformation in the gas phase ahead of the landing event. The CCS of BSA measured in N_2 for charge state +40 to +53 is 134 nm² to 144 nm²,[131] for native BSA (+14...+17) it is 45 nm².[84] Our measured heights are in good agreement with these values because high CCS, extended denatured conformations yield flatter agglomerates than native, compact ones. Therefore, protein height measurements after soft-landing can reveal pre-landing gas-phase conformations on mass spectrometers without IMS capability. This is consistent with previous observations that conformations are retained, on the level of a general shape, after soft-landing on a relatively inert surface like graphite.[112], [120], [132]

Mass-selective preparation of cryo-EM protein samples

For large, folded protein assemblies, cryo-EM has become one of the leading methods for structural characterization at atomic resolution.[104], [105] Negative-stain EM, on the other hand, is commonly used to screen sample quality before preparation of cryo-EM samples. Native ES-IBD has the potential to complement and accelerate established cryo-EM sample preparation workflows by selective sample preparation and direct correlation between cryo-EM density maps with complementary information about native interactions and small ligands from mass spectrometry.

Our ion-beam deposition instrument can cover TEM grids with mass-selected protein assemblies, with accurate landing energy control, for imaging in negative-stain EM and cryo-EM. Native gas-phase protein ions are generated via native electrospray ionization, then mass se-

lected, and deposited on TEM grids at room temperature. Grids are retrieved via the vacuum load-lock, transferred under ambient conditions and either stained using uranyl acetate or manually frozen in liquid nitrogen to create cryo-EM compatible samples while circumventing vitrification.

Fig. 12 shows negative-stain and cryo-EM micrographs from native ES-IBD samples of apo/holo-ferritin (479 kDa) and GroEL (803 kDa). 3D models from the PDB (blue) and two-dimensional (2D) classes (green) obtained from single particle analysis in RELION 3.1 are shown as inserts.

In the micrograph of a negative-stain sample of an apo/holo-ferritin mixture, Fig. 12a, individual proteins with and without iron cores can be identified. The edges of the protein shell in the 2D classes are less defined than for a control sample made by conventional liquid deposition (shown in Fig. 67). The apo-ferritin 2D class indicates structural heterogeneity, likely due to a deformation of the hollow protein shell, while the holo-ferritin is stabilized by the presence of the iron core in its centre.

Westphall et al. recently developed a similar method to deposit mass-selected proteins with a modified Q-Exactive UHMR mass spectrometer.[122] They replaced the HCD-cell quadrupole with a sample transfer rod. This set-up does not determine the landing energy or control the amount deposited via current measurements.[133] In contrast to our method, they landed the protein ions in a glycerol matrix before negative staining. Due to this final transfer from gas phase to solution, information about the gas-phase structure is not accessible. Their map of GroEL and other protein complexes shows more detail. This highlights that landing, interaction with the solid substrate, and vacuum exposure can influence the structure of protein complexes, and a high level of control is needed to minimize deviation from native structures.

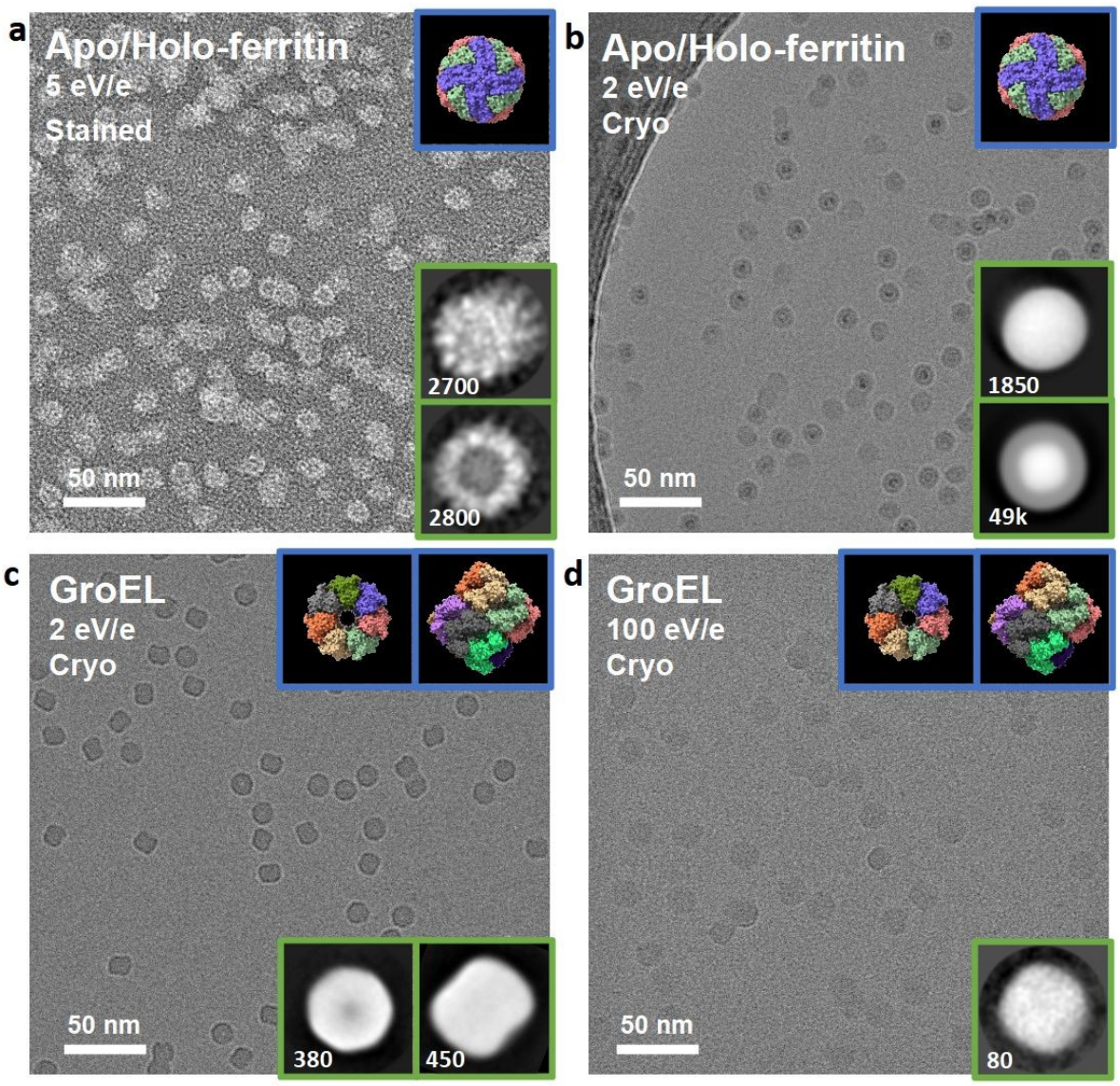


Figure 12: Negative-stain and cryo-EM micrographs of apo/holo-ferritin and GroEL after gas-phase purification and gentle deposition on TEM grids. a) Apo/holo-ferritin, landing energy of 5 eV per charge, 30 nm amorphous carbon film, stained with uranyl acetate. b) Apo/holo-ferritin, landing energy of 2 eV per charge, 3 nm amorphous carbon film, plunge-frozen in liquid nitrogen. c, d) GroEL, landing energy of 2 eV, 100 eV per charge, 3 nm amorphous carbon film, plunge-frozen in liquid nitrogen. The insets show 3D models from the PDB (blue), rendered with ChimeraX[229] using PDB entries 7A6A for apoferritin and 5W0S for GroEL, and 2D classes of native ES-IBD samples (green) obtained using RELION 3.1. The number of particles in the 2D classes is given in the insets.

Combining ES-IBD of protein complexes with negative stain TEM, with or without liquid matrix, has great potential for screening applications. However, we have focused on cryo-EM sample preparation because negative staining ultimately limits access to high-resolution and information on internal structure.

A micrograph of a native ES-IBD cryo-EM sample of the same apo/holo-ferritin mixture is shown in Fig. 12b. The particles have a significantly higher contrast compared to conventional cryo-EM micrographs, due to the use of a 3 nm thin amorphous carbon film and the absence of ice. The ferritin protein shells are clearly visible around the iron cores and demonstrate conservation of protein complex topology. A slight deformation of the apoferritin is still observed, but it is smaller than for the stained sample, and the 2D classes show sharp rather than diffuse edges.

This result indicates that the deformation observed in Fig. 12a is not only due to the deposition on dry samples at room temperature, but due to the influence by negative staining. We suspect that the exposure to the air-water interface in the staining step limits sample quality in this workflow.

Finally we compare ES-IBD samples of GroEL prepared with landing energies of 2 and 100 eV per charge, imaged by cryo-EM and shown in Fig. 12c and Fig. 12d, respectively. Top and side projections of GroEL can be identified unambiguously in the sample prepared at the lower landing energy. The features of the characteristic barrel shape, including the central cavity and heptameric symmetry in the top view, are already apparent in the single particle images. Particle dimensions indicate no lateral deviation from literature values. However, further detailed substructure, as observed in samples prepared by plunge-freezing, is not visible. We attribute this to small random changes in secondary and tertiary structure. The changes could be caused by dehydration, landing and surface interactions. They limit the amount of information that can be obtained by averaging techniques (see Esser et. al. 2022 for a detailed discussion[126]).

In the sample prepared using a landing energy of 100 eV per charge, Fig. 12d, individual particles are still clearly visible, but they are up to 30 % larger in diameter, and the distinctive

structural features have disappeared. Identification of side and top views is no longer unambiguous. This clearly shows plastic deformation of the GroEL complex due to the energetic impact on the surface, as all other conditions were kept identical. Our workflow enables systematic investigation of the landing energy dependence of this deformation to infer mechanical properties of proteins and protein assemblies.

Retention of enzymatic activity

The difference in structural detail observed between the plunge-frozen cryo-EM samples and ES-IBD samples suggest a level of structural change. To study to what degree this structural change can affect the biological function of proteins, we tested whether the non-covalent protein complex ADH retains enzymatic activity after deposition and re-solvation. So far, this has only been shown for recalcitrant single-stranded proteins with no prosthetic groups such as trypsin.[134], [135] We adapted a photometric assay to quantify ADH activity by NADH production after landing on a surface.

We deposited ADH on conductive carbon tapes with 27 ng (128 pAh) ADH for repetition A, and for repetition B with 22 ng (102 pAh). For each experiment 2 samples were made. Assuming a 2.5 mm diameter deposition spot, this corresponds to 2 monolayers on average. Fig. 13 shows production of NADH by the samples together with background control submerged conductive carbon tapes. The ADH activity is proportional to the slope in of the curves in Fig. 13b. It was 1.2 mU (A) and 1.9 mU (B). Minimal (A) or no (B) background activity was recorded in the corresponding time frame. The recovery, based on ADH data sheet activity (300 $mU \cdot g^{-1}$) was 14 % (A) and 29 % (B). When the activity of the spray solution is taken as a reference (A: 88 $mU \cdot g^{-1}$, B: 138 $mU \cdot g^{-1}$), we find activities of 48 % (A) and 65 % (B) for soft-landed ADH. The positive control activity was lower than spray solution activity (A: 56 $mU \cdot g^{-1}$, B: 117 $mU \cdot g^{-1}$). We measured no activity for a 27 ng (128 pAh) con-

ductive carbon tape after 3 days storage in vacuum (Fig. 71). (For further details on attempted ADH extraction refer to SI.)

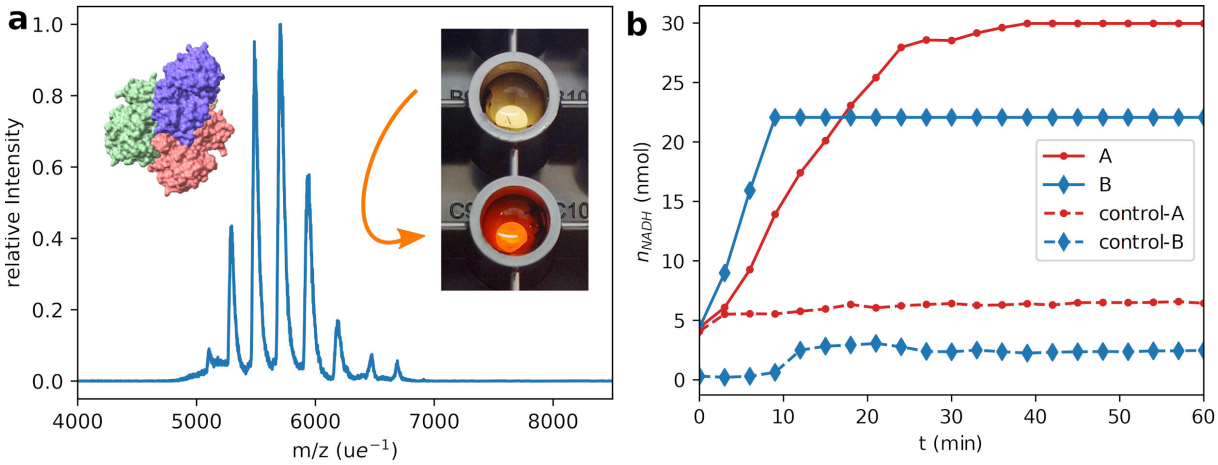


Figure 13: a) Mass spectra of deposited, mass-selected ADH tetramer. Inset: Colour change from yellow to orange indicates an active ADH in the lower well. The black objects on the well's walls are the submerged ADH-coated conductive tapes. b) Production of NADH by ADH after ES-IBD. The broken lines stagnating at the offset level are background controls, so the NADH production is specific for ADH activity. The absorbance measurement causes two separate artificial saturation levels due to different calibrations.

These results offer compelling evidence that a large, non-covalent protein complex can survive the entire ES-IBD workflow including ionisation, de-hydration, transfer into high vacuum, soft-landing, and re-solvation. It is difficult to quantify the exact proportion of intact enzyme. Instead of the numerical value, the order-of-magnitude of the activity is relevant. A number of experimental uncertainties cause this: When reconstituting the commercially obtained, crystalline ADH, it is not known which proportion of the enzyme refolds incorrectly and remains inactive. We measured the spray solution concentration photometrically using a calculated attenuation coefficient. Surprisingly, a much higher proportion of deposited ADH than expected from these references was found to be active. Thus, we used an extrapolation and later a non-linear calibration (see methods).

Additionally, the conductive carbon tape could have blocked a small part of the plate reader beam path inside the well and increased absorbance. To mitigate errors, deposited ADH quantity should be cut to a third to remain in the linear range and the reading frequency in-

creased. The loss of all activity after 3 days storage in vacuum at room temperature might be a consequence of degradation, surface interaction or desolvation. Further experiments are required to investigate if the soft-landed reconstituted ADH was the intact homo-tetramer. TEM images of ADH, soft landed under comparable conditions, indicate no fragmentation or change in quaternary structure.[126]

3.4 Conclusion

This work details the conversion of a high-mass range serial Orbitrap mass spectrometer into an instrument for molecular ion beam deposition. A native ES-IBD mass spectrometer requires high beam intensity, ion beam monitoring and control, and adjustable, low and narrow deposition energy. While existing ES-IBD prototype mass spectrometers show some of the desirable features,[32], [36], [50], [122], [127] such an instrument is currently not commercially available. The focus of this instrument modification is the deposition and imaging of native proteins in order to add chemical selectivity to the protein structure determination process.

Beyond additional ion optics and a deposition stage, it requires the complete understanding of the instruments' beam handling. This allows to align the added components with the duty cycle of the original instrument. To this end, we implemented ion current monitoring at several lenses throughout the instrument. In combination with small modifications to the existing ion optics for better transmission, we obtained a narrow energy-width (≤ 1.2 eV) native ion beam of sufficient intensity (> 20 pA). Finally, an intuitive, home-made beam guiding and monitoring software helps to characterise the beam performance and obtaining reliable, reproducible deposition results.

The instrument produced soft-landed protein samples for TEM and ambient AFM analysis. They confirmed the retention of the native-like globular conformation. However, electron density maps from samples prepared with ES-IBD currently lack the necessary resolution to determine the extent of structural change related to the current implementation of the native ES-IBD workflow.[122], [126] As an alternative approach to check the integrity of the deposited protein we have conducted an enzymatic assay. It indicated that the activity of the non-covalent protein complex ADH was retained post-deposition.

The instrument developed here shows that a commercial platform can be modified for reliable and fully controlled depositions, while the excellent performance of the mass spectrometer is retained. The extended capabilities of the mass spectrometer such as ion activation, or high-resolution selection of a fragment ion, offer interesting perspectives for future experiments.

3.5 Methods

Mass-filtered electrospray-ion-beam-deposition machine design

We converted a Thermo Scientific™ Q Exactive UHMR (Ultra-High Mass Range) into a preparative mass spectrometer (Fig. 7). The electrometer at the end of the HCD cell was removed to make space for a custom deposition stage. Analytical tandem MS still works unaffected in the modified UHMR.

The deposition stage contains a 2x8 element electrostatic lens to focus the ion beam. Steering lenses deflect the beam laterally to any position on the sample holder. A 2 mm diameter aperture separates the two lens stacks. The first lens stack is pumped via the Q Exactive UHMR quadrupole. A 67 $L \cdot s^{-1}$ turbo pump in the deposition part pumps the second part (HiPace 80, Pfeiffer Vacuum GmbH, Asslar, EU). A CF 40 gate valve (series 01, VAT Vakuumventile AG, Haag, Switzerland) decouples the deposition stage from the analytical mass spectrometer.

After the gate valve, an immersion lens shields the ion path from the electric potential of the grounded vacuum chamber. Hence, beams with negative Total Energy (E_{tot}) vs. GND can pass.

The sample holder has two sample positions for EM grids or AFM samples and an energy detector to measure beam E_{tot}. A custom sample transfer stick moves it from a load lock to high vacuum (HV). RBD 9103 HV floating picoampmeters (RBD Instruments Inc., Bend, USA) measure ion current on aperture, sample holder front plate, samples, and the energy detector. An ECH 244 crate with 2x EBS 180 ±500 V bipolar power supply insets control all DC voltages to deposition stage (ISEG Spezialelektronik GmbH, Radeberg, EU). Home-written control software for the picoampmeters and power supplies facilitates the ES-IBD workflow. It supports rapid 2D ion beam imaging, E_{tot} beam measurement and automatic beam focusing optimisation.

To use sweep gas with the nano-ESI source, we milled a 20 mm bore in the cone gas adaptor. The S-lens diameter was increased from 1.4 mm to 2.0 mm and later to 2.5 mm to improve ion transmission. Consequently, gas throughput at the source turbo pump (Splitflow 310, Pfeiffer Vakuum GmbH, Asslar, EU) rose from approximately 2.7 to 5 mbar·L·s^{-1}. We separated the fore pump system to protect the Splitflow 310. The S-lens chamber remained pumped by the factory-fitted Sogevac SV65BiFc fore pump (Atlas Copco, Stockholm, EU), and the Splitflow 310 was connected to an Edwards XDS 35i (Atlas Copco, Stockholm, EU) fore pump. This increases the pressure in the inter-flatapole chamber but does not affect the pressure in the C-Trap or Orbitrap mass analyser.

Deposition workflow

The first step is to load two EM-grid or AFM highly oriented pyrolytic graphite (HOPG) targets into the sample holder. The transfer rod moves them from the ambient load lock to the

high vacuum deposition chamber. Whilst the pressure therein decreases, we prepare the ion beam.

For native proteins, we use gold-coated 1.2 mm glass capillary emitters. We select the minimum possible pressure to push the spray solution to the tip. This maximises emitter lifetime. We start the instrument in normal analytical configuration to check if the emitter is working. We set the mass filter window, then switch to beam mode. Both samples are kept at a high, repulsive potential to avoid uncontrolled deposition. In beam mode, the C-trap and the HCD cell guide the ions without pulsing into the landing stage. All DC potentials within the Q Exactive UHMR instrument are at the default values to guarantee activation-free transmission from source to the deposition stage. In contrast, analytical native MS typically uses strong gradients, often in pulsed modes, to desolvate or dissociate protein complexes.[136] HCD gas flow is set to 7 to thermalise the ion beam in there.

To optimise the current, we change the emitter distance, backing gas pressure and the cone gas flow. If the current is sufficient for deposition, we switch to analytical mode and acquire mass spectra of the ion beam. The instrument is set beam mode again and the beam steered on the energy detector. The detector has a metal grid in front of the collector plate used to measure current. If the electric potential on the metal grid is higher than the total beam energy, the ions cannot pass. Hence, we record the detector collector plate current as a function of the grid potential to obtain the beam energy.

Then, we select the retarding potential on the sample. The difference between the beam energy and the retarding sample potential determines the landing energy, typically 5 eV per charge. We deflect the beam on the sample and start the sample current integration. Once the charge reaches the defined value, the repulsive potential is re-applied. The beam composition

is periodically controlled using the mass analyser, including every time we replace the nano spray emitter. TEM imaging deposition procedure has been already described.[126]

Energy width

We used a native and a denatured BSA beam. For preparations see below. All DC voltages within the Q Exactive UHMR instrument were at the default values. For both beams, we applied a weak or strong DC gradient in the landing stage optics. This focused them through the electrostatic lens on the energy detector. Fig. 61 shows the different voltages applied to produce a weak or strong gradient.

The voltage on the detector metal grid was swept in 40 voltage steps around the expected beam-energy value. For every voltage step, we recorded the average of 60 detector current measurements. This dampens arbitrary or short-term periodic current fluctuations.
The negative differential of the current by the voltage was fitted with a Gaussian distribution. The fit gives the mean beam energy and its FWHM.

Transmission

To measure ion current within the Q Exactive UHMR instrument, we added breakout cables. To this end, we separated the transfer capillary voltage supply from[f] S-exit lens. Breakout cables were connected to the S-Exit lens, the inter-flatapole lens, the inner Turner-Kruger (TK) lens and the HCD exit lens. A modified cone gas cap adaptor supplies the transfer capillary voltage. Each breakout cable connects a RBD 9103 picoampmeter to a DC ion optic and the corresponding power supply on the Q Exactive UHMR DC supply board.
For the current measurement in the Q Exactive UHMR, we set the DC optic (e.g. the S-exit lens) to an attractive potential and the following RF ion optics axis DC (e.g. the injection flatapole) to a repulsive potential. This ensures the entire beam is collected on the DC optic in

f Missing article in the manuscript. It should be "…we separated the transfer capillary voltage supply from the S-exit lens."

question. All voltages are in Table 7 in SI. In the deposition stage, we deflected the beam instead on the aperture or energy detector.

In the next step, we moved the emitter sidewards away from the transfer capillary to block the ion beam at a preceding element. The current offset was recorded and the emitter moved back in position. Then, we recorded the current. All values in Fig. 9 are offset corrected.

We used the heated ESI source for Rhodamine B and denatured BSA solutions. The nano-ESI source was used for native Ferritin and native BSA.

Ion beam shape analysis and control

1. On Front Plate: We obtained a 2D image of the front plate with a denatured BSA beam. We chose denatured BSA, as it reproducibly provides an intense and stable ion beam, which allows to collect high-quality images. To obtain a scanned image, we deflected the beam horizontally and vertically with the steering lenses whilst recording the current on the front plate. See Figure 74 for an explanatory scheme. A 41 x 65 pixel scan was obtained in 34 min. The image dimensions where then converted from volts to millimetres by calibration with the actual front plate size. The image represents a convolution of the sharp front plate geometry, a function of only 0 and 1, and the ion beam profile, assumed to have Gaussian shape. We used a Python script to deconvolute. It employs a binary filter to create a sharp version of the image and then applies the convolution theorem to obtain the beam profile. Finally, we used a low pass filter to remove high frequency components, originating from the non periodic image boundary.

2. On a HOPG AFM sample: We deposited 12.5 pAh of GroEL and used a NanoScope MultiMode AFM for imaging. GroEL was prepared as described in subsection "Spray solution preparation". For deposition, we followed the standard workflow. Except for the front plate voltage. It was at -10 V, as close as possible to the beam energy of (-7 ± 1.6) eV per charge, to minimise the deposition spot size. We acquired multiple 5 x 5 μm^2 images on a raster around

the deposition spot to further assess the protein distribution. We used the dimensions of the cantilever to raster across the surface and reconstruct a density map. We manually counted the number of aggregates in each image.

3. On a TEM sample: 20 pAh ferritin were deposited on an amorphous carbon TEM grid (AGS160-4, Agar Scientific, Stansted, Great Britain). The front plate was at -20 V to the standard work-flow focus. We used a mixture of apoferritin and holoferritin to obtain high contrast. Under the given conditions only holoferritin iron cores are visible. TEM images were recorded using an FEI Talos 200c at room temperature and under the given conditions only the holoferritin iron cores are visible. A python script was used to count the number of particles on the TEM images. Measuring the current on the sample for mass-selected apoferritin and ferritin, the ratio between them was determined as 40:60 and the particle counts were corrected accordingly. The density was determined on multiple grid squares as the average of particle counts of three images, divided by the image area. The coordinates of the individual grid squares were obtained according to the grid square size on a 400 mesh TEM grid.

Spray solution preparation

We purchased rhodamine B (R6626-25G), bovine serum albumin (BSA, A0281-1G), equine spleen ferritin (F4503-25MG), GroEL (chaperonin 60, C7688-1MG) and baker's yeast alcohol dehydrogenase (A7011-15KU) from Sigma Aldrich (Darmstadt, EU). Ferritin and GroEL preparation has been already described.[126] We dissolved rhodamine B in 80:20 H_2O:iPr to $1 \cdot 10^{-4}$ mol·L^{-1}. We made a denatured $4 \cdot 10^{-6}$ mol·L^{-1} BSA solution for AFM deposition in 73:23:3 MeOH:H_2O:HCOOH. For all other denatured BSA measurements, we used a $3 \cdot 10^{-6}$ mol·L^{-1} 100:100:1 ACN:H_2O:HCOOH solution.

We desalted native BSA and ADH twice with size-exclusion chromatography columns (P6, 7326222, Biorad, Hercules, USA). These were equilibrated with 0.2 mol·L^{-1} ammonium acetate (A2706-100ML, Sigma Aldrich). Resulting concentrations were 2 to $5 \cdot 10^{-6}$ mol·L^{-1}.

For all preparations, deionised water with $\rho \geq$ 18.2 MΩ·m filtered through 0.22 µm was used. All other solvents were MS grade from changing suppliers.

AFM analysis

Prior to deposition, each highly oriented pyrolytic graphite chip (HOPG, MikroMasch, Sofia, EU) was cut into 5x5 mm chunks and glued with leit-silver (09937, Sigma Aldrich) on an AFM stainless steel support. We used a multimode AFM (asmicro, Indianapolis, USA) with a Scout 350 silicon tip (Nunano, Bristol, Great Britain) in tapping mode at room temperature. The AFM images were further processed with Gwyddion. We used the graphite step-edges for height calibration. We selected the highest point of each protrusion as height measurement.

TEM

Ferritin (F4503-25MG) and GroEL (chaperonin 60, C7688-1MG) samples were purchased from Sigma Aldrich. Sample preparation was carried out using a standard native MS work-flow, including exchange of buffer to volatile ammonium acetate, as described before.[126] All samples were imaged using a Talos Arctica 200 kV (Thermo Fisher Scientific), and images were processed using RELION 3.1, as described in Esser *et. al*..[126] For staining, 30 nm amorphous carbon TEM grids (AGS160-4H, Agar Scientific) were plasma cleaned before deposition. After deposition, dry grids were placed on 25 µL of 2 % uranyl acetate, blotted, and left to dry. A control sample was prepared by applying 4 µL of 10 µM ferritin in PBS to the grid for 2 minutes, followed by blotting, washing and staining as described above.

Retention of enzymatic activity

The workflow we developed combines ES-IBD with an adapted photometric alcohol dehydrogenase detection kit (ab102533, Abcam, Cambridge, Great Britain).

Principle: ADH-catalysed oxidation of Propan-2-ol yields NADH and Propanone: NAD^+ + Propan-2-ol ⇌ NADH + Propanone. NADH reacts with a colorimetric probe to form a bright yellow complex analysed at λ = 450 nm. Whilst the manufacturer does not specify the exact mechanism of the kit, it is most likely based on the WST-8 to WST-8 formazan reaction.[137]

Preparation: All micro-centrifuge tubes and pipette tips were normal PP. All solutions were shielded from direct light and kept on ice, except where mentioned. Each kit was reconstituted according to the manual,[138] divided into 4 aliquots and refrozen at -20 °C. On the day of the deposition, we thawed one kit aliquot and the desalted ADH spray solution. We prepared two positive control ADH solutions from crystalline ADH in the supplied buffer to theoretical in-well activities of $4{\cdot}10^{-10}$ mol·min^{-1} and $4{\cdot}10^{-9}$ mol·min^{-1}. Reaction mix and background control solutions were prepared as in the manual and kept at room temperature. All solutions were prepared for a 150 µl total volume in well. This is made up of 50 µl active solution (buffer for blank, buffer for extraction or positive control) and 100 µl of either reaction mix (with substrate Propan-2-ol) or background control mix (no substrate). We measured the ADH spray solution absorbance and determined the concentration with a calculated absorbance coefficient of 195440 Lmol^{-1}cm^{-1}. Based on this concentration we prepared spray solution positive controls with the same theoretical in-well activity as the other two positive controls.

Deposition: We cut a conductive carbon double-sided tape (EM-Tec CT6, 15-000406, Labtech, Heathfield, Great Britain) in half. We removed two thirds of the protective film on the back and glued it to a stainless-steel AFM support. The entire protective film on the top side was removed and the target installed in the sample holder. We prepared two targets per repetition, one for the sample and one for the background control. To minimise contamination, we immediately installed the sample holder in the deposition vacuum chamber. The deposition followed the standard procedure. We filtered the beam to the ADH tetramer (5000...7000 m/z, see Fig. 73 in SI). The nano spray needle was protected from direct light. We deposited two

tapes with 27 ng (128 pAh) ADH for both repetition (A) and (C). For repetition (B), we deposited two tapes with 22 ng (102 pAh). The mass was determined based on the total deposited charge, most abundant charge state and molecular weight of ADH. In repetition (B), the deposited amount was lower due to low sample current. The landing energy was 5 eV per charge.

Submersion and Measurement: The entire kit except for the reaction mix / background control solutions was reverse-pipetted in a 96 Corning 3881 non-binding surface half area well plate (Corning Inc., Corning, USA). We were doing this in parallel to deposition of the second ADH target. This minimises both the time the deposited ADH targets spend in high vacuum and the time they are exposed to the atmosphere. Repetition (C) targets were left for 3 days in the high vacuum deposition chamber. Then, we put the two deposited tapes in a well with their empty side facing the wall and the centre optical path free. The wells were already filled with 50 µl assay buffer to avoid gluing the tapes to the well's wall. We added reaction mix or background control mix and closed the plate with a transparent lid. A FLUOstar Omega plate reader (BMG LABTECH GmbH, Ortenberg, EU) incubated the sample at 37 °C and read absorbance at 450 nm every 3 min for 2 h.

Data analysis: The initial slope of the NADH production (repetition (A): minute 3...15, (B): minute 0...6) was used for activity calculation. We subtracted background activity only if it was positive. Due to the high proportion of active ADH after deposition, we had to extrapolate the linear calibration for repetition (A) in the absorbance range from 1.6 to 2.5 (18 nmol NADH). To attenuate arising errors, we extended a non-linear calibration for repetition (B) to 2.7 (15 nmol NADH).

3.6 Acknowledgement

We want to thank the Nanoscale Science Department at the Max-Planck-Institute for solid state research, in particular Artur Küster, for the CAD-construction and manufacturing of the deposition stage. We acknowledge support from Thermo Fisher Scientific who provided the UHMR mass spectrometer within the framework of a technology alliance partnership. P.F. was supported by an University of Oxford chemistry departmental PhD stipend. T.K.E. acknowledges funding from the European Union's Horizon 2020 research and innovation programme under the Marie Sklodowska-Curie grant agreement No 883387. B.S. was supported by the Royal Society as a Newton International fellow (NIF/R1/181108). S.R. acknowledges funding from the BBSRC (EP/V051474/1). J.G. was supported by a Junior Research Fellowship at The Queen's College, Oxford.

Competing Interests: M.R.S., K.L.F and A.A.M. are employees of Thermo Fisher Scientific, the company that commercializes Orbitrap-based mass analyzers.

3.7 Supporting information available

The supporting information contains a detailed explanation of the factors influencing ion beam energy distribution, the voltages within the instrument and landing stage, exemplary AFM and TEM graphs used for the deposition spot size calculation, a scheme of the 2D-scan used to characterise the ion beam diameter, AFM graphs of denatured and native BSA on HOPG, a negative stain control TEM image of Apo/Holo-ferritin and additional information about the ADH activity experiment. It is available free of charge via the internet at https://pubs.acs.org/.[g]

g The SI is also available in the appendix of this document, see section 11.3

3.8 Statement of Authorship

Statement of Authorship for joint/multi-authored papers for PGR thesis

To appear at the end of each thesis chapter submitted as an article/paper

The statement shall describe the candidate's and co-authors' independent research contributions in the thesis publications. For each publication there should exist a complete statement that is to be filled out and signed by the candidate and supervisor **(only required where there isn't already a statement of contribution within the paper itself).**

Title of Paper	A preparative mass spectrometer to deposit intact large native protein complexes
Publication Status	xPublished □ Accepted for Publication □Submitted for Publication □Unpublished and unsubmitted work written in a manuscript style
Publication Details	Fremdling, P., Esser, T. K., Saha, B., Makarov, A., Fort, K. L., Reinhardt-Szyba M., Gault, J., Rauschenbach S., A Preparative Mass Spectrometer to Deposit Intact Large Native Protein Complexes, ACS Nano 2022, XXXX, XXX, XXX-XXX, Publication Date: August 29, 2022, https://doi.org/10.1021/acsnano.2c04831

Student Confirmation

Student Name:	Paul Fremdling		
Contribution to the Paper	• Converted analytical mass spectrometer for deposition: Designed half of the parts, machined small parts, assembled the landing stage, and wrote software to control it. • Performed all experiments together with T. K. E. • Developed the adapted enzymatic assay procedure with advice from B. S. • Analysed all data and drew all figures, with exception of Figure 6 • Wrote the manuscript, with exception of the section "Mass-selective preparation of cryo-EM protein samples" • Compiled the supplementary information • Revised the manuscript based on reviewer comments		
Signature	Paul Fremdling	Date	**14/09/22**

Supervisor Confirmation

By signing the Statement of Authorship, you are certifying that the candidate made a substantial contribution to the publication, and that the description described above is accurate.

Supervisor name and title: Stephan Rauschenbach, Prof. Dr.			
Supervisor comments This paper is the original work of Paul Fremdling. All data originates from his DPhil work or is closely related to it. He is the main contributor of the content of the paper, most data and analysis were made by him.			
Signature	S. Rauschenbach Stephan Rauschenbach	Date	**14/09/22**

This completed form should be included in the thesis, at the end of the relevant chapter.

4. RF ion funnel transmission

Ions generated with an atmospheric-pressure ionisation technique, such as ESI, APCI[139] or AP-MALDI[140], require transfer into high-vacuum for MS analysis. Capillaries of typically, 0.6[141] to 1 mm[96] diameter transfer the ion-droplet-air mixture into the first vacuum chamber. These large capillaries avoid large ion current losses due to space charge.[96], [142] The gas throughput of a 1 mm diameter capillary into low vacuum is about 125 mbar*l/s[h]. This is an order of magnitude too high for the capability of a powerful turbo-molecular pump[143]. High vacuum (10^{-6} mbar) necessary for MS analysis cannot be obtained in the inlet chamber. Hence, an additional differential pumping stage in low vacuum (1...10 mbar) is needed.

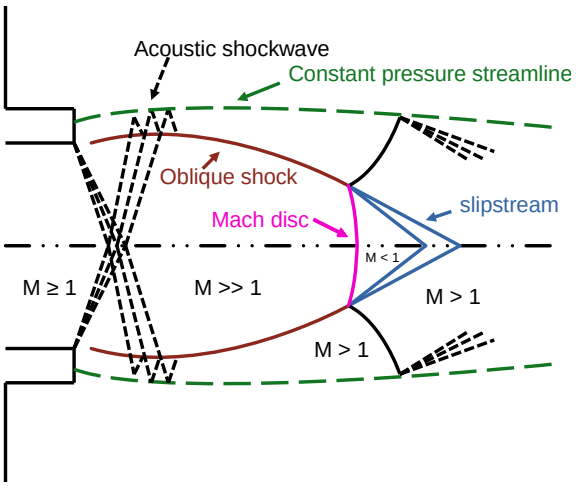


Figure 14: Structure of a very highly underexpanded jet. M is the Mach number[144]

Due to high pressure difference between the outside air and the low vacuum chamber a zone of supersonic, choked flow forms at the exit of the capillary.[144] It is a very highly underexpanded jet.[144], [145] Inside the jet, pressure and temperature are extremely low, the gas velocity is a multiple of the supersonic speed (Figure 14). The jet causes acoustic shock waves.[144] The streamline which marks the transition to the chamber pressure reflects them.[144] They compress the jet in an oblique shock.[144] A single sharp transition from supersonic to subsonic flow, the Mach disc, takes place.[144] The air flow can regain supersonic speed after a slipstream zone.[144]

h Estimation based on own measurement of 1 mbar pumping pressure with a 450 m³/h roots pump

Analyte ions accelerate in the supersonic expansion with the air. They are projected at high speed in a hemisphere. The task is to confine these high-speed ions to form a beam. This is very difficult with a conventional multipole ion guide. The guide volume needs to be larger than the dimensions of the underexpanded jet. The larger a multipole is, the lower is the depth of the effective potential well at a set RF amplitude. Figure 15a) shows the radial effective potential barrier is only 0.4 eV for small molecule in a 20 mm-radius octupole[i].

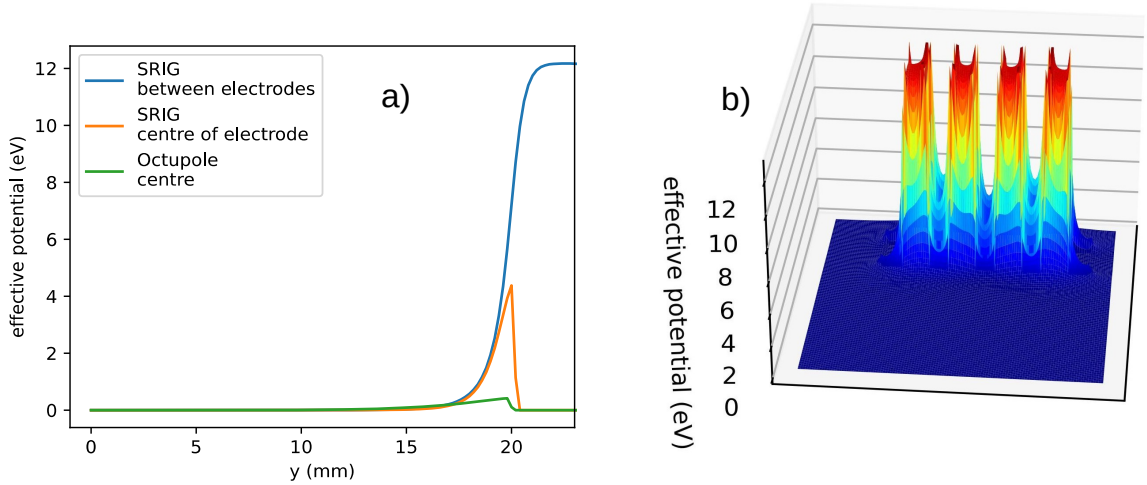


Figure 15: a) Comparison of the radial effective potential of an Octupole and a SRIG for hexamethoxyphosphazene in high vacuum. Both ion guides have 20 mm trap radius. RF Amplitude = 80 V, v=1 MHz, no DC gradient. b) 3D Projection of the effective potential across the centre plane of the SRIG. Valleys are electrode positions, maxima appear at the edges of the electrodes and have been smoothed.

In addition, with the high pressure limiting ion mobility, extremely high RF amplitudes would be required to confine the ion cloud. Instead, the problem of transferring ions requires a different solution.

4.1 Ion funnel: principle and ion transport parameters

Principle:

Early electrospray experiments used a cone-shaped skimmer placed in the centre of the supersonic expansion (Figure 16).[146] It has two functions: First, it limits the gas throughput to

i At a moderate RF amplitude of 80 V at 1 MHz for hexamethoxyphosphazene

the following vacuum chamber. Only a small fraction of the air-ion plume passes through the centre opening. Second, the sampled air-ion plume fraction has a dominant supersonic speed component in axial direction.[147] This limits the relative radial spread in the following chamber and increases transmission efficiency.[147]

However, at least 80 % of the current is lost in the air-ion plume diverging around the skimmer.[148, p. 43]. A skimmer does not discriminate between air and ion transmission. Higher ion transmission requires a bigger opening and comes with higher gas load on the following chamber. Thus, an ion guide which separates ions from air is required: The ion funnel.

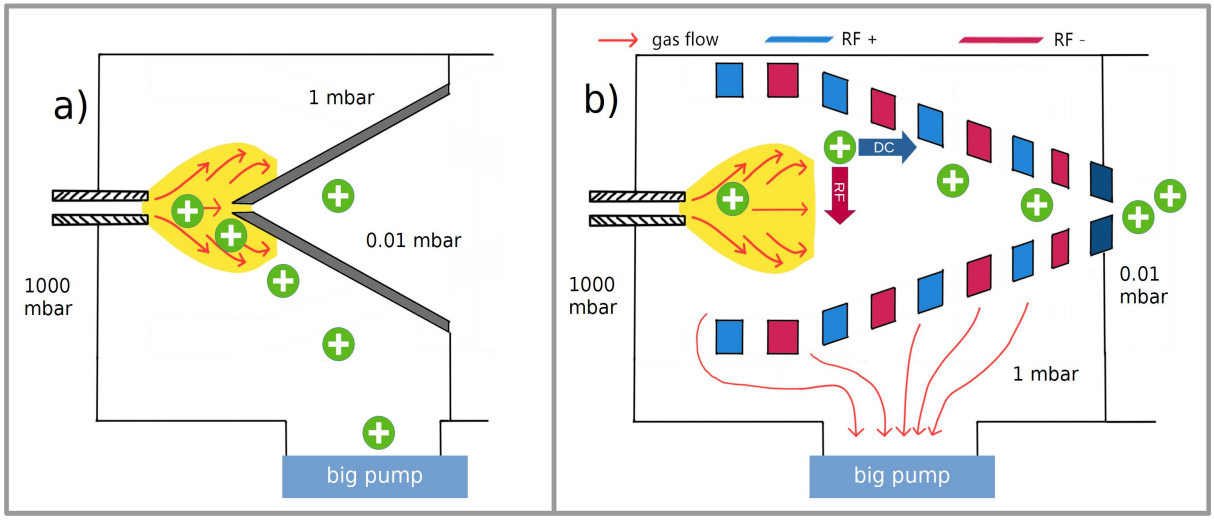


Figure 16: Schematic of a) a skimmer and of b) an ion funnel (right).

It is a stacked-ring-electrode ion guide (SRIG) with a decreasing inner diameter (Figure 16). The supersonic expansion takes place within the large-diameter section of the funnel. An RF-voltage with opposing phase applied to neighbouring ring electrodes generates a time-dependant electric field: the effective potential. This field traps the ions in the funnel laterally[149]. The air can exit the funnel through openings at the beginning of the funnel and between the electrodes to the pump. In contrast to multipole ion guides, the effective potential in the SRIG is not a function of the trap diameter (i.e. inner diameter, see Figure 15). Instead, the effective potential rises as the spacing between adjacent electrodes becomes smaller. Thus, it is possible

to confine the ions with moderate RF amplitudes (50...200 V). The tapered section of the staggered-ring-electrodes collimates the ions on the orifice to the following vacuum chamber. Often, a DC-gradient is superimposed on the RF to move the ions towards the orifice.[150]

Ion transport parameters:

To simulate ion trajectories within an ion funnel, we need to know physical properties of the ion and the funnel. Specific to the funnel are the gas flow field and the effective potential. The gas flow field is described by the local temperature T, local pressure p, and the local gas velocity $\vec{v}_g$. The effective potential is a measure for the energy landscape the electric field forms. It also depends on the ion's mass-to-charge ratio (see section 2.1). The high gas pressure dampens the motion of the ions in the funnel. They usually do not gain energy from the RF, so the adiabaticity is not a critical parameter (see section 2.2).

The ion properties which determine the behaviour in a high-pressure ion optics are the ion mobility and the particle response time. The ion mobility K is the quotient of

$$K = \frac{|\vec{v}_d|}{|\vec{E}|} \tag{4.1}$$

the steady-state drift velocity $|\vec{v}_d|$ and the electric field strength $|\vec{E}|$ [91]. The higher K, the faster an ion moves through a buffer gas at constant, low electric field. K relates to the frequency of ion-neutral collisions.[91] Thus, it depends on the gas type, T, and p. For easier comparison between different ions the reduced mobility K_0 is more useful[91]:

$$K_0 = K \frac{p}{p_0} \frac{T_0}{T} \tag{4.2}$$

It is normalised to the standard pressure $p_0 = 10^5\,\mathrm{Pa} = 1000\,\mathrm{mbar}$ and standard temperature $T_0 = 273.15\,\mathrm{K}$ [80]. Note, it often seems more common in the ion mobility community to use

$p_0 = 1013.25\,\text{mbar}$ without indicating it.[91] Furthermore, close to nobody reports experimental K_0 values. Instead, K_0 can be calculated from collisional cross section (CCS) values: [91], [151]

$$K_0 = \frac{3}{16}\sqrt{\frac{2\pi}{\mu k_B T}}\frac{ze}{N_0}\frac{1}{\Omega_c} \tag{4.3}$$

with μ the reduced mass of the ion-gas pair, k_B the Boltzmann constant, z the charge state of the ion, e the elementary charge, N_0 is Loschmidt's number and Ω_c is approximately the CCS. The ion mass m_{ion} and the gas mass m_{gas} set the reduced mass:[91]

$$\mu = \frac{m_{ion} m_{gas}}{m_{ion} + m_{gas}} \tag{4.4}$$

Note that often in the ion mobility literature important necessary parameters, such as the exact T, are not reported.[91] In addition, I used a wrong N_0 value[j]. Therefore, all K_0 values calculated for ion trajectory simulation in this work contain a systematic error of at least 7 %.

Besides the ion mobility K, the second important property is the particle response time τ_p, a measure for the inertia of an ion (see section 2.2).

State of the art:

Ion funnels are in use in many instruments. In recent years, mass spectrometrists have developed a variety of ion funnels. Some designs fundamentally differ from the original tapered, stacked-ring ion guide with axial inlet [77]. They follow three development directions: A) Control of the supersonic gas expansion, B) Control of the gas throughput and C) Other approaches to improve performance.

j $N_0 = 2.504 \cdot 10^{25}\,m^{-1}$ was wrongly used, which is the value at $T = 293.15\,\text{K}$ instead of the right value $N_0 = 2.686 \cdot 10^{25}\,m^{-1}$ at $T = 273.15\,\text{K}$. This leads to an error of 7 % on calculated K_0 values.

To control the gas flow after the supersonic expansion, Fasmatech constructed a gas-tight stacked ring ion guide coupled to a funnel.[152], [153] Tridas et al. investigated a jet disruptor to stop the supersonic flow within the funnel.[154] Draper et al. sealed the ion funnel completely to only allow pumping via the inlet opening.[95] The seal slows the gas flow in the final section, as well.[95]

Gunaratne et al. reported a tandem funnel setup to use big transfer capillaries with minimum pumping power.[142] Later, they took advantage of the high gas throughput this configuration can handle to use multiple, orthogonal inlets.[33] Walz et al. added a thin gas-tight 40 mm long SRIG to the end of the funnel.[32], [155] This reduced the gas throughput in chamber after the funnel by an order of magnitude.[32], [155]

Tolmachev et al. built a hyperbolic funnel asymptotic to the central axis.[97] It had a small electrode spacing to minimise electrodynamic trapping in the final funnel section.[97] They measured good transmission at low RF amplitudes.[97] Albrecht designed a tandem ion funnel for trace gas MS analysis.[156] The first funnel operates at 100 mbar to allow direct sampling without a transfer capillary from the stratosphere.[156] Chen et al. showed that the inner geometry of an ion funnel works even when it is rectangular.[157] Egovora et al. placed an ion funnel in the wrong position in an inductively-coupled-plasma MS and noted it did not work well.[158] Thermo Fisher Scientific commercialised an RF-only ion funnel with larger electrode spacing instead of a tapering diameter to attempt better focusing without trapping.[159]–[161] They reverted to a conventional funnel in later designs.[162] In combination with a bigger transfer capillary, overall ion current tripled.[162]

All in all, many different ion funnel setups work. Often it is not clear why. Based on the literature review, this chapter addresses two fundamental areas: The role of the gas flow and the effective potential.

Gas Flow questions:

Tridas[154], Albrecht[156], and Brunner[163] made computational fluid dynamics simulation of the gas flow within an ion funnel. The geometries (Brunner & Tridas) or pressure ratio (Albrecht) are very different from a conventional ion funnel. Hence, these simulations allow very limited conclusions on the role of the gas flow in there. As both the conventional funnel and supersonic gas expansion controlled setups (category A) have good transmission efficiency, a number of fundamental questions remain open:

- Does the gas flow support or hamper the transport of the ions?
- In particular, the role of the supersonic jet is unclear. Does it support the transport of the ions? Should it get disrupted?
- What is the effect of the pressure on trajectories of light and heavy ions?

Effective Potential questions:

Shaffer and Tolmachev calculated the RF part of the effective potential soon after the invention of the ion funnel[97], [164]. They noted that in the final section an ion trap can form. Since then, the effective potential inside an ion funnel has received little attention. Although laboratory experience suggests the DC contribution influences the trapping, no publications exist which investigate both the RF and the DC contribution. Given the range of different geometries built (category C), more questions on the effective potential landscape arise:

- What is the effect of electrode spacing and funnel shape on the effective potential landscape?
- How does the funnel shape influence electrodynamic trapping of ions in the final section?

Three principal approaches are possible to answer these questions: Ion trajectory simulation, calculating the effective potential and experiments.

Ion trajectory simulations require to calculate the gas flow field and the (dynamic) electric field. Computational fluids dynamics (CFD) can calculate numerically the entire gas flow field [165]. CFD simulation of the gas flow field in an ion funnel is a challenge because of the interaction of the supersonic expansion with the complex geometry of the electrodes. Within the supersonic expansion, several order-of-magnitude jumps in gas pressure, temperature and velocity take place. The extension of the jet depends on the flow in the inter-electrode space. This flow is computationally expensive to model due to the low inter-electrode spacing and the high number of electrodes.

The resulting gas flow field is then integrated into an electrodynamic ion trajectory simulation program, such as Simion. Simion's SDS or HS1 package allow to add ion-gas interaction.

Currently, the ion trajectory calculation software Simion has a very limited implementation to calculate the effective potential. It does neither support the calculation of the effective force, nor the adiabaticity and neglects the DC contribution. It is possible though to calculate the effective potential taking the DC contribution into account, the adiabaticity and the effective force based on the Simion potential array solutions (see section 2.4).

Experimental transmission efficiency measurements are difficult. They require to measure both the incoming and the transmitted ion current. Two problems exist: First, the incoming current is the emitter current minus the losses in the transfer capillary. The challenge is a floating measurement at the emitter voltage (several kV) of the low-nA emitter current. Besides, on the transfer capillary current leak currents from the capillary heater cartridge are superimposed. Second, the experimenter must measure the transmitted current directly after the

funnel. Otherwise, the transmission function is a convolution of the funnel with the following ion guides.

To answer the questions on the effective potential and the role of the gas flow I

- Measured transmission of a conventional funnel as a function of pressure, RF amplitude, incoming current and DC gradient. This data was used by the collaborators Laurent Bernier, Phillip Krah, Loukas Kyriakidis and Julius Reiss (TU Berlin). With it, they validated a CFD simulation of the gas flow field.[78]

- Investigated a new funnel geometry with Simion ion trajectory simulation. The model incorporates a full gas flow field, which Laurent Bernier simulated.[78] Two different transfer capillary configurations show the role of the supersonic jet. The effect of pressure and RF trapping were analysed for small and heavy ions.

- Calculated the effective potential with both DC and RF contributions. I analyse its effects on RF trapping.

Based on the results, I propose a simplified model for the processes in a conventional funnel and a new, 2-chamber design with hydrodynamic focusing to minimise the vacuum pumps.

4.2 Experimental investigation of a conventional funnel

In this section, I investigated the transmission of ion current through a conventional ion funnel. To this end, I measured the electrospray emission current, the losses on the transfer capillary and the transmitted current on an electrode in the next vacuum chamber. The funnel is part of an existing ES-IBD instrument.[166] I measured transmission as a function of the RF amplitude at different pressures and transmission as a function of the entering current. Finally,

I measured the effect of the DC gradient on transmission. Thereby, information on the function and limitations of a conventional ion funnel was gained.

Experimental details and methods

The ion funnel has 82 electrodes of 1.1 mm thickness spaced 0.7 mm apart (Figure 17). The initial cylindrical SRIG section is ~ 5 cm long and has 3 cm inner diameter. The funnel-shaped section is ~ 10 cm long. Its inner diameter decreases linearly to 2.5 mm.

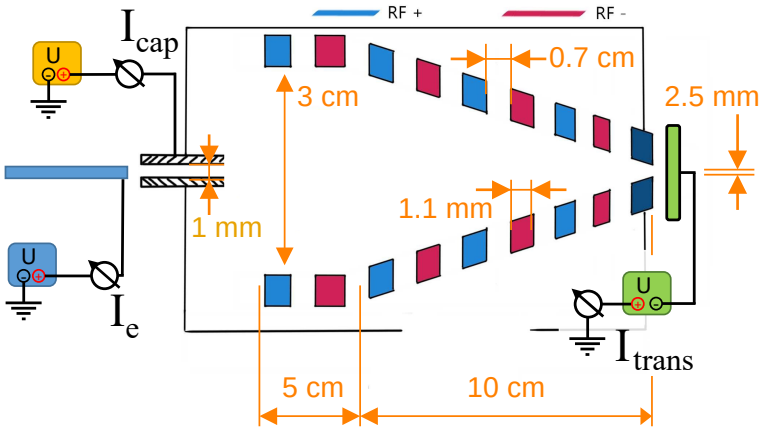


Figure 17: Funnel geometry and measurement setup used to determine transmission efficiency.

Ions enter through a 1mm diameter funnel-shaped transfer capillary. A roots pump of 490 m^3h^{-1} pumping speed allows for 1 mbar operation pressure. For more information on the geometry see Bernier 2020.[78, p. 13]

Two floating picoammeters (9103 HV, RBD Instruments Inc., Bend, USA) measured the emission current I_e and the transfer capillary current I_{cap} (Figure 17). A non-floatable RBD 9103 picoammeter monitored the transmitted current I_{trans}. The short-circuited rods of the quadrupole in the next vacuum chamber were the ion collector target. To ensure the entire transmitted current was collected, the target was biased to an attractive potential of -37 V with isolated batteries. The voltage on the online-nano-ESI emitter was +2.7 to +4.3 kV. Transfer capillary voltage was 250 V. The first funnel electrode was at 150 V, the final electrode at 100 V. All voltages are against GND. The funnel RF frequency was 1 MHz. I adapted the nitrogen curtain gas flow, the emitter voltage and emitter position for maximum transmitted current.

The probe molecule was Rhodamine B, a small organic dye. All ion specific parameters are summarised in Table 2. Spray concentration was 10^{-5} mol·l^{-1} in 1:1 EtOH:H_2O. The flow rate was 20 µl·h^{-1}.

Table 2: Mass to charge ratio, CCS, reduced mobility in nitrogen and particle response time for used ions. "" denotes calculated values*

Molecule	**m/z (ue^{-1})**	**CCS (10^{-18}m^2)**	**K_0 (10^{-4} m^{2}V^{-1}s^{-1})**	**τ_{p0} (10^{-9}s)**
Hexamethoxyphosphazene$^+$	322.05[k]	1.54 [81]	1.41 *	0.47 *
Rhodamine B cation	443.57	2.44 *	0.89 [82]	0.41 *
Apomyoglobin^{8+}	2119	22 *	0.80 [83] [l]	1.76 *
GroEL^{67+}	≈11955	220 [84]	0.66 *	8.19 *

The heating of the transfer capillary was turned off during the current measurements to avoid leak or pick-up currents from the capillary heater. Each measurement is an average of 12 s (300 data points). These are the standard experimental conditions.

Transmission ratio η is the quotient of the transmitted to the entering current. The entering current is the emitter current minus the losses on the transfer capillary:

$$\eta = \frac{I_{trans}}{-I_e - I_{cap}} = \frac{|I_{trans}|}{|I_e| - |I_{cap}|} \tag{4.5}$$

In positive mode, the emitter is the anode of an electrolytic cell, and all electrodes down-stream are cathodes. Hence, I_e has the opposite sign.

Pressure and RF-amplitude dependency

To investigate the pressure dependence of the ion funnel transmission, I recorded transmission at 3, 10, and 22 mbar. Nitrogen gas added via a dosing valve in the roots pump vacuum line decreased the effective pumping power to reach 3 and 10 mbar. A partially closed gate valve restricted the pump to attain 22 mbar. For each pressure, the RF amplitude (V_{RF}) was varied between 0 and 130 V. Initial measurements at 3 mbar include transmission at RF amplitudes

k In all Simion simulations presented here, I used 321.15 by mistake. The resulting error is negligible.

l Shelimov et al. reported $2.7 \cdot 10^{-4}$ in He, which was divided by 3.4 to get K_0 in N_2. Conversion factor 3.4 according to Matz et. al.[167].

higher than 130 V. This ignited a discharge in the funnel. So I did not record high-RF values (V_{RF} > 130 V) for other pressures.

Figure 18a shows the current as a function of the RF amplitude for 3, 10, and 22 mbar. At 3 mbar, transmission set on at 20 V_{RF}. The transmitted current rises sharply until 80 V_{RF}. It levels off to reach a plateau around 4 nA and slightly declines at high RF amplitudes. At 10 mbar, the transmission onset is at 60 V_{RF}. A plateau at 2 nA forms between 100 and 130 V_{RF}. In contrast, currents stay below 0.5 nA for all V_{RF} at 22 mbar.

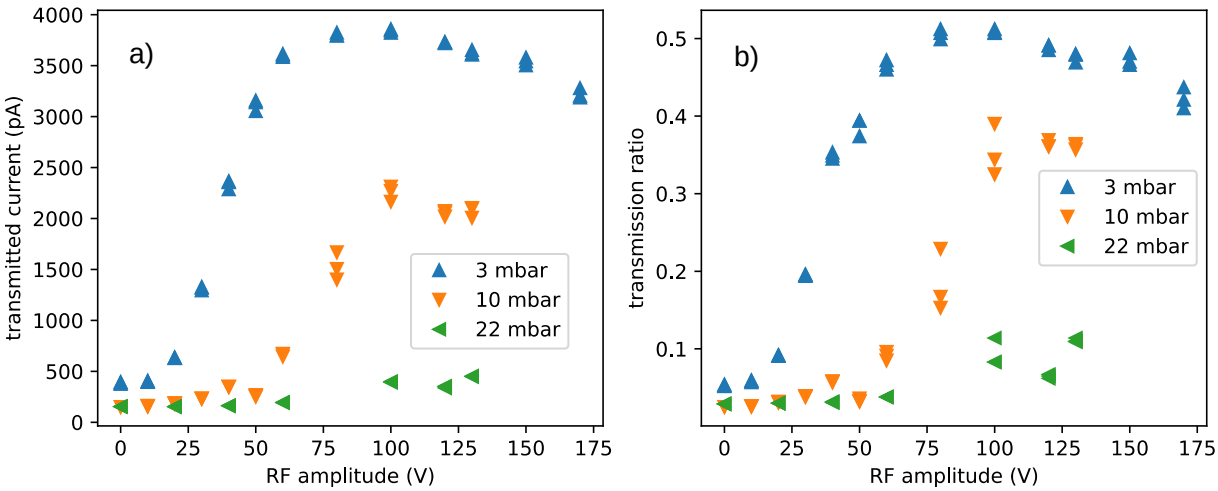


Figure 18: a) Transmitted current and b) transmission ratio for 3 different pressures as a function of the RF amplitude. Measured on the conventional 82-electrode funnel.

Transmission ratios follow the same trend (Figure 18b). Maximum transmission efficiency is 51 % at 3 mbar (V_{RF} = 100 V), 36 % at 10 mbar (V_{RF} = 120 V) and 11 % at 22 mbar (V_{RF} = 130 V).

The delayed onset of transmission current is a result of the lower ion mobility *K* at higher pressures. *K* is inversely proportional to the pressure (equation 4.2). When the ion mobility is low, the gas dampens the RF-induced motion of the ions. It becomes more difficult to confine them, i.e. the change of trajectory is reduced by the gas interaction. The ions can collide and be lost on the funnel electrodes.

In the 3 to 10 mbar pressure range, a higher RF amplitude can counterbalance the lower ion mobility. The higher RF amplitude increases the effective potential wall which keeps the ions away from the electrodes. At 22 mbar, this is not possible any more for $V_{RF} \leq 130$ V. These results are in agreement with other observations reported. The general shape of the transmission function, i.e. no transmission at low V_{RF}, increase to a maximum, slight decrease at high V_{RF}, is similar to Shaffer 1999.[164] Also, the measured data reproduces the shift to higher transmission onset voltage with higher pressure.[164] Su et al. as well observed decreasing transmission at high pressures, which indicates losses due to insufficient containment of the ions within the funnel.[33]

It is unclear if the difference in maximum transmission ratio between 3 mbar (51 %) and 10 mbar (36 %) is an effect of pressure or of fluctuating emitter performance. The online-nano emitter used generally fluctuates. Measuring one pressure condition takes 2 h due to switching the capillary heating on and of (see “Experimental details and methods”). For this reason, the measurements took place on different days. Emitter performance was not fully reproducible. For instance, at 1 mbar three attempts to obtain a smooth measurement without fluctuating emitter did not succeed. The maximum transmission ratio fluctuated between 28 % and 50% (Figure 76b in Appendix). Nevertheless, the obtained data demonstrates that transmission at 1 mbar and 3 mbar is similar (Figure 75b in Appendix).

Overall, the existing, conventional ion funnel has a high transmission ratio plateau (~ 0.5) over a large V_{RF} range for 1 to 3 mbar pressure. Therefore, the experimenter could fit either a smaller (200 $m^3 \cdot h^{-1}$ instead of 490 $m^3 \cdot h^{-1}$) pump to save energy. Or they increase the transfer capillary diameter or fit multiple transfer capillaries with the existing pump to obtain higher incoming currents.[33], [79]

Estimation of the space charge limit

The space charge limit is the maximum possible transmitted current through the funnel. At this current, the mutual repulsion of the ions within the ion beam becomes so strong that the effective potential cannot contain them anymore. The ions hit the funnel electrodes and discharge on them. An estimation of the space charge limit helps to contextualise the results of the next paragraph,"Variation of input current", which discusses the transmission as a function of the entering current.

Pauly et al.[96] proposed a simple model based on the calculation of the radial space charge force F_{sc} on an ion:

$$F_{sc} = \frac{q \cdot I \cdot r}{2\pi \cdot \epsilon \cdot v \cdot R_{beam}^2} \tag{4.6}$$

It assumes an infinitely long ion beam of radius R_{beam}. Inside the beam, the ions with charge q are travelling at the axial velocity v in a (residual) gas with permittivity ε. r is the radial distance of the ion from the beam axis and I is the beam current. For the ion funnel, this model assumes that at the space charge limit current, F_{sc} equals the effective potential force F_{eff}:

$$F_{eff} = F_{sc} \tag{4.7}$$

F_{eff} varies across the funnel. Ion losses due to space charge are most likely at the place where the beam diameter is small (maximum F_{sc}) and F_{eff} is weak. Figure 19a shows the effective potential in the funnel for the standard experimental conditions and 60 V RF-Amplitude. These are the same conditions as used for experimental investigation (see paragraph "Variation of input current" below).

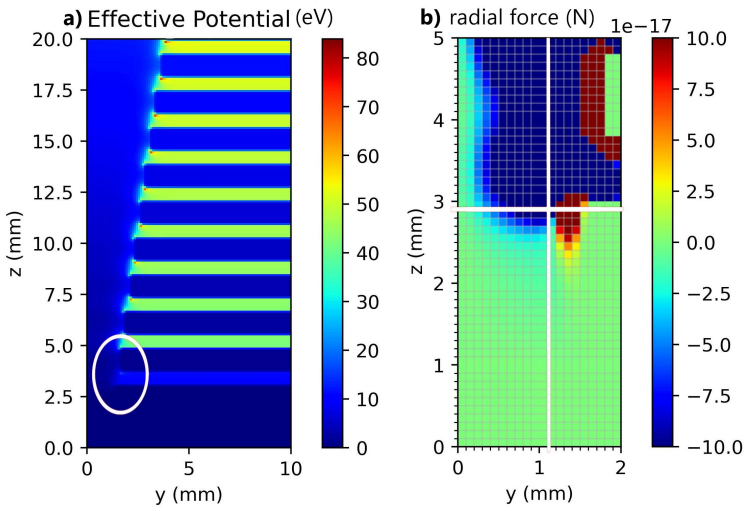


Figure 19: a) Effective Potential in HV in the centre plane of the existing ion funnel. y is the radial coordinate, z the axial. b) Effective potential force in the centre plane in HV. Final two electrodes are shown.

The white circle marks the critical region of the weakest effective potential. It is within the final electrode for the existing ion funnel. This electrode is DC-only. Hence, the effective potential barrier confining the ions is lower than for the previous electrodes. Furthermore, it has the smallest diameter (2.5 mm), so F_{sc} is maximal.

It is difficult to define the maximum beam diameter R_{beam} to calculate F_{sc} and F_{eff} . Figure 19b shows the radial effective force in the area between the final two electrodes of the existing funnel. In the opening of the last electrode (z = 1.9…3.0 mm), the effective radial force becomes attractive towards the funnel electrodes for r > 1.2 mm. Consequently, R_{beam} must be smaller. I decided to use r = R_{beam} = 1.1 mm and z = 2.9 mm to calculate F_{sc} and F_{eff} .

The maximum possible current results from equations 4.6 and 4.7. The funnel operation pressure of 1 mbar is above the critical pressure $p_{f,crit}$. (see section 2.2). Therefore, I multiply the effective force with the correction factor c_{gas} to compensate for the diminished effect of the RF. The gas velocity in the final electrode is at least 300 ms^{-1}.[78, p. 70] Assuming the ions travel at the same speed, the maximum transmitted current is:

$$I_{max} = \frac{c_{gas} F_{eff,vac} 2\pi \epsilon v_g R_{beam}}{q}$$

$$I_{max} = \frac{0.88 \cdot 4 \cdot 10^{-16}\,\mathrm{N} \cdot 2\pi \cdot 8.85 \cdot 10^{-12}\,\mathrm{Fm^{-1}} \cdot 300\,\mathrm{ms^{-1}} \cdot (1.1 \cdot 10^{-3}\,\mathrm{m})}{1.602 \cdot 10^{-19}\,\mathrm{C}} \approx 40\,\mathrm{nA} \quad (4.8)$$

It is possible to reach higher maximum currents: A higher RF amplitude increases F_{eff}, countering F_{sc}. A higher DC gradient increases the ion velocity, so F_{sc} becomes smaller. Furthermore, if the diameter of the final ion funnel electrodes and the aperture to the next ion optic is widened, a bigger beam diameter R_{beam} allows a higher current as well.

As the effective force depends on the axial position (Figure 77 in Appendix), the maximum current obtained is just an order-of-magnitude estimation. The obtained result is close to the 30 nA Gimelshein et. al reported.[168] A full ion trajectory simulation taking into account ion repulsion and the gas flow field is necessary for better accuracy.

Variation of input current

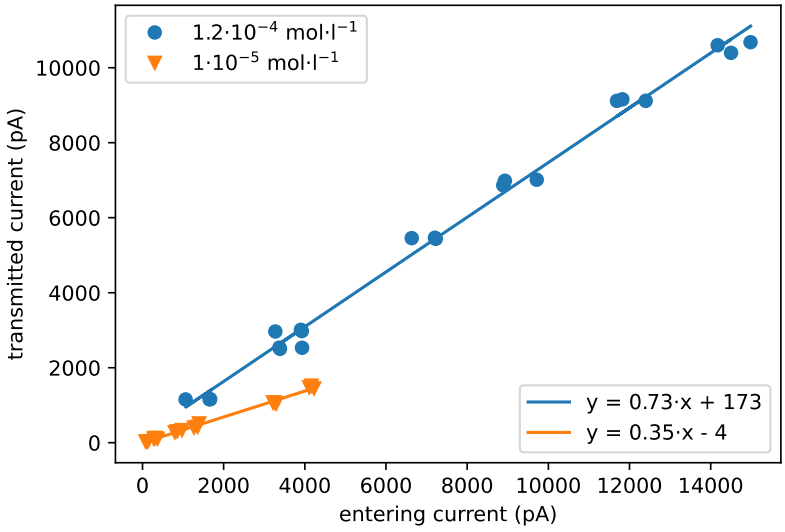


Figure 20: Offset-corrected transmitted current as a function of the entering current. Entering current varied with different emitter positions. Measured on the existing 82-electrode funnel. The slope corresponds to the transmission ratio.

In the experiment, I varied the current entering the ion funnel to test how the transmission efficiency depends on it. I used two different Rhodamine B concentrations: 10^{-5} mol·l^{-1} and $1.2 \cdot 10^{-4}$ mol·l^{-1} in 1:1 EtOH:H_2O. I applied the standard experimental conditions (see subsection "Experimental details and methods"). The RF-amplitude was 60 V, the pressure 1 mbar. To

change the entering current, I moved the spraying emitter from the centre to the edge of the transfer capillary funnel. The entering current into the ion funnel got smaller with increasing radial emitter displacement. That is because most of the emission current got lost on outside of the transfer capillary.

I also recorded the offset of both the transmitted and entering current. To do this, I moved the emitter below the rim on the outside of the transfer capillary funnel, where no transmission is possible. For all positions, emitter current was stable as I kept the distance to the transfer capillary funnel constant.

Figure 20 shows the transmission for different entering currents. Maximum transmission for $1.2 \cdot 10^{-4}$ mol·l^{-1} Rhodamine B was 73 %, for 10^{-5} mol·l^{-1} 35 %. The maximum transmitted current was 10.6 nA (c = $1.2 \cdot 10^{-4}$ mol·l^{-1}).

This is the first reported measurement of transmission as a function of the entering current. It proves that at constant emitter conditions (analyte concentration, voltage,…), the transmission is independent of the entering current. Hence, this funnel operates below its space charge limit. This is in accordance with the estimated maximum current of about 40 nA.

A reason for the lower transmission at the lower concentration (10^{-5} mol·l^{-1}) can be statistical competition of the Rhodamine B analyte ions with small impurity ions present in the solution[25], [169]. This could be Na^+ from the borosilicate emitter or H_3O^+ from water. Both have a very low m/z-ratio. It is very unlikely that RF field in the ion funnel can transport them due to the low frequency. Therefore the incoming current consisted of Rhodamine B plus small impurity ions, and the transmitted current mostly of Rhodamine B. This composition led to an overall transmission lower than unity.

Compared to maximum transmission literature values, the 35 to 73 % are in the same range: Tridas et al. investigated this for different voltages on a jet disruptor electrode, and reported

57 % maximum transmission.[154] Albrecht measured transmission through each of the two tandem funnels as a function of the RF Amplitude. He found a maximum of 29 % for the 100 mbar and 50 % for the 5 mbar funnel. Kim et al. reported a maximum of 60 % for a conventional funnel.[170]

The 10.6 nA maximum transmitted current is higher than values for other single-emitter designs. Shaffer et. al reported 4 nA for a conventional funnel,[164] Gunaratne 7.5 nA for a dual-funnel with orthogonal inlet.[142] Up to 24 nA are possible with multiple emitter and transfer capillaries.[33] Therefore, the bottleneck for maximum ion current of small organic molecules is not the existing ion funnel. The challenge is to generate enough input current. The atmosphere-pressure interface with a single emitter and a single transfer capillary limits the maximum transmitted current of small organic ions with the investigated conventional funnel.

DC-Gradient variation

I measured the transmitted current as a function of the DC-Gradient along the funnel axis. I varied the DC-Gradient between -200 V (attractive towards ion funnel exit) and +200 V (repulsive). I used the standard experimental conditions with an adaption for the transfer capillary voltage. This was at a +100 V offset to the first electrode of the funnel. I investigated three pressures: 1, 3 and 10 mbar. The RF amplitudes were different: 60 V for 1 and 3 mbar, 120 V for 10 mbar.

It was not possible to calculate the total transmission over the ion funnel. This is due to the varying voltage on the transfer capillary, which caused the transfer capillary current I_{cap} - background to change. The change due to leak currents was so big it exceeded the range of the picoammeter. Thus, instead of calculating the transmission ratio, I normalised the transmitted current of each series to its maximum.

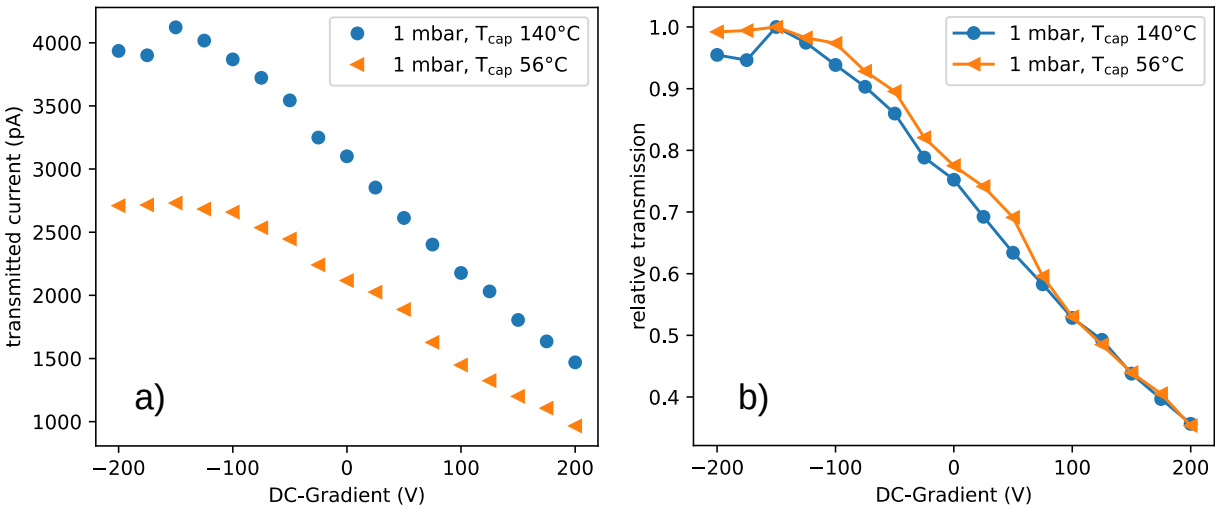


Figure 21: a) Transmitted current through the existing ion funnel as a function of the axial DC gradient for 1 mbar and two different initial transfer capillary temperatures. b) Relative transmission normalised to the maximum value for each series as a function of the DC gradient.

The transfer capillary heating was switched off in an attempt to limit the leak currents. This caused the transfer capillary to cool down during the measurement. I recorded two series at 1 mbar with different initial transfer capillary temperatures: 56°C and 140°C. Figure 21a shows this does change the absolute transmitted current. Figure 21b shows the relative transmission remains similar. I chose 140°C initial temperature for all further experiments. Furthermore, transmission increases with a stronger DC gradient towards the funnel exit in the range +200 to -150 V. Transmission remains maximal in the range -150 to -200 V. See section 4.5 for a discussion of an underlying reason.

Figure 22a shows transmitted current as a function of the DC gradient for 1, 3, and 10 mbar pressure. Transmitted current drops from 4 nA at -150 V to 1.5 nA at +200 V. The 3 mbar curve is in the same range, whereas at the 10 mbar transmitted current remains low for all DC-Gradients. The lower transmission at high pressure (10 mbar) is similar to the data for the variation of the RF amplitude (Figure 18). At 10 mbar, the ion mobility is too low for an effective confinement within the funnel.

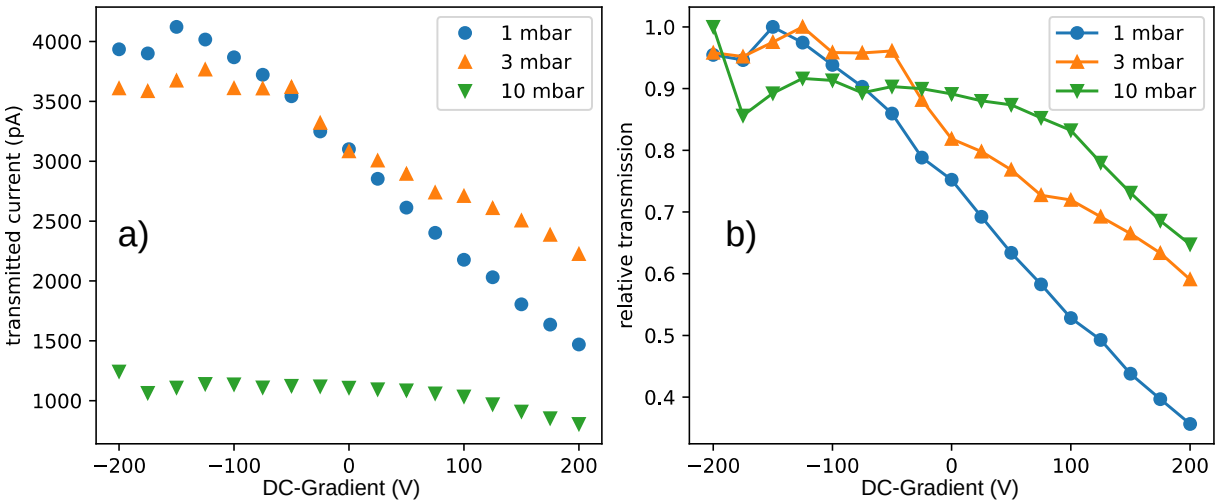


Figure 22: a) Transmitted current through the existing ion funnel as a function of the axial DC-Gradient for 1, 3 and 10 mbar. b) Relative transmission normalised to the maximum value for each series as a function of the DC-Gradient.

The relative transmission data (Figure 22b) shows the influence of the DC gradient is strong at low pressure. A 200 V repulsive DC-Gradient lowers transmission by ⅔ at 1 mbar, but only by ⅓ at 10 mbar. Once again, the decrease of the ion mobility with higher pressure is a likely explanation. At higher pressure, the ions motion is dominated by the gas flow. The DC-gradient becomes less important.

An attractive gradient of at least -150 V leads to optimum transmission. At higher pressure, the DC gradient has a smaller influence on transmission.

In summary, the conventional funnel transmits small organic ions with about 50 % efficiency with moderate RF amplitudes (80...130 V) in the 1...3 mbar pressure range. An attractive DC gradient is necessary. The funnel operates below the space-charge limit, the bottleneck for small organic ions is the emitter/transfer-capillary atmosphere-vacuum interface.

4.3 Ion trajectory simulations of new ion funnel geometries

Following the experimental investigation of the properties of an existing funnel, I used ion trajectory simulation to study the ion transport in a funnel. To that end, I chose several new funnel geometries different from the existing funnel. The first geometry, funnel A, has two main geometry changes to test if the ion funnel properties improve:

- Parabolic shape. Tolmachev et al. showed RF-trapping can occur in the final section of a conventional funnel.[97] They proposed a tight electrode stacking and a big final electrode opening to minimise the trapping (inner-electrode-diameter to electrode-spacing ratio > 1). However, tight electrode spacing impedes the gas flow from the inside of the funnel towards the pump. It also increases the electrical capacity of the RF-Electrodes. A parabolic shape is an alternative because the critical, final section with small internal electrode diameter is shorter than in a straight funnel.

- Few, thin and small-surface-area electrodes: Traditional ion funnels have big, tightly-stacked electrodes. Bernier showed that this leads to an ineffective pumping of the cavity of the existing funnel.[78] To improve the pumping efficiency, the new funnel has as few as possible, thin and low-surface electrodes. Their spacing depends on the position. In the final section, where the space charge is maximal, their spacing is 1.25 mm (face to face). It increases in three steps. First to 2.50 mm ($4<n<19$, n is the electrode number), then 5.00 mm ($18<n<28$) and finally to 10.0 mm for all remaining electrodes. The electrodes are 0.6 mm thin (see Table 8 and Figure 78 in the appendix).

To begin, I made a simple proof-of-concept simulation to check the simulation for consistency. For this, I varied the RF amplitude from 0 V to 300 V to see if the simulated transmis-

sion has any similarity to the experimental transmission of the existing funnel. The analyte was hexamethoxyphosphazene, a small organic molecule. It is a mass spectrometry calibration standard and has a high ion mobility of $1.41 \cdot 10^{-4}$ $m^2 \cdot V^{-1} s^{-1}$ (see Table 2). 80 Molecules started in a filled-circle distribution. RF frequency was 400 kHz, all ions trapped for more than 0.3 ms are removed from the simulation, the initial ion distribution had a diameter of 30 mm and was 65 mm away from the funnel exit.

There was small (accidental) difference on the funnel geometry: The spacing between the final RF electrode and the DC aperture was 2 mm instead of 1.25 mm, which was the spacing in all other simulated geometries. As the gas flow field was not known, I assumed a uniform gas flow of 300 m/s velocity towards the exit of the funnel. Pressure was 3 mbar. I used the Simion SDS package to simulate the ion-gas interaction. A 10 V DC-gradient was applied to the last four electrodes to reduce RF-trapping. Figure 23 shows how the ion trajectories change as a function of the RF amplitude.

At low RF amplitudes, the gas transports the ions along the funnel. The RF field is too weak to contain them, so they are lost on the electrodes. Transmission begins at 50 V_{RF} and remains maximal between 70 and 250 V_{RF}. At higher RF amplitudes, RF-trapping keeps the ions from reaching the funnel exit. The characteristics of no transmission, onset and RF-trapping with rising RF amplitude shows that the simple model qualitatively correlates to the transmission characteristics of a real ion funnel. Figure 23d compares both the simulation and the 3 mbar measurement of the existing ion funnel. It confirms this correlation. Therefore, the approach to use Simion with the SDS package for a simplified gas flow model can generate meaningful ion funnel transmission data.

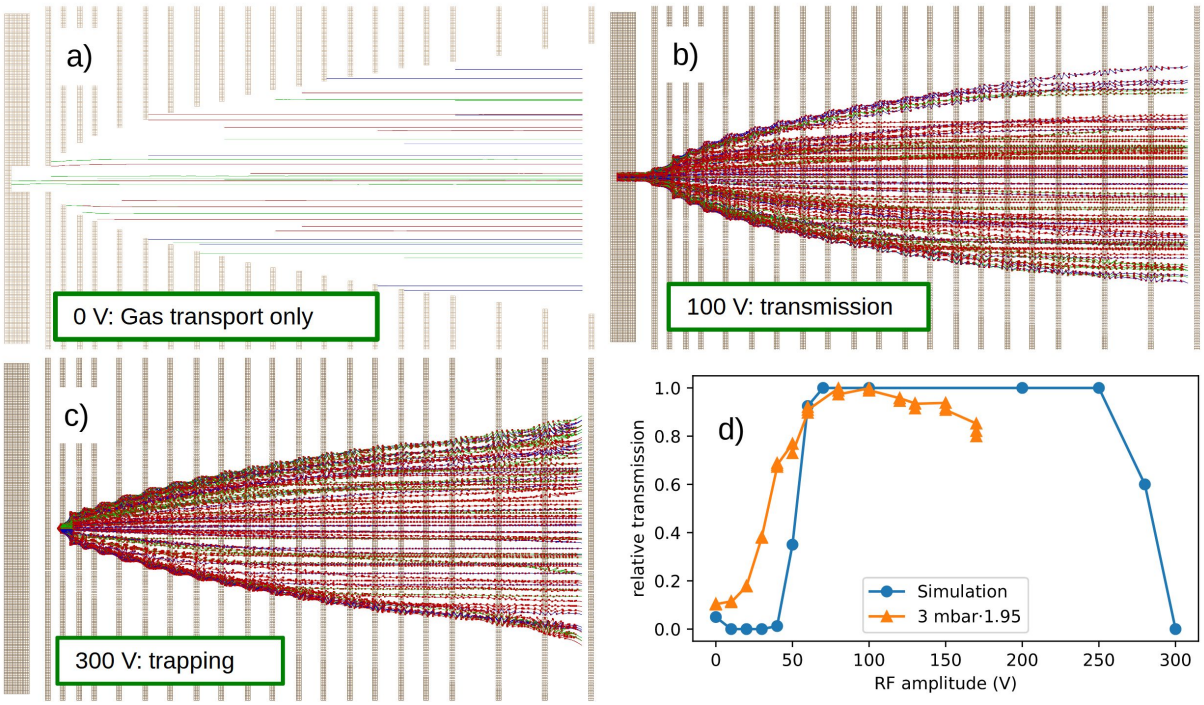


Figure 23: Simion simulation of 80 hexamethoxyphosphazene ions in a parabolic funnel at 3 mbar pressure. Transmission for different RF-Amplitudes: a) 0 V b) 100 V c) 300 V. Little red squares mark points of ion velocity reversal. d) Transmission ratio as a function of the RF-amplitude. 3 mbar measurement of existing funnel added with a factor of 1.95 to compare.

However, there are serious limitations: All ions in the simulation are hexamethoxyphosphazene, though an electrospray also emits solvent or salt ions and droplets. These react differently to the RF field.[125, p. 131] Hence, the experimental transmission remains below unity. SDS does not correctly model diffusion at low pressure in combination with RF fields (see section 2.3). In a real funnel, the supersonic expansion leads to a non-uniform ion distribution, as the ion distribution is already non-uniform at the outlet of the transfer capillary. [125] The initial uniform, circular ion distribution in the simulation does not represent this. The most serious limitation is the uniform gas flow field. It is not an accurate description of the real gas velocity, temperature, and pressure situation in an ion funnel.

To improve the ion trajectory simulation, Laurent Bernier simulated the gas flow with CFD in the ion funnel. To this end, he solved the compressible Navier-Stokes equation numerically. He approximated the ion funnel and the surrounding vacuum chamber as rotational-symmetric

to decrease the computational expense. For more details on the CFD simulation, see Bernier 2021.[78] Figure 24 shows the calculated velocity field in the funnel.

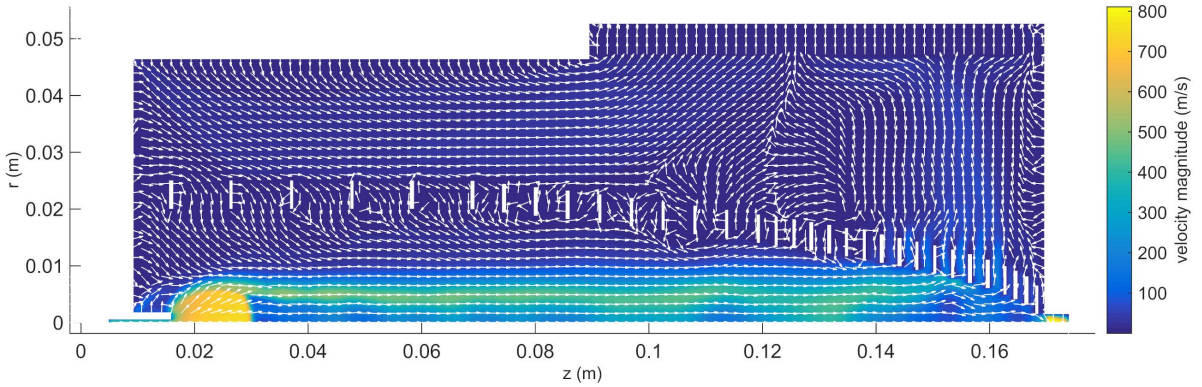


Figure 24: Velocity field for ion funnel geometry A. Computed by solving the compressible Navier-Stokes equation numerically in 2D. Algorithm: Prof. Julius Reiss & Laurent Bernier

The supersonic expansion of the jet is about 1 cm long and equally wide. From the Mach disc, a 2 cm wide, cylindrical supersonic flow extends into the funnel. The gas velocity slows to sub-sonic range in the zone where this flow comes in the vicinity of the electrodes (axial co-ordinate 0.14 to 0.16 m). In this zone, most of the gas flows out of the funnel in between the electrodes. Note that little gas flows through the gaps in between of the four tightly-stacked electrodes close to the exit of the funnel. The overall gas flow inside the funnel can support the axial ion transport because it is directed towards the funnel exit. This is different to the experimentally characterised existing ion funnel with thicker and larger-surface area electrodes. They offer a high resistance to the gas flow, such that a significant part of the gas gets pumped-off via the open side at the transfer capillary end.[78, p. 70] This causes a reverse flow of gas close to the electrodes in the initial funnel section. In summary, the simulation confirms that thin, generously-spaced and low-surface electrodes support the gas flow through the funnel. This gas flow promotes the ion transport downstream. The simulation also confirms the efficient pumping of funnel geometry A.

The pressure remains about 1.8 mbar in most of the funnel (Figure 81 in Appendix). Except for the final section, where the interaction of the supersonic gas flow with the decreasing-inner diameter electrodes takes place (axial coordinate 0.14 to 0.17 m). The gas flow slows down and a recompression to 4 mbar takes place.

I integrated the flow field in the Simion trajectory simulation of ion funnel geometry A to test how it this system transmits ions of different size. Details about the integration of flow fields into Simion are in section 2.3.

Pressure:

With the gas flow field integrated into the simulation, I investigated if the funnel geometry A can transmit different types of ions. As test molecules, I selected hexamethoxyphosphazene, apomyoglobin^{8+} and GroEL^{67+}. The RF amplitude and DC gradient were adapted to the ions, all other conditions remained constant[m]. The probe molecules cover a wide range: Hexamethoxyphosphazene is a good model for small, organic molecules. Apomyoglobin^{8+} represents small, native proteins. Its molecular weight is 17 kDa. GroEL^{67+}, an 802 kDa 14-mer chaperone[171] is a probe to test transmission of heavy, low-charged native protein complexes. The reduced mobilities of all three probe ions are similar (0.66...1.41·10^{-4} m²·V^{-1}s^{-1}, see Table 2). Note this is not true for their particle response time τ_{p0}. τ_{p0} of GroEL (8.19 ns, Table 2) is an order of magnitude higher than τ_{p0} of hexamethoxyphosphazene (0.47 ns). Hence, GroEL ions have a higher inertia and respond slower to velocity changes in the gas flow field.

Figure 25 shows trajectories of 80 ions of hexamethoxyphosphazene, apomyoglobin and GroEL.

m Hexamethoxyphosphazene DC 6V, V_{RF} = 80 V, apomyoglobin DC 3V, V_{RF} = 40 V, GroEL DC 3V, V_{RF} = 130 V.

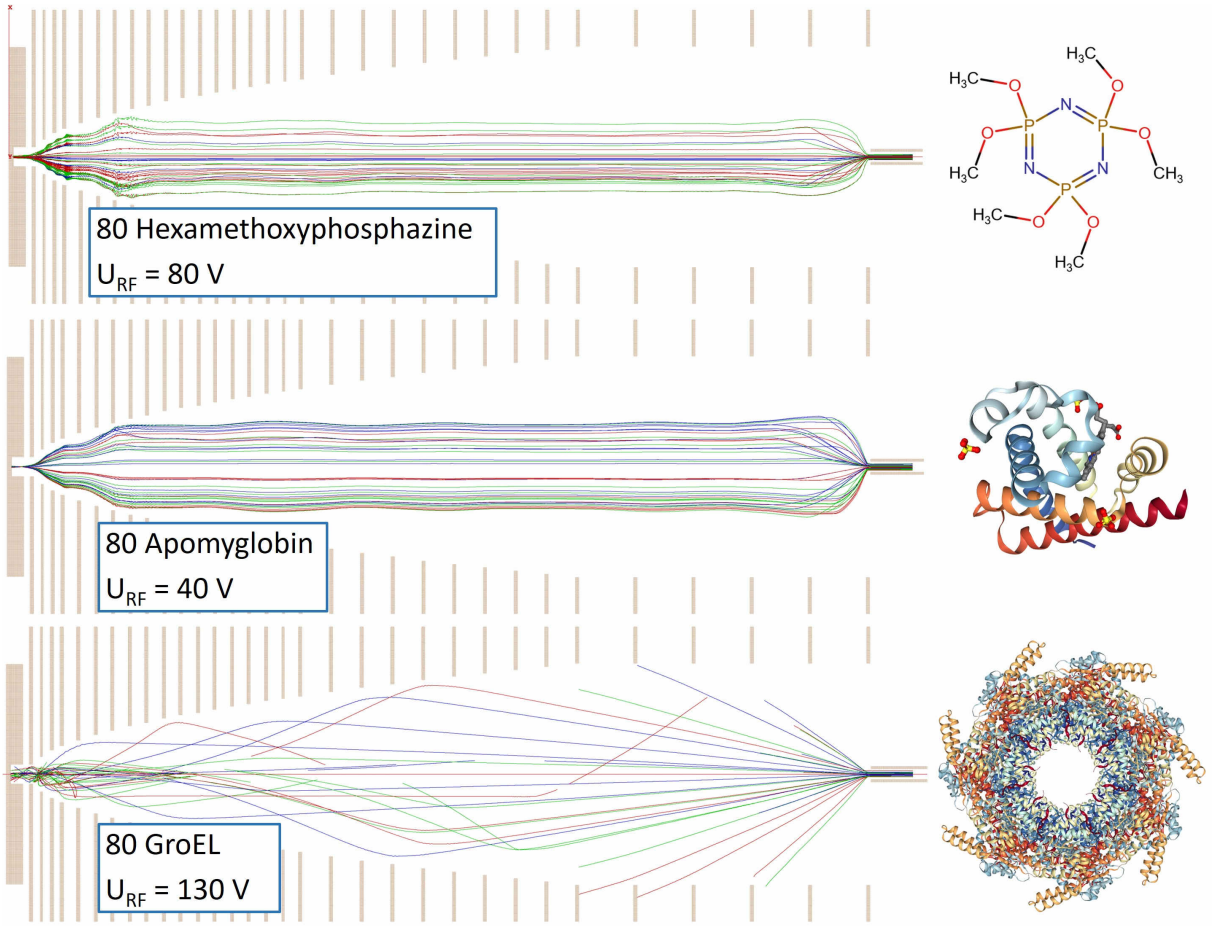


Figure 25: Ion trajectory simulation of hexamethoxyphosphazene, apomyoglobin and GroEL. Gas interaction model Simion SDS. 1.8 mbar pressure at pump, v_{RF} = 400 kHz.

Apomyoglobin and hexamethoxyphosphazene are efficiently transmitted. They follow the streamlines of the gas flow in the initial and central section of the funnel. In the final section, the effective potential confines and focuses them on the funnel exit. The trajectories of GroEL are different. In the initial section, the supersonic expansion projects half of the heavy ions radially towards the edge of the funnel. There, they hit the electrode surface because of the too high electrode spacing. The 10 mm electrode spacing in this section weakens the effective potential. It is insufficient to confine the GroEL ions. The ions projected by the supersonic expansion at smaller angle move towards the final section of the funnel. There, the effective potential barrier reflects them. The radial ion flight direction reverses abruptly. Some ions (1/6 of the total) are not reflected and hit the final electrodes.

Figure 26a) shows the axial and radial ion velocities for a single, representative trajectory of GroEL. Three radial direction reversals take place. One in the middle section (axial coordinate ≈ 90 mm) and two in the final section (red oval).

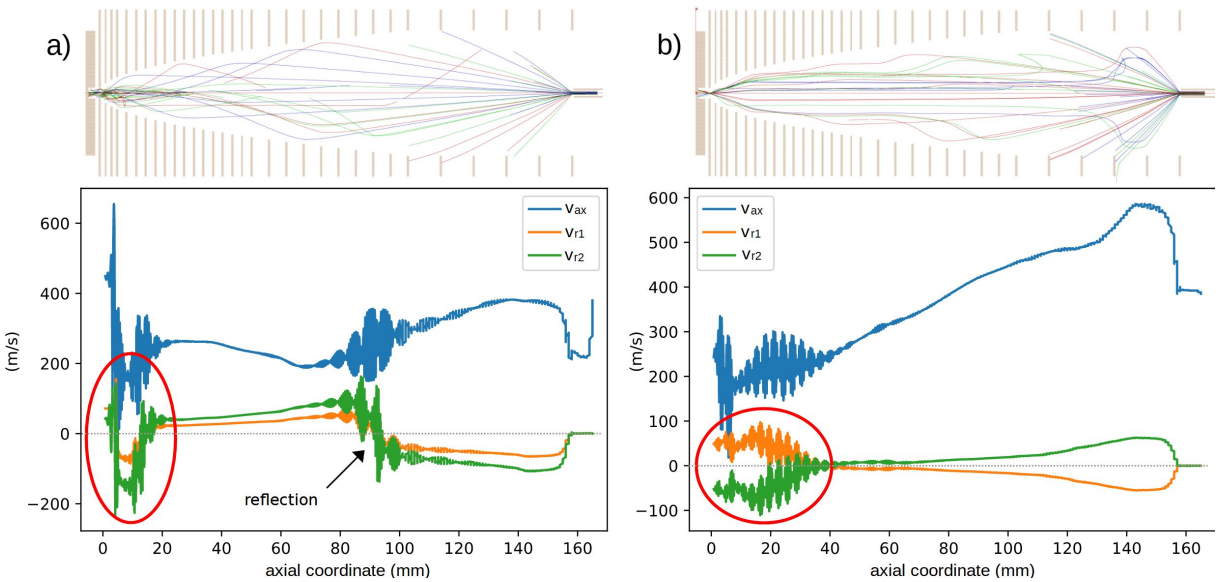


Figure 26: Trajectories (top) and exemplary trajectory velocities (bottom) of one transmitted GroEL ion at 1.8 mbar (a) and 5.4 mbar (b). At 1.8 mbar, insufficient gas damping leads to a rapid change of radial (r1 ⊥ r2) velocity of GroEL in the final section on the walls. At 5 mbar, this tumbling motion disappears.

During these two final direction reversals, the radial velocity v_{r1} changes abruptly by around 200 m/s. Thus, the GroEL ions movement in the funnel is similar to the trajectory of a ping-pong ball in a table tennis game: Free flight with very light deceleration in the cavity of the funnel (free flight over the table tennis net), and a hard bounce-back close to the electrodes (reflection of the ping pong ball on the table). This tumbling trajectory indicates the gas does not sufficiently dampen the GroEL ion motion. This is due to the high inertia of the low-charged, heavy protein complex.

To investigate if a higher pressure could promote damping of the trajectory, I multiplied the pressure field by a factor of 3 (resulting pumping pressure 5.4 mbar) and in a second simulation, by a factor of 30 (54 mbar pumping pressure). This artificial pressure increase leads to a flow field which is inconsistent. As a new simulation at a different pressure would take sev-

eral weeks to converge, I chose this computationally less expensive approach as an approximation.

The axial and radial ion velocities for a single, representative trajectory of GroEL at 5.4 mbar are shown in Figure 26b. In contrast to the trajectory at 1.8 mbar, only one direction reversal takes place in the final section (red circle). The radial velocity v_{r1} changes by less than 100 m/s. This means the spatial deflection is much smaller, too. There are still losses due to the electrodes with too wide stacking in the initial funnel section, but none in the final section. The damping is stronger, the tumbling ion motion reduced. It totally disappears at 54 mbar (Figure 80 in Appendix). At this pressure, the trajectories of the inert GroEL ions are similar to the much lighter hexamethoxyphosphazene ions at 1.8 mbar. Hence, heavy-low charged ions with a high inertia (long τ_p) require a higher pressure in the ion funnel than agile, high-charged organic ions (short τ_p). The higher pressure for heavy, low-charged inert ions dampens their motion and helps them to dissipate the kinetic energy they acquired in the supersonic expansion. The trajectory simulations confirm the observation that mass spectrometers designed for small organic molecules transmit heavy, low-charged protein complexes better when the pressure in the source region is increased.[136]

There are two counteracting mechanisms for the different damping of agile and inert ions at a set pressure. First, the mean free path determines the number of collisions an ion has in a given flight distance. At 1.8 mbar, it is about 11 µm for hexamethoxyphosphazene and about 0.07 µm for $GroEL^{67+}$. Hence, $GroEL^{67+}$ experiences a higher drag force when it enters the zone of relatively slow gas flow outside the supersonic expansion. The second mechanism counterbalances the higher drag force. $GroEL^{67+}$ is much heavier than hexamethoxyphosphazene. Due to its folded structure, the atoms hidden inside the barrel-shaped structure do not interact with the surrounding gas. Hence, they do not contribute to the drag force, but they

increase the inertia of the molecule. A simple analogy illustrates the differences between the probe molecules damping behaviour. In this model, hexamethoxyphosphazene is a chad of paper from a punch. GroEL is a paper ball, made of crunched-up paper. When projected at high speed, the chad stops immediately, but the paper ball flies for a long distance, despite being bigger.

To take into account both mechanisms (mean free path and molecular weight), the number of collisions in a set distance can be normalised to the mass of the ion. Figure 27 shows the number of collisions per mass during a 1 mm flight distance as a function of the gas pressure for the three probe ions. GroEL requires a pumping pressure of approximately 30 mbar to experience the same damping as hexamethoxyphosphazene at 1.8 mbar. This result is in good agreement with the results of the ion trajectory simulation. At 54 mbar they yielded a similar damping, which is the same order of magnitude.

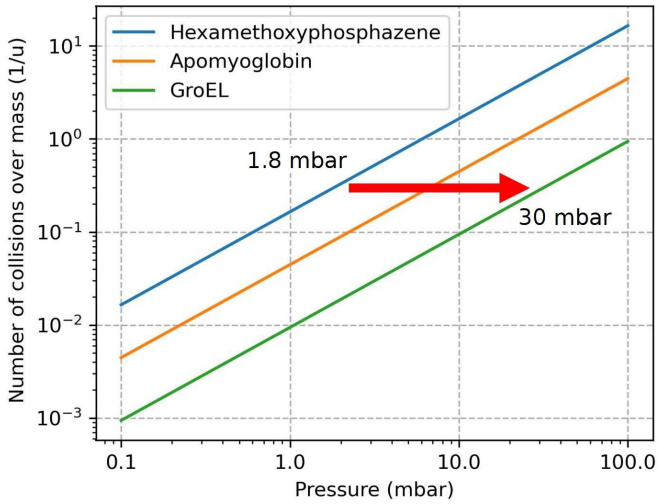


Figure 27: Number of gas-ion collisions in 1 mm flight path divided by ion mass. GroEL needs 30 mbar pressure to have the same number of collisions per mass as hexamethoxyphosphazene at 1.8 mbar.

In conclusion, the pressure in the ion funnel has to be adapted for optimal transmission of different ions. Heavy ions with a high mass-to-charge ratio and a high inertia require a higher pressure in the ion funnel than light low mass-to-charge ratio organic ions. A good measure for ion inertia is the particle response time τ_{p0} .

Capillary shape:

A different capillary outlet can lead to a different gas flow field. Funnel geometry A has a conventional tubular capillary outlet. I tested a rocket-nozzle-shaped capillary outlet to see how this influences the ion transport in comparison. The inner diameter of the capillary widens from the 1.0 mm tube to a 6.4 mm nozzle. In addition, the maximum electrode spacing is limited to 5 mm to avoid losses in the initial funnel section (funnel geometry D).

Laurent Bernier again simulated the gas flow field. Note that the data I used for the trajectory simulation is not the final converged result, but an intermediate result qualitatively similar to the final result. It differs in the maximum pressure for the final section of the funnel and the formation of a recirculation zone there. For a discussion of the final gas flow simulation data, see Bernier 2020.[78, p. 75]

Figure 28a shows the velocity field in funnel D.

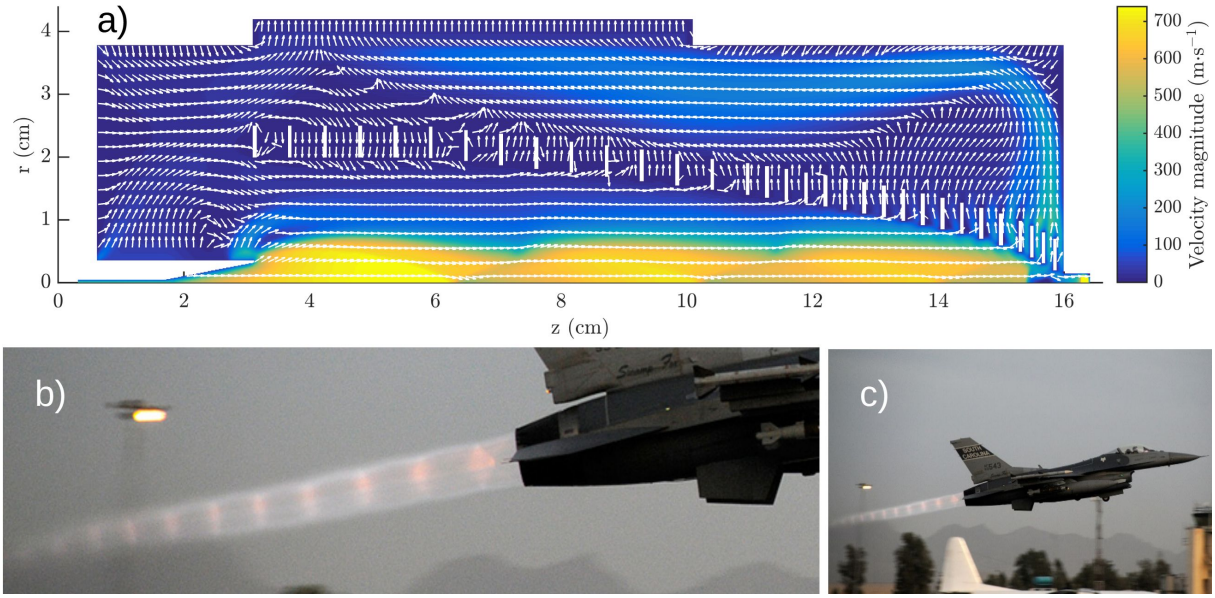


Figure 28: a) CFD simulation of the velocity field in ion funnel geometry D. Simulation not fully converged, image courtesy of Laurent Bernier. With a rocket-nozzle-shaped capillary outlet, the supersonic flow extends nearly to the funnel exit. b) Shock diamond structure visible in the afterburner exhaust jet of a turbofan engine of a c) F-16 plane taking off. Photographs b) and c) Tech. Sgt. Caycee Cook, public domain.

The supersonic jet extends to the final section of the funnel. It stops in the area where it interacts with the smaller diameter electrodes (axial coordinate ≈ 15.5 cm). In contrast to the flow field in funnel A, the gas velocity in the jet remains very high (above 600 m/s) and no Mach disc is visible. Instead, the supersonic expansion repeats three times downstream in the jet. Each re-expansion starts in a shock-diamond (axial coordinates 6.5 cm, 10.5 cm, 14 cm). The re-expansion forms when the oblique shock (see Figure 14) is reflected at the symmetry axis. [144] The shock diamond structure is best visible in the pressure field (Figure 82 in Appendix). This structure is characteristic for a moderately underexpanded jet.[144] It appears as the gas pressure decreases from 300 mbar in the tubular section of the transfer capillary to less than 10 mbar in the exit plane of the nozzle. Hence, the pressure difference to the pumping pressure in the vacuum chamber is much smaller. The jet is not any more very highly underexpanded, but just moderately underexpanded. This means the axial displacement of the gas throughout the jet is smaller due to the successive expansions and recompressions. These jets occur in the exhaust stream of turbofan aircraft engines, too (Figure 28b and c).

Hexamethoxyphosphazene trajectories for the funnel D geometry are in Figure 29a. The ions follow the gas stream lines through the funnel to the final section. Due to the rocket-nozzle-shaped outlet, the supersonic jet and with it the ions retain their velocity. That is similar to the exhaust stream of the aircraft engine in Figure 28b. However, the conserved (kinetic) momentum of the gas leads to a recompression to 15 mbar pressure in the cavity between the final four electrodes (Figure 29b).

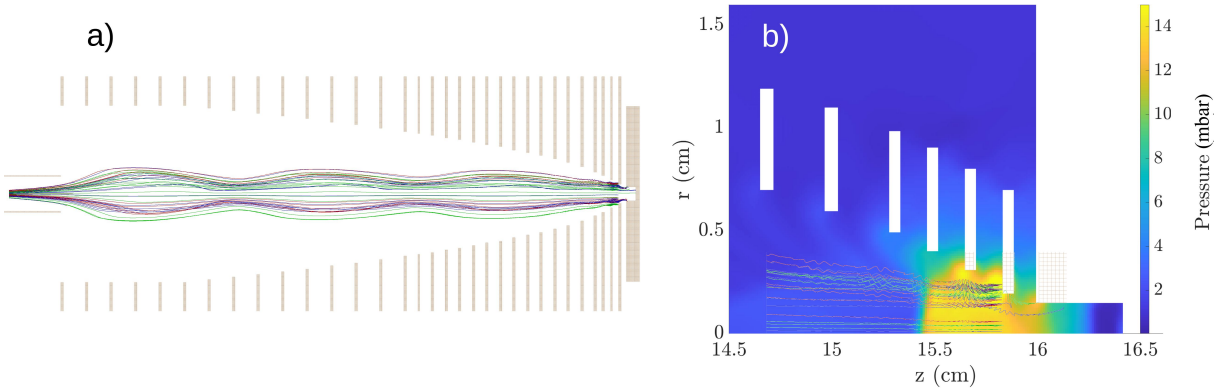


Figure 29: a) 80 hexamethoxyphosphazene trajectories with a rocket-engine-shaped capillary outlet (funnel D). v_{RF} = 1 MHz, V_{RF} = 200 V, pumping pressure 1 mbar. b) Pressure in the final section, where the supersonic jet collides with the electrodes. Overlay: trajectories. The gas velocity decreases and pressure increases to 15 mbar. Ion mobility reduces, so the RF is insufficient to keep hexamethoxyphosphazene away from the last electrode.

Although I applied harsh RF settings (v_{RF} = 1 MHz, V_{RF} = 200 V [n]), the effective potential is too weak to confine the ions in the final section of the funnel. The ion mobility loss due to the pressure rise is too big to be compensated by the RF.

A closer look reveals that most losses occur on the last RF electrode (Figure 29b) at radii of more than 2.5 mm (Figure 30a). This RF electrode is very exposed to the gas jet, as it is at the maximum curvature of the parabolic ion funnel cavity. At a radius of 2.6 mm, the effective axial force of the RF field repulses the ions only weakly (white arrow in Figure 30b). The repulsion in vacuum reaches a maximum of $1.6 \cdot 10^{-14}$ N along the white arrow (r = 2.5...2.8 mm, z= 6.5...4.8 mm in Figure 30b) and decreases rapidly the closer the ion moves

n Further simulation parameters: 50 V attractive DC gradient on final 4 electrodes, 50 V on remaining electrodes.

towards the last RF electrode. Due to the high pressure caused by the recompression of the jet, the real effective force is much lower. The correction factor c_{gas} (see section 2.2) is 0.09 or smaller. An axial gas flow velocity of 135 m/s is sufficient to overcome the maximum repulsion along the white arrow trajectory. This gas velocity is exceeded by far in the region of maximum axial repulsion. Closer to the electrode, the axial repulsion decreases stronger than the gas velocity. The gas flow pushes hexamethoxyphosphazene ion into the last RF electrode. Thus, the parabolic ion funnel cavity causes a disadvantageous effective potential landscape at the point of maximum cavity curvature. In addition, the axial gas flow works against the effective potential barrier.

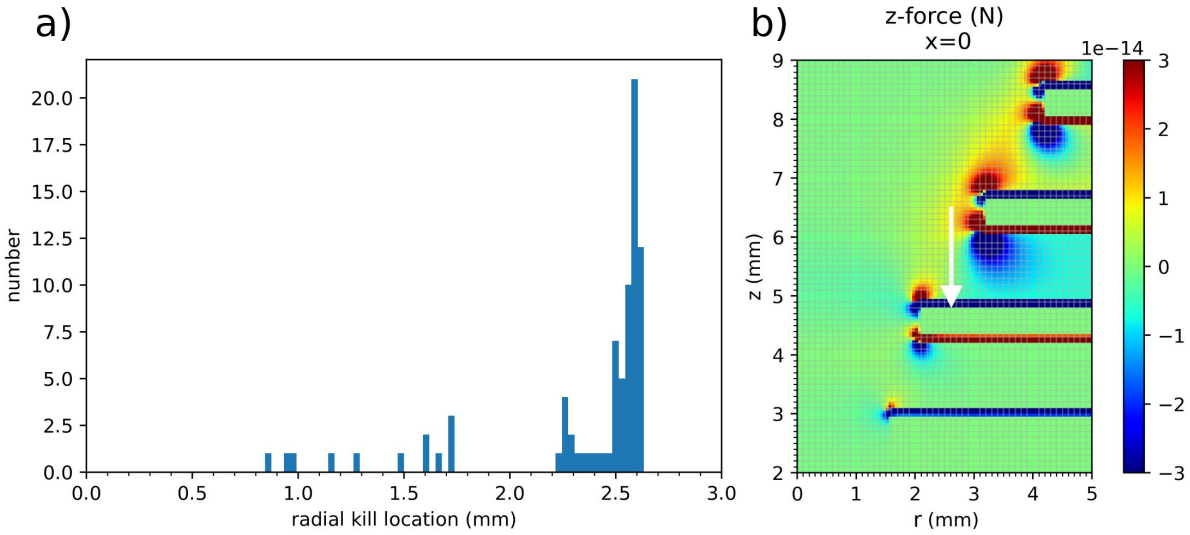


Figure 30: a) Radial coordinate of the hexamethoxyphosphazene ion losses. b) Axial (z)-force in HV for hexamethoxyphosphazene in funnel D (ν_{RF} = 1 MHz, V_{RF} = 200 V, DC gradient for last 4 electrodes 50V). White arrow at r = 2.6 mm

In general, the pumping of the ion funnel cavity should occur in a zone where a large pumping cross-section is available. In this zone, the gas velocity should be subsonic. Here, the gas velocity gets subsonic in the very confined volume at the apex of the funnel. The recompression in this zone in conjunction with the small pumping cross-section is unfavourable.

In summary, a rocket-nozzle-shaped transfer capillary outlet in combination with a parabolic ion funnel cavity are detrimental for transmission. The rocket-nozzle-shaped outlet causes an

extended supersonic gas flow. The retention of the gas (kinetic) momentum leads to a recompression in the final section. In this section with the highest curvature the ions are lost due to the high pressure. At this pressure, the effective force is only a fraction (0.09 or less) of the vacuum value. Therefore, the RF field cannot contain the ions.

4.4 Electrode spacing

In this section, I investigated how the effective potential in the ion funnel depends on the electrode spacing. With this information, I can adjust the electrode spacing to optimise transmission. To this end, I extracted four radial slices of the effective potential data in the parabolic funnel A.

The electrode spacing of funnel A varies. In the final section, it is 1.25 mm face-to-face and increases stepwise to 2.5 mm, 5 mm, and finally to 10 mm in the wider sections (Figure 25). I extracted the effective potential data in the middle between two electrodes for each spacing.

Figure 31a shows the effective potential as a function of the funnel radius for GroEL. The pressure in the simulation was more than a magnitude lower than the critical pressure $p_{V^*,crit}$ (1.8 << 68 mbar). Hence, the effective potential approximation still applies. Therefore, it is safe to assume the calculated potential barriers are similar to the high vacuum case.
To make comparing easier, I corrected the radial electrode offset. Due to the parabolic funnel shape, the radial electrode offset is different for each electrode and thus, for each extracted effective potential data slice. As a consequence, in figure 31 the electrode inner electrode edge is set to r = 10 mm for all electrodes (uncorrected data: Figure 83a in Appendix).

An increase in the electrode spacing weakens the effective potential. At 1.25 mm electrode spacing, the maximum is 440 eV. This drops to just 9 eV for 10 mm spacing. Therefore, an increase in electrode spacing leads to a strong decrease in the effective potential well depth.

This is also the explanation for the losses of GroEL ions in the initial section (Figure 25c). The radial velocity of GroEL reaches ≈ 150 m/s in the supersonic expansion (Figure 26a). This velocity corresponds to 93 eV radial kinetic energy (based on mass and velocity of a GroEL ion). The ion dissipates some of the radial kinetic energy in the gas as it moves towards the electrodes. As the radial kinetic energy is an order-of-magnitude higher than the effective potential barrier at 10 mm spacing, GroEL collides with the electrodes in the initial section.

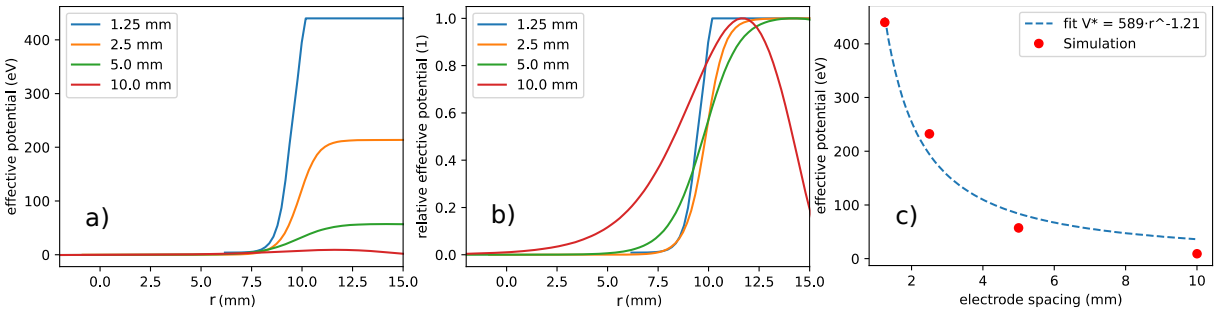


Figure 31: Effective potential for GroEL in funnel A for different electrode spacings. U_{RF} = 130 V, ν_{RF} = 400 kHz. a) Absolute effective potential assuming HV conditions as function of the radius. The data has been corrected for the differing cavity diameter so that the electrode rim is at 10 mm for all spacings. b) Normalised effective potential. The decrease for the 10 mm curve at r > 12 mm is a consequence of the wall potential (0 V) penetrating in the inter-electrode space c) Fit of the maximum value as function of the electrode spacing.

Figure 31b shows the relative effective potential as a function of the funnel radius. It is normalised to the maximum value reached between the electrodes. With increasing electrode spacing, the effective potential reaches further into the funnel cavity. At 10 mm electrode spacing, 20 % of the maximum effective potential penetrate 4 mm deep into the funnel cavity. At 1.25 mm spacing, the 20 % limit is as close as 1 mm to the electrodes. The inter-electrode spacing of the RF-only ion funnel in the Thermo Scientific Q-Exactive mass spectrometers is increased close to the exit electrode. This is presented as an alternative to a decrease in the inner diameter of the funnel cavity to focus the ions radially.[159] Nevertheless, the absolute effective potential remains always smaller with a bigger electrode spacing (Figure 31a). Thus, it is not possible to achieve better radial ion focusing with an increased electrode spacing.

Finally, equation 2.7 predicts that the effective potential should be indirect proportional to the electrode spacing. Between the electrodes, the electric field has only one direction: orthogonal to the electrode surface. It is approximately zero in the vertical and horizontal direction, which are parallel to the electrode surface. Therefore, the electric field E_0 is:

$$E_0 = \frac{V_{RF}}{d} \tag{4.9}$$

d is the electrode spacing. With equation 2.7 the effective potential should be a negative power-law function of the electrode spacing with the exponent 2:

$$V^* \propto \frac{1}{d^2} \tag{4.10}$$

A fit of the simulated effective potential yields indeed a negative power law function (Figure 31c). However, the exponent is 1.21 instead of 2. This deviation is partially due to the penetration of the potential caused by the vacuum chamber walls in the inter-electrode space at wide spacings (Figure 83b). Furthermore, the differing electrode radii can change the effective potential compared to a constant inner radius SRIG. I fitted to the maximum of the effective potential, because the common value at 80 % of the ion optic's radius is not meaningful in a funnel.

4.5 RF trapping in the final funnel section

To investigate the RF trapping in the final section of an ion funnel, I first calculated the effective potential in the existing ion funnel. In a second step, I simulated the trapping behaviour of GroEL and hexamethoxyphosphazene in the parabolic funnel A.

For the small organic molecules rhodamine B and hexamethoxyphosphazene, the effective potential approximation is only a qualitative description of the energy landscape due to the high

operation pressure. It exceeds the critical pressure $p_{V^*,crit}$ (Table 1) in both funnels (existing funnel 1 mbar, parabolic funnel A 3 mbar). Hence, I marked all energy barriers calculated for the two molecules with the suffix -“vac”. Although in reality these energy barriers occur not in vacuum, they cause an effective force in the gas-filled ion optic. With the correction factor c_{gas}, this effective force can be precisely calculated. For humans, the processes in the ion funnel are easier to understand looking at the effective potential landscape. Therefore, I focus on the qualitative discussion of the effective potential in vacuum and use the corrected effective force for quantitative analysis.

RF trapping in the existing, conventional funnel

Figure 32a shows the effective potential in the central symmetry plane for the cavity between the final 20 electrodes in the existing funnel. There is no DC gradient, so the funnel operates in RF-only mode. The other parameters are the same as for the experimental DC gradient variation in section 4.3 (ν_{RF} = 1 MHz, V_{RF} = 60 V, Rhodamine B). The effective potential resembles a tapered bathtub: Absolutely flat (zero) in the centre, with steep walls at both sides. Though, towards the funnel exit, there is a deviation from the ideal tapered bathtub. As the inner diameter of the electrode decreases, the effective potential on the axis is non-zero at some places. Hence, axial ion traps form.

These traps have higher well-depths with decreasing electrode inner diameter. The maximum axial well-depth reaches 1.3 eV_{Vac} between the last and second-last RF electrodes (Figure 32b, z = 5 mm). The last axial trap is shallower (0.5 eV_{Vac}) because the final funnel electrode is DC-only. The 1.3 eV_{Vac} trap causes an effective axial trapping force of $2.7 \cdot 10^{-16}$N to the Rhodamine B ion at 1 mbar pressure (Figure 84 in Appendix). This trapping force impedes the movement of the ion towards the funnel exit. A 160 m/s axial gas flow would be required to compensate this trapping force. Therefore in RF-only mode, a single Rhodamine B ion

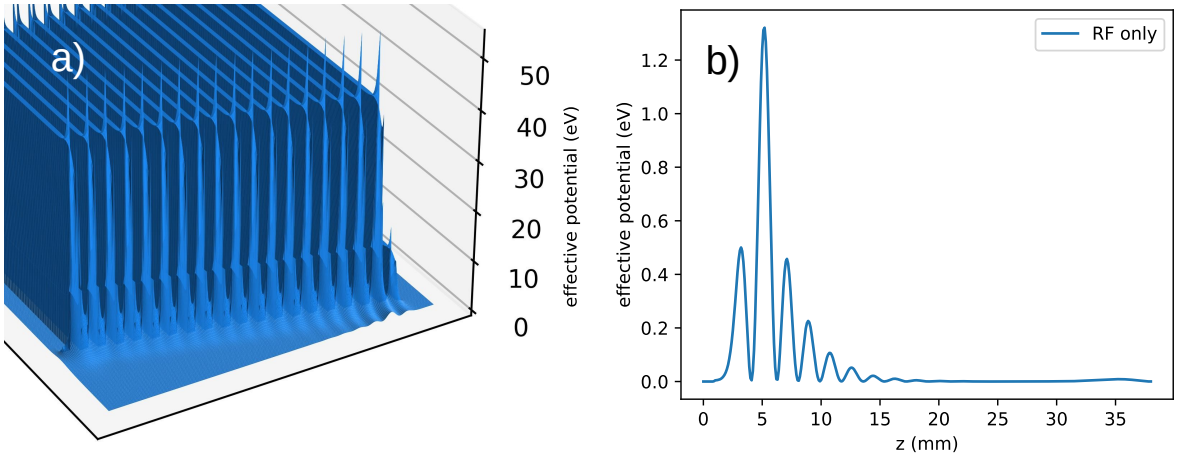


Figure 32: Effective potential of the final 20 electrodes of the existing ion funnel in RF-only mode, assuming HV. a) 3D-projection b) Slice along the central axis. Parameters: v_{RF} = 1 MHz, V_{RF} = 60 V, Rhodamine B.

could overcome this trap only with a strong gas flow towards the funnel exit. The axial trap height gets stronger the further the ions are away from the central axis. At a radial displacement of 1 mm, the effective axial trapping force more than doubles to $6.4 \cdot 10^{-16}$ N (Rhodamine B at 1 mbar). To offset the trapping force, a gas flow of nearly 400 m/s would be needed. Hence, the axial trapping is likely to significantly hamper transmission.

Experimental data proves the funnel transmits in RF only mode (Figure 21). In this configuration, the following mechanism is possible: The ion funnel traps the incoming ions. It fills up with trapped ions similar to a bathtub with water. As soon as there are enough ions trapped, their space charge counteracts the axial ion trapping potential and transmission through the funnel sets on.[78, p. 127] It is probable the trapping in the overfilled ion funnel bathtub is not ideal. Losses can occur through diffusion, the gas flow and space charge. The trapping can also lead to frequent ion-ion interaction, which limits axial transport.

Figure 33a compares the effective potential along the funnel axis for the RF-only mode with a - 150 V DC gradient. In the - 150 V case, all but the axial trap between the final two RF electrodes have disappeared. This trap's axial well-depth has reduced from 1.3 eV_{Vac} to 0.4 eV_{Vac}. Thanks to the gradient, the area where space charge can build up does not span the entire

length of the funnel any more. It is limited to a small area (length < 2 mm) between the final RF electrodes.

Hence, with the DC gradient, the situation changes from a spilling, overfilled bathtub to a steep brook interrupted by a single, small basin, which is overflowing. This is likely to minimise ion losses and accelerate ion transport. The experiment confirms that transmission is ⅓ higher at - 150 V DC gradient (Figure 21b).

However, such a high gradient poses problem in mass spectrometers with a continuous ion beam. Whilst the continuous beam supports high transmission efficiency, they require a steady decline in the effective potential in all gas-filled ion optics along the ion path. This gradient pushes the ions towards the detector or deposition chamber (very few exemptions exist, see chapter 5.3). With a -150 V drop along the ion funnel alone, the mass spectrometer requires a power supply with an extended voltage range (e.g. +500 to -500 V) to supply the DC gradients for all ion optics. These power supplies are expensive compared to DC supplies with a smaller voltage range.

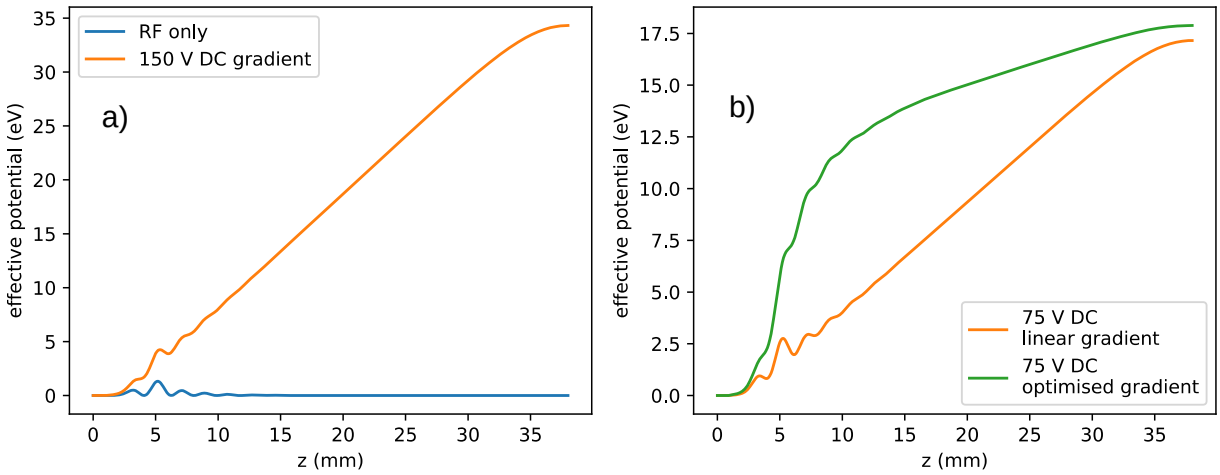


Figure 33: a) Effective potential assuming HV conditions along the central axis in the existing funnel a) in RF only mode versus a -150 V DC gradient and b) with a linear gradient compared to a non-linear -75 V gradient. Curvature at z > 30 mm is due to only first 20 electrodes modelled. v_{RF} = 1 MHz, V_{RF} = 60 V, Rhodamine B.

Figure 33a reveals that less than -10 V of the -150 V DC gradient are applied to the electrodes which cause the axial trapping wells. The remaining -140 V drag the ions more quickly through the larger diameter sections of the ion funnel. This is due to the linear DC resistor cascade. A linear resistor cascade applies the DC gradient in the same proportion to each funnel electrode.

Figure 33b presents a better alternative: A non-linear resistor cascade applies different proportions of the total DC gradient to the RF electrodes. The proportion of the DC gradient which drops between two RF electrodes can be adjusted. This happens by tuning the magnitude of the resistors in the resistor cascade which supplies the DC gradient to the RF electrodes. Here, I chose a 6:18:6:4:2:2:1:1:1… voltage partition instead of the linear 1:1:1… partition. Already with a -75 V non-linear DC gradient, all axial trapping wells disappear. There remains weak a DC gradient in the larger sections of the funnel to move the ions gently towards the final section of the funnel. It prevents ion losses if the ions are dragged backwards by a potentially present reverse gas flow in the larger sections of the funnel.

A voltage tap in the resistor cascade can separate the linear gradient in the larger funnel sections from the non-linear gradient in the final section. Consequently, the experimenter can set both gradients independently.

Tolmachev et. al. developed the criteria that the axial electrode spacing must be bigger than the electrode radius to limit the axial trapping.[97] Although the existing funnel respects this criterium, significant axial trapping wells develop. The non-linear DC gradient is a flexible alternative to suppress the axial trapping. It relaxes the constraints on the geometry of the final funnel section because it decouples the inter-electrode spacing from the electrode radius. Laurent Bernier's CFD simulation (section 4.3) illustrated that the inter-electrode spacing controls the gas flow from the funnel cavity to the pump. Therefore, a non-linear gradient allows to adapt the inter-electrode spacing for an optimal gas flow in the funnel whilst the axial trapping remains minimal.

RF trapping in the parabolic ion funnel A

To investigate the RF trapping, I tested the transmission of GroEL and hexamethoxyphosphazene under the same RF settings in funnel A. The analyte ions have an m/z-ratio so different (322 vs. 12000 m/z) that they would normally not be analysed together. The simulation serves as a model for the simultaneous transmission of two analyte ions with extremely different m/z-ratios. Transmitting ions with very different m/z ratios is important for direct analysis (or deposition) of biological samples without prior purification.[109], [172]

I used the model from section 4.3 (Figure 23). The RF amplitude was 130 V, and ν_{RF} = 400 kHz. The Simion SDS package simulated a uniform gas flow field moving with a velocity of 10 ms^{-1} towards the funnel exit. Pressure was 3 mbar. Note that the geometry had a small glitch: unlike the final funnel A geometry, the distance between the final RF electrode and the last, DC only electrode is 2.0 mm instead of the correct 1.25 mm.

Figure 34a shows the effective potential along the central axis for hexamethoxyphosphazene and GroEL^{67+}. There are two axial ion traps. One potential barrier is between the first and second electrode (z = 0...5 mm) and a second barrier spans the area between the second and the fourth electrode (z = 5...8 mm). Compared to the existing, conventional funnel (Figure 32b), the axial traps have moved towards the funnel exit and extend less in the direction of the transfer capillary. Thus, the parabolic shape moves the onset of the axial ion trapping towards the exit. Nevertheless, in RF only mode, the ions were stuck in front of the second potential barrier (Figure 34c, GroEL trajectories).

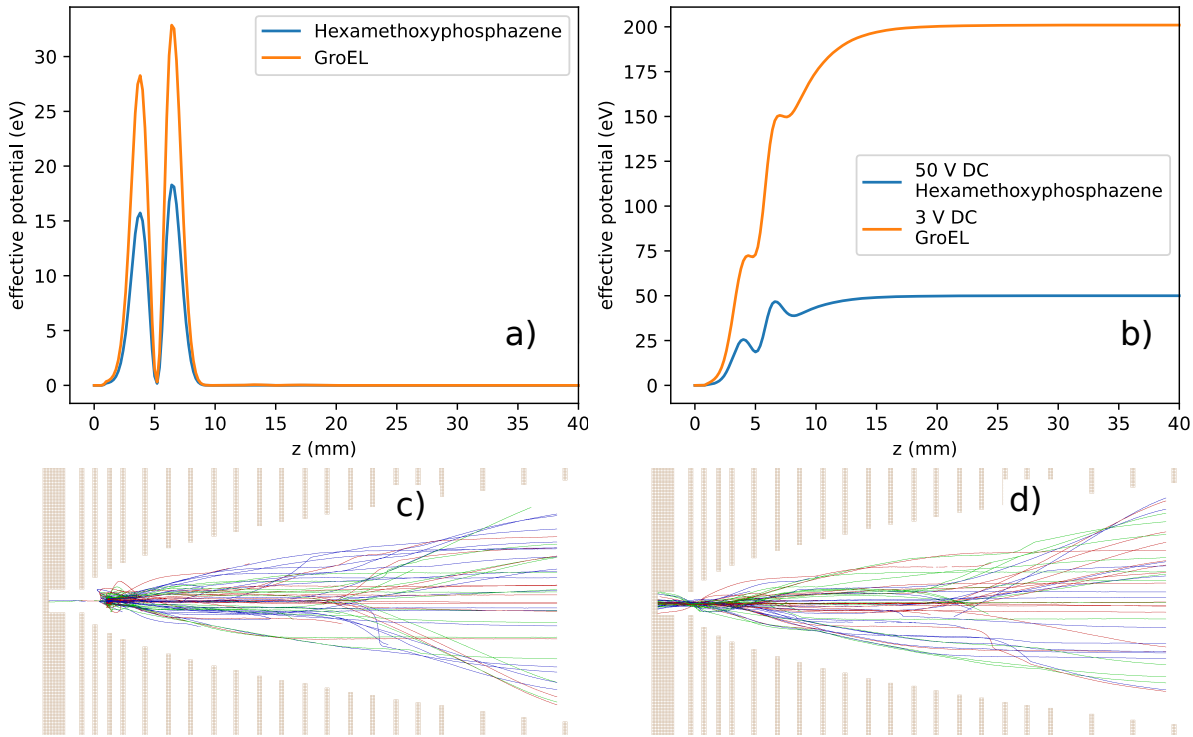


Figure 34: Effective potential along the central symmetry axis in funnel A for hexamethoxyphosphazene and GroEL. ν_{RF} = 400 kHz, V_{RF} = 130 V, uniform gas velocity of 10 m/s towards the exit. Effective potential for a) RF only b) with the minimum necessary DC gradient to overcome the RF trapping. c) Trajectories of 80 GroEL in RF only mode and d) with a 3 V DC gradient at above conditions.

In the next step, I ramped a non-linear DC gradient from 0 V to the voltage at which transmission set on. I adapted the non-linear DC gradient to the parabolic geometry. It was applied in a 4:4:1:1 partition to last four RF electrodes only.

Transmission set on at -3 V DC gradient for GroEL^{67+} (Figure 34d) and -50 V for hexamethoxyphosphazene. There are two reasons for this big difference. First, the RF amplitude of 130 V at ν_{RF} = 400 kHz is very harsh for a small molecule as hexamethoxyphosphazene. To transmit only this molecule, an experimenter would choose a lower RF amplitude (e.g. 70 V, see also Figure 23). Second, the effective potential landscape for a heavy ion with many charges such as GroEL^{67+} reacts differently to a given DC gradient (Figure 34b). Only -3 V DC gradient remove the axial ion traps for GroEL^{67+}, whereas the small singly-charged hexamethoxyphosphazene^{+1} sees still axial traps at -50 V DC gradient. Due to the bath gas, the effective force these axial traps exert on a hexamethoxyphosphazene ion are reduced to about a sixth of the vacuum value. It is likely that hexamethoxyphosphazene can overcome these weak axial traps due to diffusion.

What is the reason for this difference? The effective potential depends on the electric field as well as on the ion. There are two ion-specific parameters:

$$V^*(\vec{R}_0) = \frac{q^2}{m} \cdot \frac{1}{4\Omega^2}(\vec{E}_0 \cdot \vec{E}_0) + q \cdot \Phi_s \qquad (4.11)$$

the RF coefficient q^2m^{-1} (green in equation 4.11). And the DC coefficient q, which is the ion charge (blue). Table 3 contains these coefficients for two probe ions. The proportion DC/RF coefficient is equal to the mass-to-charge ratio of an ion.

Table 3: RF and DC coefficients for hexamethoxyphosphazene and GroEL.

	RF coefficient $\frac{q^2}{m}$ (e^2u^{-1})	**DC coefficient q (e)**	**DC/RF coefficient $\frac{m}{q}$ (ue^{-1})**
Hexamethoxyphosphazene^{+1}	$3 \cdot 10^{-3}$	1	322
GroEL^{+67}	$6 \cdot 10^{-3}$	67	≈11955

Therefore, small, light and low-charged ions react differently to the RF component of the same electric field than heavy, high-charged ions. On the one hand, the RF field dominates the hexamethoxyphosphazene (m/z 322 ue^{-1}) ion trajectory. On the other hand, the influence of the DC gradient on the heavy, high-charged GroEL (m/z 12k ue^{-1}) is much bigger.

In conclusion, low-charged, light ions require a higher DC gradient for trapping-free transmission than high-charged, heavy protein ions at the same RF amplitude and frequency. Furthermore, the geometry of the ion funnel cavity determines the voltage partition of the non-linear DC gradient.

4.6 How does a conventional ion funnel work?

This section is an overview about the processes in the funnel and the key parameters governing them. It builds upon the results gathered in the preceding sections of the ion funnel chapter.

Supersonic expansion:

When the gas flow through the transfer capillary enters the vacuum chamber, a supersonic expansion takes place (Figure 14). This expansion projects the ions in a cone-shaped volume towards the funnel electrodes (Figure 25). Especially for heavy ions, their kinetic energy can come close to or exceed the effective potential barrier the RF electrodes create. When an ion reaches the end of the supersonic jet, collisional cooling in the slower flowing gas decreases its velocity and dampens the ions motion (Figure 26). Therefore, the ion funnel diameter and length must so big that there is a gap of slow flowing gas between the supersonic jet and the electrode rims. This gap provides the braking distance for the supersonic-velocity ions. Three methods exist to limit the axial extend of the supersonic jet: An obstacle in the path of the jet (jet disruptor)[154], a rectangular, flat capillary outlet (Figure 24) or minimising the gas flow out of the funnel cavity. Either full sealing of the inter-electrode gaps[95] or a small electrode spacing in combination with large-surface electrodes minimise this gas flow[78].

Collisional cooling and confinement:

Once the ion has left the supersonic expansion, collisional cooling in the subsonic flowing gas dissipates most of the translational energy gained in the supersonic expansion. At the same time, the electrodes create an effective potential well which keeps the ions in the funnel cavity. These two processes limit the pressure range the funnel can operate in. If the pressure is too low, the gas cannot dissipate the ions kinetic energy or dampen its oscillating motion (Fig-

ure 26 and 27). If the pressure is too high, the ion mobility decreases and the effective potential cannot influence the trajectory of the ions enough to retain them in the funnel cavity (Figure 18 and 29). The upper and lower pressure limit depend on the ion's inertia τ_p and its reduced ion mobility K_0.

Ion transport

The partially thermalised ion must move to the ion funnel exit. The axial gas flow or a DC gradient can transport the ion. To suppress a reverse gas flow, Brunner et al. sealed the opening at the wide end of the funnel.[163] Alternatively, a wider electrode spacing with low-surface electrodes close to the final section is helpful. It allows a part of the gas to exit the funnel cavity close to the central sections. This causes an axial gas flow through the funnel towards the funnel exit (Figure 24). Thus, ion kinetic energy dissipation and gas-flow assisted ion transport work best with mutually excluding geometries. On the one hand, almost gas-tight electrodes with minimal spacing support the kinetic energy dissipation. On the other hand widely spaced electrodes with a low surface support gas-assisted ion transport to the funnel tip. Consequently, the electrode design can be used to select the dominating form of ion transport in the ion funnel.

If the gas flow is not sufficient or has the wrong direction, a DC gradient can transport the ions as well (Figure 21 and 22).

Extraction

The ion transport through the narrow final section of the ion funnel is a critical step. In this section, the space charge repulsion becomes maximal (Equation 4.6). The effective potential well countering the space charge is shallower at the final DC electrode (Figure 19). Axial ion traps hamper the transport of the ions. They form due to the small electrode radius (Figure 32). A non-linear DC gradient flattens the axial ion traps (Figure 33). A tight electrode spacing

in the final section ensures the effective potential remains high (Figure 31). It avoids ion losses due to insufficient confinement.

Finally, abrupt changes in the cavity geometry of the final section are detrimental for transmission (Figure 29).

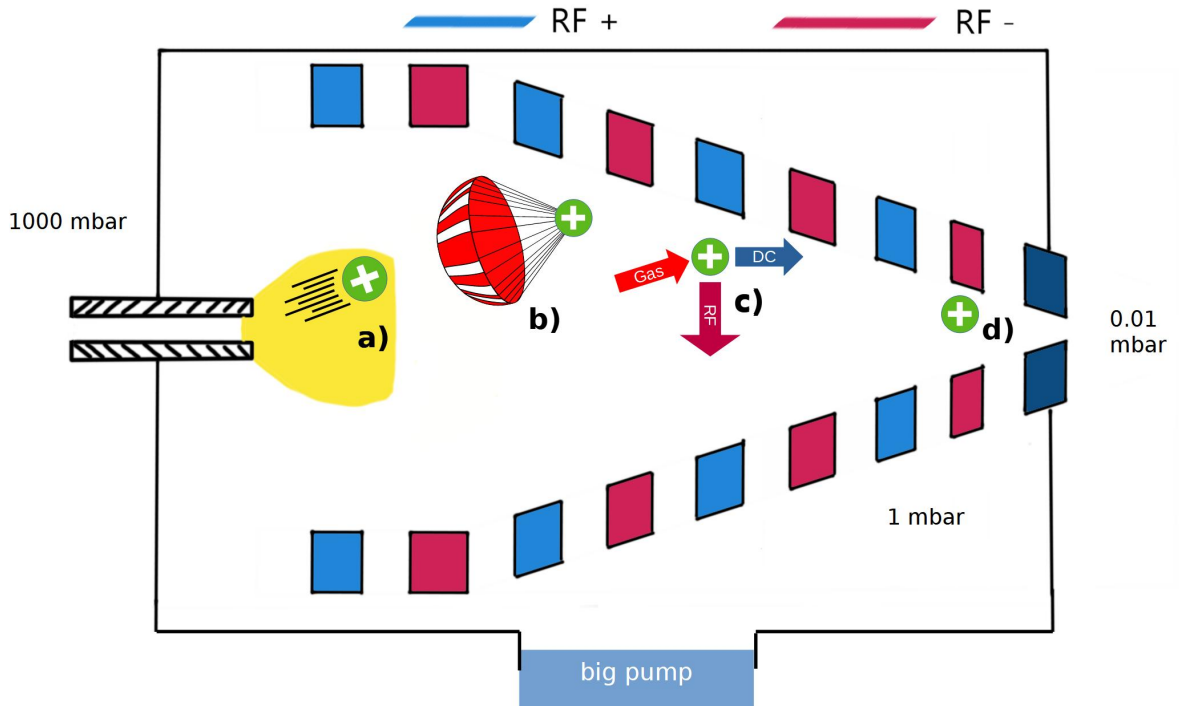


Figure 35: Main stages of ion funnel transmission: a) Acceleration in supersonic expansion b) Collisional cooling c) Ion transport d) Extraction

All main stages of the transmission process in a conventional ion funnel are summarised in Figure 35.

4.7 Outlook: 2-step atmospheric-pressure interface

Mass spectrometers equipped with large transfer capillaries (⌀ > 0.8 mm) to achieve high ion currents become increasingly common.[162] They require fore pumps of at least 100 m³/h gas throughput. Such a pump consumes about 10000 kWh electricity per year (Assumption: Pump draws half the rated power[173], so 1.1 kW and operates 365 d per year) – enough to power three households[174]. These big pumps are not only energy-hungry, but also more expensive

than smaller ones. The reason for the big pumps is the ESI process. Electrospray ionisation requires atmospheric pressure[28], but ion manipulation via electric fields in the mass spectrometer works best at low (ca. 1 mbar) to high vacuum (< 10^{-5} mbar). Thus, the ion funnel fore pump transports most of the air entering the first vacuum chamber outside again.

The gas throughput through the pump q_{pV} depends on the pumping speed S and the intake pressure p:[175, p. 13]

$$q_{pV} = pS = \frac{pV}{t} \tag{4.12}$$

with V the gas volume transported in time t.
Hence, a higher intake pressure p allows to use a smaller pump (i.e. smaller pumping speed S) for the same gas throughput. Unfortunately, the ion mobility limits the maximum pressure inside a conventional funnel (see Figure 29 and Equation 4.2).

Here I present a concept for an alternative approach. The main idea is to separate ion and gas directly in the supersonic expansion.[o] In the supersonic expansion, pressure drops by an order of magnitude (Figure 81 and 82 in Appendix) and the ion mobility increases. The drop in temperature limits the increase, but does not offset it. Figure 36a shows how the gas-ion separation in a supersonic expansion could work. Instead of an ion funnel, a small trap-diameter multipole is placed within the underexpanded jet. Rods thinner than necessary to produce a perfect multipole field[72], [176] reduce the impact on the gas flow. A high RF amplitude ensures that ions stay inside the multipole whilst the gas radially escapes. The gas also transports the ions towards the exit of the first chamber, no DC gradient is necessary. It is likely that the multipole will not be able to focus the beam to a small cross section due to the high radial gas velocities and the gas recompression which will take place close to the interface to

o Please note: I developed the idea for this concept during the collaboration with the TU Berlin. Julius Reiss had the idea to conserve the energy of the gas released during the supersonic expansion.

the next chamber. Instead, a funnel-shaped orifice uses the gas recompression zone to focus the ions onto the axis. In this zone, the pressure increases, the ion mobility decreases and the ions follow the gas stream lines. The principle is similar to the funnel-shaped capillary inlet. [96] Likewise, the gas without the ions which left the multipole is directed to the pump means of a hydrodynamically shaped chamber.

Then, the ions enter a second chamber with a conventional ion funnel. Here, they are separated from most of the remaining gas. A smaller pump is sufficient to achieve low pressure in the second chamber thanks to the smaller gas load.

Moreover, the thin multipole rods offer little resistance to the gas flow. An adapted chamber design, presumably in conjunction with a rocket-nozzle shaped capillary outlet (Figure 28) allows the gas to maintain high velocity. The pumping connections are designed to convert the kinetic energy of the gas to higher pressure, instead of stopping the gas and wasting this energy by raising the gas temperature. This increases the pump intake pressure. As a consequence, one big pump can be replaced with two significantly smaller, in sum energy-saving pumps.

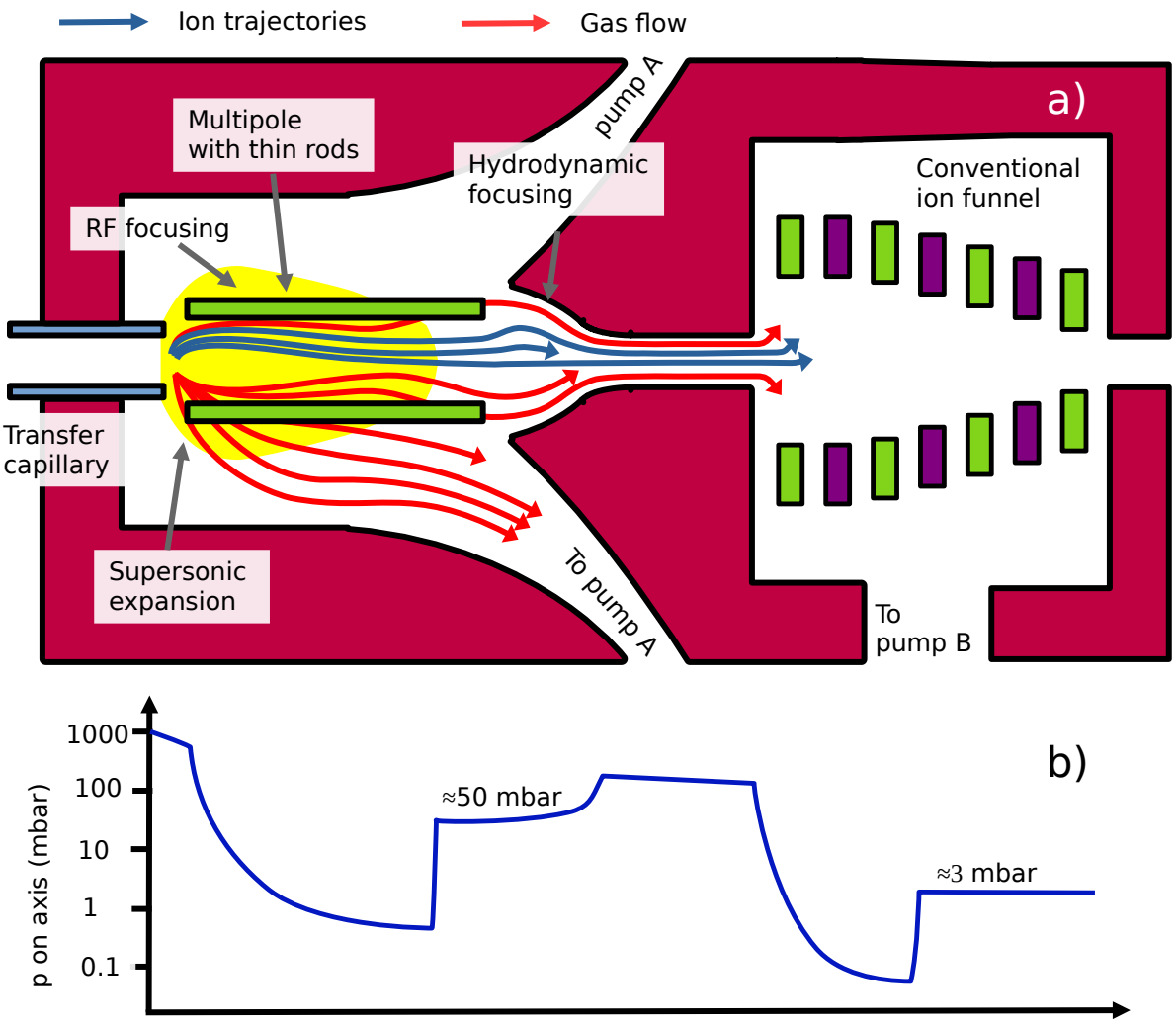


Figure 36: a) Schematic view of the 2-step interface. First ion optic is a multipole (n=2, 3 or 4) with thinnest rods to minimise disruption of the gas flow. In there and around, the supersonic expansion takes place. Gas and ion separation take place in the supersonic expansion. Ions are recollimated by the gas flow and transferred into a second chamber, where the remaining gas is removed in a conventional funnel. b) Possible estimated pressure on the central axis.

To test the viability of the concept, I conducted a simplified ion trajectory simulation with the Simion SDS package. I placed an octupole with 8 mm trap diameter and 0.8 mm rod diameter in a supersonic expansion. The small rod diameter is only ¼ of the ideal rod diameter for octupoles[176]. In high vacuum, this deformed multipole geometry could cause problematic transmission properties. Thanks to the gas damping of the ion trajectories, this is not the case here. The funnel A gas flow field (Figure 24) was integrated. In this supersonic expansion simulation, the gas reaches a velocity of about 700 m/s, the vacuum chamber pressure is 1.8 mbar. While this flow field describes the supersonic expansion well, it does not reflect the

disturbances caused by the octupole rods. To visualise the transport, 80 ions started in a filled circle with 0.8 mm diameter in the transfer capillary.

Figure 37a shows that the deformed octupole can confine a Hexamethoxyphosphazene ion beam against the forces of the expanding jet. The Paschen curve describes the limits to the maximum amplitudes which can be applied without a discharge.[177] The 200 V RF amplitude should just be achievable at 1.8 mbar pumping pressure.[178] In Figure 37b, the trajectories of 80 Apomyoglobin ions are visible. Here I multiplied the pressure field by 10 (pumping pressure 18 mbar). This is a crude model for the flow field present with a small pump, as for example the diameter of the supersonic jet would change at different pressure (See section 4.3 and equation 5.3).

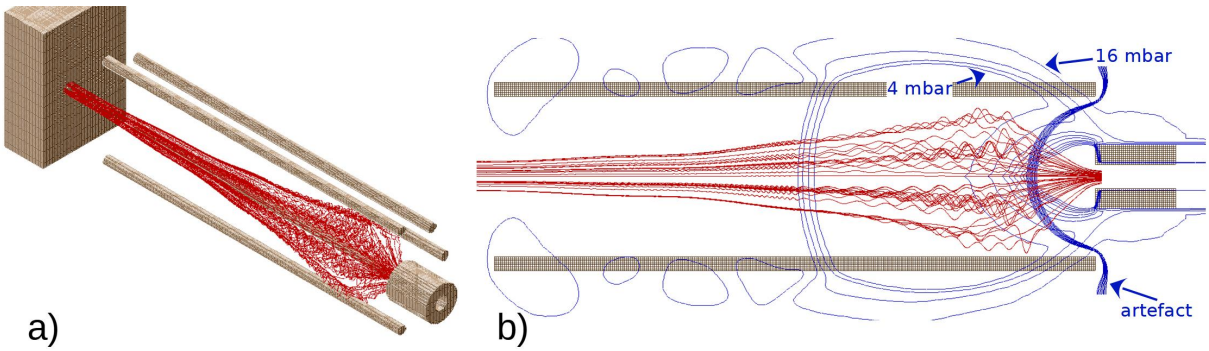


Figure 37: a) Cut-open view of an octupole placed in the supersonic expansion. 80 Hexamethoxyphosphazene trajectories at p_{pump}= 1.8 mbar, v_{RF} = 800 kHz, V_{RF} = 150 V. b) Trajectories of 80 Apomyoglobin ions at p_{pump}= 18 mbar (artificially increased), v_{RF} = 500 kHz, V_{RF} = 200 V. Only electrodes in vertical plane are visible. Blue lines: isobars in 4 mbar steps.

All ions are transmitted. The ions starting close to the wall of the transfer capillary come very close to the octupole rods before they are deflected by the effective potential. They follow the streamlines of the supersonic expansion due to the zone of high pressure originating from the transfer capillary. This zone reaches about 4 mm deep into the octupole. Inside, the ion mobility is too small, so the effective potential barrier has no effect. Only once the ions move to the low pressure zone, they can be deflected. As this happens close to the rods, it is best to use a higher-order multipole such as an octupole. Lower-order multipoles have a less steep potential gradient at high trap radii.[72, p. 32]

Whilst an ion with a medium inertia such as apomyoglobin reaches the low pressure zone before it collides with the rods, light ions of low inertia react differently. Already at 3-fold pressure (pumping pressure 5.4 mbar), some hexamethoxyphosphazene ions collide with the electrodes (Figure 85 in Appendix). This illustrates that the concept of a multipole in the supersonic expansion has to be carefully tailored to the target analyte system. The operation pressure and the multipole geometry (trap radius, rod diameter) have to fit together.

To test this concept further, a computationally expensive 3D CFD simulation of the gas flow field would be required. It could predict the disturbances caused by the multipole rods. With

this gas flow field, an ion trajectory simulation could test if it is possible to confine the ions at an RF amplitude small enough not to risk a discharge.

5. A new instrument for mass and mobility filtered deposition

Most custom preparative mass spectrometers are designed for small-molecule deposition.[21], [27], [31], [34], [37], [67], [68], [142], [179] In contrast, the modified commercial Q-Exactive UHMR mass spectrometer (see chapter 3) transmits heavy, native protein complexes best. It has a collision cell to cool the ion beam after the quadrupole mass selection. The collision cell can activate or dissociate ions. The cooled ion beam has a narrow energy-spread. This narrow spread limits losses in the deposition optics and enables small deposition spots. Unfortunately, the UHMR deposition currents for small molecules (< 0.3 nA) are less than 1/10 of custom preparative mass spectrometers (3...15 nA).[33] It does not transmit ions with a mass-to-charge-ratio of less than 350 Th. ES-IBD with small molecules for self-assembly[47], surface-collision reactions[38], [51] or ultra-pure surface preparation[47], [49], [179] are impracticable.

Hence, our laboratory required a new ES-IBD mass spectrometer. It should have a collision cell and the low-energy spread of the commercial UHMR. The new mass spectrometer should combine these features with the high deposition currents custom instruments achieve for ions in a large mass-to-charge-ratio range.

The reason the UHMR does not transmit light ions is the design of the RF generators. They supply the RF ion optics with a sinusoidal voltage at a fixed frequency. The frequency determines the mass-to-charge-ratio (m/z) range the RF ion optics transmit.[148, pp. 53–55] If an ion has a too small m/z-ratio (< 350 Th), its oscillating amplitude increases and it hits the electrodes. There is no theoretical upper limit for the transmission of high m/z-ratio ions. In practice, if the m/z-ratio is too big for the applied RF frequency and amplitude, the effective force

is insufficient to counter the always present radial energy of the ion beam.[148, pp. 53–55] The transmission efficiency of the ion guide drops.

To extend the mass range, multiple RF generators of a different frequency per ion optic can be installed. For instance, at the ES-IBD instrument I used for the investigation of the existing funnel, each quadrupole can be supplied with three different RF generators (see section 4.2). Heavy ions (450...15000 Th) require the 500 kHz generator, medium and light (26...1500 Th) the 1 or 2 MHz RF generator.[148]

An alternative to multiple, oscillation-circuit based RF generators are RF power switches, which produce rectangular signals. Prototype power switches for RF ion guides allow to set the RF frequency from a few Hz to 1 MHz.[180]

Furthermore, ion mobility information (see also section 4.1), which relates to molecular shape, remains inaccessible with current ES-IBD mass spectrometers. Often, the solvation of the native protein ions visible in the mass spectra are used as an unreliable proxy for the conformation of an ion. A folded conformation is assumed if the mass spectra show very large peaks, usually due to solvation (see Figure 73 for an example). Sharp peaks can indicate an unfolded conformation, as ion-gas collisions have stripped the solvent shell. Ion mobility data allows to calculate the collisional cross section of an ion (equation 4.3). CCS is a better indicator of conformation. Ion mobility can monitor collision-induced unfolding of native proteins in the gas phase[181] and the collision-induced release of membrane proteins from the detergent micelle necessary to preserve their native structure[182]. As a consequence, the new ES-IBD instrument requires an ion mobility analyser for a controlled use of the collision cell.

In chapter 3.3 (section “Control of conformation after landing by mass filtering and solution composition”) it has been shown that ES-IBD coupled to SPM is capable of detecting coarse differences in conformation of a protein in the gas-phase pre-deposition. Finer changes in

conformations of flexible biomolecules have been observed with ES-IBD coupled to microscopy. Angarra et. al sampled the conformation space of an oligosaccharide with soft ion-surface collisions.[48] Ochner et al. found an abundance of compact conformations on images of single IgG antibodies. The antibodies are highly flexible and can collapse in the gas-phase[183]. For both the oligosaccharide and the antibody study, the deposition instrument lacked the ability to select a conformation before deposition. The authors used molecular dynamics simulations and varied the collision energy on landing to find out how the observed surface conformations relate to the gas-phase conformations.

An ion mobility filter would fix this drawback. It adds an orthogonal separation domain to the ES-IBD process. In addition to the quadrupole mass-to-charge filtering, it separates ions pre-deposition according to their ion mobility. Selecting a specific conformation reduces sample heterogeneity. It would allow to study structure and behaviour upon deposition of different gas-phase conformations separately. In essence, it experimentally links adsorbed surface and gas phase conformations. Thereby, it would deliver data to better understand the landing process. At the same time, it gathers ion mobility information. If this information can be easily translated into CCS, it can partially substitute a separate ion mobility analyser.

A mobility filter can separate isobaric ions. For example, Wu et al. revealed the connectivity of branched glycans deposited by ES-IBD with scanning tunnelling microscopy.[45] Hence, an ion mobility filter could differentiate isomers from a glycan mixture to deposit them separately– impossible with a quadrupole mass filter. Currently, structures from Cryo-EM or LEEH protein samples prepared with ES-IBD lack amino-acid level resolution.[36], [121], [184] Should this improve, a mobility filter will enable to pre-sorting protein conformations. This could help to elucidate the structure of intrinsically disordered proteins[185], [186] or proteins with post-translational modifications[187].

In summary, the new ES-IBD mass spectrometer should have an intense, low-energy spread ion beam, a collision cell and a mobility filter. It should transmit heavy and light ions well.

5.1 Concept

Based on the requirements, I developed a plan for a new ES-IBD mass spectrometer, named *'inverted porcupine'*. The name was a constant reminder not to design over-complicated ion optics with a close-to-infinite number of sting-shaped, individually controlled electrodes, hoping to find solutions to the many desirable properties. Hence, not to build an inverted porcupine.

The instrument concept consists of two modules, A and B (Figure 38).

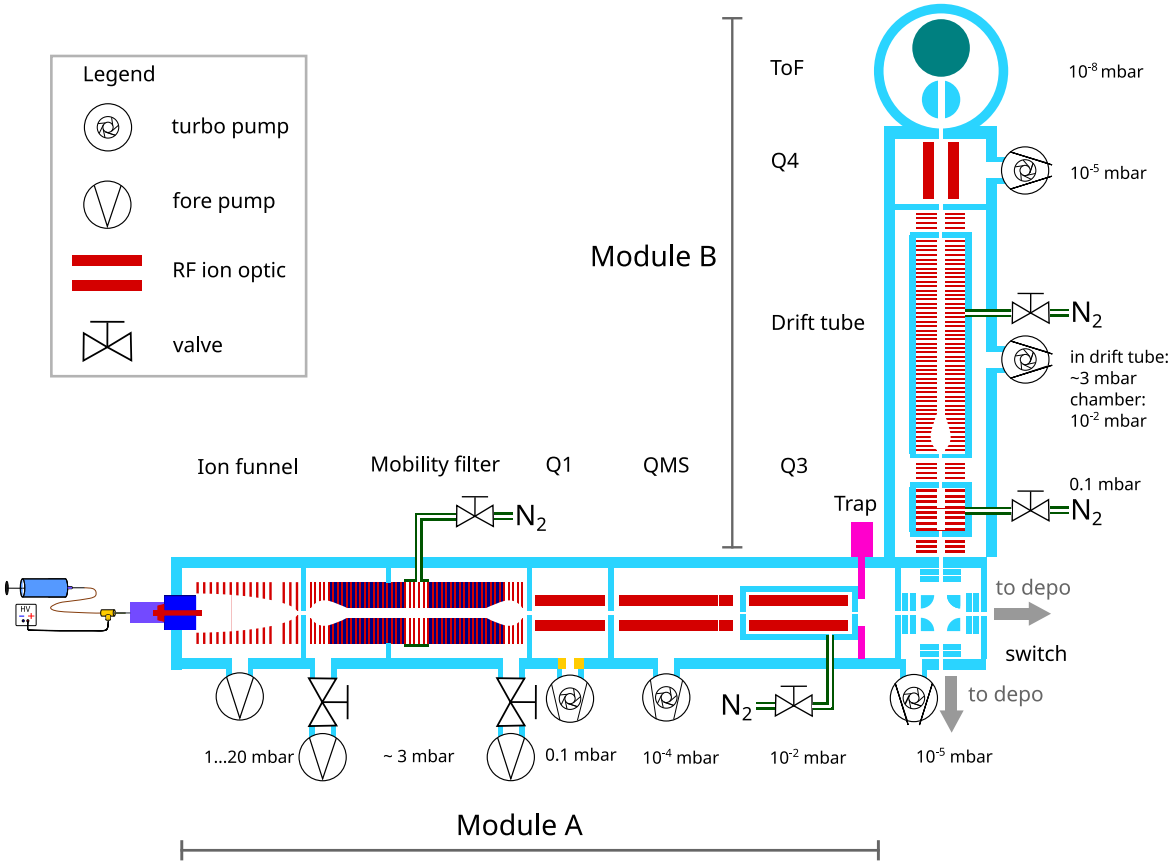


Figure 38: 'Inverted porcupine' schematic instrument overview. The preparative ion mobility mass spectrometer consists of two modules A and B. A produces a mass- and mobility filtered ion beam. B analyses the mass and mobility domain.

Module A produces a mass- and mobility-filtered ion beam. The ions are separated from the gas in a two-step hydrodynamically optimised ion funnel.

A novel, continuous, ion mobility filter selects the ions within a mobility range of interest. The RF-only quadrupole Q1 thermalises the ion beam before they enter into the quadrupole mass filter (QMS). The mass-selected ions can be further activated in the collision cell Q3, for example to change the ion's conformation. It also cools the ion beam to minimise the energy-spread. A gate-valve separates module A from the rest of the instrument (deposition stage, module B). It allows to switch off all vacuum pumps in module A to save energy without venting a connected deposition stage or module B. It also avoids vibrations from the module A pumps when a microscope is attached to a deposition stage.

Module A and B are connected with an electrostatic quadrupole deflector. It can switch the beam between four ports, two of them are free for deposition stages. Module B consist of a linear drift tube ion mobility analyser, a differential pumping stage Q4 and an orthogonal reflection ToF for mass- and mobility analysis. The linear drift tube allows to tune the mobility filter quickly and enables to obtain CCS values without prior calibration. A pair of RF power switches supplies each RF ion optic (ion funnel, mobility filter, Q1, QMS, Q3, trap cell, drift tube, Q4), so the instrument has an extremely flexible mass-to-charge range.

In a first stage, only module A was realised. I shortly describe the basic deposition procedure with it here. A typical ES-IBD deposition requires to mass-filter the ion beam. In a second step, it is necessary to analyse the composition of the filtered beam. Hence, the current configuration with module A only profits from a MS-MS capability to acquire mass spectra of the mass-filtered ion beam. Although the ToF analyser will only come with module B, the quadrupole Q3 in module A can be operated without background gas as a mass filter. This provides minimal MS-MS capability.

This chapter presents the ideas and proof-of-concept simulations of the key ion optics components of the instrument. These are the ion funnel optimised for high transmission at low pumping powers and the continuous ion mobility filter. Further, I discuss the design and limitations of the RF power switches. They have an extended frequency working range to transmit ions with a large m/z-ratio. Last, I analyse how to decouple the ion beam from the last RF ion optic Q3 to electrostatic lenses in high vacuum.

The CAD design and manufacturing of the prototype was done in collaboration with the Max-Planck-Institute for solid state research (MPI-FKF, Stuttgart, EU).

5.2 Atmosphere-vacuum interface for high transmission at low pumping powers

I designed the ion funnel on the basis of the experiments and ion trajectory simulations in chapter 4. These indicated that a steady taper in the cavity is better than an abrupt contraction (Figure 30). The electrode spacing controls the gas flow out of the funnel cavity (Figure 24). The wider the electrode spacing is, the easier the gas exits the cavity. A gas flow which supports the transport of the ions towards the funnel apex forms. However, a wide electrode spacing weakens the radial effective potential barrier which keeps the ions in the funnel (Figure 31).

The effective potential barrier should be maximal close to the apex of the ion funnel to counter space-charge effects of the collimated beam (Section 4.2). Hence, it is not possible to use a wide electrode spacing there. However, a tight electrode spacing in this region hampers the gas flow through the inter-electrode spaces. Thus, a recompression of the gas flow occurs (Figure 81 in Appendix), the local pressure increases. As the funnel apex is adjacent to the aperture connecting to the next vacuum chamber, the gas load on the next chamber increases. The next chamber requires a bigger pump. In summary, the electrode spacing at the apex presents a design dilemma: Tight spacing creates a higher effective potential barrier, generous spacing supports the gas-assisted ion transport and reduces the gas load in the next chamber.

To circumvent the problem, the *'inverted porcupine'* funnel has a gap in the tapering section (Figure 39a). This gap separates the funnel into two zones. In the first zone, the supersonic expansion takes place. After the expansion, the gas and a DC gradient move the ions towards the tip. Due to the decreasing inner diameter of the electrodes with the axial coordinate, the gas jet will come closer to the electrodes. At some point, the gas jet will start to interact with the electrode surface and recompress (Figure 39b). The gap allows most of the compressed gas to exit the ion funnel cavity with little resistance. Thereby, it drives the axial gas flow in the first

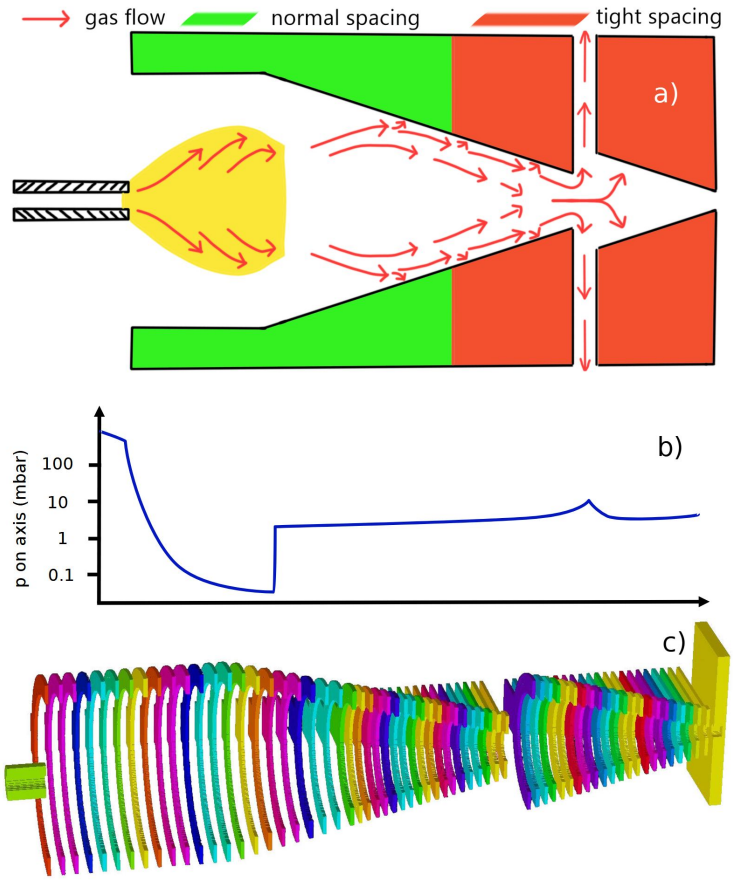


Figure 39: 2-section funnel for optimal usage of pump. a) Scheme with electrode spacing. b) Expected pressure along the central axis. c) Simion model of the electrodes.

funnel zone. This axial gas flow transports the ions through the first zone.

In the gap, the ions experience little guiding from the effective potential. There, the strong radial gas flow of the exiting gas in the gap would entrain the ions. To avoid this, two measures are necessary. First, the exit electrode of zone one must be smaller than the entry electrode of zone two. Second, a strong DC gradient between the two electrodes pulls the ions axially into the second zone cavity. The strong DC gradient increases the axial velocity of the ions and reduces their absolute radial displacement by the exiting gas in the gap.

The second zone collimates the ions for transport in the next vacuum chamber. As most of the gas from the transfer capillary has left the cavity through the gap, the pressure increase close to the aperture will be small.

Moreover, all electrodes are 0.8 mm thin and their surface area is minimal to minimise the resistance to the gas flow (Figure 39c). The electrode spacing is wider in the initial section, where space charge is negligible. Both measures decrease the load capacitance, which limits the RF amplitude (see section 5.4). The funnel has a non-linear DC gradient to avoid RF trapping in the final section at minimal DC voltage drop (see page 137).

Verification of the Hydrodynamic Properties

A CFD simulation of the gas flow in the ion funnel field helps to obtain essential design parameters. Unfortunately, there were no resources to conduct such a CFD simulation. Instead, I estimated the diameter and length of the supersonic jet (see following paragraph). Moreover, I simulated the trajectories of the ions in the gap area between the two zones.

Section 4.6 showed that the cavity of a conventional ion funnel must be bigger than the supersonic expansion jet. The space between the boundary of the jet and the electrode rims should be big enough, so that the ions can dissipate the kinetic energy gained in the jet. The supersonic jet at the apex of the transfer capillary can be either moderate-, highly-, or very highly underexpanded.[144] The type of underexpansion depends on the pressure ratio η_0.[144] It relates to the stagnation pressure p_0 and the pressure inside the vacuum chamber p_∞: [144]

$$\eta_0 = \frac{p_0}{p_\infty} \tag{5.1}$$

For a deposition of small-molecules, p_0 is the atmospheric pressure and the vacuum chamber pressure p_∞ is 3 mbar. In this case, a very highly under-expanded jet with a single Mach disc will form.[144], [145] Crist et al. derived a formula for the axial position L_{MD} of the Mach disc: [188]

$$L_{MD} = D_e \cdot \sqrt{\frac{\eta_0}{2.4}} \tag{5.2}$$

with D_e = 1.5 mm, the inner diameter of the transfer capillary. Formula 5.2 predicts 18 mm length of the very highly underexpanded jet. Therefore, the straight section should be longer than those 18 mm. I used a safety margin of approximately two, setting the straight section to 43 mm length.

Franquet et al. fitted experimental data from different sources to find a formula for the diameter D_M of the Mach disc:[144]

$$D_M = 0.28 \cdot D_e \eta_0^{0.53} \tag{5.3}$$

It predicts 9 mm Mach disc diameter. I chose 40 mm diameter for the straight cavity section to provide enough space for a deceleration region for the supersonic ions exiting the jet.

To check if the gas entrains ions in the gap between the first and second funnel zone, I simulated the trajectories of hexamethoxyphosphazene in the ion funnel. Due to its low inertia, it is a good probe ion (Table 1). Heavier, folded ions will react slower to the axial gas flow and will pass the gap with less axial displacement. As no CFD gas flow field was available, I set a global gas velocity orthogonal to the funnel axis of 200 m/s. This is approximately the radial gas velocity between the electrodes in funnel A (Figure 24).

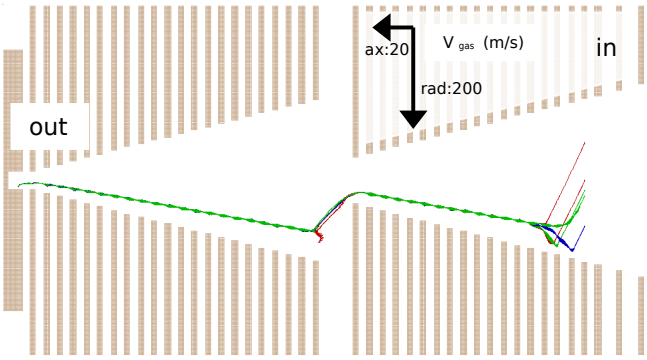


Figure 40: Trajectories of 6 hexamethoxyphosphazene ions in the 'inverted porcupine' funnel. v_{RF} = 1 MHz, V_{RF} = 110 V (rectangular), p = 3 mbar.

Figure 40 shows the trajectory of six hexamethoxyphosphazene ions. The high radial gas velocity pushes the ions close to the rim of the funnel electrodes. An axial gas velocity of 20 m/s and a 22 V DC gradient over the gap are sufficient to transport five of six ions over the gap in the ion trajectory simulation.

To ensure all ions are transmitted, the gap DC-gradient should be higher (approximately 30 V). In summary, the funnel cavity is large and long enough to accommodate the underexpanded supersonic jet. The gap will not lead to ion losses as a moderate DC gradient transports the ions over it.

DC Gradient

The tapered section in the *'inverted porcupine'* funnel is at an angle of 14° to the central axis. This reduces the length of the 2-zone construction as compared to the existing conventional funnel, which has an angle of 7° (see section 4.2). The electrode spacing is 1.25 mm face-to-face in the tight-spaced areas and 2.5 mm in the initial section. With a minimum electrode diameter of 2.6 mm, axial trapping wells form in the narrow final section of the funnel (Figure 41). These can lead to RF-induced trapping, which can reduce the transmission due to space-charge (see section 4.5).

With a 30 V non-linear DC gradient applied in a 7:2:1 partition to RF electrodes 2, 3 and 4, the axial trapping wells disappear (Figure 41).[p] I used these values for the non-linear resistor cascade.

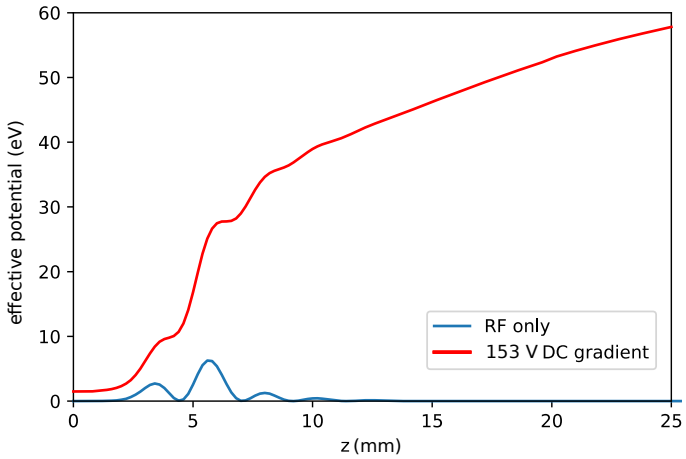


Figure 41: Effective potential on the 'inverted porcupine' funnel axis for hexamethoxyphosphazene. ν_{RF} = 1 MHz, V_{RF} = 110 V. Of the 153 V DC gradient over the full ion funnel, 30 V are applied to the final four electrodes.

The funnel has six DC taps. These allow to set the DC gradients of the different funnel sections independently (Figure 42).

The final electrode, the aperture ion-funnel/filter, is DC-only. It is not connected to the funnel DC cascade because it is intended for ion current measurement. It has its own DC power supply. The recommended DC gradients for the transmission of a small organic ion such as hexamethoxyphosphazene are shown in Figure 42.

All voltages marked with a '~' symbol are approximated. They support the transport of the ions only. More important is the DC gradient from electrode 25 to 20, which are separated by

p The final RF electrode has a voltage tap and defines the begin of the non-linear resistor cascade.

the gap between the two funnel section. This axial DC gradient attracts the ions towards the apex of the funnel. It limits the gas-flow-induced radial displacement of the ions in the gap between the two funnel zones. The DC gradients between electrode 4, 1, and the aperture reduce axial trapping wells.

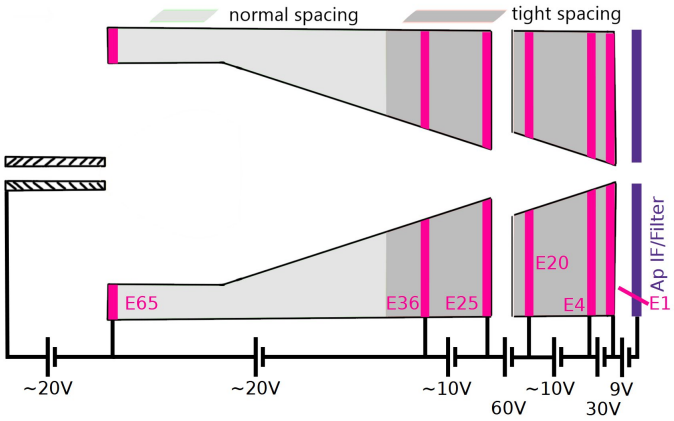


Figure 42: Recommended DC Gradients for the transmission of hexamethoxyphosphazene at v_{RF} = 1 MHz, V_{RF} = 110 V. Electrode taps are marked with the number of the corresponding electrode.

Mechanical construction

The 65 funnel electrodes and the lateral holders are made of printed circuit boards (Figure 43). The material is a glass-reinforced epoxy material (RF4). Each RF-Phase is supplied via one lateral printed circuit board holder. The two holders span the entire length of the funnel.

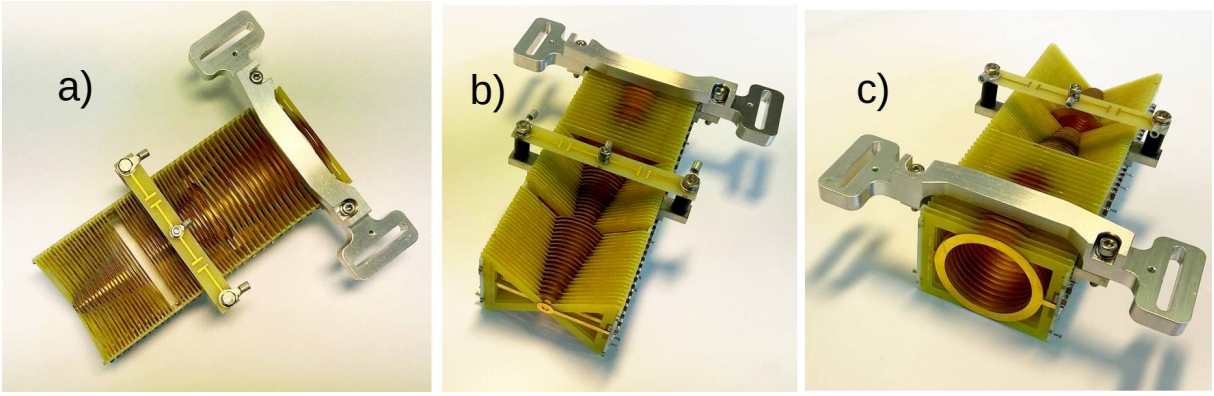


Figure 43: Inverted porcupine funnel. a) Top view b) view from Ion mobility filter side c) view from transfer capillary side. Photos: Moritz Edte

To keep the resistance to the gas flow from the funnel cavity to the pump small, the electrodes are 0.76 mm thin (in imperial units: 30 mil) and their surface area is minimal. An X-shaped

geometry supports the conductive part of the small-inner diameter electrodes (Figure 43b). It allows the gas to leave the cavity via the bottom and top side. For the larger electrodes, a rectangular geometry was chosen.

The electrodes are plated with electro-less nickel immersion gold. The gold-plating is limited to a depth of 2.5 mm for the 1.25 mm spaced electrodes and to 5 mm for the 2.5 mm spaced electrodes. The gold-plating acts as a plate capacitor between the two RF phases. Thanks to the limited plating depth, the surface area of the gold-plating is reduced. This limits the capacity to only 190 pF between the RF electrodes. A conventional funnel with solid metal electrodes has an approximate capacity of 1 nF.[q] The low capacity is necessary to attain high RF amplitudes at high frequencies with the square wave RF power switches (see section 5.4).

Due to its position directly after the spray capillary, the ion funnel gets contaminated very quickly. Transmitted large and small droplets from an ill-defined electrospray can deposit thick layers of non-conductive material on the electrodes. To ensure good transmission, it is necessary to clean the ion funnel on a regular basis. To this end, the electronics contractor CGC Instruments (Chemnitz, European Union) tested several cleaning procedures on the funnel electrodes. They applied oil and graphite to the electro-less nickel immersion gold plating. They cleaned it with isopropanol, 30 % hydrochloric acid and a rubber eraser with no visible damage to the gold plating. Only a heavy-duty scrub sponge left marks. Hence, the full ion funnel can be cleaned in the assembled state with isopropanol, rubber or a soft brush. Hydrochloric acid could damage the solder joints and surface-mounted capacitors and resistors. It must be avoided.

q Calculated assuming the existing funnel geometry (see 4.2 Experimental investigation of a conventional funnel), 45x45 mm square plates with the cavity cutting a 50 % hole in each electrode.

5.3 Continuous mobility filter

Ion mobility spectrometry (IMS) uses an electric field to separate ions of different mobility K_0 in a bath gas. Most IMS techniques, such as drift time IMS, travelling-wave IMS and trapped IMS require a gate to introduce ions as a discrete package into the mobility analyser.[189] The gate opens for a short time.[189] Ions with different K_0 are separated spatially along the ion flight path axis.[189] An observer at the exit of the IMS device sees the ions with different K_0 passing one after another along the same flight path. For the observer, they are separated in time along the beam path. In an ES-IBD instrument depositing such a beam, ions of all mobilities would accumulate on the sample. These time-discrete IMS techniques could only be used for deposition if a kill-electrode was placed at the exit of the mobility analyser. When active, the kill electrode would deflect any ions nearby with a high electric field and would remove them permanently from the ion beam. The kill electrode activation would be tuned to the timing of the entrance gate to remove ions with unwanted mobility exiting the mobility analyser. The result is a pulsed, mobility-filtered ion beam. Bruker, a mass spectrometry manufacturer, patented such an IMS-ES-IBD instrument, but never commercialised it.[190]

The big problem with a pulsed ion beam is transmission. Warnke estimated a current of only 40 fA transmitted through a drift-time IMS trapping and injecting ubiquitin ions at 20 Hz. [191, p. 53] The same instrument generated a 10 pA bradykinin current in continuous transmission mode.[192, p. 74] Note that the currents were measured under different conditions. However, the stark difference illustrates the issue.

The reason for the low transmission in pulsed operation are losses during the trapping and subsequent release process. During the trapping, the constant incoming current I_{in} accumulates ions in the trap. When the gate opens, a short high current ion beam pulse is released (I_{out}). If

the trapping is assumed to be lossless, the proportion between the fill time t_{fill} and the release time $t_{gate\ open}$ amplifies I_{out}:

$$I_{out} = I_{\text{in}} \frac{t_{fill}}{t_{gate\ open}} \tag{5.4}$$

The amplification is particularly important for ES-IBD due to the high ion currents. For example, an ES-IBD instrument generates a 5 nA ion beam. If it operates with a typical frequency for pulsed IMS of 40 Hz (t_{fill}= 25 ms) and releases its trap within 0.5 ms[193], a short current pulse of 250 nA arises. That is six times the space-charge limited calculated for a conventional ion funnel (see section 4.2). It is likely that neither the gate trapping and accumulating the ions, nor the downstream ion guides can generate the necessary effective force to counter the space-charge of such a current pulse. Thus, a pulsed ion mobility module will lead to significant current losses in ES-IBD.

Consequently, an ES-IBD instrument requires a continuous ion mobility filter. A common mobility filter is high field asymmetric wave-form ion mobility spectrometry (FAIMS).[189], [194], [195] It exploits the differences in ion mobility in low- and high electric fields.[189] It is widely commercially available as an additional module placed in front of the atmospheric pressure inlet of a mass spectrometer.[196]–[198] Unfortunately, FAIMS cannot determine CCS due to the high electric field it requires.[199] The reason is that at high electric field the ion mobility becomes a function of the electric field.[93] The high field also heats the ions by a temperature of about 50 K, which unfolds native protein ions.[200] Thus, FAIMS is unsuitable to select a certain molecule conformation prior to deposition.

Other continuous mobility filters are the differential mobility analyser (DMA) and overtone mobility spectrometry (OMS).[189] DMA uses a constant, low electrical field orthogonal to a linear gas flow to separate ions in space.[201] Planar and cylindrical DMAs exist.[189] Cur-

rent DMA designs have no RF ion guiding[202], and the principle of the analyser allows for RF guiding in one axis only. Significant ion losses due to diffusion or gas turbulence cannot be avoided.

OMS could be the ideal continuous mobility filter because it confines the beam radially with RF and eliminates ions with kill electrodes.[203] Therefore, it would not encounter any space-charge issues. However OMS is challenging to operate because it requires the modulation of several DC gradients with different frequencies and has not exceeded proof-of-concept demonstrations.[204]–[207] In conclusion, there is currently no suitable concept to mobility-filter high current ion beams gently without activation.

High-pass Low-pass Parallel Flow Mobility Filter

The traditional axial ion mobility analysers, for example drift time IMS and travelling-wave IMS, use a resting bath gas and move the ions through it by an electric field. As early as 1898, Zeleny had the idea to use an axial gas counter flow to measure ion mobility in a constant electric field – a parallel flow analyser.[208]

In the early 2000s, scientists at the University of Manitboa designed a trapped ion mobility parallel flow analyser.[209] To improve transmission, they built a gas-tight, segmented quadrupole.[209] The RF confinement limits losses while the ions move against the gas flow. The DC gradient moving the ions is swept periodically to elute ions according to their mobility.[209] A weak DC gradient elutes ions with high mobility, a high DC gradient is necessary to transmit ions with low mobility. The system acts as a high-pass mobility filter. Sciex (a mass spectrometry manufacturer) later patented the system.[210] Shortly after, Bruker (a competitor) presented a similar mobility filter, but with inverted gas flow.[211] This is a low-pass ion mobility filter.

On their own, both the high- and low-pass mobility filter require trapped operation to separate ions of different mobility. For example, if a high pass mobility filter is set to transmit ions of low mobility, ions of high mobility will elute as well. Therefore, an upstream gate has to interrupt the supply of new ions from the source during the DC gradient sweep.

Only a combination of a high- and low-pass filter can create a continuous ion-mobility filtered beam. Figure 44 explains the principle and shows the basic design of the high-pass low-pass parallel flow mobility filter.

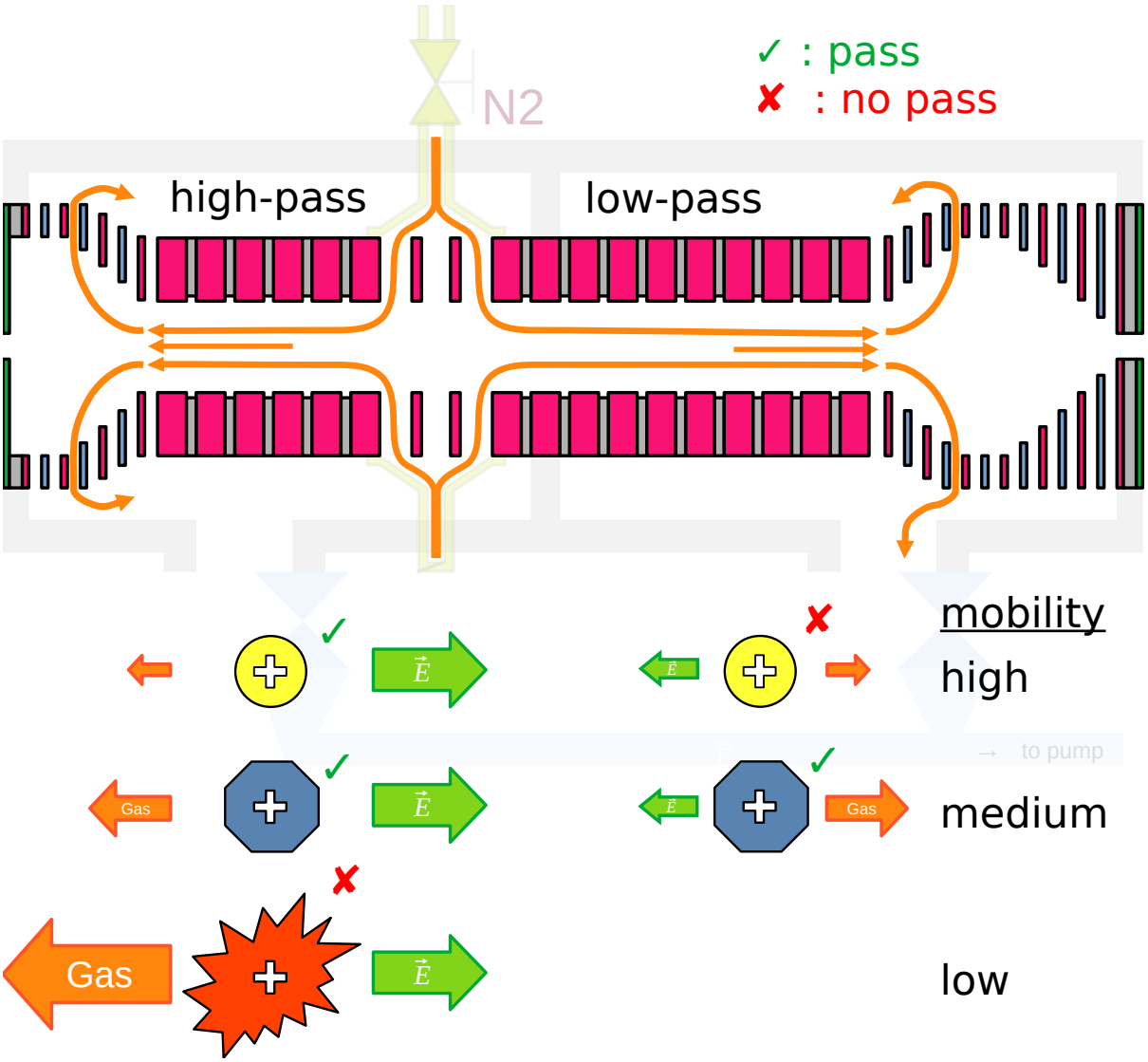


Figure 44: Principle of the high-pass low-pass parallel flow mobility filter. The high-pass filter transports ions of high mobility (pass indicated with "✓") with an electric field against a counter-gas flow. The low pass filter only transmits ions of low mobility entrained by the gas flow. Together, they transmit ions within a clearly defined mobility range.

The high- and low-pass filter have each a pumping section and a tunnel section, separated by a central gas inlet. The pumping sections are stacked-ring-electrode ion guides (SRIG). Between each electrode is a small open space to allow the gas to flow out of the cavity. The tunnel sections and the gas inlet are segmented quadrupoles.

In this example, ions of three different mobilities enter the segmented quadrupole from the left side. All ions have the same charge, but their collisional cross section is different. The yellow ion has the smallest CCS and the highest mobility. The blue ion has a medium mobility.

The red ion has a small mobility and the biggest CCS. All three ions experience the same DC electric force in the high-pass filter (green arrows). It transports the ions against the gas flow. The high pass filter transmits the yellow and the blue ion. It retains the red ion, because the counter gas flow produces a friction force superior to the DC electric force due to the high CCS.

When the yellow and blue ion reach the low-pass filter, they again experience the same DC force. The gas flow and electric force direction in the low-pass filter are inverted compared to the high-pass filter. This time, the DC force vector points backwards (upstream). It retains the ions against the gas flow friction. The blue ion has a smaller CCS than the yellow ion, so the gas friction manages to push it through the low-pass filter. The DC force retains the yellow ion. Overall, only the blue, medium-mobility ion passes the entire high-low-pass filter combination.

This example illustrates the parallel flow analyser separates ions with different mobilities in space. It does not require a kill electrode at the exit. By tuning the gas velocity and the DC gradients in both filter parts, the mobility filter transmits only ions within a specific mobility range.

Nevertheless, the ions with too low mobility accumulate in the high-pass filter region and the ions with too high mobility in the low pass filter region. At very high currents and a narrow filter width, large ion clouds of retained ions could form in the filtering regions. These ion clouds could clog the mobility filter or lead to space-charge-induced breakthrough. To avoid both scenarios, the RF power switches (see section 5.4) can pause the RF for several RF periods in tuneable intervals. A pause in the RF voltages empties the entire filter. All ions crash into the closest RF electrode.

DC electric field

In a parallel flow mobility filter, the ratio of the local gas velocity and the local electric DC field $\vec{E}$ define a critical ion mobility K_{crit}.[212] An ion with K_{crit} moves neither forward nor backwards in the filter, it is trapped due to the balance between the gas drag force and the electric force. In this case, the drift velocity equals the negative local gas velocity v_g.[212]

In the analyser sections of the mobility filter, the gas velocity vector $\vec{v}_g$ and the electric field vector $\vec{E}$ are parallel to the z-axis. The z-axis is oriented along the beam path in the vacuum chamber. The vacuum chamber is the reference system. To simplify the calculation of K_{crit}, $\vec{v}_g$ and $\vec{E}$ can be projected on the z-axis (Figure 45). The result of this projection are two scalars E and v_g. The scalars are positive if the original vectors pointed in positive z-direction (towards Q1) and negative if the original vectors pointed in negative z-direction (towards the ion funnel).

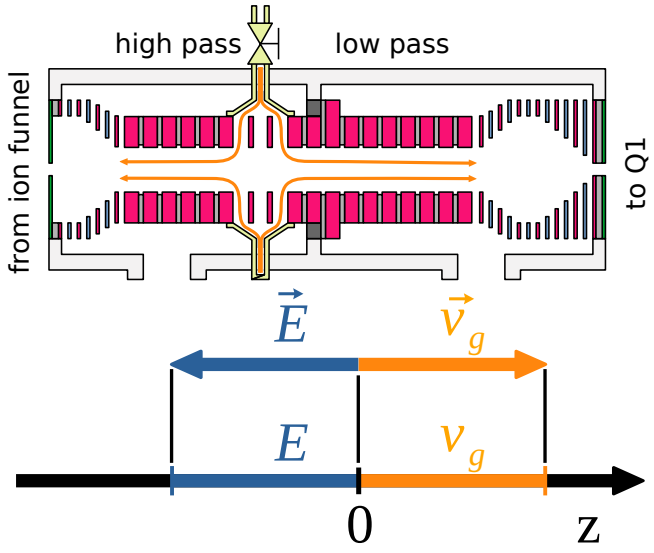


Figure 45: Projection of the gas velocity and the electric field on the z-axis. Example is for low-pass filter and a positive ion.

With this simplification and equation 4.1, the transmission criterium K_{crit} is:

$$K_{crit} = \frac{|\vec{v}_d|}{|\vec{E}|} = \frac{-v_g}{E} \cdot \chi \qquad (5.5)$$

χ is 1 for a cation and -1 for an anion. K_{crit} has a different meaning in the high- and low-pass filter. On one hand, in the high-pass filter, the electric field transports the ions against the gas flow. K_{crit} is the minimum mobility an ion needs to travel through the filter. On the other hand,

in the low-pass filter, the gas flow pushes the ion against the electric field. K_{crit} is the permitted maximum mobility the ion can have so that the low-pass filter transmits it.

In both the high- and low-pass filter, the following applies: If the two vectors point in opposite directions, K_{crit} is a positive scalar. If they point in the same direction, K_{crit} is a negative scalar and meaningless, as any ion will be transmitted. K_{crit} depends on the local pressure p and the local temperature T. With equation 4.2, it can be normalised to standard conditions:

$$K_{0,crit} = \frac{-v_g}{E} \cdot \chi \cdot \frac{p}{p_0} \cdot \frac{T_0}{T} \tag{5.6}$$

with the local gas velocity v_g, the DC electric field E, the local pressure p and the local temperature T, the critical mobility K_{crit} can be calculated at any point. Consequently, these are the key parameters for an accurate simulation and design of a parallel flow mobility filter.

Due to limited resources, it was not possible to realise a CFD simulation of the gas flow field in a potential high-pass-low-pass filter geometry. Instead, I built an analytical expression for the gas flow field based on the CFD simulation of a low-pass trapped IMS computed by Silveira et al.[213] I made the following assumptions:

- The pressure at the gas inlet is 2.6 mbar. It decreases along the quadrupole section in both directions and reaches a plateau of 2.3 mbar in the pumping sections at each end (Figure 46a).

- The gas velocity increases/decreases linearly from the gas inlet and reaches its maximum/minimum at the end of each analyser section (Figure 46b). In both pumping sections, the velocity decreases again. The radial velocity profile is parabolic in the quadrupole sections (maximal on the central symmetry axis and zero at the walls). Underestimating the gas velocity in the high-pass section can lead to a total blockage

of the mobility filter if the gas drag force cannot be countered by the electric field. To avoid this, the maximum gas velocity in the high-pass tunnel was set to -160 m/s. This is higher than the 121 m/s Silveira et al. calculated[213] because Michelmann et al. reported gas velocities of up to 180 m/s, albeit at stronger pressure gradients[214]. Furthermore, the gas velocity in the pumping region was set to -50 m/s instead of zero for the same reason.

In the low-pass tunnel, the velocity on the symmetry axis rises to 150 m/s.

- The temperature in the entire filter is 300 K. Silveira et al. calculated a 2 K change along the analyser tunnel[213], which I did not take into account.

This simplified analytical gas flow field neither takes the radial gas velocity nor turbulence into account. In the stacked-ring pumping sections at both ends of the mobility filter, the gas has to change its direction from an axial flow to a radial flow to leave the filter. I expect the radial gas velocity and turbulence to be strongest there. In the parallel flow high- and low-pass tunnels, they will be small. Hence the consequences on the simulation of the filter tunnels should be small.

Apart from the gas flow field, it was necessary to define an initial geometry. Each section was 4 cm long, including the two analyser tunnels. This is slightly shorter than the 46 mm length Bruker uses for its trapped low-pass filter design.[212], [215] In later iterations, I lengthened the low-pass filter to 141 mm to minimise the overall voltage drop (explanation below). I set the trap radius to 4 mm for the quadrupole, the same as in the Bruker devices.[212], [215] The pumping sections have 7 mm maximum trap radius to slow the gas flow.

With the gas flow-field and the geometry, I determined the DC electric field. Figure 46c shows the final iteration. The DC electric field and the gas velocity (Figure 46b) are the pivotal parameters for the critical mobility along the axis of the mobility filter (Figure 46d). In

the first part of the high-pass pumping section, there is a 3 kV/m electric field to transport the ions against the potentially turbulent gas flow from the high-pass analyser. In the tapering section to the high-pass tunnel, the electric field increases linearly to 7 kV/m. This increase counters the rapidly increasing gas velocity to avoid that ions get trapped before they reach the high-pass filter tunnel. Once the ions have reached the high-pass filter tunnel, the electric field drops to a 4 kV/m plateau. The rapid drop creates a defined high-pass filtering zone with a single maximum for the required minimum mobility (Figure 46d). The filtering zone begins at 49 mm axial length, the start of the 4 kV/m plateau. That is a few millimetres after the entrance of the high-pass filter tunnel. In this zone, the gas should be flowing parallel without disturbance from the potential turbulent flow in the pumping section. This should maximise the resolution of the filter. The high-pass filtering will take place within a short (~ few mm) zone at the beginning of the 4 kV/m plateau, because the gas velocity magnitude decreases closer to the gas inlet.

With the decreasing gas velocity, the electric field decreases as well. It changes its direction from attractive to repulsive at 170 mm axial length. In theory, this change could take place in the centre of the gas inlet. However, it is safer to keep an attractive DC field in the regions with low, positive gas velocity.

In the zone from 170 mm to 250 mm, the DC electric field decreases linearly (magnitude increase) to - 4 kV/m. This repulsive field is not necessary for the function of the low-pass filter. However, it is beneficial because in the low pass-filter, the gas drag force moves the ions to a higher electric potential (see Figure 46e). The work the gas flow does increases the ion potential energy. A long zone with repulsive electric field leads to a big increase in potential energy. Therefore, the low-pass filter is longer than the high-pass filter. This limits the overall voltage drop along the mobility analyser and removes the need for an expensive high-voltage power supply.

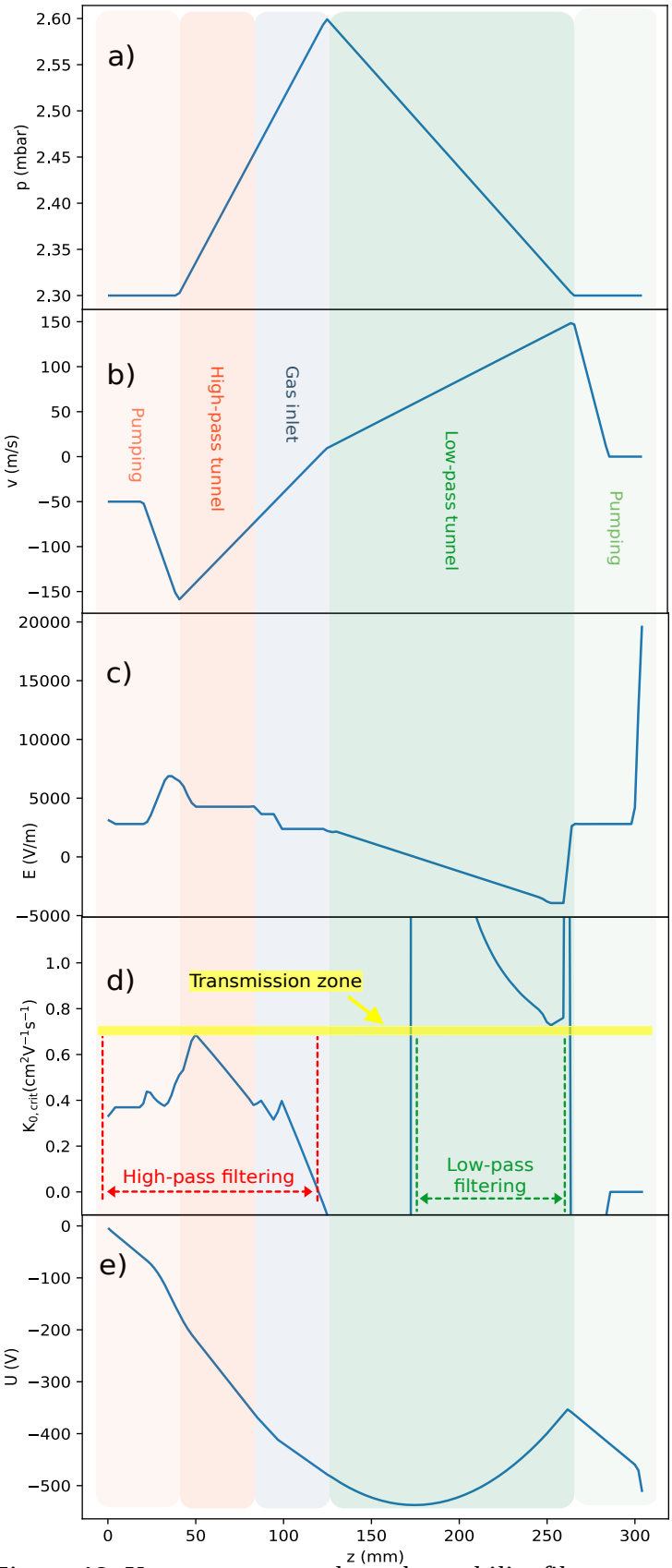


Figure 46: Key parameters along the mobility filter central axis. a) Pressure. b) Gas velocity. c) Electric field d) Critical reduced mobility. Transmission only for ions with $K_{0,crit,\ high\ pass} < K_{0,crit} < K_{0,crit,\ low\ pass}$ e) DC Potential.

Between 248 and 257 mm, the electric field reaches a minimum plateau. In there, the critical mobility reaches a single minimum, the low-pass filtering will happen there (Figure 46d). The minimum plateau in the low-pass filter and the maximum plateau in the high-pass filter define a mobility pass band from K_0= 0.687 to 0.728 cm²/Vs (yellow band in Figure 46d).

In the low-pass pumping section, the electric field assures the transport of the ions into the quadrupole 1. Here, it is the same as in the initial pumping section (3 kV/m). At the very end, it increases to 20 kV/m to avoid RF trapping. For more information on selecting the correct electric field in operation, see section 11.7 in Appendix.

Ion trajectory simulation

To check if the continuous mobility filter could work, I carried out an

ion trajectory simulation. The simulation workbench uses the theoretically determined DC gradient (Figure 46d). To take ion-gas interaction into account, the Simion SDS package reads the analytical gas flow field data. The simulation uses three probe ions (see Table 4). They share the same phosphazene central ring, but have fluorinated side-chains in different lengths (Figure 87 in Appendix). Due to a lack of common names, I colour-coded the ions: Red (short side-chains, high mobility), green (medium side-chains, medium mobility) and blue (long side-chains, low mobility). I chose these ions because they are well suited for the experimental evaluation and calibration of the mobility filter. Their reduced mobilities are in the range of a native, folded protein ion ($0.6...0.7x10^{-4}\,m^2V^{-1}s^{-1}$). They have different mobilities and m/z-ratios, so a low-resolution mass filter (e.g. a quadrupole) is sufficient to distinguish them. Besides, they deliver excellent ion currents and are commercially available in an undiluted component mixture (Ultramark 1621, CAS 105809-15-2).

*Table 4: Charge, mass-to-charge ratio and reduced mobility for three phosphazene probe molecules. As no common names are available, they have been colour-coded. Hexamethoxyphosphazene and GroEL shown for comparison. * denotes calculated values*

Molecule	**Colour code**	**Charge**	**m/z (ue^{-1})**	**K_0 ($10^{-4}\,m^2V^{-1}s^{-1}$)**	**PubChem CID**
Hexamethoxyphosphazene	/	+1	322.05	1.41 [81]*	136772
Hexakis(1H,1H,4H-perfluorobutoxy)phosphazene	Red	+1	1222	0.78 [81]	51342023
Hexakis(1H,1H,5H-perfluoropentoxy)phosphazene	Green	+1	1522	0.69 [81]	2775070
No common name	Blue	+1	1822	0.62 [81]	53792706
GroEL	/	+67	≈11955	0.66 [84]*	Not available

Figure 47 shows the trajectories of 16 red, green, and blue ions. The high-pass filter transmits the red and green ions, but retains the low-mobility blue ions. Only the green ions can pass the low-pass filter. Their mobility is within the theoretical band pass width the DC gradient defines (Figure 46d). Therefore, the simulation has confirmed the calculation of the critical reduced mobility along the filter.

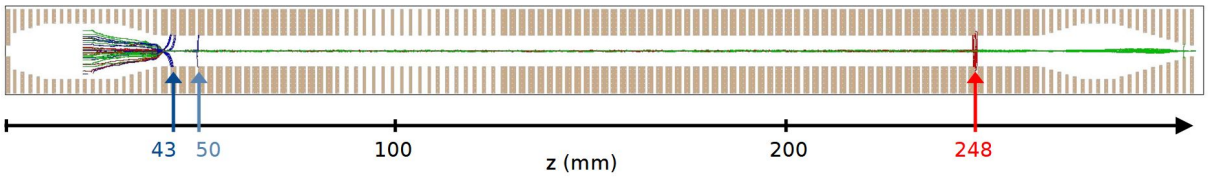


Figure 47: Mobility filter ion trajectory simulation. 3 x 16 ions with K_0 of 0.62 (blue, low), 0.69 (green, medium) and 0.78 (red, high mobility) $cm^2V^{-1}s^{-1}$. v_{RF} = 400 kHz, V_{RF} = 140 V (rectangular). Kill locations: dark-blue (43 mm) and light-blue (50 mm) arrow for low mobility blue ion, red arrow (248 mm) for high mobility red ion.

The trajectories of the retained ions (blue and red) end on a top- or bottom quadrupole electrode because a pause in the RF oscillation after 9 ms destabilised their trajectories. This function will be implemented in the RF power switches to avoid space-charge issues.

Besides, the simulation revealed that there is an issue with the ion guiding at the interface between the SRIG high-pass pumping section and the high-pass analyser tunnel section (z ≈ 40 mm in Figure 47). The blue, low-mobility ions became trapped there. Theory predicted they should become trapped at the plateau with the maximum electric field instead(z ≈ 50 mm in Figure 47 and Figure 46c).

To check if the trapping at the geometry-change interface could be caused by the harsh RF conditions, I repeated the simulation with 500 and 600 kHz RF frequency (Figure 48). The simulations confirmed that the trapping at the geometry change disappeared at 500 kHz RF frequency. Hence, a combination of the gas drag force and RF trapping wells traps the ions at the geometry-change interface.

The higher RF frequency decreases the depth of the effective potential wells (Equation 2.7). Nevertheless, the RF guiding in the xz-plane remains good at 500 and 600 kHz. However, in the perpendicular yz-plane, the RF confinement is insufficient and especially at 600 kHz, the ions crash against the quadrupole electrodes. The transmission band between RF-trapping at low frequencies and insufficient RF confinement at high frequencies is very narrow.

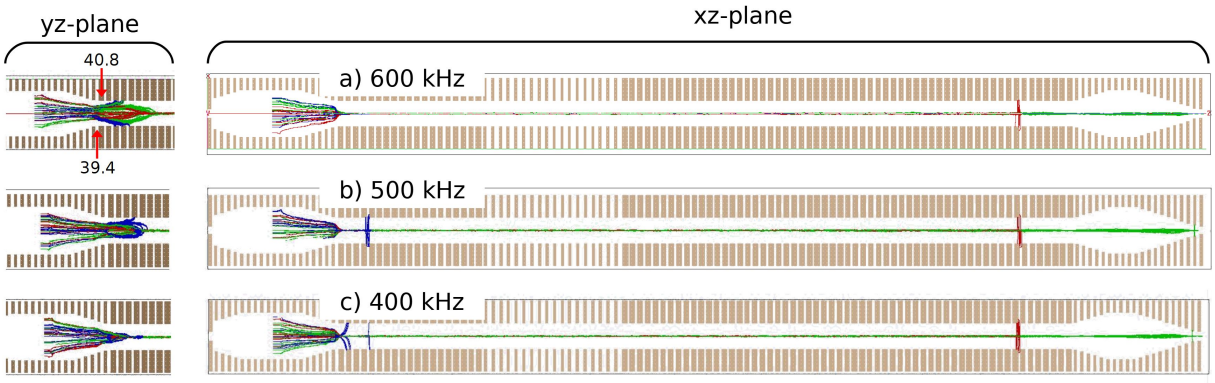


Figure 48: Mobility filter ion trajectory simulation at three different RF frequencies. v_{RF} = a) 600 kHz, b) 500 kHz c) 400 kHz. 3 x 16 ions with K_0 of 0.62 (blue, low), 0.69 (green, medium) and 0.78 (red, high mobility) $cm^2V^{-1}s^{-1}$. V_{RF} = 140 V (rectangular).

The likely culprit for this problematic transmission behaviour is the geometry change from a stacked-ring to a quadrupole ion guide. In an ion guide, the regular pattern of electrodes of opposite phases placed around the volume of the ion optic creates an inhomogeneous RF field which confines the ions. At the interface, this is the case in the xz-plane, where electrode of opposite phases meet (Figure 49). However, in the perpendicular yz-plane, electrodes of the same phase are adjacent.

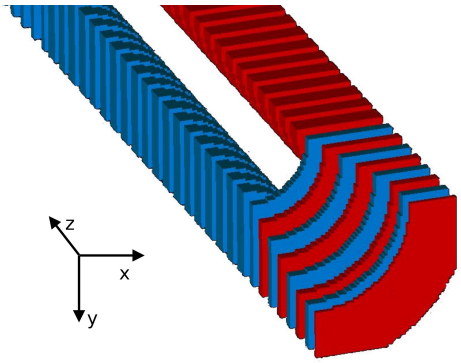


Figure 49: RF Phase distribution of the electrodes at the stack-ring/quadrupole interface. Blue is phase 1, red phase 2.

To investigate how this affects the ion guiding, I calculated the effective potential in the xy-plane between the final stacked-ring electrode and the first quadrupole electrode (z = 39.4 mm, Figure 50a) and at the centre of the first quadrupole electrode (z =40.8 mm, Figure 50b). Red arrows indicate the z-location of both planes in Figure 48a, too. At both locations, there is a high potential barrier in the x-direction, but only a small barrier in the y-direction. Due to the high bath gas pressure (2.3 mbar), the effective potential values are limited to qualitative comparisons (see section 2.2).

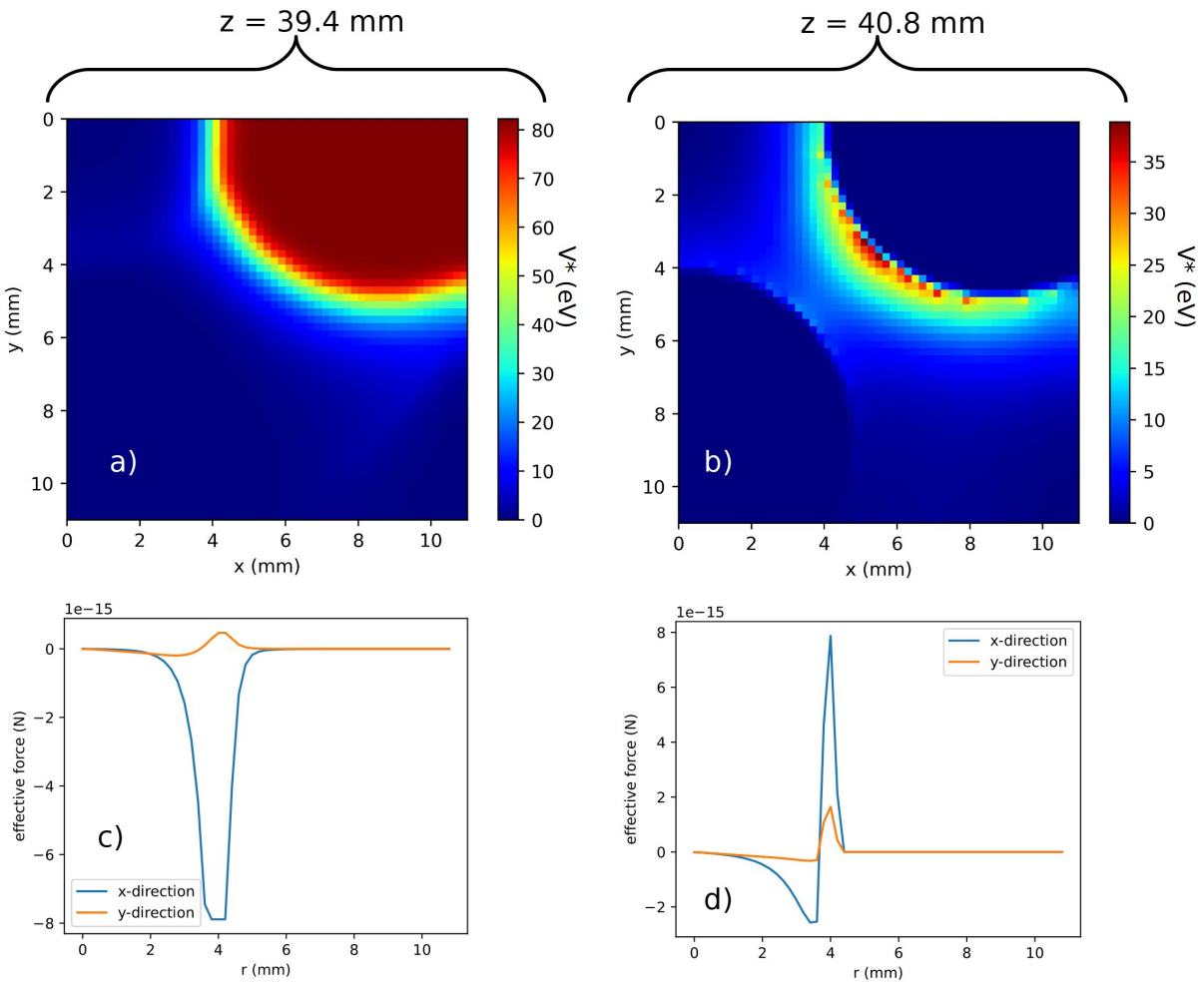


Figure 50: Effective potential for the blue ion assuming high vacuum in the mobility filter in the xy-plane at a) 39.4 mm and b) 40.8 mm. The effective force at the same conditions at c) 39.4 mm and d) 40.8 mm.

The effective force, corrected by c_{gas} to account for the bath gas present, can quantify the difference. For the blue (1822 m/z) ion, c_{gas} is 0.10 at 2.3 mbar and 300 K. Figure 48c shows that between the final stacked-ring electrode and the first quadrupole electrode (z = 39.4 mm) the maximum centring effective force in y-direction ($-2 \cdot 10^{-17}$ N) is only 2 % of the force in y-direction ($-8 \cdot 10^{-16}$ N). The maximum effective centring force in y-direction improves slightly to $-3 \cdot 10^{-17}$ N at the centre of the first quadrupole electrode (z =40.8 mm), but remains an order-of-magnitude below the corresponding force in x-direction ($-3 \cdot 10^{-16}$ N).

This confirms that the adjacent RF electrodes of the same phase in the yz-plane are responsible for the poor ion confinement at the interface between the stacked-ring and quadrupole ion guide. Three solutions exist to mitigate the problem:

- The DC electric field in the interface region should be independent from the DC field in the high-pass separation zone. In this case, a stronger DC gradient in the interface region could enlarge the transmission band to lower RF frequencies without trapping. I did not implement this in the trajectory simulation to avoid overcomplexity. The built mobility filter has additional DC taps, so there the two DC fields are independent.

- The first quadrupole electrode segments along the y-axis could be DC only. This would amplify the effective potential well depth along the y-axis. A drawback would be the slightly decreased effective potential barrier in x-direction. To retrofit this design change to the built mobility filter, a minor change in the layout of one lateral printed circuit board is required.

- For an evolution of the current mobility filter design, the entire stacked-ring high-pass pumping section could be replaced with a segmented, gas-permeable quadrupole section. This would eliminate the interface problem. However, it would also affect the gas flow field. With no resources available to simulate the resulting gas flow field, I did not implement this design change for the built version of the mobility filter.

Implemented design

The mobility filter is made of RF4 laminate material. Its overall length is 31 cm. It consists of five sections: The high- and low-pass filter have each a stacked-ring electrode pumping section and a tunnel section (Figure 52). They share a central gas inlet. The tunnel sections and the gas inlet are segmented quadrupoles with 4 mm trap radius. Each 1.55 mm segment is separated by a thin RF4 laminate isolator. No additional seal is necessary to keep the tunnel sec-

tion gas-tight. The central gas inlet is a segmented quadrupole as well. A summary of the geometry is in Table 5.

Table 5: Main geometric parameters of the mobility filter sections

Section	Geometry	Length (mm)	Electrode thickness (mm)	Inter-electrode spacing (mm)	Gas tight
High-pass pumping	SRIG	37.1	0.76	1.2	✘
High-pass filter tunnel	Segmented quadrupole	42.0	1.55	0.76	✓
Gas inlet	Segmented quadrupole	40.6	0.76	1.55	✘
Low-pass filter tunnel	Segmented quadrupole	148.9	1.55	0.76	✓
Low-pass pumping	SRIG	37.2	0.76	1.2	✘

I had to add seven additional electrodes in the low-pass filter tunnel to reach the projected 31 cm overall length. These electrodes lengthened the tunnel section from 141 mm 148.9 mm to compensate for manufacturing tolerances in the thickness of the RF4 laminate material. Hence, the simulated geometry (Figures 46 to 48) differs slightly from the built mobility filter (Figure 51).

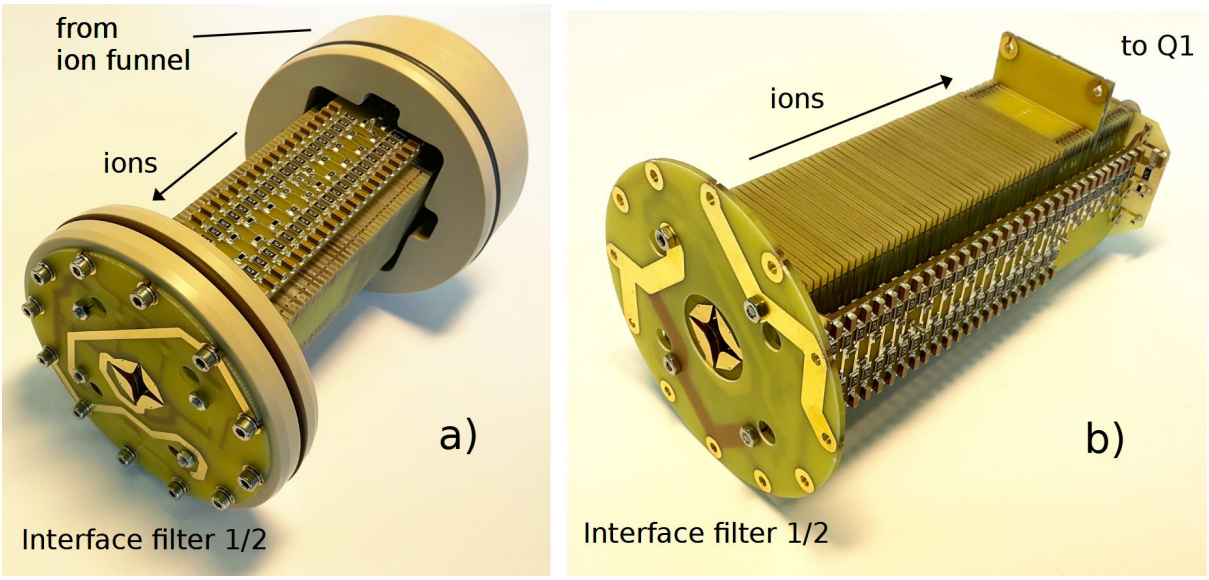


Figure 51: Built ion mobility filter. a) Section filter 1, which houses the high-pass filter, the gas inlet and the beginning of the low-pass filter. b) Section filter 2, which houses the remaining length of the low-pass filter. Both sections are connected at the interface filter 1/2. Photos: Moritz Edte

To regulate the gas flow velocity in the high- and low-pass filter, a manual needle valve controls the N_2 flow through the central gas inlet (Figure 52). A valve in each pumping port of the filters allows to set the gas flow velocity of each filter separately. Both pumping ports lead to a common screw pump with 100 m^3/h pumping speed. When the mobility filter is used as an ion guide to transmit all ions, the high-pass pumping valve must be closed to avoid any reverse gas flow. In addition, the low-pass pumping valve should be partially closed to keep the pressure in the low-pass filter above 1 mbar. At lower pressure, the collisional cooling of the ions might be insufficient. This could lower transmission.

The independent pumping of the high- and low-pass filter require separated vacuum chambers for each end. The first chamber contains the high-pass filter pumping section, the high-pass filter, the gas inlet and the initial section of the low-pass filter. These four sections form one part, filter 1. The second chamber contains the second part of the low-pass filter and its pumping section. These two sections form filter 2. Filter 1 and filter 2 have a gas-tight connection in the low-pass filter tunnel.

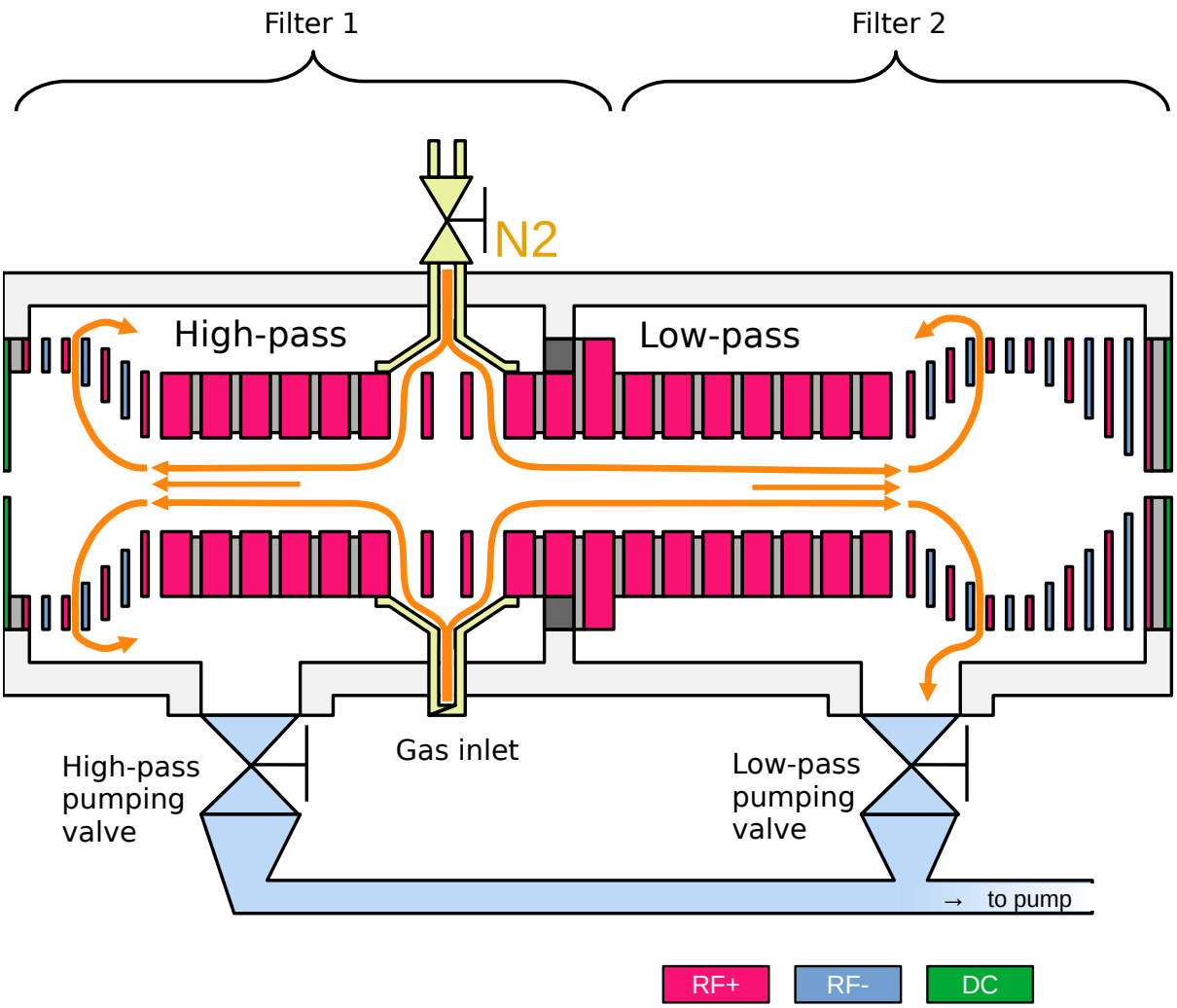


Figure 52: Mechanical construction scheme of the mobility filter. The mechanical separation between Filter 1 and Filter 2 (see Figure 51) is in the low-pass section. A common 100 m³/h screw pump pumps both the high- and low-pass filter. The gas flow speed and -pressure can be set independently via two choking valves and the gas inlet pressure.

Implemented DC-Gradient

The electric field, which the resistor cascades define in the built mobility filter (Figure 53), is similar to the theoretical DC gradient (Figure 46c). There are two changes. First, there is a step-change at the point where the electric field changes its direction in the low-pass filter (z = 172 mm, electrode 80). This avoids too high differences between the resistor values in the non-linear resistor cascades.

Second, the additional seven electrodes, which were added in the low-pass tunnel section, increase the total energy of the ions in filtering mode (between electrodes 80 and 115, z = 172...250 mm).

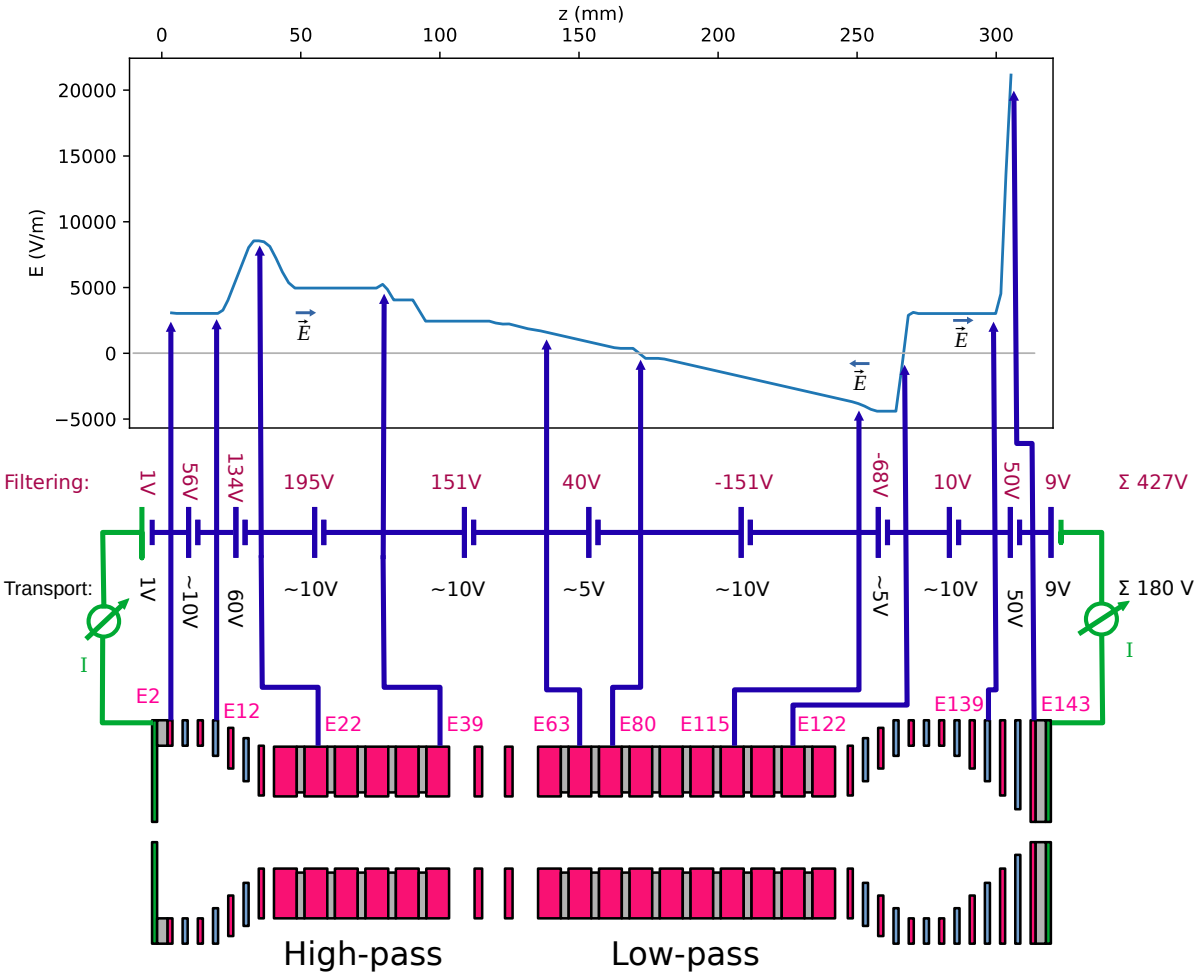


Figure 53: Implemented DC gradient and location of the DC taps for mobility filtering of an ion with K_0 = 0.7 $cm^2V^{-1}s^{-1}$. The voltages between the taps are necessary to mobility-filter (red, upper row) or transport (black, lower row) a small organic ion.

Ten DC taps on the RF electrodes allow to tune the electric field in each section of the mobility filter for ion transport or mobility filtering. Furthermore, an individual power supply sets the voltage on each of the DC-only apertures on the end of the filter. They are prepared for ion current measurement.

A step-by-step manual to tune the voltages for mobility filtering is in the Appendix (Section 11.7).

Gas velocity calibration

For each setting of the gas flow through the gas inlet and the choking valves at the high- and low pass filter pumping ports, a certain gas velocity in the filter tunnels will result. To this

end, at each pumping port and at the gas inlet a high-accuracy capacitance diaphragm gauge measures the pressure (accuracy 0.2 % of the measured pressure).

In theory, the gas velocity inside of the low-pass high-pass parallel flow mobility filter could be measured. In practice, it is easier to determine the gas velocity experimentally with a calibrant ion of known reduced mobility. Ultramark 1621 is ideal, because Stow et al. measured the reduced mobility of its individual compounds with high accuracy in an interlaboratory evaluation.[81] For the experimental calibration, the current of a mass-selected calibrant ion needs to be monitored. With a constant gas flow, the DC voltage in the separation zone is scanned to the point at which transmission sets on / stops. This has to be done individually for both the high-pass and low-pass filter.

With this voltage, it is possible to calculate the electric field in the separation zones of the high- and low-pass filter. Based on the built geometry, the magnitude of the electric field on the high pass filter plateau E_{HP} is:

$$E_{HP} = U_{plateau,HP} \cdot 25.489\,\mathrm{m}^{-1} \tag{5.7}$$

with $U_{plateau,\,HP}$ the voltage between the taps at electrode 39 and 22.
For the low pass filter, the magnitude of the electric field on the plateau E_{LP} is:

$$E_{LP} = U_{plateau,LP} \cdot 65.510\,\mathrm{m}^{-1} \tag{5.8}$$

with $U_{plateau,\,LP}$ the voltage between the taps at electrode 122 and 115. With the electric field on the plateau, I can rearrange equation 5.6 to retrieve the magnitude of the gas velocity in the separation zone:

$$v_{g(LP\text{ or }HP)} = -K_0 E_{LP\text{ or }HP} \cdot \chi \cdot \frac{p}{p_0} \cdot \frac{T}{T_0} \tag{5.9}$$

Note that the E and v_g are the projections of the electric field or gas velocity vector on the z-axis (see Figure 45). For a positive ion in the high-pass filter, the gas velocity vector points in negative z-direction, and the electric field vector in positive z-direction. For the low-pass filter, it is the opposite (gas velocity positive z-direction, electric field negative z-direction). With the gas velocity determined in both the high- and low-pass filter, they can be used to measure the ion mobility of any analyte ion.

5.4 RF power switches

At the heart of the instrument are the power switches, which supply the RF voltage to the ion funnel, the mobility filter, the ion guides and the quadrupole mass filter. In contrast to conventional sinusoidal RF generators based on a resonant circuit,[30, p. 15] they switch the voltage on an RF electrode between two DC supply voltages.[216] This creates a nearly rectangular wave-form with two states, the two supply voltages. Due to this wave form, the ion optics supplied by an RF power switches are often referred to as “digital ion traps”[217] or “digital waveform generator” driven[218], although the electronic component delivering the wave-form is an analogue switch.[216], [219] Each RF phase requires one switch, so a pair of power switches supplies each RF optic.

RF power switches can operate in a large frequency range. The lower limit is defined by the reference clock, for example a field-programmable gate array.[180] In practice, the lower limit is so low (< 1 Hz) that it is irrelevant for the operation. The rise time is the time it takes for a signal to change from a low to a high value. In this case, it describes how quickly the power switches can change between the two DC supply voltages. The rise time of the analogue switch inside the power switch defines the theoretical upper frequency limit. Usually, current designs use an order-of-magnitude lower upper frequency limit, between 1 and 3 MHz.[180], [216]

Unlike conventional sinusoidal RF generators, RF power switches can operate with a flexible duty cycle. The flexible duty cycle can be tuned to mass-filter an ion beam without an additional, superimposed differential DC voltage in a quadrupole.[220] Here, this feature is employed to periodically interrupt the RF at the mobility filter to remove trapped ions.

For an ion optic, the stability diagram describes at which operation parameters (RF amplitude and differential DC voltage) an ion with a specific mass-to-charge radio has a stable trajectory. The stability diagram of a square-form-driven ion optic and a sinusoidal-driven ion optic are very similar.[221] They superimpose if the amplitude of the square-form ion optic is scaled with the factor 4/π.[217], [221], [222] I have used this factor to calculate the effective potential.

For *'inverted porcupine'*, the electronics company CGC instruments (Chemnitz, EU) designed a four channel power switch (AMX700-4EDW). It is based on Silicon metal–oxide–semiconductor field-effect transistors (Si-MOSFETs). As each unit can supply two RF ion optics, the mass spectrometer is equipped with 3 units.

In a conventional sinusoidal RF generator, the energy is periodically transferred from the capacitor (the ion optic) to the inductor coil.[223] The external drive compensates just for the losses due to the resistance of the circuit.[224] This is different for an RF power switch. It has to charge the capacitor (the ion optic) and dissipate the full energy stored in its electric field for every RF cycle.[216] For one cycle, it dissipates the energy W_{tot}:[216]

$$W_{tot} = c_L \cdot V_0^2 \tag{5.10}$$

V_0 is the RF amplitude, c_L the load capacitance. The capacitance of the ion optic, the cables, the atmosphere-vacuum feedthrough and the internal capacitance of the power switch contribute to c_L.

The required power P_{tot} per channel of the power switch is proportional to the RF frequency Ω:[216]

$$P_{tot} = \frac{\Omega}{2\pi} c_L \cdot V_0^2 \tag{5.11}$$

Therefore, it is not possible to operate the power switches at the maximum rated (RF-) amplitude of 350 V for any frequency. The AMX700-4EDW power switches are water-cooled and can dissipate up to P_{tot} = 200 W per channel in continuous operation. The maximum 200 W heat dissipation per channel limits the RF amplitude.

Figure 54 shows the calculated maximum RF amplitudes possible as a function of the RF frequency. Q3 is an RF-only quadrupole ion guide with a small load capacitance (90 pF + ca. 200 pF internal capacitance of the switch).

It can be operated with at least 180 V RF amplitude up to the maximum 5 MHz frequency of the power switch. The RF amplitudes for ion optics with higher load capacitance are lower. The ion mobility filter has a very high load capacitance due to design constraints (1.3 nF + 0.2 nF for the switch). It is limited to 130 V RF amplitude at 2 MHz, but can be operated with its maximum design amplitude of 180 V below 1 MHz. Note that the internal capacitance of the switch is inversely proportional to the applied RF amplitude.[216] It exceeds 200 pF below 110 V RF amplitude, hence the possible amplitudes for the mobility filter will be slightly lower than calculated in figure 54 at frequencies over 3 MHz.

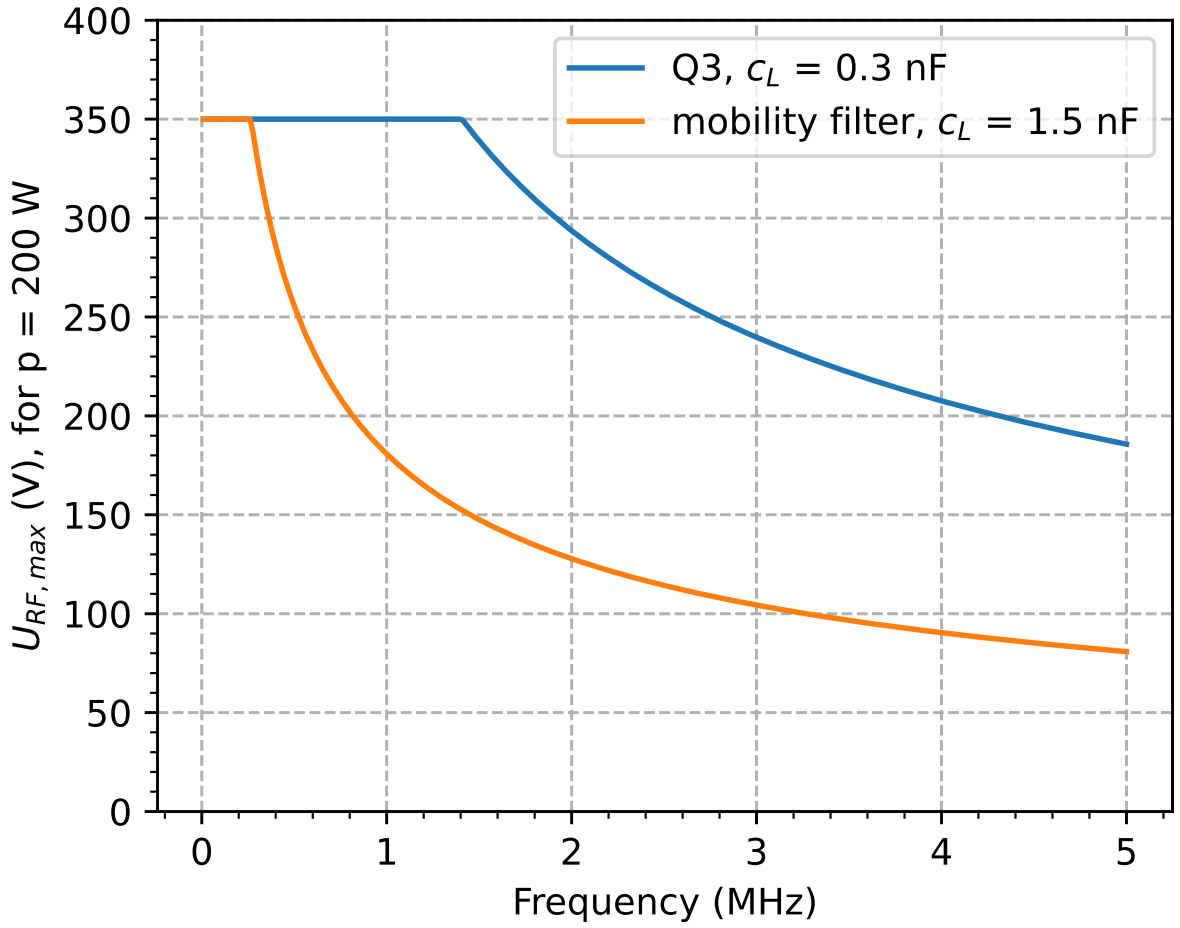


Figure 54: Maximum RF amplitude for the ion mobility filter and the RF-only quadrupole Q3. The load capacities and with it the maximum RF amplitudes of the other ion optics are between these two extremes.

The calculated maximum RF amplitudes allow good ion guiding in the frequency range up to 2 MHz for all ion optics. In this frequency range, the mass-filter will operate without problems, too. Thus, the mass spectrometer should work well for all ions with a m/z > 50 Th. Even very small ions, such as Lithium$^+$ (m/z = 6 Th) can be transmitted at 5 MHz, albeit with a lower transmission efficiency due to the limited RF amplitudes.

In summary, the flexible frequency of the RF power switches create a universal ES-IBD mass spectrometer with good performance for small, medium, large and very large ions. It offers limited transmission of very small ions, too.

5.5 Beam transfer into high vacuum free flight

In the instrument, the ions are first separated from the gas in the ion funnel. Only ions with the selected mobility pass the mobility filter. After a quadrupole ion guide, which acts as a differential pumping stage, just ions with the right mass-to-charge-ratio remain stable in the QMS. At this stage, the ion beam is mass- and mobility filtered, but not ready to be used for deposition. This is due to the principle of quadrupole mass filtering. It destabilises the trajectories of unwanted ions.[225] To this end, high RF-amplitudes[74, pp. 47–50], which exceed the validity region of the adiabatic approximation[72, p. 34] are necessary. The ions gain energy during the mass-filtering. Figure 55 illustrates the trajectories of ten hexamethoxyphosphazene ions in the *'inverted porcupine'* QMS.

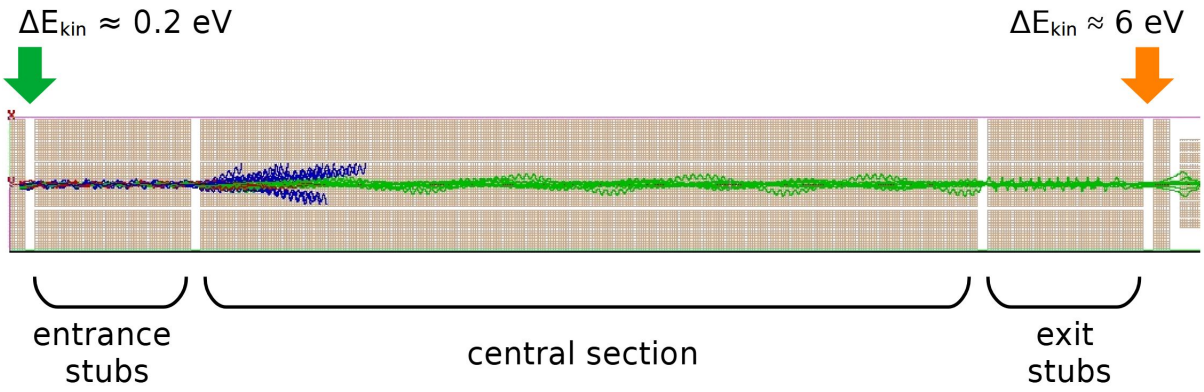


Figure 55: Mass filtering to separate hexamethoxyphosphazene ions (green, 322 m/z) from ions with 310 m/z (red) and 332 m/z (blue). v_{RF} = 904 kHz, V_{RF} = 225 V (rectangular). The differential DC on opposite rod pairs of 47 V causes the mass-to-charge filtering and is only applied to central section. ΔE_{kin} is FWHM.

The energy width of the beam increases from 0.2 eV FWHM at the QMS entrance to 6 eV at the exit. This is too wide to efficiently guide the beam through the deposition optics. Furthermore, the wide kinetic energy distribution leads to a poorly defined, wide distribution of collision energies with the sample (see also section 3.2). Therefore, a gas-filled ion guide after the QMS is required to thermalise the ion beam with gas-ion collisions. The drawback of a colli-

sion cell is that the ion beam must be decoupled from the high pressure (10^{-3} to 10^{-2} mbar) in the cell to the high vacuum ($p \leq 10^{-4}$ mbar) region in the landing stage.

The transition from high pressure to high vacuum can take place in two different ion optics, either an RF multipole ion guide, or an electrostatic lens. Compared to the RF ion guide, the electrostatic lens is cheap (no need for a RF power supply). If one lens element is split into four (see Figure 74 in the Appendix), it can steer the ion beam through an unguided region of the ion optics column. As I want to install a gate-valve between module A and the beam switch (see Figure 38), this is advantageous. On the downside, the interaction of the ions subject to strong potential gradients in a transitional pressure domain in the electrostatic lens can lead to ion activation and widening of the beam energy distribution. In section 3.3, paragraph "Beam-energy distribution", we have experimentally demonstrated that the decoupling from high pressure to high vacuum with an electrostatic lens is possible with a low energy width for medium-sized protein ions. Here, I use ion trajectory simulations to test if an electrostatic lens is suitable to decouple a beam of small organic ions from RF ion guides to high vacuum. The increase in the width of the energy distribution should remain small.

The boundary conditions given by the unguided gate-valve region are challenging. The cavity of the gate-valve receives a significant gas load from the 2.5 mm aperture of the collision cell. The gas has to escape from the cavity in the space between the collision cell Q3 and the vacuum chamber to reach the QMS turbo pump. Therefore, a large-diameter gate-valve is required to ensure a sufficient cross-section for pumping the gate-valve cavity. I chose a DN 80 gate-valve, which allows for about 2 cm radial space all around between the housing of the collision cell Q3 and the QMS chamber wall. However, this big gate-valve requires 32 mm axial installation length – with a 2 mm safety standoff on each side this results in a 36 mm long unguided region (see Figure 56a). The total energy E_{tot} of the ions (sum of their potential and kinetic energy, reference is electrical ground, see "Beam-energy distribution" in section

3.3) in normal, mass- and mobility filtered operation will be negative. With a ± 500 V power supply and a voltage drop of about 600 V along the ion funnel and mobility filter (Figure 42 and 53), the collision cell DC potential is approximatively -100 V. Consequently, the ions thermalise to -100 eV E_{tot}. The camber wall and the gate-valve housing are at ground potential (0 V). This is a potential barrier which the ions cannot overcome due to their negative E_{tot}. The ion flight path has to be shielded from this high barrier by sufficient electrostatic field from the electrodes both sided of the unguided region.

I simulated the trajectories of the small organic ion hexamethoxyphosphazene in the unguided region with Simion. I used the integrated hard-sphere 1 collision model to find out if an electrostatic lens is a viable option to transfer the beam to high vacuum. Furthermore, I investigated the influence on the beam energy distribution.

I assumed an exponential decrease in pressure along the axial coordinate from the collision cell Q3 pressure of $5 \cdot 10^{-2}$ mbar to the pressure in the gate-valve cavity of $2.5 \cdot 10^{-4}$ mbar (Figure 56c). The $5 \cdot 10^{-2}$ mbar is the pressure simulations yielded to thermalise a GroEL ion after strong activation (250 eV per charge) within the length of the collision cell. Therefore, it represents a worst-case assumption. The pressure necessary to thermalise hexamethoxyphosphazene is likely to be an order-of-magnitude lower (compare Figure 27). On the built instrument, I measured the pressure in the cavity and the QMS chamber as a function of the collision cell Q3 pressure (Figure 56d). This measurement verified that the assumed pressure difference between the collision cell ($5 \cdot 10^{-2}$ mbar) and the gate valve cavity ($2.5 \cdot 10^{-4}$ mbar) was reasonable.

I investigated two different gradients. The weak gradient is a 30 V difference between the Q3 aperture and the collector electrode (Figure 56a). The steering lens electrodes act as a barrier to shield the flight path from the electric field between the chamber walls and the ion optics.

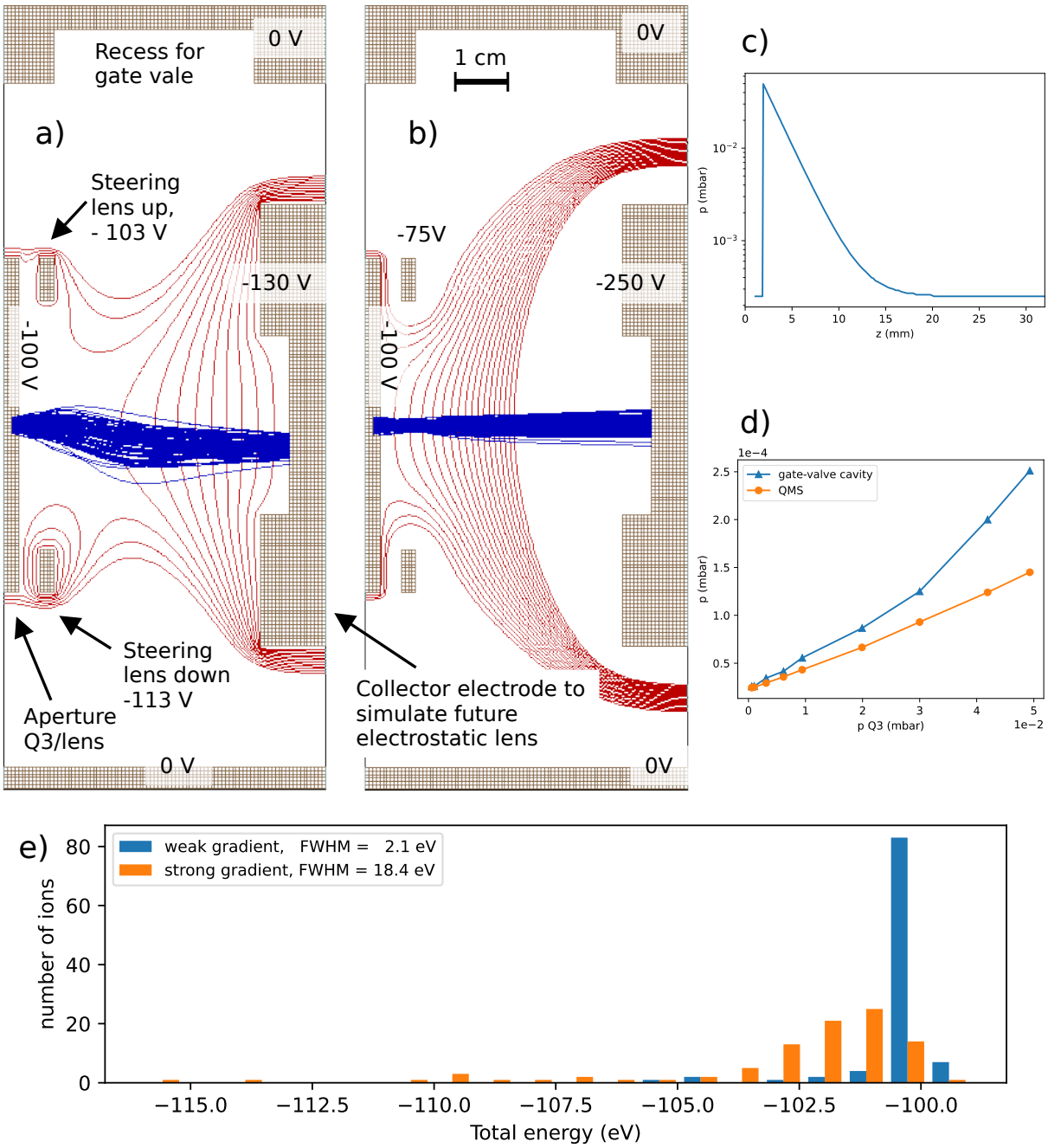


Figure 56: Trajectory simulation of 100 hexamethoxyphosphazene ions to investigate beam decoupling from high pressure to high vacuum. a) Weak gradient conditions. Initial energy distribution: E_{tot} = -99.7 eV, FWHM = 0.13 eV b) Strong gradient conditions. Initial energy distribution: E_{tot} = -99.9 eV, FWHM = 0.16 eV. Equipotential lines mark range from -100 to -130 V in 3 V steps. c) Assumed pressure in the cavity. d) Measured pressure in the gate-valve cavity and QMS chamber as a function of the pressure in Q3. e) Resulting total energy distribution. Ions with E_{tot} < -120 eV have been omitted for better clarity.

Due to the weak gradient, the chamber wall barrier potential penetrates deep radially towards the flight path of the ions. As the gate valve cavity shape is not necessarily radially symmet-

ric, this could bend the ion trajectories. I applied a +5 V steering voltage to compensate in the example shown.

In strong gradient conditions, there is a 150 V difference between the Q3 aperture and the collector electrode (Figure 56b). No steering is needed, because the very low (-250 V) negative potential of the collector electrode displaces the chamber wall barrier potential.

With a weak gradient, the E_{tot} decreases by 0.6 eV (initial -99.7 eV, final -100.4 eV). The energy width increases from 0.1 eV FWHM to 2.1 eV FWHM (Figure 56e). In contrast, with the strong gradient, E_{tot} drops by 4.8 eV (initial -99.9 eV final -104.7 eV), the energy width increases to 18.4 eV FWHM (initial 0.2 eV). The beam diameter increases to about 4 mm in both conditions.

These results proof that an electrostatic lens can decouple a beam composed of small-organic ions from high pressure to high vacuum through an unguided region. However, only a weak gradient can keep the energy width down in the unfavourable high pressure conditions ($5 \cdot 10^{-2}$ mbar) in the vicinity of the collision cell aperture. This confirms the experimental results obtained on the modified UHMR (see section “Beam-energy distribution” in section 3.3). For a detailed discussion of the underlying physics, please refer to the paragraph “Beam energy” in section 11.3.

5.6 Current state and outlook

Module A has been completely assembled at the site of collaboration partner (Max-Planck-Institute for solid state research, Stuttgart, EU). Figure 57 shows the current state of the setup. The vacuum chamber is divided into three modules milled from solid Aluminium. The RF power switches are mounted adjacent to the vacuum chamber to keep the cables to the ion optics as short as possible. This reduces the load capacity. To reduce the footprint and to keep

the centre-of-gravity low, the heavy ±350 V power supplies, which supply the power switches, are mounted below the vacuum chamber.

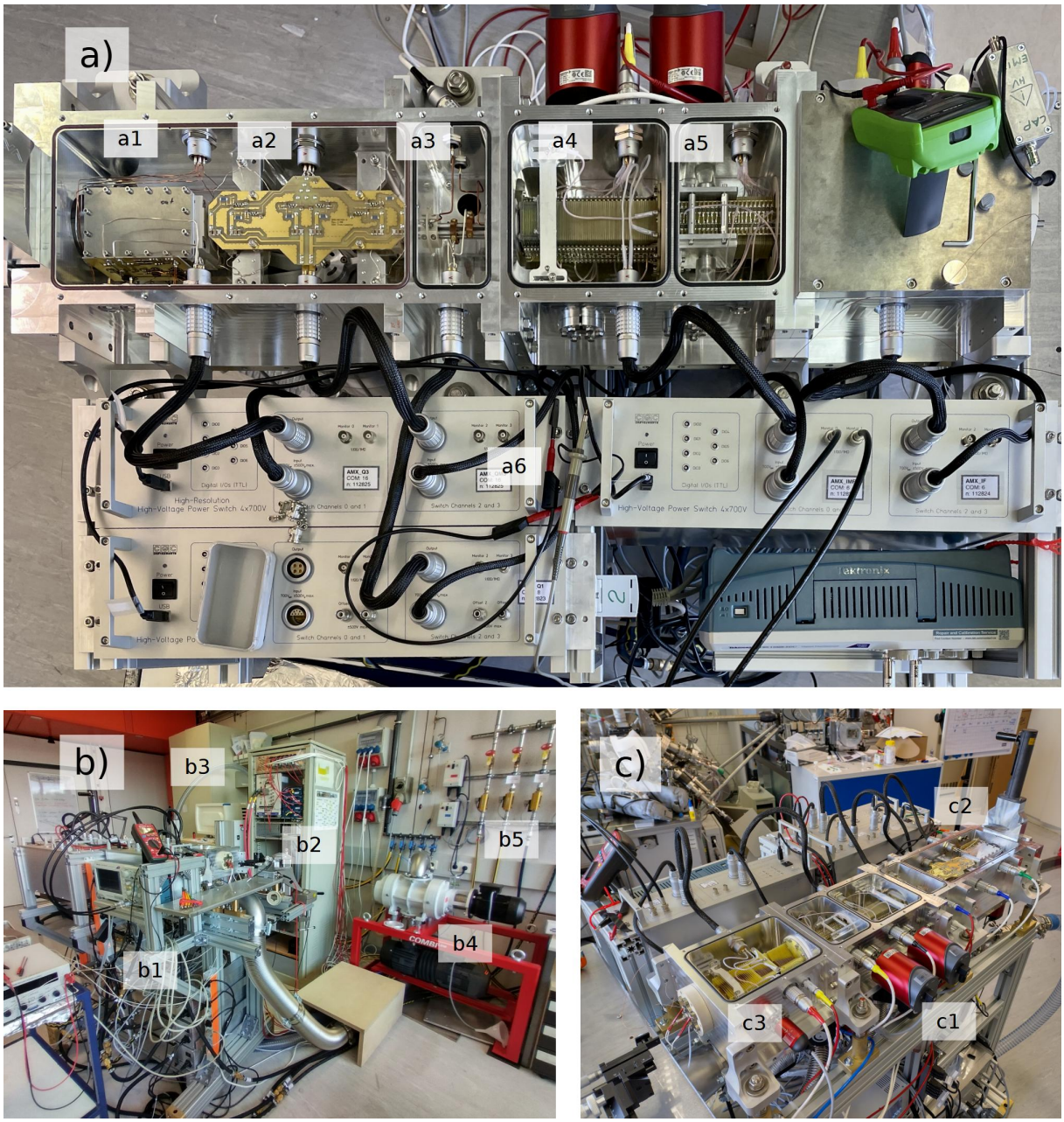


Figure 57: Preparative mass spectrometer 'inverted porcupine'. a) Top view. Visible are the collision cell Q3 (a1), the mass-selective quadrupole QMS (a2), the quadrupole Q1 (a3), filter 2 (a4), filter 1 (a5) and the RF power switches (a6). b) The mass spectrometer (b1) and its auxiliary units: The DC power supplies and picoammeters (b2), the fore pumps for the mobility filter and the quadruple chambers (b3), the roots blower/rotary vane pumping station which pumps the ion funnel (b4) and the water cooling supply (b5). c) Side view. Visible are the high-accuracy capacitance diaphragm gauges (c1), the gate valve (c2) and the ion funnel (c3).

The entire instrument is just 89 cm wide, so it fits through standard-size 90 cm doors.

Currently, the instrument is in a trial running phase. The functionality of all RF ion optics has been tested with a rhodamine B ion beam (solution concentration 10^{-6} mol·L^{-1}). The measured ion currents are in Table 6.

Table 6: Transmitted currents with a 10^{-6} mol·L^{-1} rhodamine B solution for the 'inverted porcupine'.

Aperture	**Ion funnel / mobility filter**	**Mobility filter / Q1**	**Q3 / steering lens**
Achieved current (pA)	370	120	50

It is likely that higher currents can be attained with more concentrated solutions and optimised transmission parameters (ion optics voltages, RF amplitudes and frequencies…). The quadrupole mass filter (QMS) can interrupt the beam if a differential DC voltage is applied. The first element of the mobility filter, the high-pass filter, has been tested with a counter-gas flow. It blocks the ion beam when the attractive DC gradient is low and transmits the ion beam at a higher DC gradient (see Figure 88 in the Appendix). This is the expected transmission behaviour and will enable mobility selection.

As a next step, a software interface for an intuitive control of the RF amplitude and frequency of the power switches has to be developed. It should enable to record mass spectra by scanning the frequency of the QMS or Q3. This requires simultaneous sweeping of the RF frequency and current recording, which is not feasible manually due to the many linked parameters. Once it is possible to record mass spectra, the ion mobility filter can be fully tested.

6. Conclusion

This thesis investigates the instrumentation for the mass-filtered deposition of large, native protein complexes. To this end, I converted a commercial mass spectrometer for ES-IBD together with others and designed a flexible mass-range preparative mass spectrometer. Moreover, I investigated the transmission performance of the atmosphere-vacuum interface, the ion funnel. The objective was to identify potential bottlenecks for the transmission of small and large ions.

Most ES-IBD instruments are academic prototypes focused on the deposition of small molecules.[27], [31], [33], [35], [37], [67]–[69], [113] Some instruments have limited deposition capabilities for large, native protein complexes. For example they can transmit ions with medium to high m/z-range.[36], [50], [120], [127] However, there are no readily available instruments targeted for deposition of large, native protein complexes.

The first part of this work details the conversion of a commercially available Thermo Scientific Q-Exactive UHMR mass spectrometer to deposit large, native protein complexes. The UHMR is a proven analytical native MS platform. The converted instrument has an adequate beam intensity (> 20 pA on the sample) to deposit samples of large, native protein complexes for microscopy in a short time. Due to the recollimation of the ion beam in the collision cell prior to deposition, the energy width of the ion beam is very small (≤ 1.2 eV per charge). This guarantees that all ions experience a similar landing energy upon the collision with the sample and enables very soft (low landing energy) depositions. Protein samples (BSA, ferritin and GroEL) deposited under native conditions with this instrument showed the retention of a globular conformation in AFM and TEM. Finally, the non-covalent protein complex ADH retained its activity after deposition and re-hydration. Therefore, the modified UHMR is a good deposition platform to produce samples of large native protein complexes. Figure 58 gives a

recent example from literature. It shows large native protein complexes deposited with the modified UHMR and imaged in Cryo-EM.[226]

To enlarge the capabilities of the modified UHMR, it is necessary to extend the deposition module with a cryogenic sample holder operating in ultra-high vacuum ($p < 10^{-9}$ mbar). With this sample holder and a sample transfer under vacuum, biomolecule samples for single-molecule-resolved analysis with scanning tunnelling microscopy could be prepared.[45], [116] Cryogenic landing is also a possible path to increase the resolution of cryo-EM structures of proteins deposited with ES-IBD.[126]

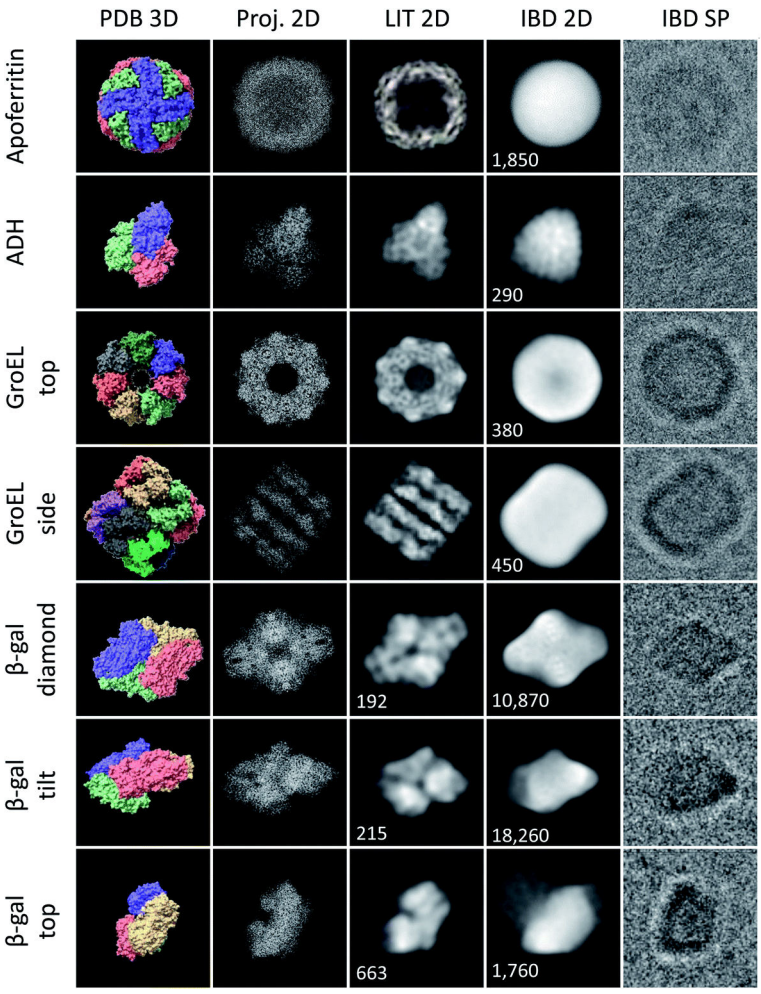


Figure 58: Comparison of protein complex shapes obtained from ice-free native ES-IBD samples by cryo-EM (IBD 2D and IBD SP) with literature data. The ES-IBD samples were deposited with the commercial mass spectrometer I modified (chapter 3). Graphic reproduced from Esser et. al. 2022.[226]

The modified commercial mass spectrometer is limited to medium and large mass-to-charge-ratio ions. It does not provide any information on the conformation of the molecule in the gas phase prior to deposition.

To fill this gap, I designed a preparative mass spectrometer equipped with a continuous ion mobility filter, the *'inverted porcupine'*. The RF power switches supply the RF ion optics with frequencies up to 5 MHz, so the instrument transmits any molecule with an m/z-range over

50 Th. The continuous high-pass low-pass parallel flow ion mobility filter can select ions of a certain mobility domain from the beam. Thereby, it permits to select an ion of a specific conformation from a mixture and to deposit it. All ion optics, particularly the mobility filter and the ion funnel, have been designed to transmit high ion currents (> 1 nA) efficiently. Initial transmission tests with a dilute (10^{-6} mol·L^{-1}) rhodamine B solution, a small organic ion, indicated a current of 50 pA at the exit of the collision cell Q3. Significantly higher currents can be expected with optimised ion optic's voltages and more concentrated solutions. The collision cell Q3 is located in the beam path after the quadrupole mass filter. The energy distribution of the ion beam widens when this quadruple selects ions of a specific mass-to-charge range from the beam. The gas inside Q3 thermalises the ion beam, so the *'inverted porcupine'* should produce an ion beam with a similar narrow energy distribution width as the modified UHMR. In summary, the *'inverted porcupine'* combines the good beam control (high m/z-range, collision cell) of commercial mass spectrometers for large, native protein complex ions with the flexibility and beam intensity of custom-made instruments. It is also the first reported preparative ion mobility spectrometer.

The next step to commission the *'inverted porcupine'* is to develop an intuitive user-interface for the control of the RF power switches. With this, it should be possible to record mass-spectra and mass-filter the ion beam. This step enables the development of a deposition workflow. Moreover, once a mass spectrum can be obtained, the performance of the continuous ion mobility filter can be evaluated. This is the prerequisite for mobility-filtered deposition.

The basis for the construction of the high pressure ion optics of the '*inverted porcupine'* was the thorough investigation of the processes within an ion funnel. To my surprise, the experimental investigation of a conventional ion funnel yielded a constant transmission of 0.7 for currents up to 10.6 nA (10^{-4} mol·L^{-1} rhodamine B solution). With the solutions to the Laplace equation exported from the ion trajectory simulation software Simion, I analysed the energy

landscape in an ion funnel. With this information, I optimised the DC gradient along the axis of an ion funnel. The optimised DC gradient can help to reduce RF-induced ion trapping and avoid ion losses due to space-charge in the final, low-diameter section of the funnel. Ion trajectory simulations with integrated gas-flow fields calculated by CFD showed that light ions are transmitted through the ion funnel best at low pressure (≈1 mbar), whereas large, native protein complexes require higher pressure (> 10 mbar). I formulated a 4-step model to describe the transmission of an ion within a conventional ion funnel. The model is based on the combined results of the experimental transmission measurement, the energy landscape investigation and the ion trajectory simulations. I hope this model will help others to understand and develop good ion funnels.

In summary, I have developed instrumentation to extend the application of preparative mass spectrometry from small molecules to large biomolecules. I studied the influence of pressure, the DC gradient and molecular size on the transmission in high pressure ion optics. This enabled the design of a high-intensity ion funnel and a continuous ion mobility filter. These developments already contributed to the study of cryo-EM structures obtained from mass-selected deposited protein complexes.[126], [226]

7. Bibliography

[1] W. P. McCray, ‘MBE deserves a place in the history books’, *Nat. Nanotech*, vol. 2, no. 5, pp. 259–261, May 2007, doi: 10.1038/nnano.2007.121.

[2] P. Frigeri, L. Seravalli, G. Trevisi, and S. Franchi, ‘3.12 - Molecular Beam Epitaxy: An Overview’, in *Comprehensive Semiconductor Science and Technology*, P. Bhattacharya, R. Fornari, and H. Kamimura, Eds. Amsterdam: Elsevier, 2011, pp. 480–522. doi: 10.1016/B978-0-44-453153-7.00099-7.

[3] National Inventors Hall of Fame, ‘NIHF Inductee Alfred Y. Cho Invented Molecular Beam Epitaxy’, *Alfred Y. Cho*, 2009. https://www.invent.org/inductees/alfred-y-cho (accessed Sep. 14, 2022).

[4] P. Chang, W. C. Lee, T. D. Lin, C. H. Hsu, J. Kwo, and M. Hong, ‘MBE—Enabling technology beyond Si CMOS’, *J. Cryst. Growth*, vol. 323, no. 1, pp. 511–517, May 2011, doi: 10.1016/j.jcrysgro.2010.11.102.

[5] E. de Hoffmann and V. Stroobant, *Mass spectrometry: principles and applications*, 3rd ed. Chichester, West Sussex, England ; Hoboken, NJ: J. Wiley, 2007.

[6] J. Aldana, A. Romero-Otero, and M. P. Cala, ‘Exploring the Lipidome: Current Lipid Extraction Techniques for Mass Spectrometry Analysis’, *Metabolites*, vol. 10, no. 6, p. 231, Jun. 2020, doi: 10.3390/metabo10060231.

[7] I. C. Roseboom, H. Rosing, J. H. Beijnen, and T. P. C. Dorlo, ‘Skin tissue sample collection, sample homogenization, and analyte extraction strategies for liquid chromatographic mass spectrometry quantification of pharmaceutical compounds’, *J. Pharm. Biomed. Anal.*, vol. 191, p. 113590, Nov. 2020, doi: 10.1016/j.jpba.2020.113590.

[8] G. Cassani, F. Tibaldi, G. Donato, and N. Andriollo, ‘Determination of Alcohol Ethoxylates derivatized with Naphthoyl Chloride, in Waste Water Treatment Plant Influent, Effluent and Sludge Samples by Liquid Chromatography Mass Spectrometry’, *J. Surfactants Deterg.*, vol. 14, no. 1, pp. 139–150, Jan. 2011, doi: 10.1007/s11743-010-1215-6.

[9] P. Herrero, F. Borrull, R. M. Marce, and E. Pocurull, ‘Determination of polyether ionophores in urban sewage sludge by pressurised liquid extraction and liquid chromatography-tandem mass spectrometry: Study of different clean-up strategies’, *J. Chromatogr. A*, vol. 1285, pp. 31–39, Apr. 2013, doi: 10.1016/j.chroma.2013.02.034.

[10] A. Stehmann, R. J. W. Meesters, and H. F. Schroder, ‘Mass spectrometric analytical methods for the determination of endocrine disrupting chemicals (EDCs)’, *Water Sci. Technol.*, vol. 50, no. 5, pp. 165–171, 2004, doi: 10.2166/wst.2004.0324.

[11] D. A. Skoog, F. J. Holler, S. R. Crouch, and D. A. Skoog, *Instrumentelle Analytik: Grundlagen - Geräte - Anwendungen*, 6., Vollst. überarb. erw. Aufl. Berlin Heidelberg: Springer Spektrum, 2013. doi: 10.1007/978-3-642-39726-4.

[12] L. Nichols, ‘4: Extraction’, *Chemistry LibreTexts*, Oct. 05, 2017. https://chem.libretexts.org/Bookshelves/Organic_Chemistry/Organic_Chemistry_Lab_Techniques_(Nichols)/04%3A_Extraction (accessed Aug. 07, 2022).

[13] E. Gerdes, *Qualitative anorganische Analyse: ein Begleiter für Theorie und Praxis*, 2., Korrigierte und überarb. Aufl. 1998, Nachdr. Berlin: Springer, 2001.

[14] H. Schmidt-Traub, *Preparative Chromatography: of Fine Chemicals and Pharmaceutical Agents*. John Wiley & Sons, 2006.

[15] C. H. Geow, M. C. Tan, S. P. Yeap, and N. L. Chin, ‘A Review on Extraction Techniques and Its Future Applications in Industry’, *Eur. J. Lipid Sci. Technol.*, vol. 123, no. 4, p. 2000302, 2021, doi: 10.1002/ejlt.202000302.

[16] C. Pratt, S. A. Parsons, A. Soares, and B. D. Martin, ‘Biologically and chemically mediated adsorption and precipitation of phosphorus from wastewater’, *Curr. Opin. Biotechnol.*, vol. 23, no. 6, pp. 890–896, Dec. 2012, doi: 10.1016/j.copbio.2012.07.003.
[17] M. K. Perera, J. D. Englehardt, and A. C. Dvorak, ‘Technologies for Recovering Nutrients from Wastewater: A Critical Review’, *Environ. Eng. Sci.*, vol. 36, no. 5, pp. 511–529, May 2019, doi: 10.1089/ees.2018.0436.
[18] Z. Bubnik, V. Pour, A. Gruberova, H. Starhova, A. Hinkova, and P. Kadlec, ‘Application of continuous chromatographic separation in sugar processing’, *J. Food Eng.*, vol. 61, no. 4, pp. 509–513, Mar. 2004, doi: 10.1016/S0260-8774(03)00221-8.
[19] E. Gordon, ‘12.1: Isotopes’, *Chemistry LibreTexts*, Nov. 04, 2020. https://chem.libretexts.org/Courses/Monterey_Peninsula_College/MPC_CHEM_30A_Introduction_to_Chemistry_for_Health_Sciences/12%3A_Nuclear_Reactions/12.01%3A_Isotopes (accessed Aug. 08, 2022).
[20] W. E. Parkins, ‘The Uranium Bomb, the Calutron, and the Space-Charge Problem’, *Phys. Today*, vol. 58, no. 5, pp. 45–51, May 2005, doi: 10.1063/1.1995747.
[21] L. P. Smith, ‘On the Separation of Isotopes in Quantity by Electromagnetic Means’, *Phys. Rev.*, vol. 72, no. 11, pp. 989–1002, 1947, doi: 10.1103/PhysRev.72.989.
[22] I. G. Brown, ‘Vacuum arc ion sources’, *Rev. Sci. Instrum.*, vol. 65, no. 10, pp. 3061–3081, Oct. 1994, doi: 10.1063/1.1144756.
[23] L. Konermann, E. Ahadi, A. D. Rodriguez, and S. Vahidi, ‘Unraveling the Mechanism of Electrospray Ionization’, *Anal. Chem.*, vol. 85, no. 1, pp. 2–9, Jan. 2013, doi: 10.1021/ac302789c.
[24] M. Yamashita and J. B. Fenn, ‘Electrospray ion source. Another variation on the free-jet theme’, *J. Phys. Chem.*, vol. 88, no. 20, pp. 4451–4459, Sep. 1984, doi: 10.1021/j150664a002.
[25] P. Kebarle and U. H. Verkerk, ‘Electrospray: From ions in solution to ions in the gas phase, what we know now’, *Mass Spectrom. Rev.*, vol. 28, no. 6, pp. 898–917, Nov. 2009, doi: 10.1002/mas.20247.
[26] W. Bleakney, ‘A New Method of Positive Ray Analysis and Its Application to the Measurement of Ionization Potentials in Mercury Vapor’, *Phys. Rev.*, vol. 34, no. 1, pp. 157–160, Jul. 1929, doi: 10.1103/PhysRev.34.157.
[27] V. Franchetti, B. H. Solka, W. E. Baitinger, J. W. Amy, and R. G. Cooks, ‘Soft landing of ions as a means of surface modification’, *Int. J. Mass Spectrom. Ion Phys.*, vol. 23, no. 1, pp. 29–35, Jan. 1977, doi: 10.1016/0020-7381(77)80004-1.
[28] J. B. Fenn, ‘Electrospray Wings for Molecular Elephants (Nobel Lecture)’, *Angew. Chem. Int. Ed.*, vol. 42, no. 33, pp. 3871–3894, Aug. 2003, doi: 10.1002/anie.200300605.
[29] J. M. López-Herrera, A. Barrero, A. Boucard, I. G. Loscertales, and M. Márquez, ‘An experimental study of the electrospraying of water in air at atmospheric pressure’, *J. Am. Soc. Mass Spectrom.*, vol. 15, no. 2, pp. 253–259, Feb. 2004, doi: 10.1016/j.jasms.2003.10.018.
[30] T. Esser, ‘A Cryogenic Mass Spectrometer for Action Spectroscopy of Single Nanoparticles’, Doctoral Thesis, Universität Leipzig, Leipzig, 2019. [Online]. Available: https://nbn-resolving.org/urn:nbn:de:bsz:15-qucosa2-337501
[31] U. Heiz, F. Vanolli, L. Trento, and W.-D. Schneider, ‘Chemical reactivity of size-selected supported clusters: An experimental setup’, *Rev. Sci. Instrum.*, vol. 68, no. 5, pp. 1986–1994, May 1997, doi: 10.1063/1.1148113.
[32] A. Walz, ‘Compact and versatile electrospray - controlled ion beam deposition with adjustable frequency RF ion guides and extended mass range’, Doctoral Thesis,

Technische Universität München, 2020. [Online]. Available: http://nbn-resolving.de/urn/resolver.pl?urn:nbn:de:bvb:91-diss-20201217-1575832-1-0
[33] P. Su *et al.*, 'Multiplexing of Electrospray Ionization Sources Using Orthogonal Injection into an Electrodynamic Ion Funnel', *Anal. Chem.*, vol. 93, no. 33, pp. 11576–11584, Aug. 2021, doi: 10.1021/acs.analchem.1c02092.
[34] C. Hamann, 'An Electrospray Ion Source for Ultra–High Vacuum Deposition of Organic Molecules', Doctoral Thesis, Christian–Albrechts–Universität zu Kiel, Kiel, 2011. [Online]. Available: https://nbn-resolving.org/urn:nbn:de:gbv:8-diss-74778
[35] S. Rauschenbach, M. Ternes, L. Harnau, and K. Kern, 'Mass Spectrometry as a Preparative Tool for the Surface Science of Large Molecules', *Annu. Rev. Anal. Chem.*, vol. 9, no. 1, pp. 473–498, Jun. 2016, doi: 10.1146/annurev-anchem-071015-041633.
[36] H. Ochner *et al.*, 'Low-energy electron holography imaging of conformational variability of single-antibody molecules from electrospray ion beam deposition', *Proc. Natl. Acad. Sci. U. S. A.*, vol. 118, no. 51, Dec. 2021, doi: 10.1073/pnas.2112651118.
[37] H. Y. Samayoa-Oviedo *et al.*, 'Design and Performance of a Soft-Landing Instrument for Fragment Ion Deposition', *Anal. Chem.*, vol. 93, no. 43, pp. 14489–14496, Nov. 2021, doi: 10.1021/acs.analchem.1c03009.
[38] F. Yang *et al.*, 'Anion–Anion Chemistry with Mass-Selected Molecular Fragments on Surfaces', *Angew. Chem. Int. Ed.*, vol. 60, no. 47, pp. 24910–24914, Sep. 2021, doi: 10.1002/anie.202109249.
[39] P. Fremdling *et al.*, 'A Preparative Mass Spectrometer to Deposit Intact Large Native Protein Complexes', *ACS Nano*, Aug. 2022, doi: 10.1021/acsnano.2c04831.
[40] H. Gholipour-Ranjbar, L. Sertse, and J. Laskin, 'Designing new condensed phase materials using soft landing of reactive fragment ions - conference poster', presented at the ASMS 2022, Minneapolis, Jun. 2022.
[41] M. F. Crommie, C. P. Lutz, and D. M. Eigler, 'Confinement of Electrons to Quantum Corrals on a Metal Surface', *Science*, vol. 262, no. 5131, pp. 218–220, Oct. 1993, doi: 10.1126/science.262.5131.218.
[42] L. Gross, F. Mohn, N. Moll, P. Liljeroth, and G. Meyer, 'The Chemical Structure of a Molecule Resolved by Atomic Force Microscopy', *Science*, vol. 325, no. 5944, pp. 1110–1114, Aug. 2009, doi: 10.1126/science.1176210.
[43] K. Bian, C. Gerber, A. J. Heinrich, D. J. Müller, S. Scheuring, and Y. Jiang, 'Scanning probe microscopy', *Nat. Rev. Methods Primer*, vol. 1, no. 1, pp. 1–29, May 2021, doi: 10.1038/s43586-021-00033-2.
[44] J. W. Lee, L. C. Thomas, and S. J. Schmidt, 'Investigation of the Heating Rate Dependency Associated with the Loss of Crystalline Structure in Sucrose, Glucose, and Fructose Using a Thermal Analysis Approach (Part I)', *J. Agric. Food Chem.*, vol. 59, no. 2, pp. 684–701, Jan. 2011, doi: 10.1021/jf1042344.
[45] X. Wu *et al.*, 'Imaging single glycans', *Nature*, vol. 582, no. 7812, Art. no. 7812, Jun. 2020, doi: 10.1038/s41586-020-2362-1.
[46] S. Abb, L. Harnau, R. Gutzler, S. Rauschenbach, and K. Kern, 'Two-dimensional honeycomb network through sequence-controlled self-assembly of oligopeptides', *Nat. Commun.*, vol. 7, no. 1, pp. 1–7, Jan. 2016, doi: 10.1038/ncomms10335.
[47] S. Abb *et al.*, 'Carbohydrate Self-Assembly at Surfaces: STM Imaging of Sucrose Conformation and Ordering on Cu(100)', *Angew. Chem. Int. Ed.*, vol. 58, no. 25, pp. 8336–8340, Jun. 2019, doi: 10.1002/anie.201901340.
[48] K. Anggara *et al.*, 'Exploring the Molecular Conformation Space by Soft Molecule–Surface Collision', *J. Am. Chem. Soc.*, vol. 142, no. 51, pp. 21420–21427, Dec. 2020, doi: 10.1021/jacs.0c09933.

[49] K. Hankins *et al.*, ‘Role of Polysulfide Anions in Solid-Electrolyte Interphase Formation at the Lithium Metal Surface in Li–S Batteries’, *J. Phys. Chem. Lett.*, vol. 12, no. 38, pp. 9360–9367, Sep. 2021, doi: 10.1021/acs.jpclett.1c01930.
[50] J.-N. Longchamp *et al.*, ‘Imaging proteins at the single-molecule level’, *Proc. Natl. Acad. Sci.*, vol. 114, no. 7, Art. no. 7, Feb. 2017, doi: 10.1073/pnas.1614519114.
[51] L. Krumbein *et al.*, ‘Fast Molecular Compression by a Hyperthermal Collision Gives Bond-Selective Mechanochemistry’, *Phys. Rev. Lett.*, vol. 126, no. 5, p. 056001, Feb. 2021, doi: 10.1103/PhysRevLett.126.056001.
[52] EMBL-EBI, ‘Proteins | Biomacromolecular structures’. https://www.ebi.ac.uk/training/online/courses/biomacromolecular-structures/proteins/ (accessed Jan. 04, 2023).
[53] H.-W. Wang and J.-W. Wang, ‘How cryo-electron microscopy and X-ray crystallography complement each other’, *Protein Sci.*, vol. 26, no. 1, pp. 32–39, 2017, doi: 10.1002/pro.3022.
[54] J. Birch, H. Cheruvara, N. Gamage, P. J. Harrison, R. Lithgo, and A. Quigley, ‘Changes in Membrane Protein Structural Biology’, *Biology*, vol. 9, no. 11, Art. no. 11, Nov. 2020, doi: 10.3390/biology9110401.
[55] R. Santos *et al.*, ‘A comprehensive map of molecular drug targets’, *Nat. Rev. Drug Discov.*, vol. 16, no. 1, Art. no. 1, Jan. 2017, doi: 10.1038/nrd.2016.230.
[56] J. H. Van Drie and L. Tong, ‘Cryo-EM as a powerful tool for drug discovery’, *Bioorg. Med. Chem. Lett.*, vol. 30, no. 22, p. 127524, Nov. 2020, doi: 10.1016/j.bmcl.2020.127524.
[57] J.-P. Renaud *et al.*, ‘Cryo-EM in drug discovery: achievements, limitations and prospects’, *Nat. Rev. Drug Discov.*, vol. 17, no. 7, pp. 471–492, Jul. 2018, doi: 10.1038/nrd.2018.77.
[58] J. Dubochet *et al.*, ‘Cryo-electron microscopy of vitrified specimens’, *Q. Rev. Biophys.*, vol. 21, no. 2, pp. 129–228, May 1988, doi: 10.1017/S0033583500004297.
[59] A. J. Noble *et al.*, ‘Routine single particle CryoEM sample and grid characterization by tomography’, *eLife*, vol. 7, p. e34257, May 2018, doi: 10.7554/eLife.34257.
[60] R. M. Glaeser and B.-G. Han, ‘Opinion: hazards faced by macromolecules when confined to thin aqueous films’, *Biophys. Rep.*, vol. 3, no. 1, pp. 1–7, Jun. 2017, doi: 10.1007/s41048-016-0026-3.
[61] I. Drulyte *et al.*, ‘Approaches to altering particle distributions in cryo-electron microscopy sample preparation’, *Acta Crystallogr. Sect. Struct. Biol.*, vol. 74, no. 6, Art. no. 6, Jun. 2018, doi: 10.1107/S2059798318006496.
[62] D. Agard, Y. Cheng, R. M. Glaeser, and S. Subramaniam, ‘Chapter Two - Single-Particle Cryo-Electron Microscopy (Cryo-EM): Progress, Challenges, and Perspectives for Further Improvement’, in *Advances in Imaging and Electron Physics*, vol. 185, P. W. Hawkes, Ed. London: Academic Press, 2014, pp. 113–137. doi: 10.1016/B978-0-12-800144-8.00002-1.
[63] A. J. R. Heck, ‘Native mass spectrometry: a bridge between interactomics and structural biology’, *Nat. Methods*, vol. 5, no. 11, Art. no. 11, Nov. 2008, doi: 10.1038/nmeth.1265.
[64] M. Bakhtiari and L. Konermann, ‘Protein Ions Generated by Native Electrospray Ionization: Comparison of Gas Phase, Solution, and Crystal Structures’, *J. Phys. Chem. B*, vol. 123, no. 8, pp. 1784–1796, Feb. 2019, doi: 10.1021/acs.jpcb.8b12173.
[65] M. Sharon, S. Witt, E. Glasmacher, W. Baumeister, and C. V. Robinson, ‘Mass Spectrometry Reveals the Missing Links in the Assembly Pathway of the Bacterial 20 S Proteasome’, *J. Biol. Chem.*, vol. 282, no. 25, pp. 18448–18457, Jun. 2007, doi: 10.1074/jbc.M701534200.

[66] S. Tamara, M. A. den Boer, and A. J. R. Heck, ‘High-Resolution Native Mass Spectrometry’, *Chem. Rev.*, vol. 122, no. 8, pp. 7269–7326, Aug. 2021, doi: 10.1021/acs.chemrev.1c00212.
[67] S. A. Miller, H. Luo, S. J. Pachuta, and R. G. Cooks, ‘Soft-Landing of Polyatomic Ions at Fluorinated Self-Assembled Monolayer Surfaces’, *Science*, vol. 275, no. 5305, pp. 1447–1450, Mar. 1997, doi: 10.1126/science.275.5305.1447.
[68] J. Laskin, P. Wang, and O. Hadjar, ‘Soft-landing of peptide ions onto self-assembled monolayer surfaces: An overview’, *Phys. Chem. Chem. Phys.*, vol. 10, no. 8, pp. 1079–1090, 2008, doi: 10.1039/B712710C.
[69] J. Warneke *et al.*, ‘Direct functionalization of C−H bonds by electrophilic anions’, *Proc. Natl. Acad. Sci.*, vol. 117, no. 38, pp. 23374–23379, Sep. 2020, doi: 10.1073/pnas.2004432117.
[70] R. A. Scheltema *et al.*, ‘The Q Exactive HF, a Benchtop Mass Spectrometer with a Pre-filter, High-performance Quadrupole and an Ultra-high-field Orbitrap Analyzer’, *Mol. Cell. Proteomics*, vol. 13, no. 12, pp. 3698–3708, Dec. 2014, doi: 10.1074/mcp.M114.043489.
[71] F. W. Aston, ‘LXXIV. A positive ray spectrograph’, *Lond. Edinb. Dublin Philos. Mag. J. Sci.*, vol. 38, no. 228, pp. 707–714, Dec. 1919, doi: 10.1080/14786441208636004.
[72] D. Gerlich, ‘Inhomogeneous RF Fields: A Versatile Tool for the Study of Processes with Slow Ions’, in *Advances in Chemical Physics*, C.-Y. Ng, M. Baer, I. Prigogine, and S. A. Rice, Eds. Hoboken, NJ, USA: John Wiley & Sons, Inc., 1992, pp. 1–176. doi: 10.1002/9780470141397.ch1.
[73] R. Wester, ‘Radiofrequency multipole traps: tools for spectroscopy and dynamics of cold molecular ions’, *J. Phys. B At. Mol. Opt. Phys.*, vol. 42, no. 15, p. 154001, Jul. 2009, doi: 10.1088/0953-4075/42/15/154001.
[74] R. E. March and J. F. J. Todd, *Quadrupole ion trap mass spectrometry*, 2nd ed. Hoboken, N.J: J. Wiley, 2005.
[75] E. Teloy and D. Gerlich, ‘Integral cross sections for ion—molecule reactions. I. The guided beam technique’, *Chem. Phys.*, vol. 4, no. 3, pp. 417–427, Jun. 1974, doi: 10.1016/0301-0104(74)85008-1.
[76] D. Gerlich, ‘No title’, in *Electronic and Atomic Collisions: Invited Papers of the XIV International Conference on the Physics of Electronic and Atomic Collisions, Palo Alto, California, 24-30 July, 1985*, 1986, pp. 541–553. Accessed: May 09, 2022. [Online]. Available: https://www.biblio.com/book/electronic-atomic-collisions-invited-papers-xiv/d/137422822
[77] A. V. Tolmachev, I. V. Chernushevich, A. F. Dodonov, and K. G. Standing, ‘A collisional focusing ion guide for coupling an atmospheric pressure ion source to a mass spectrometer’, *Nucl. Instrum. Methods Phys. Res. Sect. B Beam Interact. Mater. At.*, vol. 124, no. 1, pp. 112–119, Apr. 1997, doi: 10.1016/S0168-583X(97)00068-2.
[78] L. Bernier, ‘Simulation of the Atmospheric Pressure Interface of a Mass Spectrometry Device’, Doctoral Thesis, Technische Universität Berlin, Berlin, 2021. [Online]. Available: https://doi.org/10.14279/depositonce-15449
[79] L. Bernier, H. Pinfold, M. Pauly, S. Rauschenbach, and J. Reiss, ‘Gas Flow and Ion Transfer in Heated ESI Capillary Interfaces’, *J. Am. Soc. Mass Spectrom.*, pp. 1–13, Feb. 2018, doi: 10.1007/s13361-018-1895-0.
[80] A. D. McNaught, A. Wilkinson, and International Union of Pure and Applied Chemistry, Eds., *Compendium of chemical terminology: IUPAC recommendations*, 2nd ed. Oxford [England] ; Malden, MA, USA: Blackwell Science, 1997.

[81] S. M. Stow *et al.*, ‘An Interlaboratory Evaluation of Drift Tube Ion Mobility–Mass Spectrometry Collision Cross Section Measurements’, *Anal. Chem.*, vol. 89, no. 17, pp. 9048–9055, Sep. 2017, doi: 10.1021/acs.analchem.7b01729.
[82] A. J. Midey, A. Camacho, J. Sampathkumaran, C. A. Krueger, M. A. Osgood, and C. Wu, ‘High-performance ion mobility spectrometry with direct electrospray ionization (ESI-HPIMS) for the detection of additives and contaminants in food’, *Anal. Chim. Acta*, vol. 804, pp. 197–206, Dec. 2013, doi: 10.1016/j.aca.2013.10.010.
[83] K. B. Shelimov and M. F. Jarrold, ‘Conformations, Unfolding, and Refolding of Apomyoglobin in Vacuum: An Activation Barrier for Gas-Phase Protein Folding’, *J. Am. Chem. Soc.*, vol. 119, no. 13, pp. 2987–2994, Apr. 1997, doi: 10.1021/ja962914k.
[84] M. F. Bush, Z. Hall, K. Giles, J. Hoyes, C. V. Robinson, and B. T. Ruotolo, ‘Collision Cross Sections of Proteins and Their Complexes: A Calibration Framework and Database for Gas-Phase Structural Biology’, *Anal. Chem.*, vol. 82, no. 22, pp. 9557–9565, Nov. 2010, doi: 10.1021/ac1022953.
[85] S. Ellingson, *Electromagnetics*, 1st ed. VT Publishing, 2018. doi: 10.21061/electromagnetics-vol-1.
[86] Scientific Instrument Services, ‘Chapter 2. SIMION Basics (SIMION® 8.0 User Manual)’. https://simion.com/manual/chap2.html (accessed May 19, 2022).
[87] ‘Chapter 10: Laplace’s Equation | Physics’. https://www.physics.uoguelph.ca/chapter-10-laplaces-equation (accessed May 19, 2022).
[88] A. D. Appelhans and D. A. Dahl, ‘Measurement of external ion injection and trapping efficiency in the ion trap mass spectrometer and comparison with a predictive model’, *Int. J. Mass Spectrom.*, vol. 216, no. 3, pp. 269–284, May 2002, doi: 10.1016/S1387-3806(02)00627-9.
[89] Scientific Instrument Services, ‘Ion-Gas Collisions’, 2021. https://simion.com/info/ion_gas_collisions.html (accessed May 20, 2022).
[90] A. D. Appelhans and D. A. Dahl, ‘SIMION ion optics simulations at atmospheric pressure’, *Int. J. Mass Spectrom.*, vol. 244, no. 1, pp. 1–14, Jun. 2005, doi: 10.1016/j.ijms.2005.03.010.
[91] V. Gabelica *et al.*, ‘Recommendations for reporting ion mobility Mass Spectrometry measurements’, *Mass Spectrom. Rev.*, vol. 38, no. 3, pp. 291–320, 2019, doi: 10.1002/mas.21585.
[92] J. A. Picache *et al.*, ‘Collision cross section compendium to annotate and predict multi-omic compound identities’, *Chem. Sci.*, vol. 10, no. 4, pp. 983–993, 2019, doi: 10.1039/C8SC04396E.
[93] V. Gabelica and E. Marklund, ‘Fundamentals of ion mobility spectrometry’, *Curr. Opin. Chem. Biol.*, vol. 42, pp. 51–59, Feb. 2018, doi: 10.1016/j.cbpa.2017.10.022.
[94] S. Poteshin, A. Burykina, A. Adamov, and A. Sysoev, ‘Investigation by simulation of the RF carpets for the transport of ions at atmospheric pressures’, *Eur. J. Mass Spectrom.*, p. 1469066720912194, Mar. 2020, doi: 10.1177/1469066720912194.
[95] B. E. Draper, S. N. Anthony, and M. F. Jarrold, ‘The FUNPET—a New Hybrid Ion Funnel-Ion Carpet Atmospheric Pressure Interface for the Simultaneous Transmission of a Broad Mass Range’, *J. Am. Soc. Mass Spectrom.*, vol. 29, no. 11, pp. 2160–2172, Nov. 2018, doi: 10.1007/s13361-018-2038-3.
[96] M. Pauly *et al.*, ‘A hydrodynamically optimized nano-electrospray ionization source and vacuum interface’, *The Analyst*, vol. 139, no. 8, p. 1856, 2014, doi: 10.1039/c3an01836a.
[97] A. V. Tolmachev, T. Kim, H. R. Udseth, R. D. Smith, T. H. Bailey, and J. H. Futrell, ‘Simulation-based optimization of the electrodynamic ion funnel for high sensitivity electrospray ionization mass spectrometry’, *Int. J. Mass Spectrom.*, vol. 203, no. 1, pp. 31–47, Dec. 2000, doi: 10.1016/S1387-3806(00)00265-7.

[98] S. Fanghänel, O. Asvany, and S. Schlemmer, ‘Optimization of RF multipole ion trap geometries’, *J. Mol. Spectrosc.*, vol. 332, pp. 124–133, Feb. 2017, doi: 10.1016/j.jms.2016.12.003.
[99] S. Fanghaenel, ‘Low Temperature Collisions and Reactions in a 22-Pole Ion Trap’, Doctoral Thesis, Universität zu Köln, 2018. Accessed: Feb. 15, 2022. [Online]. Available: http://www.uni-koeln.de/
[100] Scientific Instrument Services, ‘Potential Array File Types (Comparison)’, in *Simion 8.1 Supplemental Documentation*, Scientific Instrument Services, Inc., 2012.
[101] Scientific Instrument Services, ‘Additional Fast Proportional Scaling Solutions’, in *Simion 8.1 Supplemental Documentation*, Scientific Instrument Services, Inc., 2012.
[102] ‘mplot3d FAQ — Matplotlib 3.5.2 documentation’. https://matplotlib.org/stable/api/toolkits/mplot3d/faq.html?highlight=mplot3d%20faq (accessed May 18, 2022).
[103] D. J. Müller and Y. F. Dufrêne, ‘Atomic force microscopy as a multifunctional molecular toolbox in nanobiotechnology’, *Nat. Nanotechnol.*, vol. 3, no. 5, pp. 261–269, May 2008, doi: 10.1038/nnano.2008.100.
[104] W. Kühlbrandt, ‘The Resolution Revolution’, *Science*, vol. 343, no. 6178, Art. no. 6178, Mar. 2014, doi: 10.1126/science.1251652.
[105] X. Bai, G. McMullan, and S. H. W. Scheres, ‘How cryo-EM is revolutionizing structural biology’, *Trends Biochem. Sci.*, vol. 40, no. 1, Art. no. 1, Jan. 2015, doi: 10.1016/j.tibs.2014.10.005.
[106] K. M. Yip, N. Fischer, E. Paknia, A. Chari, and H. Stark, ‘Atomic-resolution protein structure determination by cryo-EM’, *Nature*, vol. 587, no. 7832, pp. 157–161, Nov. 2020, doi: 10.1038/s41586-020-2833-4.
[107] S. Kahle *et al.*, ‘The Quantum Magnetism of Individual Manganese-12-Acetate Molecular Magnets Anchored at Surfaces’, *Nano Lett.*, vol. 12, no. 1, pp. 518–521, Jan. 2012, doi: 10.1021/nl204141z.
[108] C. S. Kley *et al.*, ‘Atomic-Scale Observation of Multiconformational Binding and Energy Level Alignment of Ruthenium-Based Photosensitizers on TiO2 Anatase’, *Nano Lett.*, vol. 14, no. 2, pp. 563–569, Feb. 2014, doi: 10.1021/nl403717d.
[109] D. S. Chorev *et al.*, ‘The use of sonicated lipid vesicles for mass spectrometry of membrane protein complexes’, *Nat. Protoc.*, vol. 15, no. 5, pp. 1690–1706, May 2020, doi: 10.1038/s41596-020-0303-y.
[110] J. Cyriac, T. Pradeep, H. Kang, R. Souda, and R. G. Cooks, ‘Low-Energy Ionic Collisions at Molecular Solids’, *Chem. Rev.*, vol. 112, no. 10, pp. 5356–5411, Oct. 2012, doi: 10.1021/cr200384k.
[111] G. E. Johnson, D. Gunaratne, and J. Laskin, ‘Soft- and reactive landing of ions onto surfaces: Concepts and applications’, *Mass Spectrom. Rev.*, vol. 35, no. 3, pp. 439–479, May 2016, doi: 10.1002/mas.21451.
[112] S. Rauschenbach *et al.*, ‘Electrospray Ion Beam Deposition of Clusters and Biomolecules’, *Small*, vol. 2, no. 4, pp. 540–547, 2006, doi: 10.1002/smll.200500479.
[113] Chr. Hamann, R. Woltmann, I.-P. Hong, N. Hauptmann, S. Karan, and R. Berndt, ‘Ultrahigh vacuum deposition of organic molecules by electrospray ionization’, *Rev. Sci. Instrum.*, vol. 82, no. 3, p. 033903, Mar. 2011, doi: 10.1063/1.3553010.
[114] A. Walz, K. Stoiber, A. Huettig, H. Schlichting, and J. V. Barth, ‘Navigate Flying Molecular Elephants Safely to the Ground: Mass-Selective Soft Landing up to the Mega-Dalton Range by Electrospray Controlled Ion-Beam Deposition’, *Anal. Chem.*, vol. 94, no. 22, pp. 7767–7778, Jun. 2022, doi: 10.1021/acs.analchem.1c04495.

[115] Z. Deng *et al.*, ‘A Close Look at Proteins: Submolecular Resolution of Two- and Three-Dimensionally Folded Cytochrome c at Surfaces’, *Nano Lett.*, vol. 12, no. 5, Art. no. 5, May 2012, doi: 10.1021/nl3005385.
[116] G. Rinke, S. Rauschenbach, L. Harnau, A. Albarghash, M. Pauly, and K. Kern, ‘Active Conformation Control of Unfolded Proteins by Hyperthermal Collision with a Metal Surface’, *Nano Lett.*, vol. 14, no. 10, pp. 5609–5615, Oct. 2014, doi: 10.1021/nl502122j.
[117] N. Vats *et al.*, ‘Electron microscopy of polyoxometalate ions on graphene by electrospray ion beam deposition’, *Nanoscale*, vol. 10, no. 10, pp. 4952–4961, 2018, doi: 10.1039/C8NR00402A.
[118] N. Vats *et al.*, ‘Catalyzing Bond-Dissociation in Graphene via Alkali-Iodide Molecules’, *Small Weinh. Bergstr. Ger.*, vol. n/a, no. n/a, p. 2102037, 2021, doi: 10.1002/smll.202102037.
[119] V. Prabhakaran *et al.*, ‘Rational design of efficient Electrode–Electrolyte interfaces for solid-state energy storage using ion soft landing’, *Nat. Comm.*, vol. 7, p. 11399, Apr. 2016, doi: 10.1038/ncomms11399.
[120] V. A. Mikhailov, T. H. Mize, J. L. P. Benesch, and C. V. Robinson, ‘Mass-Selective Soft-Landing of Protein Assemblies with Controlled Landing Energies’, *Anal. Chem.*, vol. 86, no. 16, pp. 8321–8328, Aug. 2014, doi: 10.1021/ac5018327.
[121] T. K. Esser *et al.*, ‘Mass-selective and ice-free cryo-EM protein sample preparation via native electrospray ion-beam deposition’. Oct. 19, 2021. doi: 10.1101/2021.10.18.464782.
[122] M. S. Westphall, K. W. Lee, A. Z. Salome, J. M. Lodge, T. Grant, and J. J. Coon, ‘Three-dimensional structure determination of protein complexes using matrix-landing mass spectrometry’, *Nat. Commun.*, vol. 13, no. 1, Art. no. 1, Apr. 2022, doi: 10.1038/s41467-022-29964-4.
[123] A. Koma, ‘Molecular beam epitaxial growth of organic thin films’, *Prog. Cryst. Growth Charact. Mater.*, vol. 30, no. 2, pp. 129–152, Jan. 1995, doi: 10.1016/0960-8974(95)00009-V.
[124] P. Su, H. Hu, J. Warneke, M. E. Belov, G. A. Anderson, and J. Laskin, ‘Design and Performance of a Dual-Polarity Instrument for Ion Soft Landing’, *Anal. Chem.*, vol. 91, no. 9, pp. 5904–5912, May 2019, doi: 10.1021/acs.analchem.9b00309.
[125] L. Bernier, M. Taesch, S. Rauschenbach, and J. Reiss, ‘Transfer conditions and transmission bias in capillaries of vacuum interfaces’, *Int. J. Mass Spectrom.*, vol. 447, p. 116239, Jan. 2020, doi: 10.1016/j.ijms.2019.116239.
[126] T. K. Esser *et al.*, ‘Mass-selective and ice-free cryo-EM protein sample preparation via native electrospray ion-beam deposition’, *PNAS Nexus*, Aug. 2022, doi: 10.1093/pnasnexus/pgac153.
[127] J. L. P. Benesch *et al.*, ‘Separating and visualising protein assemblies by means of preparative mass spectrometry and microscopy’, *J. Struct. Biol.*, vol. 172, no. 2, pp. 161–168, Nov. 2010, doi: 10.1016/j.jsb.2010.03.004.
[128] D. J. Douglas and J. B. French, ‘Collisional focusing effects in radio frequency quadrupoles’, *J. Am. Soc. Mass Spectrom.*, vol. 3, no. 4, pp. 398–408, May 1992, doi: 10.1016/1044-0305(92)87067-9.
[129] K. B. Shelimov, D. E. Clemmer, R. R. Hudgins, and M. F. Jarrold, ‘Protein Structure in Vacuo: Gas-Phase Conformations of BPTI and Cytochrome c’, *J. Am. Chem. Soc.*, vol. 119, no. 9, pp. 2240–2248, Mar. 1997, doi: 10.1021/ja9619059.
[130] Z. Zhang and M. G. Lagally, ‘Atomistic Processes in the Early Stages of Thin-Film Growth’, *Science*, vol. 276, no. 5311, pp. 377–383, Apr. 1997, doi: 10.1126/science.276.5311.377.

[131] A. G. Elliott, C. C. Harper, H.-W. Lin, A. C. Susa, Z. Xia, and E. R. Williams, ‘Simultaneous Measurements of Mass and Collisional Cross-Section of Single Ions with Charge Detection Mass Spectrometry’, *Anal. Chem.*, vol. 89, no. 14, pp. 7701–7708, Jul. 2017, doi: 10.1021/acs.analchem.7b01675.
[132] G. Siuzdak *et al.*, ‘Mass spectrometry and viral analysis’, *Chem. Biol.*, vol. 3, no. 1, pp. 45–48, Jan. 1996, doi: 10.1016/S1074-5521(96)90083-6.
[133] M. S. Westphall, K. W. Lee, A. Z. Salome, J. M. Lodge, T. Grant, and J. J. Coon, ‘Peer review report to “Three-dimensional structure determination of protein complexes using matrix-landing mass spectrometry”’, *Nat. Commun.*, vol. 13, no. 1, p. 2276, Apr. 2022, doi: 10.1038/s41467-022-29964-4.
[134] Z. Ouyang *et al.*, ‘Preparing Protein Microarrays by Soft-Landing of Mass-Selected Ions’, *Science*, vol. 301, no. 5638, pp. 1351–1354, Sep. 2003, doi: 10.1126/science.1088776.
[135] M. Volný, W. T. Elam, A. Branca, B. D. Ratner, and F. Tureček, ‘Preparative Soft and Reactive Landing of Multiply Charged Protein Ions on a Plasma-Treated Metal Surface’, *Anal. Chem.*, vol. 77, no. 15, pp. 4890–4896, Aug. 2005, doi: 10.1021/ac0507136.
[136] H. Hernández and C. V. Robinson, ‘Determining the stoichiometry and interactions of macromolecular assemblies from mass spectrometry’, *Nat. Protoc.*, vol. 2, no. 3, pp. 715–726, Mar. 2007, doi: 10.1038/nprot.2007.73.
[137] K. Chamchoy, D. Pakotiprapha, P. Pumirat, U. Leartsakulpanich, and U. Boonyuen, ‘Application of WST-8 based colorimetric NAD(P)H detection for quantitative dehydrogenase assays’, *BMC Biochem.*, vol. 20, no. 1, p. 4, Apr. 2019, doi: 10.1186/s12858-019-0108-1.
[138] ‘ab102533 Alcohol Dehydrogenase Detection Kit Protocol v2b’. Abcam, Mar. 28, 2014. Accessed: Mar. 06, 2020. [Online]. Available: https://www.abcam.com/ps/products/102/ab102533/documents/ab102533%20Alcohol%20Dehydrogenase%20Detection%20Kit%20Protocol%20v2b%20(website).pdf
[139] B. A. Thomson, ‘Atmospheric pressure ionization and liquid chromatography/mass spectrometry—together at last’, *J. Am. Soc. Mass Spectrom.*, vol. 9, no. 3, pp. 187–193, Mar. 1998, doi: 10.1016/S1044-0305(97)00285-7.
[140] P. Ryumin, J. Brown, M. Morris, and R. Cramer, ‘Investigation and optimization of parameters affecting the multiply charged ion yield in AP-MALDI MS’, *Methods*, vol. 104, pp. 11–20, Jul. 2016, doi: 10.1016/j.ymeth.2016.01.015.
[141] M. G. Skoblin *et al.*, ‘Numerical simulation of ion transport in an atmosphere-to-vacuum interface taking into account gas dynamics and space charge’, *Eur. J. Mass Spectrom.*, vol. 23, no. 4, pp. 187–191, Aug. 2017, doi: 10.1177/1469066717719556.
[142] K. D. D. Gunaratne, V. Prabhakaran, Y. M. Ibrahim, R. V. Norheim, G. E. Johnson, and J. Laskin, ‘Design and performance of a high-flux electrospray ionization source for ion soft landing’, *The Analyst*, vol. 140, no. 9, pp. 2957–2963, 2015, doi: 10.1039/C5AN00220F.
[143] Pfeiffer Vacuum GmbH, ‘HiPace® 300 | Pfeiffer Vacuum’, *HiPace 300 Datasheet*. https://www.pfeiffer-vacuum.com/en/products/vacuum-generation/turbopumps/hybrid-bearing/hipace-300/4500/hipace-300-with-tc-400-dn-100-iso-k (accessed Jan. 17, 2022).
[144] E. Franquet, V. Perrier, S. Gibout, and P. Bruel, ‘Free underexpanded jets in a quiescent medium: A review’, *Prog. Aerosp. Sci.*, vol. 77, pp. 25–53, Aug. 2015, doi: 10.1016/j.paerosci.2015.06.006.
[145] N. J. Dam, M. Rodenburg, R. A. L. Tolboom, G. G. M. Stoffels, P. M. Huisman-Kleinherenbrink, and J. J. ter Meulen, ‘Imaging of an underexpanded nozzle flow by UV laser Rayleigh scattering’, *Exp. Fluids*, vol. 24, no. 2, pp. 93–101, Feb. 1998, doi: 10.1007/s003480050156.

[146] M. Dole, L. L. Mack, R. L. Hines, R. C. Mobley, L. D. Ferguson, and M. B. Alice, ‘Molecular Beams of Macroions’, *J. Chem. Phys.*, vol. 49, no. 5, pp. 2240–2249, Sep. 1968, doi: 10.1063/1.1670391.
[147] A. Kantrowitz and J. Grey, ‘A High Intensity Source for the Molecular Beam. Part I. Theoretical’, *Rev. Sci. Instrum.*, vol. 22, no. 5, pp. 328–332, May 1951, doi: 10.1063/1.1745921.
[148] S. Rauschenbach, ‘Electrospray Ion Beam Deposition and Mass Spectrometry of nonvolatile Molecules and Nanomaterials’, Doctoral Thesis, EPF Lausanne, Lausanne, 2007.
[149] S. A. Shaffer, D. C. Prior, G. A. Anderson, H. R. Udseth, and R. D. Smith, ‘An Ion Funnel Interface for Improved Ion Focusing and Sensitivity Using Electrospray Ionization Mass Spectrometry’, *Anal. Chem.*, vol. 70, no. 19, pp. 4111–4119, Oct. 1998, doi: 10.1021/ac9802170.
[150] R. T. Kelly, A. V. Tolmachev, J. S. Page, K. Tang, and R. D. Smith, ‘The ion funnel: Theory, implementations, and applications’, *Mass Spectrom. Rev.*, vol. 29, no. 2, pp. 294–312, 2010, doi: 10.1002/mas.20232.
[151] H. E. Revercomb and E. A. Mason, ‘Theory of plasma chromatography/gaseous electrophoresis. Review’, *Anal. Chem.*, vol. 47, no. 7, pp. 970–983, Jun. 1975, doi: 10.1021/ac60357a043.
[152] E. Raptakis *et al.*, ‘The Aerolens: A Novel Ion-Optical Design for Ion Focusing in Laminarized Under-expanded Gas Flows - Conference Poster’, in *ASMS 2013*, 2013.
[153] A. Lekkas, D. Papanastasiou, D. Kounadis, and E. Raptakis, ‘An RF transfer interface operable over an extended pressure range for gating high mass ions into an oaTOF mass spectrometer’, presented at the 65th ASMS, Indianapolis, IN, USA, Jun. 2017.
[154] E. Tridas, J. M. Anthony, R. Guldiken, and R. Schlaf, ‘Enhanced simulation of an RF ion funnel including gas turbulence’, *J. Mass Spectrom.*, vol. 50, no. 1, pp. 206–211, 2015, doi: 10.1002/jms.3519.
[155] T. Kaposi, H. Schlichting, J. Barth, and A. Walz, ‘Partly sealed ion guide and ion beam deposition system’, WO2019193170A1, Oct. 10, 2019 Accessed: Jan. 19, 2022. [Online]. Available: https://patents.google.com/patent/WO2019193170A1/en?oq=wo2019%2f193170
[156] S. Albrecht, ‘Development of a highly sensitive and versatile mass spectrometer system for laboratory and atmospheric measurements’, Doctoral Thesis, Forschungszentrum Jülich GmbH Zentralbibliothek, Verlag, Jülich, 2014. [Online]. Available: http://hdl.handle.net/2128/8414
[157] T.-C. Chen *et al.*, ‘Rectangular Ion Funnel: A New Ion Funnel Interface for Structures for Lossless Ion Manipulations’, *Anal. Chem.*, vol. 87, no. 1, pp. 716–722, Jan. 2015, doi: 10.1021/ac503564c.
[158] T. Egorova, R. Dietiker, B. Hattendorf, and D. Günther, ‘Characteristics of an ion funnel as ion guide in an inductively coupled plasma mass spectrometer’, *Spectrochim. Acta Part B At. Spectrosc.*, vol. 76, pp. 40–47, Oct. 2012, doi: 10.1016/j.sab.2012.06.010.
[159] Mass Spec pro, ‘Ion Funnel’, *Ion Funnel*. http://www.massspecpro.com/technology/ion-optics/ion-funnel-0 (accessed Jan. 24, 2022).
[160] M. W. Senko *et al.*, ‘Ion transport device and modes of operation thereof’, US7781728B2, Aug. 24, 2010 Accessed: Jan. 24, 2022. [Online]. Available: https://patents.google.com/patent/US7781728/en
[161] Thermo Fisher Scientific, ‘Q Exactive HF Orbitrap LC-MS/MS System . Higher Quality Data, Faster Than Ever’, *Q Exactive HF Orbitrap LC-MS/MS System - Thermo*

Fisher, 2016. https://www.google.com/url?sa=t&rct=j&q=&esrc=s&source=web&cd=&cad=rja&uact=8&ved=2ahUKEwj7kKP44sr1AhX1QEEAHdxrDKwQFnoECA0QAQ&url=https%3A%2F%2Fassets.thermofisher.com%2FTFS-Assets%2FCMD%2Fbrochures%2FBR-64052-LC-MS-Q-Exactive-HF-Orbitrap-BR64052-EN.pdf&usg=AOvVaw3LdT6xgzAlHX65PUo3LiF2 (accessed Jan. 24, 2022).

[162] T. N. Arrey *et al.*, 'New innovations implemented on the Q Exactive HF mass spectrometer', *Thermo Scientific Mass Spectrometry Support Centre*, 2017. https://assets.thermofisher.com/TFS-Assets/CMD/posters/PN-65057-Q-Exactive-HF-X-MS-ASMS2017-PN65057-EN.pdf (accessed Jan. 24, 2022).

[163] T. Brunner *et al.*, 'An RF-only ion-funnel for extraction from high-pressure gases', *Int. J. Mass Spectrom.*, vol. 379, pp. 110–120, Mar. 2015, doi: 10.1016/j.ijms.2015.01.003.

[164] S. A. Shaffer, A. Tolmachev, D. C. Prior, G. A. Anderson, H. R. Udseth, and R. D. Smith, 'Characterization of an Improved Electrodynamic Ion Funnel Interface for Electrospray Ionization Mass Spectrometry', *Anal. Chem.*, vol. 71, no. 15, pp. 2957–2964, Aug. 1999, doi: 10.1021/ac990346w.

[165] H. H. Hu, 'Chapter 10 - Computational Fluid Dynamics', in *Fluid Mechanics (Fifth Edition)*, P. K. Kundu, I. M. Cohen, and D. R. Dowling, Eds. Boston: Academic Press, 2012, pp. 421–472. doi: 10.1016/B978-0-12-382100-3.10010-1.

[166] G. Rinke *et al.*, 'Soft-landing electrospray ion beam deposition of sensitive oligoynes on surfaces in vacuum', *Int. J. Mass Spectrom.*, vol. 377, pp. 228–234, Feb. 2015, doi: 10.1016/j.ijms.2014.06.026.

[167] L. M. Matz, H. H. Hill, L. W. Beegle, and I. Kanik, 'Investigation of drift gas selectivity in high resolution ion mobility spectrometry with mass spectrometry detection', *J. Am. Soc. Mass Spectrom.*, vol. 13, no. 4, pp. 300–307, Apr. 2002, doi: 10.1016/S1044-0305(01)00366-X.

[168] S. Gimelshein, T. Lilly, and E. Moskovets, 'Numerical Analysis of Ion-Funnel Transmission Efficiency in an API-MS System with a Continuum/Microscopic Approach', *J. Am. Soc. Mass Spectrom.*, vol. 26, no. 11, pp. 1911–1922, Nov. 2015, doi: 10.1007/s13361-015-1214-y.

[169] P. Kebarle and L. Tang, 'From ions in solution to ions in the gas phase - the mechanism of electrospray mass spectrometry', *Anal. Chem.*, vol. 65, no. 22, pp. 972A-986A, Nov. 1993, doi: 10.1021/ac00070a001.

[170] T. Kim, H. R. Udseth, and R. D. Smith, 'Improved Ion Transmission from Atmospheric Pressure to High Vacuum Using a Multicapillary Inlet and Electrodynamic Ion Funnel Interface', *Anal. Chem.*, vol. 72, no. 20, pp. 5014–5019, Oct. 2000, doi: 10.1021/ac0003549.

[171] S.-H. Roh *et al.*, 'Subunit conformational variation within individual GroEL oligomers resolved by Cryo-EM', *Proc. Natl. Acad. Sci.*, vol. 114, no. 31, pp. 8259–8264, Aug. 2017, doi: 10.1073/pnas.1704725114.

[172] D. S. Chorev *et al.*, 'Protein assemblies ejected directly from native membranes yield complexes for mass spectrometry', *Science*, vol. 362, no. 6416, pp. 829–834, Nov. 2018, doi: 10.1126/science.aau0976.

[173] Leybold, 'VARODRY - Dry Screw Pumps Leybold', *Leybold*, Apr. 05, 2022. https://www.leybold.com/en-uk/products/vacuum-pumps/industrial-dry-vacuum-pumps/varodry (accessed May 04, 2022).

[174] H. Forster, 'Energy Follow Up Survey: Household Energy Consumption & Affordability', UK Department for Business, Energy and Industrial Strategy, London, 2021. Accessed: Sep. 19, 2022. [Online]. Available:

https://www.gov.uk/government/publications/energy-follow-up-survey-efus-2017-reports
[175] U. Walter, *Grundlagen der Vakuumtechnik*. Köln: Leybold, 2016.
[176] J. J. Everdij, A. Huijser, and N. F. Verster, ‘Improved Space Focusing of Polar Diatomic Molecules in a System of Quadrupole and Hexapole Fields’, *Rev. Sci. Instrum.*, vol. 44, no. 6, pp. 721–725, Jun. 1973, doi: 10.1063/1.1686230.
[177] F. Paschen, ‘Ueber die zum Funkenübergang in Luft, Wasserstoff und Kohlensäure bei verschiedenen Drucken erforderliche Potentialdifferenz’, *Ann. Phys.*, vol. 273, no. 5, pp. 69–96, 1889, doi: 10.1002/andp.18892730505.
[178] K. T. a. L. Burm, ‘Calculation of the Townsend Discharge Coefficients and the Paschen Curve Coefficients’, *Contrib. Plasma Phys.*, vol. 47, no. 3, pp. 177–182, 2007, doi: 10.1002/ctpp.200710025.
[179] P. Su *et al.*, ‘Preparative Mass Spectrometry Using a Rotating-Wall Mass Analyzer’, *Angew. Chem. Int. Ed.*, vol. 59, no. 20, pp. 7711–7716, 2020, doi: 10.1002/anie.202000065.
[180] N. M. Hoffman, B. Opačić, and P. T. A. Reilly, ‘Note: An inexpensive square waveform ion funnel driver’, *Rev. Sci. Instrum.*, vol. 88, no. 1, p. 016104, Jan. 2017, doi: 10.1063/1.4974345.
[181] Y. Liu, X. Cong, W. Liu, and A. Laganowsky, ‘Characterization of Membrane Protein–Lipid Interactions by Mass Spectrometry Ion Mobility Mass Spectrometry’, *J. Am. Soc. Mass Spectrom.*, vol. 28, no. 4, pp. 579–586, Apr. 2017, doi: 10.1007/s13361-016-1555-1.
[182] T. M. Allison and C. Bechara, ‘Structural mass spectrometry comes of age: new insight into protein structure, function and interactions’, *Biochem. Soc. Trans.*, vol. 47, no. 1, pp. 317–327, Feb. 2019, doi: 10.1042/BST20180356.
[183] P. W. A. Devine *et al.*, ‘Investigating the Structural Compaction of Biomolecules Upon Transition to the Gas-Phase Using ESI-TWIMS-MS’, *J. Am. Soc. Mass Spectrom.*, vol. 28, no. 9, pp. 1855–1862, Sep. 2017, doi: 10.1007/s13361-017-1689-9.
[184] M. S. Westphall, K. W. Lee, A. Z. Salome, J. Lodge, T. Grant, and J. Coon, ‘3D Structure Determination of Protein Complexes using Matrix-Landing Mass Spectrometry’. Oct. 13, 2021. doi: 10.1101/2021.10.13.464253.
[185] R. Beveridge, Q. Chappuis, C. Macphee, and P. Barran, ‘Mass spectrometry methods for intrinsically disordered proteins’, *Analyst*, vol. 138, no. 1, pp. 32–42, Nov. 2012, doi: 10.1039/C2AN35665A.
[186] E. Jurneczko *et al.*, ‘Intrinsic disorder in proteins: a challenge for (un)structural biology met by ion mobility–mass spectrometry’, *Biochem. Soc. Trans.*, vol. 40, no. 5, pp. 1021–1026, Sep. 2012, doi: 10.1042/BST20120125.
[187] C. Bleiholder and F. C. Liu, ‘Structure Relaxation Approximation (SRA) for Elucidation of Protein Structures from Ion Mobility Measurements’, *J. Phys. Chem. B*, vol. 123, no. 13, pp. 2756–2769, Apr. 2019, doi: 10.1021/acs.jpcb.8b11818.
[188] S. Crist, D. R. Glass, and P. M. Sherman, ‘Study of the highly underexpanded sonic jet.’, *AIAA J.*, vol. 4, no. 1, pp. 68–71, Jan. 1966, doi: 10.2514/3.3386.
[189] R. Cumeras, E. Figueras, C. E. Davis, J. I. Baumbach, and I. Gràcia, ‘Review on Ion Mobility Spectrometry. Part 1: current instrumentation’, *Analyst*, vol. 140, no. 5, pp. 1376–1390, Feb. 2015, doi: 10.1039/C4AN01100G.
[190] Baykut, Gökhan and Bergquist, Jonas, ‘Präparative Ionenmobilitätsspektrometrie’, DE 10 2007 035 827.1, Oct. 31, 2012 [Online]. Available: https://register.dpma.de/DPMAregister/pat/register?AKZ=1020070358271
[191] S. Warnke, ‘A Gas-Phase Approach to Biomolecular Structure: Combining Ion Mobility-Mass Spectrometry with Spectroscopy’, Doctoral Thesis, Freie Universität

Berlin, Berlin, 2015. Accessed: Jun. 22, 2022. [Online]. Available: https://refubium.fu-berlin.de/handle/fub188/13083
[192] S. Warnke, ‘Ein Ionenmobilitätsspektrometer zur Spektroskopie an konformations- und massenselektierten Biomolekülen’, Diploma, Eberhard Karls Universität Tübingen, Tübingen, 2010.
[193] L. Deng *et al.*, ‘Ultra-High Resolution Ion Mobility Separations Utilizing Traveling Waves in a 13 m Serpentine Path Length Structures for Lossless Ion Manipulations Module’, *Anal. Chem.*, vol. 88, no. 18, pp. 8957–8964, Sep. 2016, doi: 10.1021/acs.analchem.6b01915.
[194] I. Buryakov, E. Krylov, A. Makas, E. Nazarov, V. Pervukhin, and U. Rasulev, ‘Separation of ions according to their mobility in a strong alternating current electric field’, *Sov. Tech. Phys. Lett.*, vol. 17, no. 6, pp. 446–447, 1991.
[195] H. Borsdorf and G. A. Eiceman, ‘Ion Mobility Spectrometry: Principles and Applications’, *Appl. Spectrosc. Rev.*, vol. 41, no. 4, pp. 323–375, Aug. 2006, doi: 10.1080/05704920600663469.
[196] Thermo Fisher Scientific, ‘FAIMS Pro™ Interface’. https://www.thermofisher.com/order/catalog/product/FMS02-10001 (accessed Jun. 23, 2022).
[197] Sciex, ‘SelexION Differential Mobility’. https://sciex.com/products/ion-mobility-spectrometry/selexion-differential-mobility-separation-device.html (accessed Jun. 23, 2022).
[198] Waters, ‘High Field Asymmetric Waveform Ion Mobility Spectrometry (FAIMS) for Waters® Micromass® Mass Spectrometers’, *www.waters.com*. http://www.waters.com/waters/library.htm?lid=1545440 (accessed Jun. 23, 2022).
[199] F. Lanucara, S. W. Holman, C. J. Gray, and C. E. Eyers, ‘The power of ion mobility-mass spectrometry for structural characterization and the study of conformational dynamics’, *Nat. Chem.*, vol. 6, no. 4, pp. 281–294, Apr. 2014, doi: 10.1038/nchem.1889.
[200] A. A. Shvartsburg, F. Li, K. Tang, and R. D. Smith, ‘Distortion of Ion Structures by Field Asymmetric Waveform Ion Mobility Spectrometry’, *Anal. Chem.*, vol. 79, no. 4, pp. 1523–1528, Feb. 2007, doi: 10.1021/ac061306c.
[201] Assoc. Prof. Dr. P. Intra and N. Tippayawong, ‘An overview of differential mobility analyzers for size classification of nanometer-sized aerosol particles’, *Songklanakarin J. Sci. Technol.*, vol. 30, no. 2, pp. 243–256, Mar. 2008.
[202] V. Pomareda, S. Lopez-Vidal, D. Calvo, A. Pardo, and S. Marco, ‘A novel differential mobility analyzer as a VOC detector and multivariate techniques for identification and quantification’, *Analyst*, vol. 138, no. 12, pp. 3512–3521, May 2013, doi: 10.1039/C3AN00078H.
[203] S. M. Zucker, M. A. Ewing, and D. E. Clemmer, ‘Gridless Overtone Mobility Spectrometry’, *Anal. Chem.*, vol. 85, no. 21, pp. 10174–10179, Nov. 2013, doi: 10.1021/ac401568r.
[204] R. T. Kurulugama, F. M. Nachtigall, S. Lee, S. J. Valentine, and D. E. Clemmer, ‘Overtone mobility spectrometry: Part 1. Experimental observations’, *J. Am. Soc. Mass Spectrom.*, vol. 20, no. 5, pp. 729–737, May 2009, doi: 10.1016/j.jasms.2008.11.022.
[205] S. Valentine, S. Stokes, R. Kurulugama, F. Nachtigall, and D. Clemmer, ‘Overtone Mobility Spectrometry: Part 2. Theoretical Considerations of Resolving Power’, *J. Am. Soc. MASS Spectrom.*, vol. 20, no. 5, pp. 738–750, May 2009, doi: 10.1016/j.jasms.2009.01.001.
[206] S. Valentine, R. Kurulugama, and D. Clemmer, ‘Overtone Mobility Spectrometry: Part 3. On the Origin of Peaks’, *J. Am. Soc. MASS Spectrom.*, vol. 22, no. 5, pp. 804–816, May 2011, doi: 10.1007/s13361-011-0087-y.

[207] M. Ewing, S. Zucker, S. Valentine, and D. Clemmer, ‘Overtone Mobility Spectrometry: Part 5. Simulations and Analytical Expressions Describing Overtone Limits’, *J. Am. Soc. MASS Spectrom.*, vol. 24, no. 4, pp. 615–621, Apr. 2013, doi: 10.1007/s13361-012-0559-8.
[208] J. Zeleny, ‘VI. On the ratio of the velocities of the two ions produced in gases by Röntgen radiation, and on some related phenomena’, *Lond. Edinb. Dublin Philos. Mag. J. Sci.*, vol. 46, no. 278, pp. 120–154, Jul. 1898, doi: 10.1080/14786449808621173.
[209] A. Loboda, ‘Novel ion mobility setup combined with collision cell and time-of-flight mass spectrometer’, *J. Am. Soc. Mass Spectrom.*, vol. 17, no. 5, pp. 691–699, May 2006, doi: 10.1016/j.jasms.2006.01.013.
[210] A. V. Loboda, ‘Setup for mobility separation of ions implementing an ion guide with an axial field and counterflow of gas’, US6630662B1, Oct. 07, 2003 Accessed: Jun. 24, 2022. [Online]. Available: https://patents.google.com/patent/US6630662B1/en
[211] F. Fernandez-Lima, D. A. Kaplan, J. Suetering, and M. A. Park, ‘Gas-phase separation using a trapped ion mobility spectrometer’, *Int. J. Ion Mobil. Spectrom.*, vol. 14, no. 2, pp. 93–98, Sep. 2011, doi: 10.1007/s12127-011-0067-8.
[212] D. R. Hernandez, J. D. DeBord, M. E. Ridgeway, D. A. Kaplan, M. A. Park, and F. Fernandez-Lima, ‘Ion dynamics in a trapped ion mobility spectrometer’, *Analyst*, vol. 139, no. 8, pp. 1913–1921, Mar. 2014, doi: 10.1039/C3AN02174B.
[213] J. A. Silveira, K. Michelmann, M. E. Ridgeway, and M. A. Park, ‘Fundamentals of Trapped Ion Mobility Spectrometry Part II: Fluid Dynamics’, *J. Am. Soc. Mass Spectrom.*, vol. 27, no. 4, pp. 585–595, Apr. 2016, doi: 10.1007/s13361-015-1310-z.
[214] K. Michelmann, J. A. Silveira, M. E. Ridgeway, and M. A. Park, ‘Fundamentals of Trapped Ion Mobility Spectrometry’, *J. Am. Soc. Mass Spectrom.*, vol. 26, no. 1, pp. 14–24, Jan. 2015, doi: 10.1021/jasms.8b04886.
[215] F. C. Liu, M. E. Ridgeway, M. A. Park, and C. Bleiholder, ‘Tandem trapped ion mobility spectrometry’, *Analyst*, vol. 143, no. 10, pp. 2249–2258, May 2018, doi: 10.1039/C7AN02054F.
[216] I. Čermak, ‘AMX250–4E Universeller digital gesteuerter vierfacher Analogschalter/Multiplexer für Spannungen bis 250 V - Bedienungsanleitung Version 1.00’. CGC Instruments, Mar. 07, 2018. Accessed: Jul. 22, 2022. [Online]. Available: https://www.cgc-instruments.com/data/Products/Switches/19-AMX/Preconfigured/19-AMX250-4E_Files/Beschreibung_B.pdf
[217] S. Bandelow, G. Marx, and L. Schweikhard, ‘The stability diagram of the digital ion trap’, *Int. J. Mass Spectrom.*, vol. 336, pp. 47–52, Feb. 2013, doi: 10.1016/j.ijms.2012.12.013.
[218] N. M. Hoffman, Z. P. Gotlib, B. Opačić, B. H. Clowers, and P. T. A. Reilly, ‘A comparison based digital waveform generator for high resolution duty cycle’, *Rev. Sci. Instrum.*, vol. 89, no. 8, p. 084101, Aug. 2018, doi: 10.1063/1.5004798.
[219] D. T. Horn, *Analog switches: applications & projects*, 1st ed. Blue Ridge Summit, PA: TAB Books, 1990.
[220] J. A. Richards, R. M. Huey, and J. Hiller, ‘A new operating mode for the quadrupole mass filter’, *Int. J. Mass Spectrom. Ion Phys.*, vol. 12, no. 4, pp. 317–339, Nov. 1973, doi: 10.1016/0020-7381(73)80102-0.
[221] N. M. Hoffman *et al.*, ‘Digital Waveform Technology and the Next Generation of Mass Spectrometers’, *J. Am. Soc. Mass Spectrom.*, vol. 29, no. 2, pp. 331–341, Feb. 2018, doi: 10.1007/s13361-017-1807-8.
[222] G. F. Brabeck and P. T. A. Reilly, ‘Mapping ion stability in digitally driven ion traps and guides’, *Int. J. Mass Spectrom.*, vol. 364, pp. 1–8, May 2014, doi: 10.1016/j.ijms.2014.03.008.

[223] W. Demtröder, *Experimentalphysik. 2: Elektrizität und Optik: mit 19 Tabellen, zahlreichen durchgerechneten Beispielen und 145 Übungsaufgaben mit ausführlichen Lösungen*, 4., Überarb. u. erw. Aufl. Berlin [u.a]: Springer, 2006.
[224] D. Staelin H., '3.5: Two-element circuits and RLC resonators', *Physics LibreTexts*, Mar. 05, 2022. https://phys.libretexts.org/Bookshelves/Electricity_and_Magnetism/Electromagnetics_and_Applications_(Staelin)/03%3A_Electromagnetic_fields_in_simple_devices_and_circuits/3.05%3A_Two-element_circuits_and_RLC_resonators (accessed Aug. 31, 2022).
[225] R. E. Pedder, 'Practical Quadrupole Theory: Graphical Theory', *Extrel Appl. Note*, vol. RA2010E, p. 5, May 2001.
[226] T. K. Esser, J. Böhning, P. Fremdling, T. Bharat, J. Gault, and S. Rauschenbach, 'Cryo-EM samples of gas-phase purified protein assemblies using native electrospray ion-beam deposition', *Faraday Discuss.*, Sep. 2022, doi: 10.1039/D2FD00065B.
[227] D. J. Douglas, 'Mechanism of the collision-induced dissociation of polyatomic ions studied by triple quadrupole mass spectrometry', *J. Phys. Chem.*, vol. 86, no. 2, pp. 185–191, Jan. 1982, doi: 10.1021/j100391a011.
[228] R. G. Cooks, Ed., *Collision Spectroscopy*. Springer US, 1978. doi: 10.1007/978-1-4613-3955-7.
[229] E. F. Pettersen *et al.*, 'UCSF ChimeraX: Structure visualization for researchers, educators, and developers', *Protein Sci.*, vol. 30, no. 1, Art. no. 1, 2021, doi: 10.1002/pro.3943.

8. Table of Figures

Figure 1: Principle of Electrospray ion beam deposition (ES-IBD). Process steps: a) Electrospray ionisation and transfer into the gas phase. b) Mass-to-charge filtering in vacuum. c) Energy- and amount-controlled deposition onto a substrate.....14

Figure 2: Common RF ion optics. a) Quadrupole b) Octupole c) Stacked-ring ion guide. The blue and red colour of the electrodes symbolise the two RF phases.....19

Figure 3: Rapid oscillating motion, the secular motion, in an RF field leads to a smooth drift motion. a) In an homogenous electric field, the smooth drift motion follows a straight line. b) In an inhomogeneous RF field, the secular motion influences the trajectory of an ion.....21

Figure 4: Adiabaticity parameter for the central plane of a gas-filled ion optic, an ion funnel. Typical operation parameters ν_{RF} = 1 MHz, V_{RF} = 60 V, m = 443 u and q = 1 e (Rhodamine B). y = 0 is a symmetry plane.....25

Figure 5: Correction factor for the effective force to account for gas presence according to Bernier 2020. Four probe ions at typical operation conditions are shown.....27

Figure 6: Trajectories of 20 hexamethoxyphosphazene ions at 3 mbar in an RF ion optic. a) SDS with no diffusion: fully deterministic trajectories b) unmodified SDS diffusion, starting conditions do not fully determine trajectories c) at least 10^5 collisions per diffusion step, 40x diffusion length. The difference between the trajectories is well visible in the blue circle.....34

Figure 7: Schematic view of the Q Exactive UHMR mass spectrometer modified for deposition. Custom landing stage to deposit two microscopy samples and measure energy on the left. UHMR with improved source for better transmission on the right.....43

Figure 8: Beam-energy distribution measured for denatured and native BSA ion beams for two different potential gradient settings as shown in Fig. 61b. Dots: Ion current measured as function of the retarding grid potential $I(U_{bias})$. Lines: Gaussian fit for first derivative dI/dU_{bias}, corresponding to the total beam energy per charge (E_{tot}) in eV per charge. FWHM is given in parentheses.....47

Figure 9: Transmission properties. a) Ion current across the instrument before and after increasing the S-exit-lens diameter, measured at different ion optics. b) Typical ion currents at the energy detector for different S-lens diameters. (Values equivalent to sample currents). Protein ion currents increase with aperture size. RhoB currents don't follow the trend, due to a defocusing effect. Currents on preceding optical element are shown in light colours. c) Native BSA currents on energy detector (Det.) and aperture (Ap.) decrease with the narrowing width of the mass filter window.....49

Figure 10: Ion Beam Shape Analysis: a) Ion-beam image of the sample holder front plate. b) Sample holder section view: Different voltages influence focusing. c) Ion-beam shape from deconvolution of a. d) Data points and Gaussian fit of ion-beam intensity distribution. e) HOPG sample used for AFM measurements and protein density distribution in the screened area. f) Measured protein distribution on e (black dots), Gaussian fit (blue), and single monolayer model (orange). g) Amorphous carbon grid used for TEM measurements and protein density distribution in particles per µm². h) Gaussian fit (blue) of density distribution in g. Individual AFM and TEM micrographs are shown in Fig. 64 in the SI.....52

Figure 11: Native BSA (red) and denatured BSA (yellow) mass spectra and height histograms. Spray solution composition: Native 200mM NH_4Ac, denatured 73:24:3 MeOH:H_2O:HCOOH.

a) Mass spectra for native (filter window 2000...5000 m/z) and denatured (1250...1700 m/z) BSA. b) Resulting height distribution measured with AFM after soft-landing on HOPG. Native BSA sample size = 47, denatured BSA = 60.....55

Figure 12: Negative-stain and cryo-EM micrographs of apo/holo-ferritin and GroEL after gas-phase purification and gentle deposition on TEM grids. a) Apo/holo-ferritin, landing energy of 5 eV per charge, 30 nm amorphous carbon film, stained with uranyl acetate. b) Apo/holo-ferritin, landing energy of 2 eV per charge, 3 nm amorphous carbon film, plunge-frozen in liquid nitrogen. c, d) GroEL, landing energy of 2 eV, 100 eV per charge, 3 nm amorphous carbon film, plunge-frozen in liquid nitrogen. The insets show 3D models from the PDB (blue), rendered with ChimeraX[229] using PDB entries 7A6A for apoferritin and 5W0S for GroEL, and 2D classes of native ES-IBD samples (green) obtained using RELION 3.1. The number of particles in the 2D classes is given in the insets.....58

Figure 13: a) Mass spectra of deposited, mass-selected ADH tetramer. Inset: Colour change from yellow to orange indicates an active ADH in the lower well. The black objects on the well's walls are the submerged ADH-coated conductive tapes. b) Production of NADH by ADH after ES-IBD. The broken lines stagnating at the offset level are background controls, so the NADH production is specific for ADH activity. The absorbance measurement causes two separate artificial saturation levels due to different calibrations.....61

Figure 14: Structure of a very highly underexpanded jet. M is the Mach number[144].....74

Figure 15: a) Comparison of the radial effective potential of an Octupole and a SRIG for hexamethoxyphosphazene in high vacuum. Both ion guides have 20 mm trap radius. RF Amplitude = 80 V, ν=1 MHz, no DC gradient. b) 3D Projection of the effective potential across the centre plane of the SRIG. Valleys are electrode positions, maxima appear at the edges of the electrodes and have been smoothed.....75

Figure 16: Schematic of a) a skimmer and of b) an ion funnel (right).....76

Figure 17: Funnel geometry and measurement setup used to determine transmission efficiency.....83

Figure 18: a) Transmitted current and b) transmission ratio for 3 different pressures as a function of the RF amplitude. Measured on the conventional 82-electrode funnel.....85

Figure 19: a) Effective Potential in HV in the centre plane of the existing ion funnel. y is the radial coordinate, z the axial. b) Effective potential force in the centre plane in HV. Final two electrodes are shown.....88

Figure 20: Offset-corrected transmitted current as a function of the entering current. Entering current varied with different emitter positions. Measured on the existing 82-electrode funnel. The slope corresponds to the transmission ratio.....89

Figure 21: a) Transmitted current through the existing ion funnel as a function of the axial DC gradient for 1 mbar and two different initial transfer capillary temperatures. b) Relative transmission normalised to the maximum value for each series as a function of the DC gradient.....92

Figure 22: a) Transmitted current through the existing ion funnel as a function of the axial DC-Gradient for 1, 3 and 10 mbar. b) Relative transmission normalised to the maximum value for each series as a function of the DC-Gradient.....93

Figure 23: Simion simulation of 80 hexamethoxyphosphazene ions in a parabolic funnel at 3 mbar pressure. Transmission for different RF-Amplitudes: a) 0 V b) 100 V c) 300 V. Little red

squares mark points of ion velocity reversal. d) Transmission ratio as a function of the RF-amplitude. 3 mbar measurement of existing funnel added with a factor of 1.95 to compare...96

Figure 24: Velocity field for ion funnel geometry A. Computed by solving the compressible Navier-Stokes equation numerically in 2D. Algorithm: Prof. Julius Reiss & Laurent Bernier 97

Figure 25: Ion trajectory simulation of hexamethoxyphosphazene, apomyoglobin and GroEL. Gas interaction model Simion SDS. 1.8 mbar pressure at pump, ν_{RF} = 400 kHz.....99

Figure 26: Trajectories (top) and exemplary trajectory velocities (bottom) of one transmitted GroEL ion at 1.8 mbar (a) and 5.4 mbar (b). At 1.8 mbar, insufficient gas damping leads to a rapid change of radial (r1 ⊥ r2) velocity of GroEL in the final section on the walls. At 5 mbar, this tumbling motion disappears.....100

Figure 27: Number of gas-ion collisions in 1 mm flight path divided by ion mass. GroEL needs 30 mbar pressure to have the same number of collisions per mass as hexamethoxyphosphazene at 1.8 mbar.....102

Figure 28: a) CFD simulation of the velocity field in ion funnel geometry D. Simulation not fully converged, image courtesy of Laurent Bernier. With a rocket-nozzle-shaped capillary outlet, the supersonic flow extends nearly to the funnel exit. b) Shock diamond structure visible in the afterburner exhaust jet of a turbofan engine of a c) F-16 plane taking off. Photographs b) and c) Tech. Sgt. Caycee Cook, public domain.....104

Figure 29: a) 80 hexamethoxyphosphazene trajectories with a rocket-engine-shaped capillary outlet (funnel D). ν_{RF} = 1 MHz, V_{RF} = 200 V, pumping pressure 1 mbar. b) Pressure in the final section, where the supersonic jet collides with the electrodes. Overlay: trajectories. The gas velocity decreases and pressure increases to 15 mbar. Ion mobility reduces, so the RF is insufficient to keep hexamethoxyphosphazene away from the last electrode.....105

Figure 30: a) Radial coordinate of the hexamethoxyphosphazene ion losses. b) Axial (z)-force in HV for hexamethoxyphosphazene in funnel D (ν_{RF} = 1 MHz, V_{RF} = 200 V, DC gradient for last 4 electrodes 50V). White arrow at r = 2.6 mm.....106

Figure 31: Effective potential for GroEL in funnel A for different electrode spacings. U_{RF} = 130 V, ν_{RF} = 400 kHz. a) Absolute effective potential assuming HV conditions as function of the radius. The data has been corrected for the differing cavity diameter so that the electrode rim is at 10 mm for all spacings. b) Normalised effective potential. The decrease for the 10 mm curve at r > 12 mm is a consequence of the wall potential (0 V) penetrating in the inter-electrode space c) Fit of the maximum value as function of the electrode spacing.....108

Figure 32: Effective potential of the final 20 electrodes of the existing ion funnel in RF-only mode, assuming HV. a) 3D-projection b) Slice along the central axis. Parameters: ν_{RF} = 1 MHz, V_{RF} = 60 V, Rhodamine B.....111

Figure 33: a) Effective potential assuming HV conditions along the central axis in the existing funnel a) in RF only mode versus a -150 V DC gradient and b) with a linear gradient compared to a non-linear -75 V gradient. Curvature at z > 30 mm is due to only first 20 electrodes modelled. ν_{RF} = 1 MHz, V_{RF} = 60 V, Rhodamine B.....113

Figure 34: Effective potential along the central symmetry axis in funnel A for hexamethoxyphosphazene and GroEL. ν_{RF} = 400 kHz, V_{RF} = 130 V, uniform gas velocity of 10 m/s towards the exit. Effective potential for a) RF only b) with the minimum necessary DC gradient to overcome the RF trapping. c) Trajectories of 80 GroEL in RF only mode and d) with a 3 V DC gradient at above conditions.....115

Figure 35: Main stages of ion funnel transmission: a) Acceleration in supersonic expansion b) Collisional cooling c) Ion transport d) Extraction.....120

Figure 36: a) Schematic view of the 2-step interface. First ion optic is a multipole (n=2, 3 or 4) with thinnest rods to minimise disruption of the gas flow. In there and around, the supersonic expansion takes place. Gas and ion separation take place in the supersonic expansion. Ions are recollimated by the gas flow and transferred into a second chamber, where the remaining gas is removed in a conventional funnel. b) Possible estimated pressure on the central axis.....123

Figure 37: a) Cut-open view of an octupole placed in the supersonic expansion. 80 Hexamethoxyphosphazene trajectories at p_{pump}= 1.8 mbar, ν_{RF} = 800 kHz, V_{RF} = 150 V. b) Trajectories of 80 Apomyoglobin ions at p_{pump}= 18 mbar (artificially increased), ν_{RF} = 500 kHz, V_{RF} = 200 V. Only electrodes in vertical plane are visible. Blue lines: isobars in 4 mbar steps.....125

Figure 38: 'Inverted porcupine' schematic instrument overview. The preparative ion mobility mass spectrometer consists of two modules A and B. A produces a mass- and mobility filtered ion beam. B analyses the mass and mobility domain.....131

Figure 39: 2-section funnel for optimal usage of pump. a) Scheme with electrode spacing. b) Expected pressure along the central axis. c) Simion model of the electrodes.....134

Figure 40: Trajectories of 6 hexamethoxyphosphazene ions in the 'inverted porcupine' funnel. ν_{RF} = 1 MHz, V_{RF} = 110 V (rectangular), p = 3 mbar.....136

Figure 41: Effective potential on the 'inverted porcupine' funnel axis for hexamethoxyphosphazene. ν_{RF} = 1 MHz, V_{RF} = 110 V. Of the 153 V DC gradient over the full ion funnel, 30 V are applied to the final four electrodes.....137

Figure 42: Recommended DC Gradients for the transmission of hexamethoxyphosphazene at ν_{RF} = 1 MHz, V_{RF} = 110 V. Electrode taps are marked with the number of the corresponding electrode.....138

Figure 43: Inverted porcupine funnel. a) Top view b) view from Ion mobility filter side c) view from transfer capillary side. Photos: Moritz Edte.....138

Figure 44: Principle of the high-pass low-pass parallel flow mobility filter. The high-pass filter transports ions of high mobility (pass indicated with "✓") with an electric field against a counter-gas flow. The low pass filter only transmits ions of low mobility entrained by the gas flow. Together, they transmit ions within a clearly defined mobility range.....144

Figure 45: Projection of the gas velocity and the electric field on the z-axis. Example is for low-pass filter and a positive ion.....146

Figure 46: Key parameters along the mobility filter central axis. a) Pressure. b) Gas velocity. c) Electric field d) Critical reduced mobility. Transmission only for ions with $K_{0,crit,\ high\ pass} < K_{0,crit} < K_{0,crit,\ low\ pass}$ e) DC Potential.....150

Figure 47: Mobility filter ion trajectory simulation. 3 x 16 ions with K_0 of 0.62 (blue, low), 0.69 (green, medium) and 0.78 (red, high mobility) $cm^2V^{-1}s^{-1}$. ν_{RF} = 400 kHz, V_{RF} = 140 V (rectangular). Kill locations: dark-blue (43 mm) and light-blue (50 mm) arrow for low mobility blue ion, red arrow (248 mm) for high mobility red ion.....152

Figure 48: Mobility filter ion trajectory simulation at three different RF frequencies. ν_{RF} = a) 600 kHz, b) 500 kHz c) 400 kHz. 3 x 16 ions with K_0 of 0.62 (blue, low), 0.69 (green, medium) and 0.78 (red, high mobility) $cm^2V^{-1}s^{-1}$. V_{RF} = 140 V (rectangular).....153

Figure 49: RF Phase distribution of the electrodes at the stack-ring/quadrupole interface. Blue is phase 1, red phase 2.....153

Figure 50: Effective potential for the blue ion assuming high vacuum in the mobility filter in the xy-plane at a) 39.4 mm and b) 40.8 mm. The effective force at the same conditions at c) 39.4 mm and d) 40.8 mm.....154

Figure 51: Built ion mobility filter. a) Section filter 1, which houses the high-pass filter, the gas inlet and the beginning of the low-pass filter. b) Section filter 2, which houses the remaining length of the low-pass filter. Both sections are connected at the interface filter 1/2. Photos: Moritz Edte.....157

Figure 52: Mechanical construction scheme of the mobility filter. The mechanical separation between Filter 1 and Filter 2 (see Figure 51) is in the low-pass section. A common 100 m³/h screw pump pumps both the high- and low-pass filter. The gas flow speed and -pressure can be set independently via two choking valves and the gas inlet pressure.....158

Figure 53: Implemented DC gradient and location of the DC taps for mobility filtering of an ion with K_0 = 0.7 $cm^2V^{-1}s^{-1}$. The voltages between the taps are necessary to mobility-filter (red, upper row) or transport (black, lower row) a small organic ion.....159

Figure 54: Maximum RF amplitude for the ion mobility filter and the RF-only quadrupole Q3. The load capacities and with it the maximum RF amplitudes of the other ion optics are between these two extremes.....164

Figure 55: Mass filtering to separate hexamethoxyphosphazene ions (green, 322 m/z) from ions with 310 m/z (red) and 332 m/z (blue). ν_{RF} = 904 kHz, V_{RF} = 225 V (rectangular). The differential DC on opposite rod pairs of 47 V causes the mass-to-charge filtering and is only applied to central section. ΔE_{kin} is FWHM.....165

Figure 56: Trajectory simulation of 100 hexamethoxyphosphazene ions to investigate beam decoupling from high pressure to high vacuum. a) Weak gradient conditions. Initial energy distribution: E_{tot} = -99.7 eV, FWHM = 0.13 eV b) Strong gradient conditions. Initial energy distribution: E_{tot} = -99.9 eV, FWHM = 0.16 eV. Equipotential lines mark range from -100 to -130 V in 3 V steps. c) Assumed pressure in the cavity. d) Measured pressure in the gate-valve cavity and QMS chamber as a function of the pressure in Q3. e) Resulting total energy distribution. Ions with E_{tot} < -120 eV have been omitted for better clarity.....168

Figure 57: Preparative mass spectrometer 'inverted porcupine'. a) Top view. Visible are the collision cell Q3 (a1), the mass-selective quadrupole QMS (a2), the quadrupole Q1 (a3), filter 2 (a4), filter 1 (a5) and the RF power switches (a6). b) The mass spectrometer (b1) and its auxiliary units: The DC power supplies and picoammeters (b2), the fore pumps for the mobility filter and the quadruple chambers (b3), the roots blower/rotary vane pumping station which pumps the ion funnel (b4) and the water cooling supply (b5). c) Side view. Visible are the high-accuracy capacitance diaphragm gauges (c1), the gate valve (c2) and the ion funnel (c3).....170

Figure 58: Comparison of protein complex shapes obtained from ice-free native ES-IBD samples by cryo-EM (IBD 2D and IBD SP) with literature data. The ES-IBD samples were deposited with the commercial mass spectrometer I modified (chapter 3). Graphic reproduced from Esser et. al. 2022.[226].....173

Figure 59: Trajectories of 80 GroEL ions at the critical pressure $p_{V^*,crit}$ of 68 mbar. Simulation of the gas pressure with Simion SDS. Initial kinetic energy: a) 1/3 of the potential barrier V* b) 3x the potential barrier V*. A 5 m/s gas flow towards the rectangular target was applied to better distinguish between confined ions and ions lost on the quadrupole rods. Quadrupole

trap diameter: 2 mm. V_{RF} = 200 V, ν_{RF} = 400 kHz. Adiabaticity inside the guide just below 0.3. 201

Figure 60: Number of collisions in 1 mm flight path length as a function of pressure. Calculated with the kinetic theory of gas.....202

Figure 61: DC Potentials applied within a the mass spectrometer and b the custom landing stage for higher and lower DC gradients.....206

Figure 62: Kinetic energy loss per collision in N_2 for BSA (mass 66500 u) and Iodine (mass 127 u) as a function of the scattering angle. Minimum for BSA is 0.99832 at 180°.....207

Figure 63: Mass spectra of a denatured BSA and b native BSA. Both mass spectra are acquired with non-activating conditions used for deposition.....208

Figure 64: Exemplary AFM and TEM data for the beam shape characterization. a) and b) show low (250 particles per µm²) and high (1500 particles per µm²) density areas on the TEM grid. c) shows an area in the centre of the deposition spot with more than monolayer coverage. Therefore, the line profile d) shows no well-defined baseline. e) shows a less dense area with 4 particles per µm². The corresponding line profile f) shows a clear baseline and allows to determine the particle heights.....209

Figure 65: Native BSA on HOPG imaged with ambient AFM.....210

Figure 66: Denatured BSA on HOPG imaged with ambient AFM.....210

Figure 67: Negative stain apo/holo-ferritin control sample. The 2D classes show the same characteristic features as observed for the native ES-IBD samples, though they are better defined and there is less deformation in the control, despite the lower number of particles.. 211

Figure 68: Assay-buffer-extraction of 128 pAh deposited ADH on EM grid with either vortex or sonication yields blank activity. The same applies for washing-off 175 pAh deposited ADH on EM grids. We tried to wash ADH off by moving the deposited grid around with tweezers in ADH buffer.....213

Figure 69: Submersion of an EM-grid in assay reaction mix causes a strong increase in absorbance, conductive tape doesn't.....213

Figure 70: Production of NADH by ADH after electrospray deposition at atmospheric pressure. The broken lines stagnating at the offset level are background controls, so the NADH production is specific for ADH activity.....214

Figure 71: 128 pAh deposition (repetition C) retains no activity after 3 day storage in vacuum. The corresponding control was inactive as well, but showed a high absorbance due to the conductive tape having moved into the beam path (see Fig. 72).....214

Figure 72: Left: 3 day storage background control (repetition C) moved into plate reader optical path. Note the liquid is still yellow, meaning no reaction has occurred during incubation. Right: 2D scan of bottom well confirms absorbance is still at blank level after incubation.....215

Figure 73: Mass spectra of the ADH beam prior and after 5000...7000 m/z filtering. The mass-selected beam was used for deposition.....215

Figure 74: Scheme of the 2D-scan used to characterise the ion beam diameter on the front plate. A single picoammeter measures the current on the sample holder front plate. The data is recorded as a function of the deflection voltages applied to the electrostatic steering lens. The recorded current data can be represented as a 2d map. This shows an ion current image of the

front plate. The 2D-scan function is also routinely used to find the sample (dark pink) and energy detector (light pink) positions.....216

Figure 75: a) Transmitted current and b) transmission ratio at 1, 3, 10 and 22 mbar measured with the existing conventional ion funnel.....217

Figure 76: a) Transmitted current and b) transmission ratio for three measurement series at 1 mbar. Causes are an unstable emitter for two sets, and once I forgot to switch the capillary heating off. 200 VRF value is an outlier as a plasma ignited.....217

Figure 77: Radial effective force along r = 1.1 mm for the existing ion funnel.....218

Figure 78: Funnel A section view.....219

Figure 79: Funnel D section view.....219

Figure 80: Trajectories of 80 GroEL ions with gas interaction in the funnel geometry A at a) 1.8 mbar, b) 5.4 mbar and c) 54 mbar pumping pressure. The 1.8 mbar pressure flow field was used for all simulations, but multiplied by 3 (b) and 30 (b). RF-parameters: a) and b): V_{RF} = 130 V, ν_{RF} = 400 kHz. c) V_{RF} = 80 V, ν_{RF} = 200 kHz.....220

Figure 81: Pressure field for ion funnel geometry A. Computed by solving the compressible Navier-Stokes equation numerically in 2D. Algorithm: Prof. Julius Reiss & Laurent Bernier 220

Figure 82: CFD simulation of the pressure field in ion funnel geometry D. Simulation not fully converged, image courtesy of Laurent Bernier. With a rocket-nozzle-shaped capillary outlet a shock-diamond structure forms (axial coordinates: 6.5, 10.5 and 14 cm).....221

Figure 83: Effective Potential in Funnel A. a) Effective potential for different electrode spacings as a function of the funnel radius. b) Effective potential as a function of the axial coordinate at r = 23 mm. Note that with increasing electrode spacing the effective potential has local minima between two electrodes. Differing values between 10 mm and 50 mm (2.5 mm electrode spacing) are due to the limited resolution of the Simion workbench (0.2 mm/grid unit, so electrode spacing varied from 2.4 to 2.6 mm).....221

Figure 84: Effective axial force for rhodamine B in RF only mode in the existing ion funnel. Parameters: ν_{RF} = 1 MHz, V_{RF} = 60 V, assuming vacuum. The correction factor to account for a gas pressure of 1 mbar is 0.88.....222

Figure 85: Trajectories of 80 hexamethoxyphosphazene ions at p_{pump}= 5.4 mbar (artificially increased), ν_{RF} = 800 kHz, V_{RF} = 300 V. Only electrodes in vertical plane are visible. Blue lines: isobars in 1.6 mbar steps.....222

Figure 86: Example for a .pa+ file. The yellow arrows mark the columns which address the original electrodes 1,2,3 etc. created in the .gem file. The new scalable potential array combines them to a set of three electrode solutions. Line [1] is RF+, line [2] is RF- and line [3] is DC. They can be independently scaled.....223

Figure 87: Structure formula of three molecules used for the ion mobility filter trajectory simulation. The structures a) red b) green and c) blue show the neutral molecules, not the ions, which have an additional proton.....233

Figure 88: Extract of the laboratory book of the ‘inverted porcupine’. It shows the first test of the high-pass mobility filter. With an increased DC-gradient, the beam can be transmitted against a gas counterflow.....235

9. Index of Tables

Table 1: Mass-to-charge ratio, particle response time at standard pressure and critical pressure the effective potential approximation for four probe ions. * denotes calculated values.....26

Table 2: Mass to charge ratio, CCS, reduced mobility in nitrogen and particle response time for used ions. "*" denotes calculated values.....84

Table 3: RF and DC coefficients for hexamethoxyphosphazene and GroEL.....116

Table 4: Charge, mass-to-charge ratio and reduced mobility for three phosphazene probe molecules. As no common names are available, they have been colour-coded. Hexamethoxyphosphazene and GroEL shown for comparison. * denotes calculated values 151

Table 5: Main geometric parameters of the mobility filter sections.....156

Table 6: Transmitted currents with a 10^{-6} mol·L^{-1} rhodamine B solution for the 'inverted porcupine'.....171

Table 7: Potentials applied to ion optics when measuring current. Emitter potential is for nano-spray setup.....208

Table 8: Geometry summary of ion funnel geometries A and D. n is the electrode number. See also Figure 78 and Figure 79 for a section view.....218

10. Acronyms

ADH	**A**lcohol **d**e**h**ydrogenase
AFM	**A**tomic **f**orce **m**icroscopy
AP-MALDI	**A**tmospheric **p**ressure **m**atrix **a**ssisted **l**aser **d**esorption and **i**onisation
APCI	**A**tmospheric **p**ressure **c**hemical **i**onisation
BSA	**B**ovine **s**erum **a**lbumin
CCS	**C**ollisional **c**ross-**s**ection
CFD	**C**omputation **f**luid **d**ynamics
Cryo-EM	**C**ryo **e**lectron **m**icroscopy
DC	**D**irect **c**urrent
DMA	**D**ifferential **m**obility **a**nalyser
EM	**E**lectron **m**icroscopy
ES-IBD	**E**lectro**s**pray **i**on **b**eam **d**eposition
ESI	**E**lectro**s**pray **i**onisation
EU	**E**uropean **U**nion
FAIMS	**F**ield **a**symmetric wave-form **i**on **m**obility **s**pectrometry
FWHM	**F**ull **w**idth at **h**alf **m**aximum
GND	Electrical **G**rou**nd**
HCD	**H**igher Energy **C**ollisional **D**issociation
HOPG	**H**ighly **o**riented **p**yrolytic **g**raphite
HV	**H**igh **v**acuum
IMS	**I**on **m**obility **s**pectrometry
LEEH	**L**ow **e**nergy **e**lectron **h**olography
MALDI	**M**atrix **a**ssisted **l**aser **d**esorption and **i**onisation
MBE	**M**olecular **b**eam **e**pitaxy
MPI-FKF	**M**ax-**P**lanck-**I**nstitut für **F**es**t**körper**f**orschung
MS	**M**ass **s**pectrometry or **M**ass **s**pectrometer

NADH	**N**icotinamide **a**denine **d**inucleotide-**H**
OMBE	**O**rganic **m**olecular **b**eam **e**pitaxy
OMS	**O**vertone **m**obility **s**pectrometry
PBS	**P**hosphate-**b**uffered **s**aline
PDB	**P**rotein **d**ata **b**ank
PP	**P**oly**p**ropylene
Q	**Q**uadrupole
QMS	**Q**uadrupole **m**ass **f**ilter
RF	**R**adio **f**requency
SDS	**S**tatistical **d**iffusion **s**imulation
Si-MOSFET	**Si**licon **m**etal–**o**xide–**s**emiconductor **f**ield-**e**ffect **t**ransistor
SPM	**S**canning **p**robe **m**icroscopy
SRIG	**S**tacked-**r**ing-electrode **i**on **g**uide
STM	**S**canning **t**unnelling **m**icroscopy
TEM	**T**ransmission **e**lectron **m**icroscopy
TK	Turner-Kruger (lens)
ToF	**T**ime **o**f **f**light mass analyser
UHMR	Thermo scientific Q-Exactive **u**ltra-**h**igh **m**ass **r**ange mass spectrometer
UHV	**U**ltra **h**igh **v**acuum
USA	**U**nited **S**tates of **A**merica
V_{RF}	**RF** Amplitude

11. Appendix

11.1 Limits of the effective potential approximation

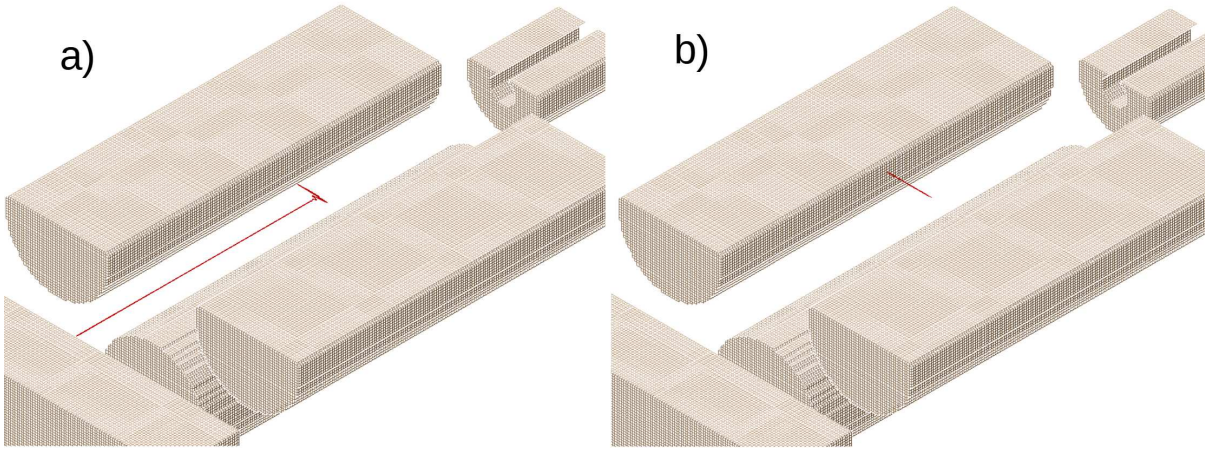


Figure 59: Trajectories of 80 GroEL ions at the critical pressure $p_{V^*,crit}$ of 68 mbar. Simulation of the gas pressure with Simion SDS. Initial kinetic energy: a) 1/3 of the potential barrier V b) 3x the potential barrier V*. A 5 m/s gas flow towards the rectangular target was applied to better distinguish between confined ions and ions lost on the quadrupole rods. Quadrupole trap diameter: 2 mm. V_{RF} = 200 V, ν_{RF} = 400 kHz. Adiabaticity inside the guide just below 0.3.*

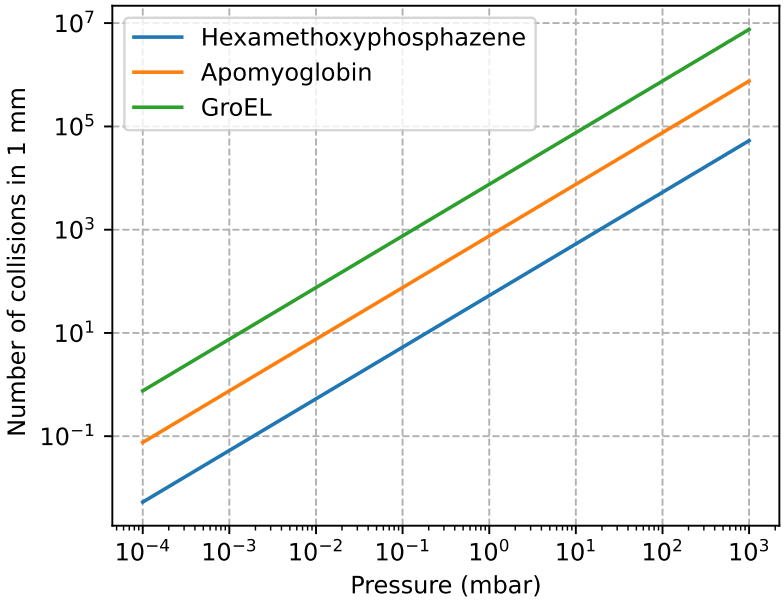


Figure 60: Number of collisions in 1 mm flight path length as a function of pressure. Calculated with the kinetic theory of gas.

11.2 SDS integration

Lua-script to integrate a numerical gas flow field as a Simion potential array

The script requires the data in a text file with one data point per line. Each line has to be in the format ‘axial coordinate’, ‘radial coordinate’ and ‘value’, separated by a white-space string. I consent to any non-commercial use of the below script.

```
-- Script to convert a 2D flowfield into a 2D Simion Potential Array
-- Run via Simion -> Run Lua File
-- All points being in the array from its dimensions but not filled with a value will be either 0 (pressure) or 1 (temperature)
-- Paul Fremdling 14/6/2021

local debugger = false   -- To print additonal information

if debugger == true then
   -- enable 'output' directory exists
   os.execute("mkdir output")

   -- cleanup any old files.
   os.remove("output/results.csv")

   -- Open output files.
   results_file = assert(io.open("output/results.csv", "w")) -- write mode
   results_file:write('Coord1 (gu), Coord2 (gu), Coord1 (m),  Coord2 (m),    Value\n')
end

-- Roundes a float to integer
function round(num)
  return math.floor(num + 0.5)
end

-- From Stackoverflow, separates a string and converts it to a number
-- Returns a table containing an entry for every split section
function mysplit (inputstr, sep)
```

```
28          if sep == nil then
29                  sep = "%s"
30          end
31          local t={}
32          for str in string.gmatch(inputstr, "([^"..sep.."]+)") do
33                  table.insert(t, tonumber(str))
34          end
35          return t
36  end
37
38  -- Intialise a 2D array to hold the flow data
39  -- This is not the cleanest way to do this in lua
40  function intialiseArray(flowfield, firstDMax, secondDMax, wsf, istemp)
41    if istemp == true then
42            zeroValue = 1
43    else
44            zeroValue = 0
45    end
46    for i=0,(round(firstDMax/wsf)) do                          -- first coordinate
47            flowfield[i] = {}                                  -- second coordinate
48            for j=0,(round(secondDMax/wsf)) do
49                    flowfield[i][j] = zeroValue
50            end
51    end
52    -- print(round(firstDMax/wsf),round(secondDMax/wsf))
53    return(flowfield)
54  end
55
56  -- Assigns the values from the textfile to the correct
57  -- position in the 2 D array
58  function readAssignLines(flowfield, filename, div)
59    --local temp = {}
60    for line in io.lines(filename) do
61            t = mysplit(line)
62            -- coord 1 (eg x) = t[1], coord 2 (e.g. r) = t[2], value = t[3]
63            coord1 = round(t[1]/div) -- Get integer coordinates
64            coord2 = round(t[2]/div)
65            flowfield[coord1][coord2] = t[3]
66            if debugger == true then
67                    results_file:write(string.format('% 9.4f, % 9.4f, % 11.6f, % 11.6f, %
9.4f\n',coord1, coord2, t[1], t[2], t[3]))
68                    results_file:flush()  -- immediately output to disk
69            end
70    end
71    if debugger == true then
72            results_file:close()
73    end
74    return flowfield
75  end
76
77  -- Loads the values from the read-in flowfield and then
78  -- converts them into a simion Potential Array
79  -- Scales the values
80  -- Additional x=0 mirroring could be introduced
81  -- The upper limits of the Dimensions are NOT included
82  -- For vectors: save as '_vx.pa' for axial and '_vy.pa' for radial flow
83  -- For temperatures, pressures: save as '_t.pa' or '_p.pa'
84  function convertToPa(savename, flowfield, firstDMax, secondDMax, wsf, scale)
85    local pa = simion.pas:open()
86    -- size must be 1 bigger than dimensions to accomodate 0,0
87    pa:size(round(firstDMax/wsf) + 1, round(secondDMax/wsf) + 1, 1)
88    -- index between brackets are mirror plane, for 2dcylindrical y is default mirror
(hence the radial coord)
89    pa.symmetry = '2dcylindrical'
90    print(pa.symmetry, round(firstDMax/wsf) + 1, round(secondDMax/wsf) + 1)
91    pa.refinable = false
92    for x,y in pa:points() do
93      pa:potential(x,y,0, (flowfield[x][y])*scale)
94    end
95    pa:save(savename)
96  end
97
98
99
100 local flowfield = {}
101 -- Funnel A v2
```

```
-- ax_max        = 178.6       -- max coordinate in axial direction (in mm), not in-
cluded
-- r_max         = 55.5        -- max coordinate in radial direction (in mm), not in-
cluded
-- div           = 0.000174414 -- smallest length divider in flow field coordinates
-- wsf           = 0.174414          -- Workbench scaling factor of new PA
-- multipl       = 1.0               -- factor to multiply the field with (e.g. Pa to
Torr)

-- Funnel D
-- ax_max        = 178.6       -- max coordinate in axial direction (in mm), not in-
cluded
-- r_max         = 55.5        -- max coordinate in radial direction (in mm), not in-
cluded
-- div           = 0.000116352 -- smallest length divider in flow field coordinates
-- wsf           = 0.116352          -- Workbench scaling factor of new PA
-- multipl       = 0.00750062  -- factor to multiply the field with (e.g. Pa to Torr)

-- High pass A
-- ax_max        = 99.8        -- max coordinate in axial direction (in mm), not in-
cluded
-- r_max         = 8                 -- max coordinate in radial direction (in mm), not
included
-- div           = 1                 -- smallest length divider in flow field coordin-
ates
-- wsf           = 0.2         -- Workbench scaling factor of new PA
-- multipl       = 0.750062          -- factor to multiply the field with (e.g. Pa to
Torr)

-- High pass F
ax_max           = 306.6       -- max coordinate in axial direction (in mm), not in-
cluded
r_max            = 8                 -- max coordinate in radial direction (in mm), not
included
div              = 1                 -- smallest length divider in flow field coordin-
ates
wsf              = 0.2         -- Workbench scaling factor of new PA
multipl   = 0.750062           -- factor to multiply the field with (e.g. Pa to Torr)


-- Set always: filename, potential array name, conversion factor, and temperature flag
print('---Conversion----')
flowfield = intialiseArray(flowfield, ax_max, r_max,wsf,false) -- set true if temperature

-- flowfield = readAssignLines(flowfield, 'vz_defs.dat', div)
-- convertToPa('_vx.pa',flowfield, ax_max, r_max, wsf, multipl) -- set correct multiplier

--print(flowfield[3][1])

flowfield = readAssignLines(flowfield, 'p_defs.dat', div)
convertToPa('_p.pa',flowfield, ax_max, r_max, wsf, multipl) -- set correct multiplier
```

11.3 Supporting information: A preparative mass spectrometer to deposit intact large native protein complexes

Paul Fremdling[a], *Tim K. Esser*[a,♪], *Bodhisattwa Saha*[a], *Alexander A. Makarov*[b,c], *Kyle L. Fort*[b], *Maria Reinhardt-Szyba*[b], *Joseph Gault*[a,♫] *and Stephan Rauschenbach*[*,a,d]

a: Chemistry Research Laboratory, Department of Chemistry, University of Oxford, 12 Mansfield Road, Oxford OX1 3TA, United Kingdom
b: Thermo Fisher Scientific, Bremen, 28199, Germany
c: Biomolecular Mass Spectrometry and Proteomics, Bijvoet Center for Biomolecular Research and Utrecht Institute for Pharmaceutical Sciences, University of Utrecht, Padualaan 8, 3584 CH Utrecht, The Netherlands
d: Max Planck Institute for Solid State Research, Heisenbergstrasse 1, Stuttgart DE-70569, Germany
♪: Present address: Thermo Fisher Scientific, 1 Boundary Park, Hemel Hempstead, HP2 7GE, United Kingdom
♫: Present address: Vertex Pharmaceuticals, 86-88 Jubilee Avenue, Milton Park, Abingdon, OX14 4RW, United Kingdom
*: E-mail: stephan.rauschenbach@chem.ox.ac.uk

Beam energy

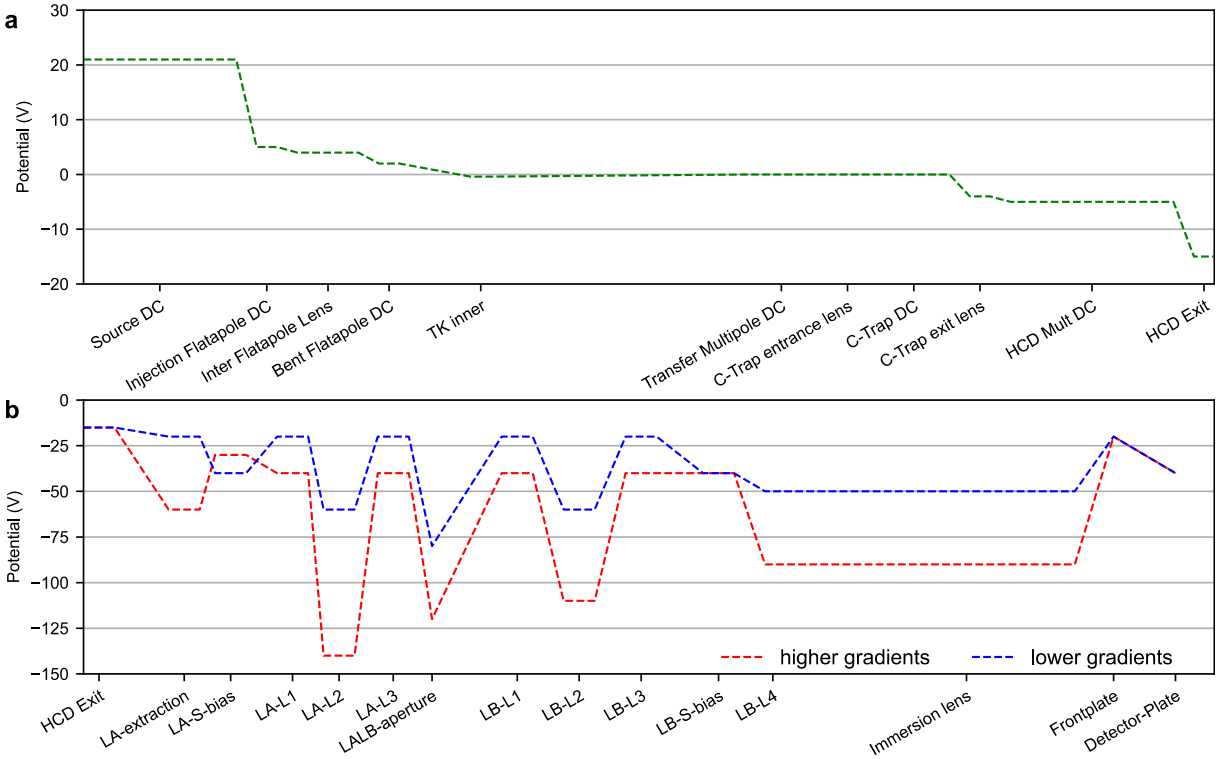


*Figure 61: DC Potentials applied within **a** the mass spectrometer and **b** the custom landing stage for higher and lower DC gradients.*

The ion beam is thermalised in the HCD cell at approx. 10^{-2} mbar. The total ion beam energy (TE) is close to the effective potential therein (-5 eVz^{-1}). When the ions leave the HCD cell, they are accelerated in the electrostatic lens. In there, the pressure decreases from high 10^{-3} mbar (HCD side) to 10^{-6} mbar (deposition chamber side). As the electrostatic lens is longer (60 mm for high-pressure part) than BSA mean free path (0.1 mm for a native BSA^{+14} ion at 7e-3 mbar), collisions with the background gas occur. For a hard-sphere collision, the kinetic energy E' of an ion after the collision is:[128], [227], [228]

$$\frac{E'}{E} = \frac{m_1^2 + m_2^2}{M^2} + \frac{2 m_1 m_2}{M^2} \cdot \cos\left(\theta_{cm}\right) \tag{11.1}$$

where θ_{cm} is the scattering angle in centre-of-mass coordinates, m_1 the ion mass, m_2 the gas molecule mass, $M = m_1 + m_2$ and E the pre-collision ion kinetic energy. As $m_1 >> m_2$, the second term is close to zero. Thus, equation 11.1 predicts E' is a fraction of E depending

mostly on the ion and gas mass. Fig. 62 compares this effect for heavy and light ions. The decrease in ion kinetic energy *E*-*E'* is bigger for higher *E*. *E* in the lab frame is proportional to the potential within the electrostatic lens. *E* maximum is 135 eVz^{-1} (strong gradient). As only 8.8 eVz^{-1} (denatured) respectively 5.2 eVz^{-1} (native) are dissipated in the electrostatic lens (Fig. 8 "Beam-energy distribution" in main article), few high energy collisions occur. For each *E'* is close to the initial kinetic energy. Therefore, the E_{tot} is lower after passing through stronger gradient conditions.

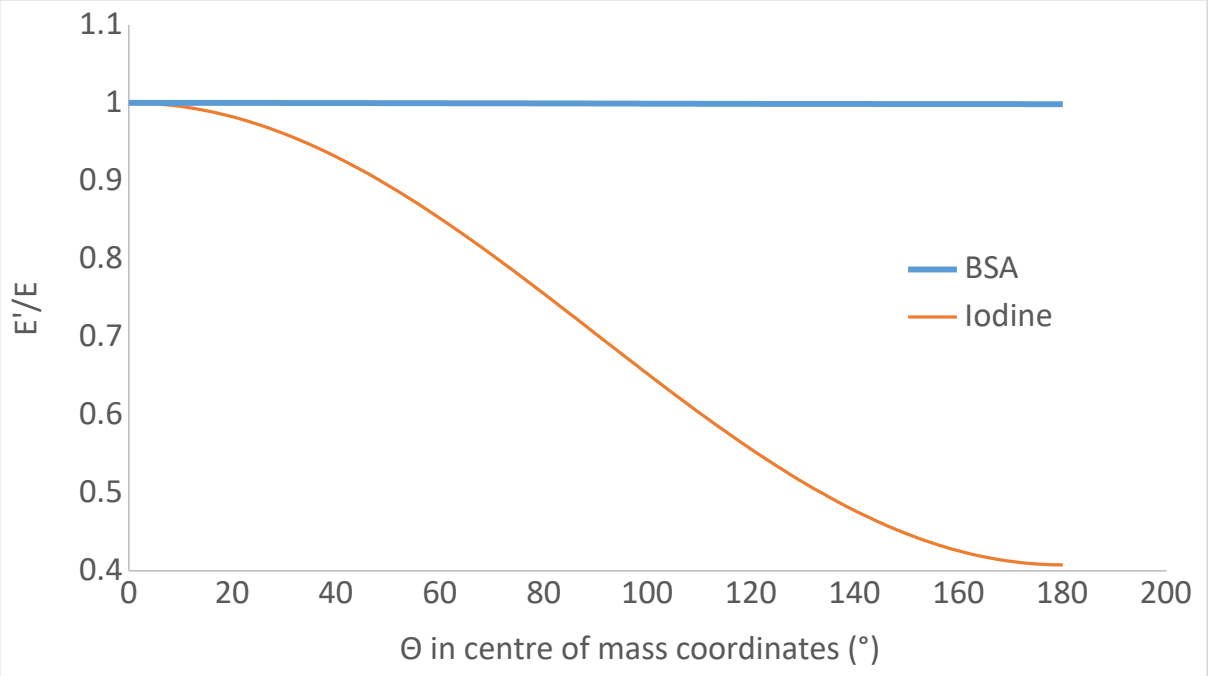


Figure 62: Kinetic energy loss per collision in N_2 for BSA (mass 66500 u) and Iodine (mass 127 u) as a function of the scattering angle. Minimum for BSA is 0.99832 at 180°.

A similar argument applies to the distribution width: Arbitrary variations of the impact angle between a gas molecule and an ion cause variations in the scattering angle. Term 2 in equation 11.1 varies accordingly and again *E'* is a fraction of *E*, meaning absolute variations in ion kinetic energy *E*-*E'* are bigger for higher *E*.

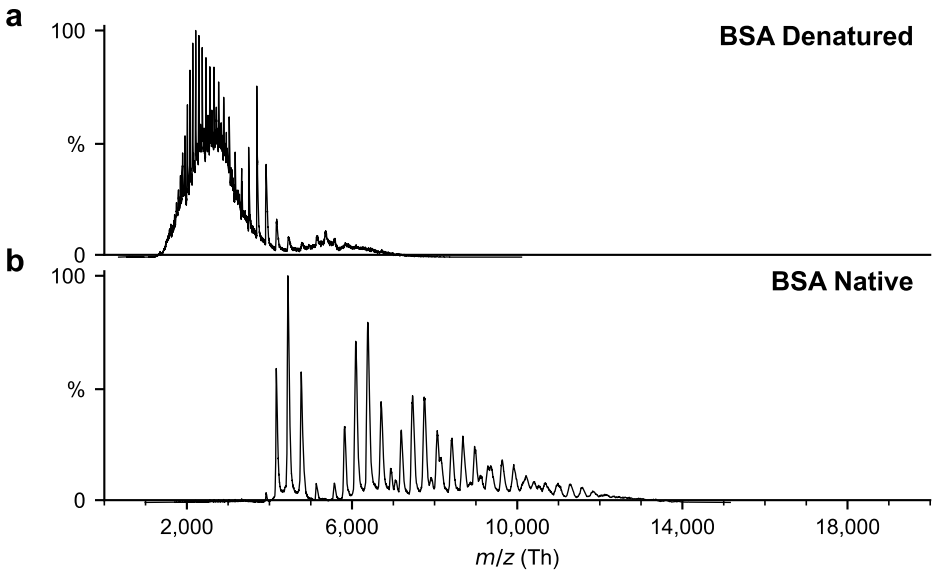


*Figure 63: Mass spectra of **a** denatured BSA and **b** native BSA. Both mass spectra are acquired with non-activating conditions used for deposition.*

Transmission

Native BSA emission current for the +15 charge state and a nano-ESI flow rate of 1 µl h^{-1}

$$I = \frac{cVzF}{t} = \frac{3 \cdot 10^{-6}\,\mathrm{mol\,L^{-1}} \cdot 1 \cdot 10^{-6}\,\mathrm{L} \cdot 15 \cdot 96485\,\mathrm{C \cdot mol^{-1}}}{3600\,\mathrm{s}} = 1.2\,\mathrm{nA} \qquad (11.2)$$

with concentration *c*, Volume *V*, number of charges *z*, Faraday constant *F* and time *t*.

Table 7: Potentials applied to ion optics when measuring current. Emitter potential is for nano-spray setup.

Measure at	Φ Optic (V)	Repulsive Optic (RO)	Φ RO (V)
Emitter	~1200	n.A.	n.A.
Transfer capillary	21	n.A.	n.A.
S exit lens	-100	Injection flatapole DC	50
Inter flatapole lens	-50	Bent flatpole	50
Inner TK lens	0	Outer TK	60
Aperture	-60	steer beam	n.A.
Current detector	-20	steer beam	n.A.

Ion beam size

SIMION simulations are consistent with the observations in figure 10 "Ion Beam Shape analysis" in main article. However, since the angular velocity distribution of the beam upstream of the sample holder cannot be determined experimentally, a quantitative comparison of simulated and observed beam profiles is currently not meaningful.

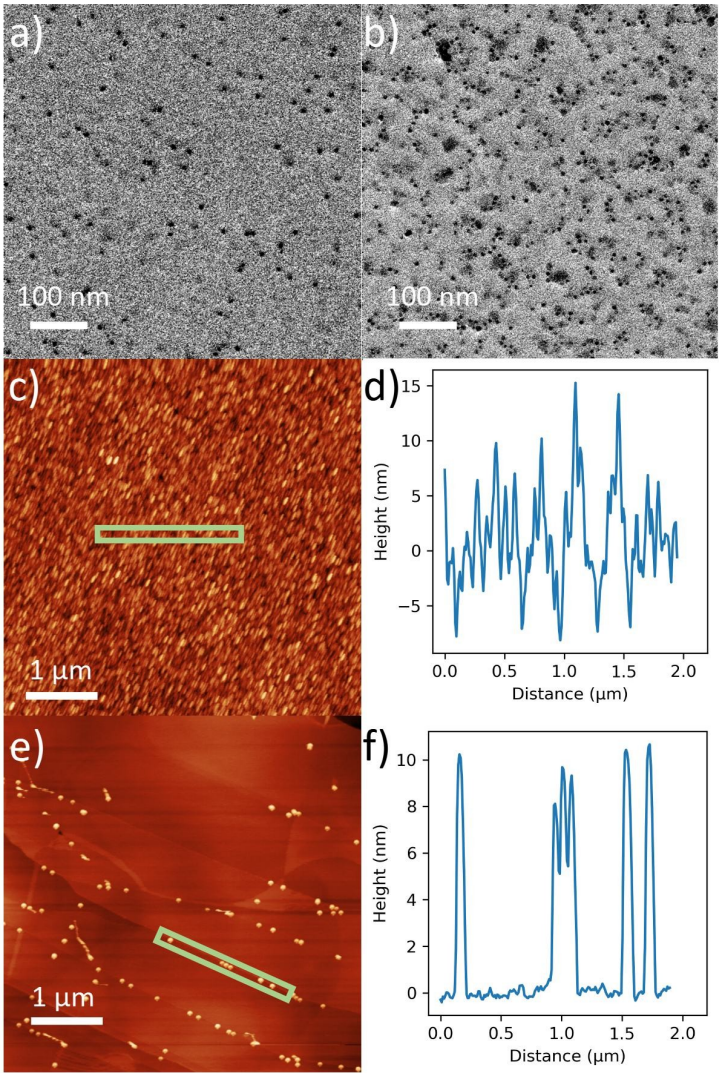


Figure 64: Exemplary AFM and TEM data for the beam shape characterization. ***a)*** *and* ***b)*** *show low (250 particles per µm²) and high (1500 particles per µm²) density areas on the TEM grid.* ***c)*** *shows an area in the centre of the deposition spot with more than monolayer coverage. Therefore, the line profile* ***d)*** *shows no well-defined baseline.* ***e)*** *shows a less dense area with 4 particles per µm². The corresponding line profile f) shows a clear baseline and allows to determine the particle heights.*

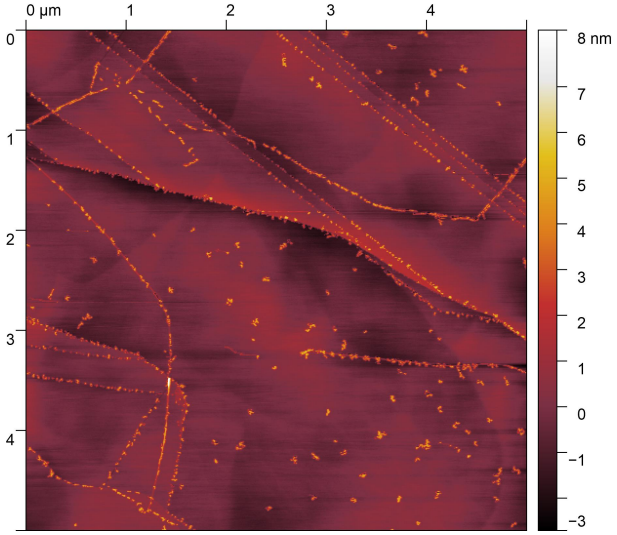


Figure 65: Native BSA on HOPG imaged with ambient AFM

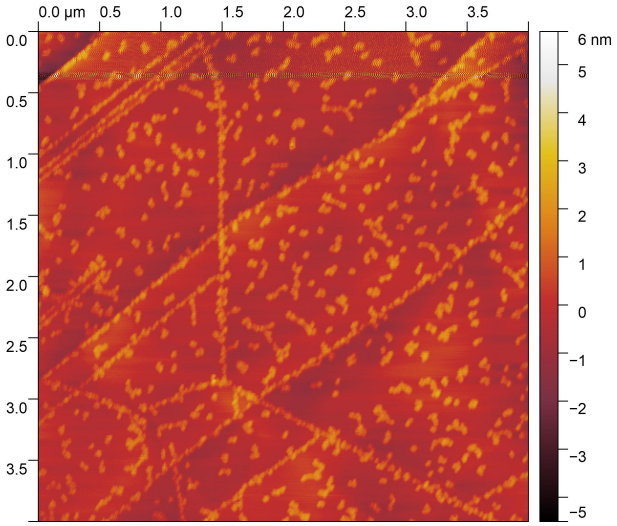


Figure 66: Denatured BSA on HOPG imaged with ambient AFM

TEM

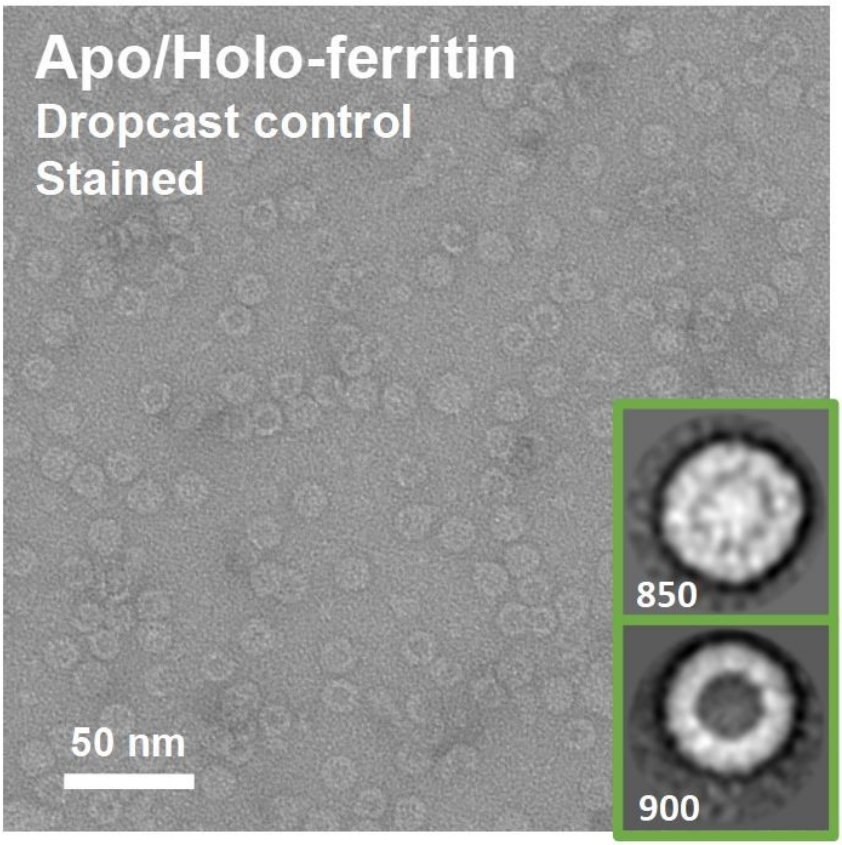


Figure 67: Negative stain apo/holo-ferritin control sample. The 2D classes show the same characteristic features as observed for the native ES-IBD samples, though they are better defined and there is less deformation in the control, despite the lower number of particles.

ADH activity

Method for extraction: Before we established the successful protocol, we tried to extract the deposited ADH. All steps were the same as described for the submersion, except: We deposited two times 27 ng (128 pAh) and two times 37 ng (175 pAh) on four amorphous Carbon EM Grids (AGS160-4H, Agar Scientific Ltd, Stansted, Great Britain). Each 27 ng grid was left for 2 days after deposition in ambient conditions. Then, we put in 50 µL assay buffer in a PP micro centrifuge vial. One 27 ng grid was vortexed for 15 min, the other sonicated for the same time. Then, the we transferred the extract in the 96 well plate. For the 37 ng grids, both were transferred immediately after deposition in a well with 50 µL assay buffer. We moved them around for 6 min with tweezers to wash ADH off. Then, we removed the grids.

Results: Neither sonication- nor vortex- nor washed-off-extracted ADH from EM-grids was active (Fig. 68). Submersion of the EM grid was not possible due to high background activity. We attribute this to a redox-reaction between the kit's components and the grid's copper support, which turned dull. Submersed conductive carbon tape was inert and used for all further work (Fig. 69). To check if the adapted assay protocol was working, we used the nano-electrospray source to deposit two tapes at atmospheric pressure. Sample activity was 2.1 mU, no background activity was present (Fig. 70). Although charge can be measured, recovery calculation is not possible due to unknown composition of the ion-droplet-plume.

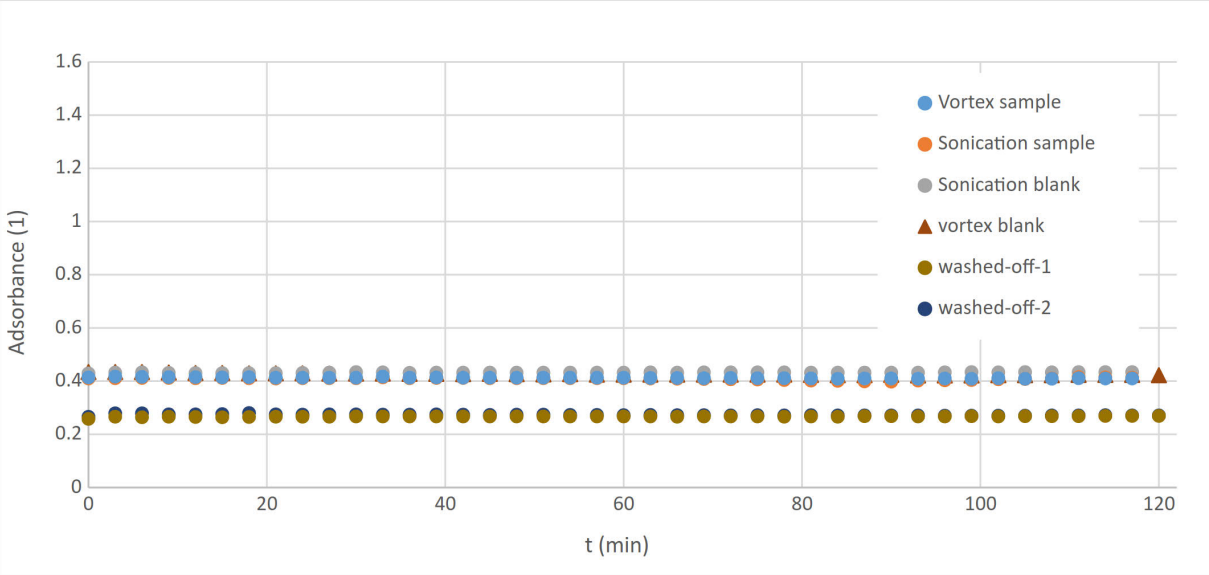


Figure 68: Assay-buffer-extraction of 128 pAh deposited ADH on EM grid with either vortex or sonication yields blank activity. The same applies for washing-off 175 pAh deposited ADH on EM grids. We tried to wash ADH off by moving the deposited grid around with tweezers in ADH buffer.

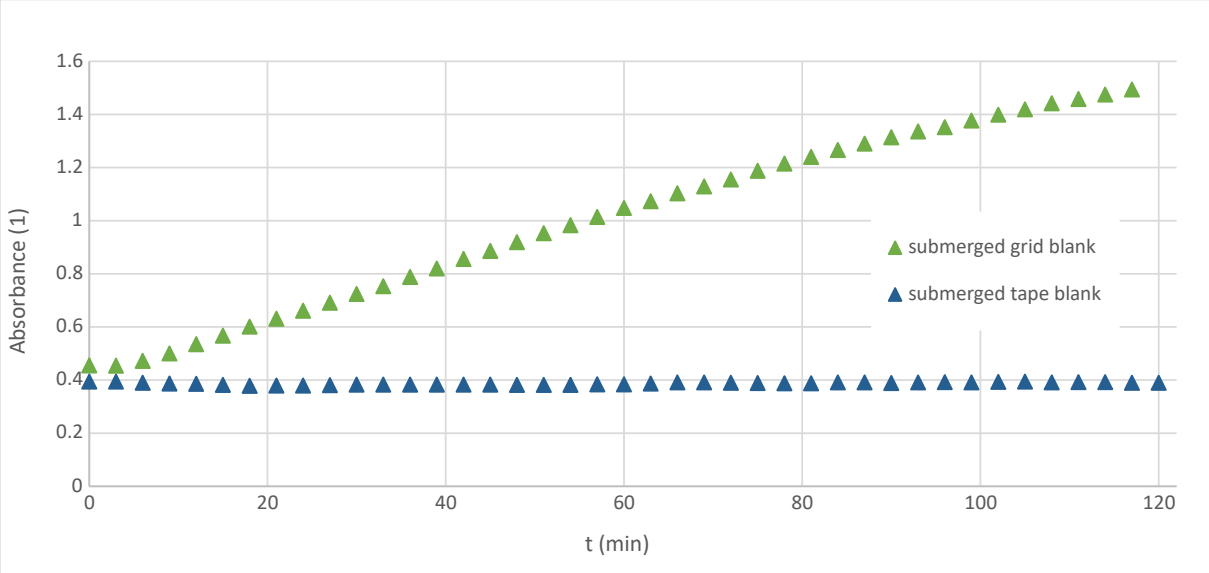


Figure 69: Submersion of an EM-grid in assay reaction mix causes a strong increase in absorbance, conductive tape doesn't.

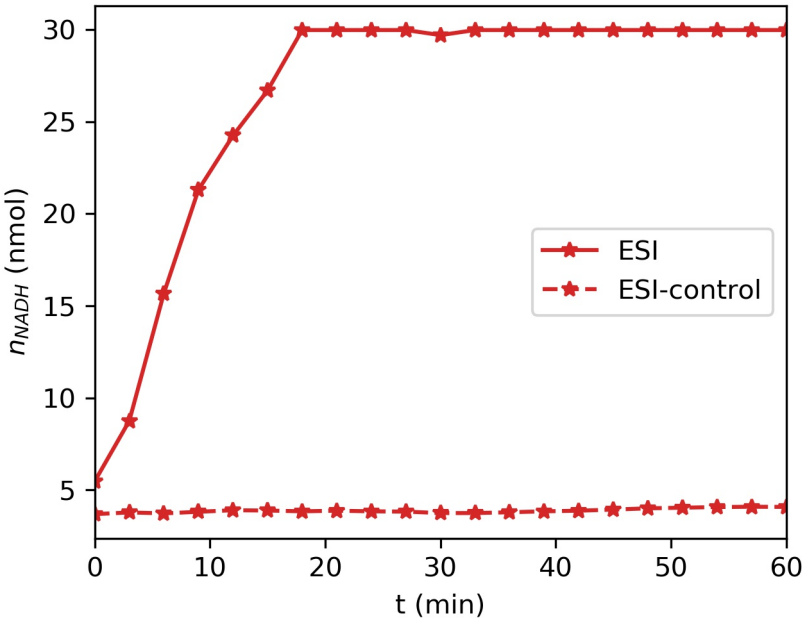


Figure 70: Production of NADH by ADH after electrospray deposition at atmospheric pressure. The broken lines stagnating at the offset level are background controls, so the NADH production is specific for ADH activity.

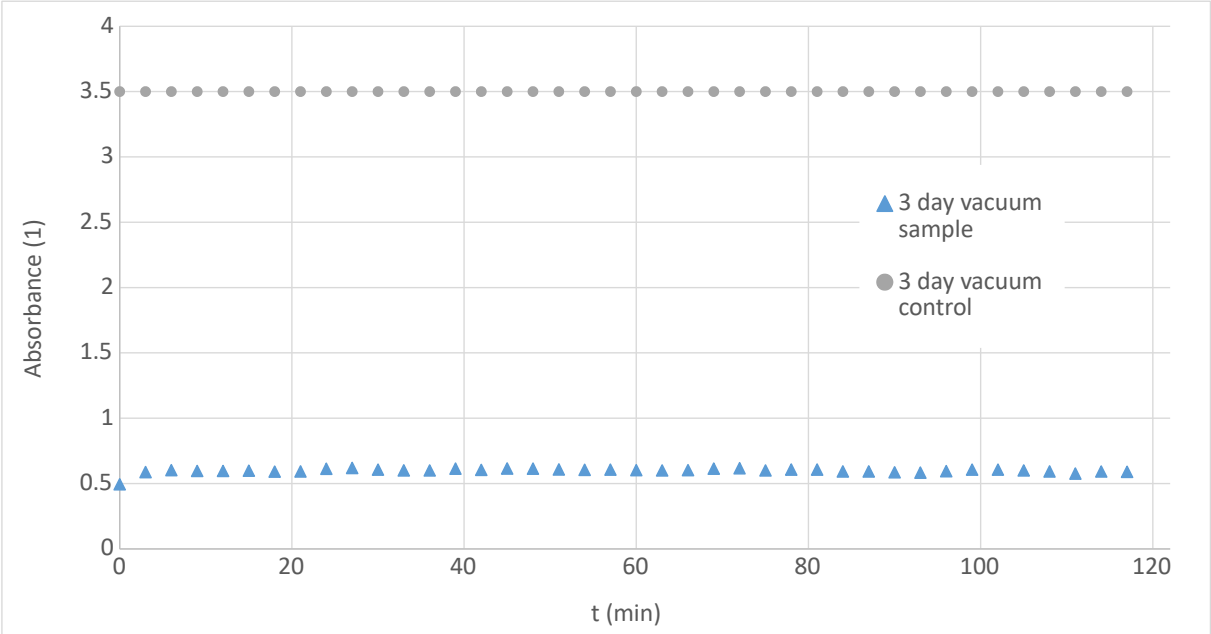


Figure 71: 128 pAh deposition (repetition C) retains no activity after 3 day storage in vacuum. The corresponding control was inactive as well, but showed a high absorbance due to the conductive tape having moved into the beam path (see Fig. 72).

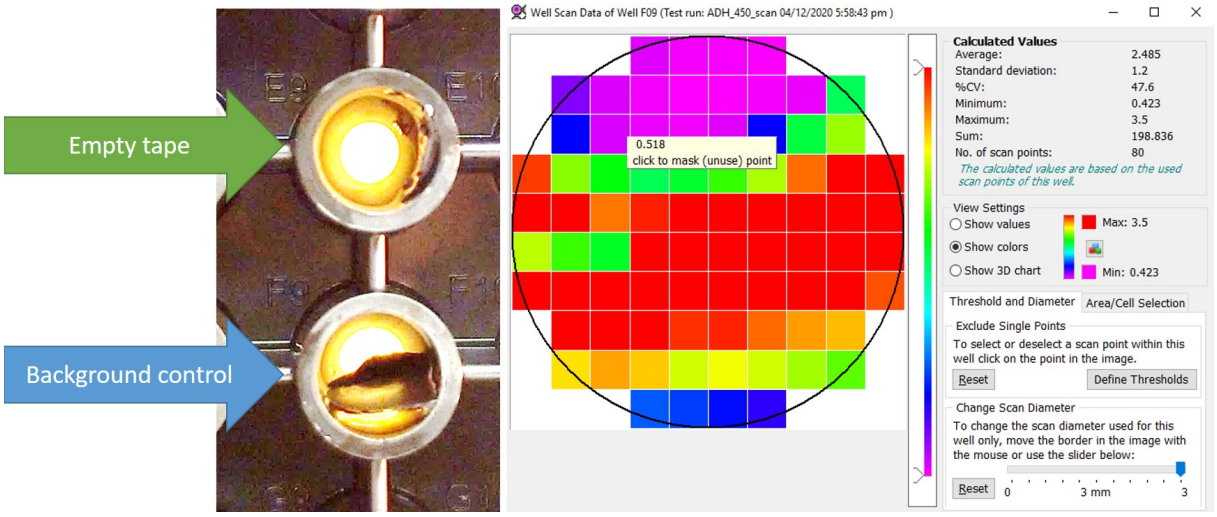


Figure 72: Left: 3 day storage background control (repetition C) moved into plate reader optical path. Note the liquid is still yellow, meaning no reaction has occurred during incubation. Right: 2D scan of bottom well confirms absorbance is still at blank level after incubation.

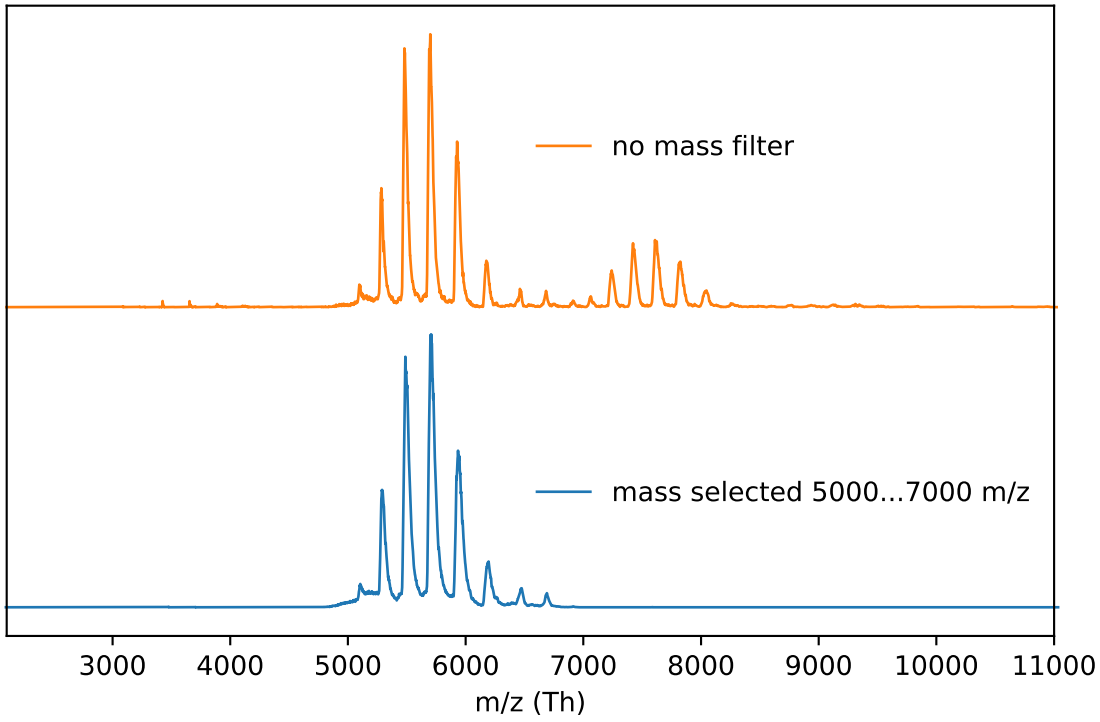


Figure 73: Mass spectra of the ADH beam prior and after 5000...7000 m/z filtering. The mass-selected beam was used for deposition.

2D scan scheme

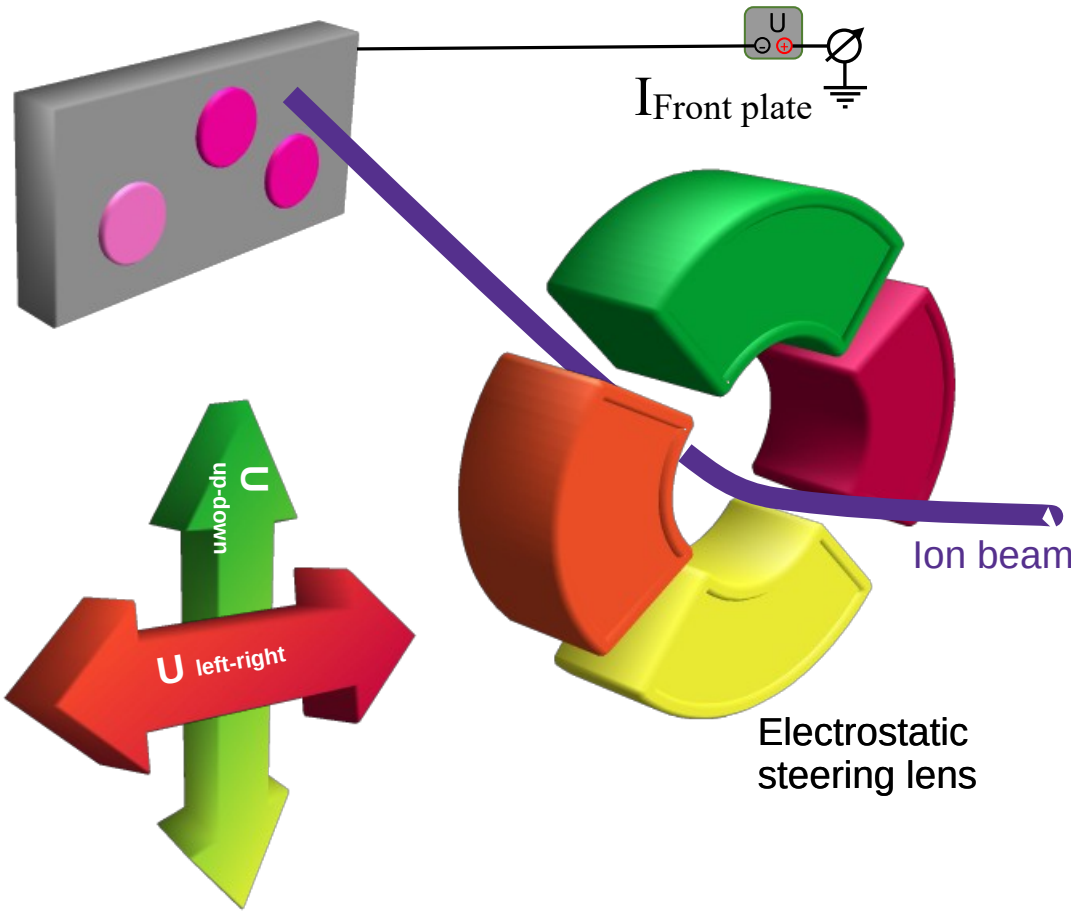


Figure 74: Scheme of the 2D-scan used to characterise the ion beam diameter on the front plate. A single picoammeter measures the current on the sample holder front plate. The data is recorded as a function of the deflection voltages applied to the electrostatic steering lens. The recorded current data can be represented as a 2d map. This shows an ion current image of the front plate. The 2D-scan function is also routinely used to find the sample (dark pink) and energy detector (light pink) positions.

11.4 Ion funnel

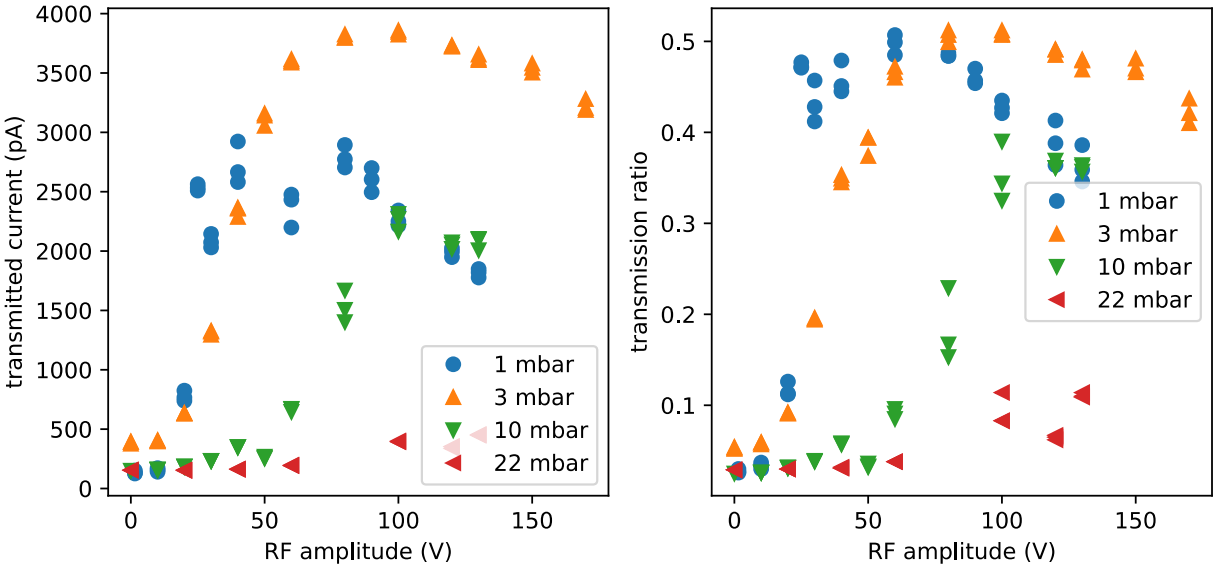


Figure 75: a) Transmitted current and b) transmission ratio at 1, 3, 10 and 22 mbar measured with the existing conventional ion funnel.

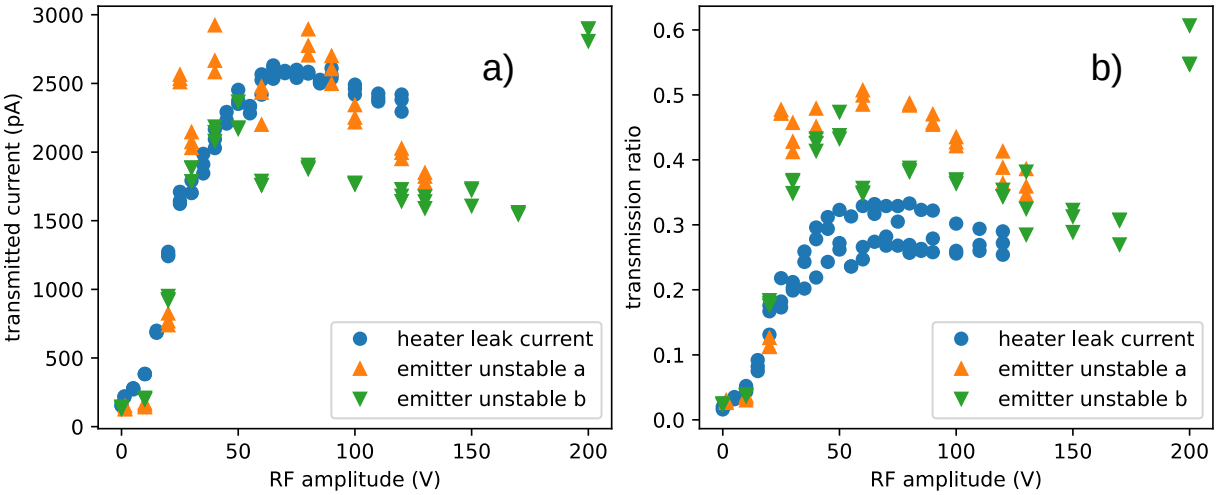


Figure 76: a) Transmitted current and b) transmission ratio for three measurement series at 1 mbar. Causes are an unstable emitter for two sets, and once I forgot to switch the capillary heating off. 200 VRF value is an outlier as a plasma ignited.

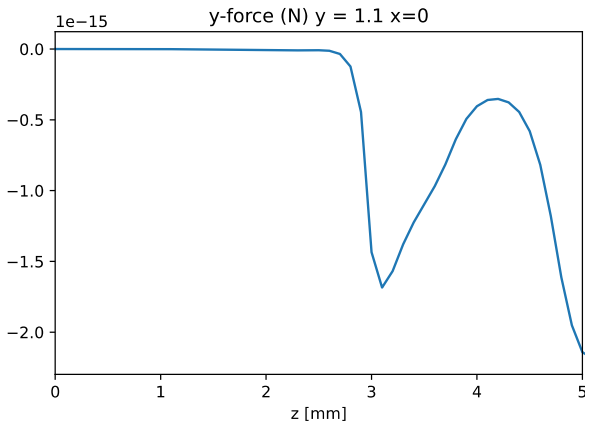


Figure 77: Radial effective force along r = 1.1 mm for the existing ion funnel.

Ion funnel geometries A and D

Radius for the parabolic cavity of the funnel A and D calculated with the equation

$$r_{funnel} = a \cdot x^2 + b \tag{11.3}$$

x is the axial coordinate in mm.

Table 8: Geometry summary of ion funnel geometries A and D. n is the electrode number. See also Figure 78 and Figure 79 for a section view.

Geometry	**A**	**D**
Parabola parameter a	400/1591	400/1591
Parabola parameter b	-(900/1591)	-(900/1591)
1. inter-electrode spacing (mm)	1.25 (n = 1...4)	1.25 (n = 1...4)
2. inter-electrode spacing (mm)	2.50 (n = 5...18)	2.50 (n = 5...18)
3. inter-electrode spacing (mm)	5.00 (n = 19...27)	5.00 (n = 19...32)
4. inter-electrode spacing (mm)	10.0 (n = 28...32)	/
Electrode thickness (mm)	0.6	0.6
Aperture radius (mm)	1.5	1.5
Length (mm)	ca. 153	ca. 128



Figure 78: Funnel A section view



Figure 79: Funnel D section view

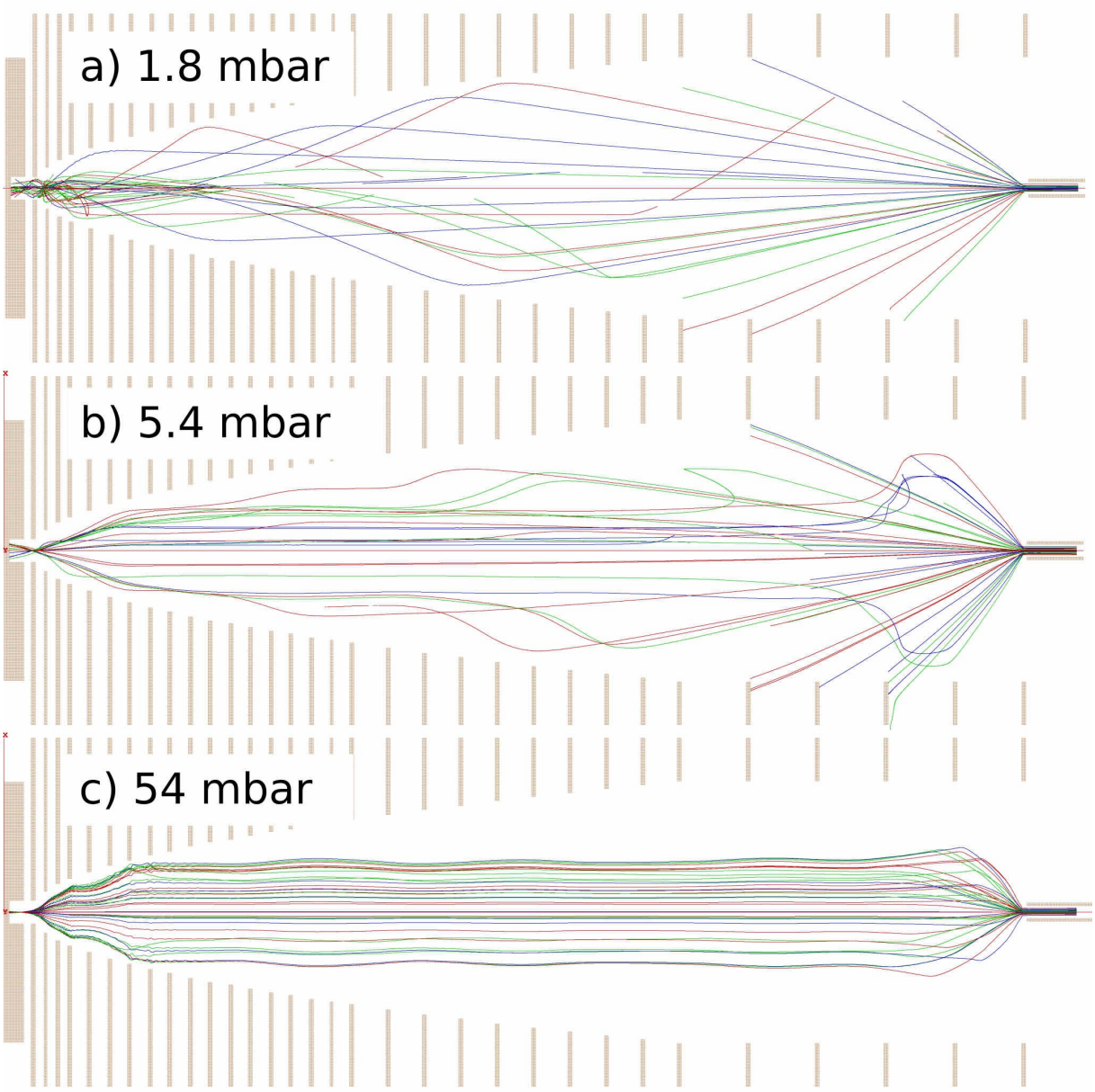


Figure 80: Trajectories of 80 GroEL ions with gas interaction in the funnel geometry A at a) 1.8 mbar, b) 5.4 mbar and c) 54 mbar pumping pressure. The 1.8 mbar pressure flow field was used for all simulations, but multiplied by 3 (b) and 30 (b). RF-parameters: a) and b): V_{RF} = 130 V, ν_{RF} = 400 kHz. c) V_{RF} = 80 V, ν_{RF} = 200 kHz

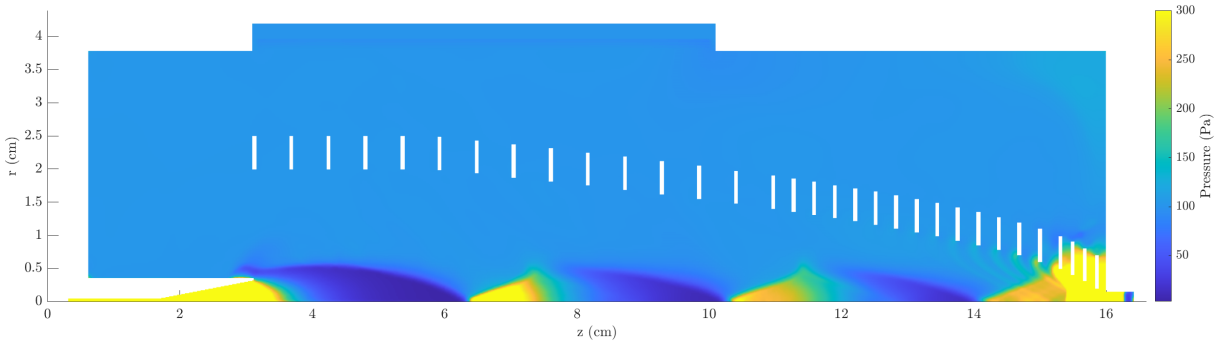


Figure 82: CFD simulation of the pressure field in ion funnel geometry D. Simulation not fully converged, image courtesy of Laurent Bernier. With a rocket-nozzle-shaped capillary outlet a shock-diamond structure forms (axial coordinates: 6.5, 10.5 and 14 cm).

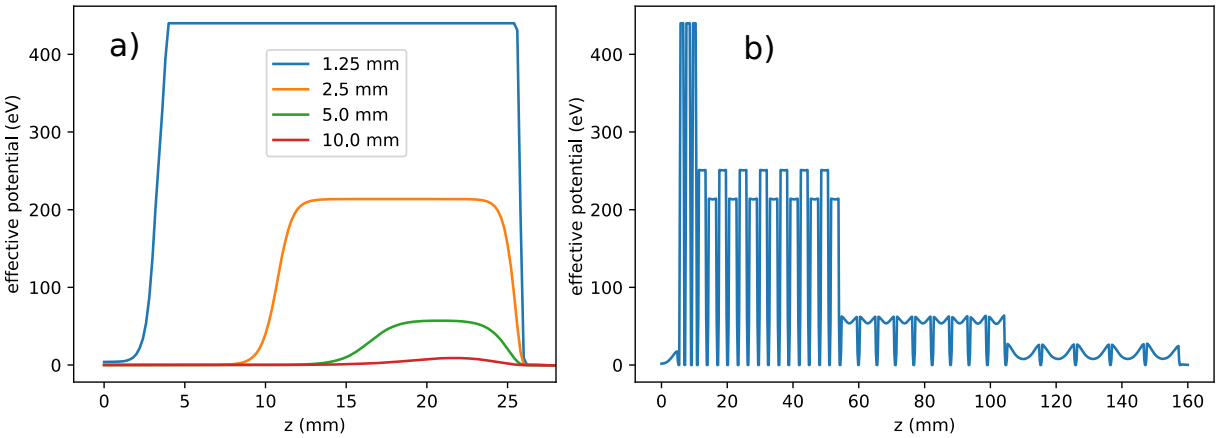


Figure 83: Effective Potential in Funnel A. a) Effective potential for different electrode spacings as a function of the funnel radius. b) Effective potential as a function of the axial coordinate at r = 23 mm. Note that with increasing electrode spacing the effective potential has local minima between two electrodes. Differing values between 10 mm and 50 mm (2.5 mm electrode spacing) are due to the limited resolution of the Simion workbench (0.2 mm/grid unit, so electrode spacing varied from 2.4 to 2.6 mm).

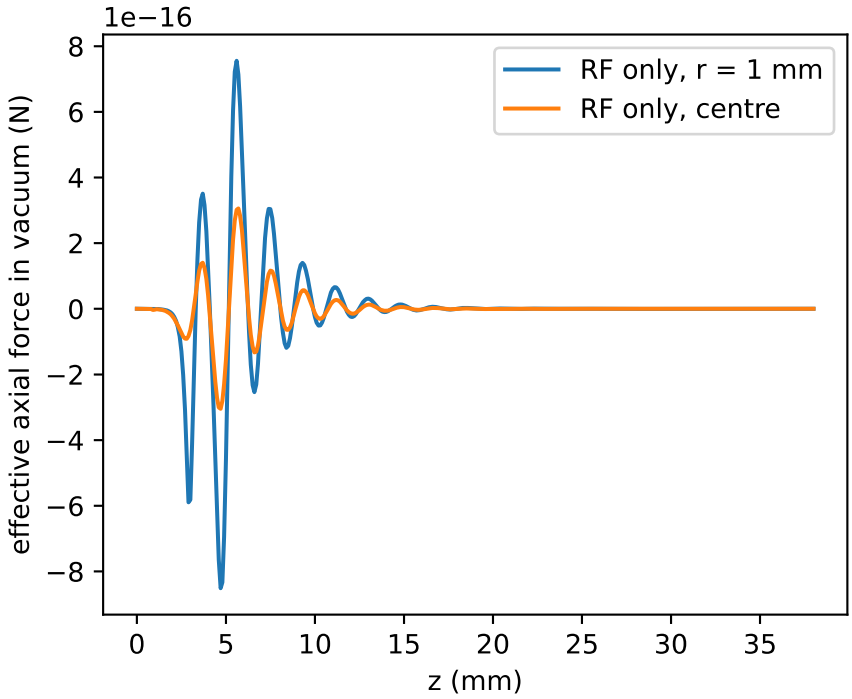


Figure 84: Effective axial force for rhodamine B in RF only mode in the existing ion funnel. Parameters: ν_{RF} = 1 MHz, V_{RF} = 60 V, assuming vacuum. The correction factor to account for a gas pressure of 1 mbar is 0.88.

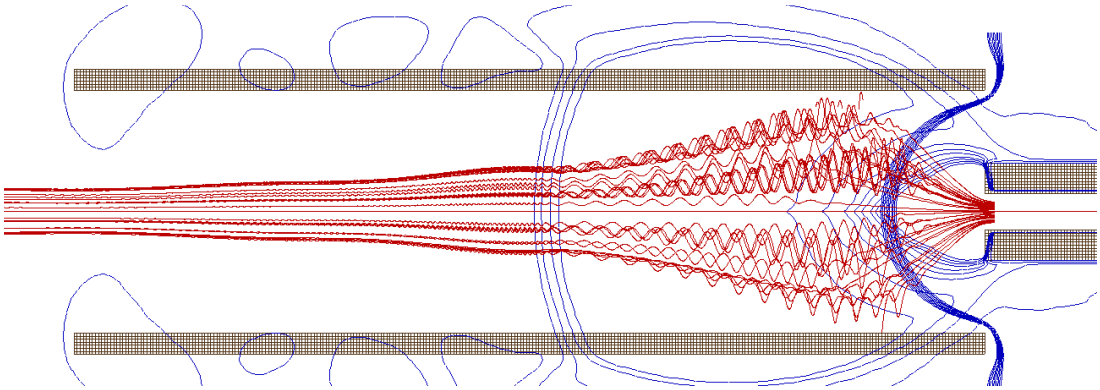


Figure 85: Trajectories of 80 hexamethoxyphosphazene ions at p_{pump}= 5.4 mbar (artificially increased), ν_{RF} = 800 kHz, V_{RF} = 300 V. Only electrodes in vertical plane are visible. Blue lines: isobars in 1.6 mbar steps.

11.5 Using the python script to calculate the effective potential

- Simion version used for testing: 8.1.1.32

- Create a Simion 8.x geometry file (.gem) with as many electrodes as you need, for example 5 in Figure 86.

- Group these electrodes into 3 adjustable electrodes: RF+, RF-, DC. Optionally: 2 different DC gradients are possible. Use fast-adjust potential arrays with multiple proportional scalable electrodes to create three electrode solutions. Write a .pa+ file to define your linear potential combinations (More information: see https://simion.com/info/fast_scale_extension.html and [101])

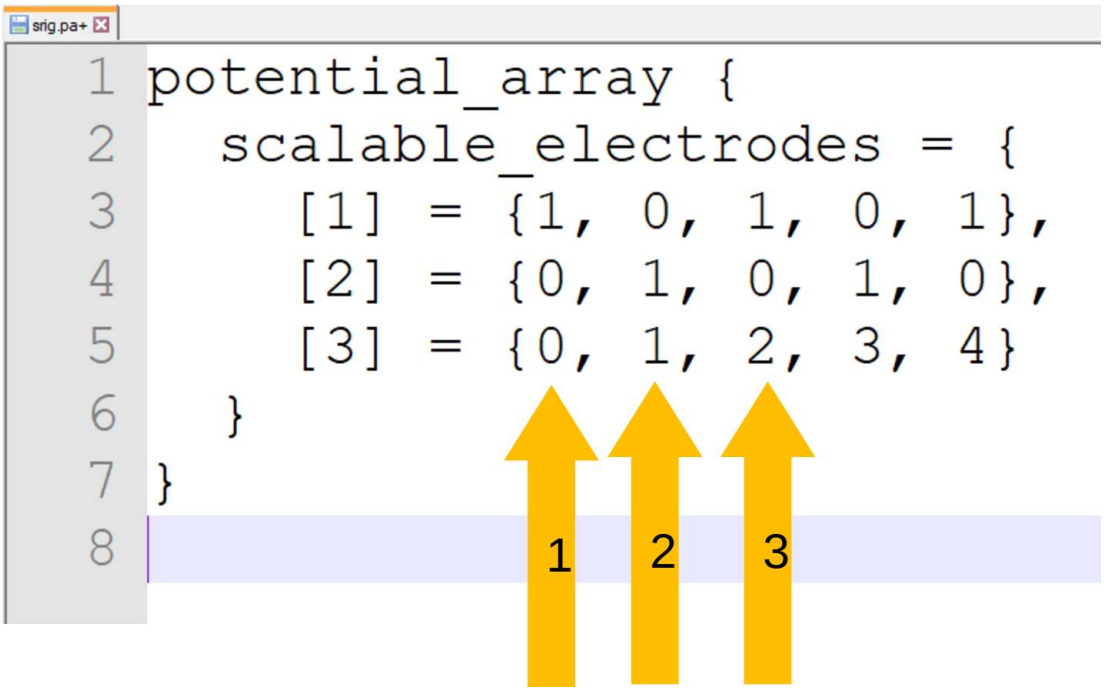
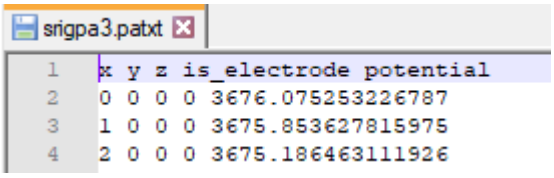


Figure 86: Example for a .pa+ file. The yellow arrows mark the columns which address the original electrodes 1,2,3 etc. created in the .gem file. The new scalable potential array combines them to a set of three electrode solutions. Line [1] is RF+, line [2] is RF- and line [3] is DC. They can be independently scaled.

- Save your potential array as .pa#
- Refine it. Four .pa files should be saved: .pa0, pa1 (RF+), .pa2 (RF-) and .pa3 (DC). If you have two DC Gradients, five .pa files should be saved (pa0 to pa4).
- Then, run any Lua program which is in the same folder as your potential arrays (this is to set the active folder for Simion only). Use the “Run Lua Program” function for it
- Open the SL tools window
- Select “PA → Text”
    - Load .pa1 file as input
    - Make sure the output file has only one dot in the file name (xxxpa1.patxt instead of xxx.pa1.patxt)
    - Tick “include header”, “Include data”, “include coords”
    - Hit “Convert”
    - In the Output .patxt file, delete the last 2 lines: end_points, end_potential_array. Then copy the header “x y z is_electrode potential” to line 19. Delete lines 1 to 18 to make the file readable with the pyhton pandas package. Your .patxt file should now look like this:



    - Repeat for pa2.patxt, pa3.txt and optionally for pa4.txt

- If you wish, cut or copy all three .patxt files to a new folder
- Open the python script “plot_Potential.py”
- Set the parameters of your molecule, the RF amplitude, the DC gradient and the work-space scaling:

```
42
43  #---------CONSTANTS-------##
44  RF_amp  = 80               # Give RF Amplitude (1/
45  DC_grad = 10               # DC gradient/highest D
46  wsf     = 0.2              # workbench scaling fac
47  freq_Hz = 1000E3           # frequency of RF field
48  q       = 1 * const.elementary_charge # q in coul
49  m       = 321 * const.atomic_mass   # mass in kg
50
```

- Use the readPA(…) function to load the .patxt files. It loads the Simon potential arrays in numpy arrays and saves them as binary files for later use
- Then, run LoadPA(…) to load the numpy potential arrays again
- Draw your potential with the CalcDraw(…) function

Copy of the python script included in the minimal working example:

```
1  # -*- coding: utf-8 -*-
2  """
3  @author: fremdling
4
5  Calculates the effective potential resulting from
6  a set of 2 RF electrodes and 1 DC potential array
7
8  Export from Simion with SL Tools with coordinates.
9
10 """
11
12
13 from matplotlib import pyplot as plt
14 import numpy as np
15 import pandas as pd
16 import datetime  # to save the historgram with a unique filename
17 import os   # for new folder
18 from scipy import constants as const # to convert J to eV etc...
19 import shutil # to copy entire script to results folder
20
21
22 #   Append filename with date and time
23 def giveDateTime():
24     now = datetime.datetime.now()
25     now = now.strftime("%Y%m%d_%Hh%M")
26     return now
27
```

```
#   Makes a new Subdirectory for the results if necessare
def checkMakeDir():
    script_dir = os.path.dirname(__file__)
    resultsDirName = giveDateTime() + '_plot_Results/'
    results_dir = os.path.join(script_dir, resultsDirName)
    if not os.path.isdir(results_dir):
        os.makedirs(results_dir)
    return results_dir

#---------CONSTANTS-------##
RF_amp      = 60              # Give RF Amplitude (1/2*Vpp) in Volt
DC_grad_a   = 24              # DC gradient/highest DC potential in Volt
DC_grad_b   = 0              # DC gradient/highest DC potential in Volt
wsf         = 0.2             # workbench scaling factor [mm/gu]
freq_Hz     = 1000E3          # frequency of RF field in Hertz
q           = 1 * const.elementary_charge # q in coulomb
m           = 443.57 * const.atomic_mass   # mass in kg



#------Calculated from constants------#
freq     = freq_Hz*2*const.pi           # Frequency in rad, the SI unit
spacing  = wsf/1000                     # spacing between datapoints in 3D array [m]
Eff_fact = (q**2) / (4*m*(freq**2))     # all constants for effective potential
ad_fact  = (2*q) / (m * (freq**2))      # Prefactor for Adiabacity parameter
f_fact   = -Eff_fact                    # all constants for the RF force part



# readPA(RFtxtplus, RFtxtminus)
# Copy header in line 19, delete last 2 lines before execution
def readPA(RfPlus,RfMinus, dctxt_a = None, dctxt_b = None, yslice_mm = 0):
    potData1 = pd.read_csv(RfPlus, delimiter='\s+', skiprows = 0)
    print(potData1[:5])
    potData2 = pd.read_csv(RfMinus, delimiter='\s+', skiprows = 0)
    potData = potData1
    potData['diff_pot'] = potData1['potential'] - potData2['potential']


    # Retrieve max of all dimensions - min assumed as always 0
    print(potData[:5] )
    z_max = np.max(potData['z'])
    x_max = np.max(potData['x'])
    y_max = np.max(potData['y'])
    print(x_max, y_max, z_max)

    # Convert the pandas df to a numpy array to make it faster
    potData = potData.drop(['is_electrode', 'potential'], axis = 1)
    potDataNp = potData.to_numpy()

    # Create and asing values in  the RF array
    pot = fillNpArray(potDataNp, x_max, y_max, z_max)

    # Do the same to the DC PA a
    if dctxt_a !=None:
        dcData   = pd.read_csv(dctxt_a, delimiter='\s+', skiprows = 0)
        dcData = dcData.drop(['is_electrode'], axis = 1)
        dcDataNp = dcData.to_numpy()
        print(dcDataNp[:5, :])
        dc_a = fillNpArray(dcDataNp, x_max, y_max, z_max)
    else:
        dc_a = np.zeros((z_max + 1, y_max + 1, x_max + 1), dtype = np.float64)

    # and for dc b
    if dctxt_b !=None:
        dcData   = pd.read_csv(dctxt_b, delimiter='\s+', skiprows = 0)
        dcData = dcData.drop(['is_electrode'], axis = 1)
        dcDataNp = dcData.to_numpy()
        print(dcDataNp[:5, :])
        dc_b = fillNpArray(dcDataNp, x_max, y_max, z_max)
    else:
        dc_b = np.zeros((z_max + 1, y_max + 1, x_max + 1), dtype = np.float64)


```

```
105      # Calculate the coordinates for drawing
106      yslice = int(yslice_mm/wsf)
107      # Print Potential from the Pandas DF
108      x_zero_bool = potData['x'] == 0
109      y_def_bool  = potData['y'] == yslice
110
111      subPot = potData[x_zero_bool & y_def_bool]
112      print(subPot[:5])
113      _, ax1 = plt.subplots()
114      ax1.plot(subPot['z']*wsf, subPot['diff_pot'])
115      plt.title('Potential from Pandas DF')
116      plt.show()
117
118      # Plot the Numpy 3D potential after reading in for x=0, y = yslice
119      _,ax3 = plt.subplots()
120      ax3.plot(np.arange(0, z_max + 1)*wsf, pot[ : ,yslice, 0])
121      plt.title('Potential from 3D numpy')
122      plt.show()
123      return dc_a, dc_b, pot, x_max, y_max, z_max
124
125  # Assings the values potential values correctly in the 3D np array
126  # The potential can be RF or DC, does not care!
127  def fillNpArray(npArrayPandas, x_max, y_max, z_max):
128      # Intialise a new 3D array for the potential values
129      potential = np.ones((z_max + 1, y_max + 1, x_max + 1), dtype = np.float64)
130      potential.fill(999999)      # Max Potential value in Simion is 10000
131
132
133      # Iterate through 2D original array to write data in 3d array
134      for row in npArrayPandas:
135          # Check if coordinates are integer
136          if (row[0].is_integer() & row[1].is_integer() & row[2].is_integer()):
137              z = int(row[2])
138              y = int(row[1])
139              x = int(row[0])
140          else:
141              raise NameError('Your coordiantes are not integer')
142          #print(x,y,z)
143          potential[z, y, x] = row[-1]  #potential value saved in last column
144
145      #print(potential[-1: , :, :4])
146
147      # Check if any cell has not been intialized
148      uninit = (potential == 999999)    # create a mask
149      if potential[uninit].size != 0:
150          raise NameError('Not all Elements in the 3D array have been intialised')
151      return potential
152
153
154  # Saves the numpy arrays to a binary file
155  def SavePA(pot, dc_a, dc_b, x_max, y_max, z_max):
156      np.save('RfArray.npy', pot)
157      np.save('DcArray_a.npy', dc_a)
158      np.save('DcArray_b.npy', dc_b)
159      dimensions = np.array([x_max, y_max, z_max])
160      np.save('dimensions.npy', dimensions)
161      return
162
163  # Reloads the numpy arrays from the binary file
164  def LoadPA(RF, DCbinary_a, DCbinary_b, dimensions):
165      pot = np.load(RF)
166      dc_a  = np.load(DCbinary_a)
167      dc_b  = np.load(DCbinary_b)
168      dim = np.load(dimensions)
169      x_max = dim[0]
170      y_max = dim[1]
171      z_max = dim[2]
172      return pot, dc_a, dc_b, x_max, y_max, z_max
173
174  # RF smoothing reduces peaks in the effective potential caused by sharp edges in the
electrode geometry
175  # smoothing factor must be not zero and positive.
176  def CalcDraw(pot, dc_a, dc_b, x_max, y_max, z_max,
177               slices, RFsmoothing = False, smoothing_factor = 2, drawRF = True, drawDC =
True):
178      # set the not wanted Component to 0
179      if drawRF == False:
```

```
180         pot.fill(0)
181     if drawDC == False:
182         dc_a.fill(0)
183         dc_b.fill(0)
184 
185     # Adapt the RF Array to the RF Amplitude, DC to DC max
186     RF_adapt    = RF_amp/10000
187     DC_adapt_a  = DC_grad_a/10000
188     DC_adapt_b  = DC_grad_b/10000
189     pot         = pot * RF_adapt
190     dc_a        = dc_a * DC_adapt_a
191     dc_b        = dc_b * DC_adapt_b
192 
193     # add the two DC components
194     dc_all      = dc_a + dc_b
195 
196     # Calculate the gradient and Scalar product
197     effPot = DiffAndDot(pot, spacing)
198 
199     # Calculate the Adiabacity
200     # effPot at this point is the square of the electric field
201     eta = DiffAndDot(np.sqrt(effPot), spacing)
202     eta = np.sqrt(eta) # length of vector
203     eta = eta * ad_fact
204 
205     # Calculate the average force
206     # effPot at this point is still the square of the electric field
207     z_force, y_force, x_force, force_mag = Force(dotproduct= effPot, dcpot = dc_all,
charge = q, spacing_i = spacing,
208                                                  RFsmoothing = RFsmoothing,
smoothing_factor= smoothing_factor)
209 
210     #print(effPot[:1, :2, :2])
211     effPot = effPot * Eff_fact # linear prefactors, effective Potential in eV
212 
213     # smooth RF part to avoid spikes on sharp geometry changes
214     if (RFsmoothing == True): effPot = Smooth(field = effPot, smoothing_factor= smooth-
ing_factor)
215 
216 
217     # Add DC component
218     effPot = effPot + (q * dc_all)
219 
220     # Convert to eV
221     effPot = effPot / const.eV
222     #print(effPot[:1, :2, :2])
223 
224 
225 
226     # # Plot the effective Potential for selected plane in 2D
227     # Plot2D(effPot, y_max, z_max, x_max, minValue =None, maxValue = None, title = 'Ef-
fective Potential in eV',
228     #         fileAppen = '_Effective_Potential_xeq_0_.jpg', plane= 'x', slice_plane =0)
229 
230     # # Plot the effective Potential for selected plane in 2D
231     # Plot2D(effPot, y_max, z_max, x_max, minValue =None, maxValue = None, title = 'Ef-
fective Potential in eV',
232     #         fileAppen = '_Effective_Potential_xeq_0_.jpg', plane= 'y', slice_plane =0)
233 
234     # Plot the effective Potential for selected plane in 2D
235     Plot2D(effPot, y_max, z_max, x_max, minValue =None, maxValue = None, title = 'Effect-
ive Potential in eV',
236             fileAppen = '_Effective_Potential_xeq_0_.jpg', plane= 'z', slice_plane =0)
237 
238     # Plot the adabacitý Parameter for selected plane in 2D
239     Plot2D(eta, y_max, z_max, x_max, maxValue = 0.3, title = 'Adiabacity parameter',
240             fileAppen = '_adiabacity_xeq_0_.jpg', plane= 'x', slice_plane =0)
241 
242     # Plot the effective Force for for selected plane in 2D
243     Plot2D(force_mag, y_max, z_max, x_max, maxValue = None, title = 'Effective Force in
N',
244             fileAppen = '_Effective_Force_xeq_0_.jpg', plane= 'x', slice_plane =0)
245 
246     # # Plot the y-Force (radial) for for selected plane in 2D
247     # Plot2D(y_force, y_max, z_max, x_max, minValue= None, maxValue =  None, title = 'y-
force (N)',
248     #         fileAppen = '_Y_Force_Force_xeq_0_.jpg', plane= 'x', slice_plane =0)
```

```
249
250       # # Plot the z-Force (axial) for for selected plane in 2D
251       # Plot2D(z_force, y_max, z_max, x_max, minValue= None, maxValue = None, title = 'z-
force (N)',
252       #         fileAppen = '_z_Force_Force_xeq_0_.jpg', plane= 'x', slice_plane =0)
253
254
255       # Plot the effective Potential for x=0 in 3D
256       Plot3D(effPot, fileAppen = '_Effective_Potential3D_xeq_0_.jpg', title = 'effective
potential (eV)', y_max = y_max, z_max = z_max)
257
258       # # Plot the Adabacity parameter for x=0 in 3D
259       # Plot3D(eta, fileAppen = '_adiabacity_3D_xeq_0_.jpg', title = 'adiabacity (1)',
y_max = y_max, z_max = z_max, maxValue = 0.5)
260
261       # # Plot the effective Force for x=0 in 3D
262       # Plot3D(force_mag, fileAppen = '_Effective_Force_mag3D_xeq_0_.jpg', title = 'effect-
ive Force \n magnitude (N)',  y_max = y_max, z_max = z_max)
263
264       # Plot the Effective Potential in 1 D
265       Plot1D(slices_mm  = slices, field = effPot, x_max = x_max, y_max = y_max, z_max =
z_max,
266              title = 'Effective Potential in eV', type_string ='_Effective_Potential_')
267
268       # # Plot the y (radial) force in 1D
269       # Plot1D(slices_mm = slices, field = y_force, x_max = x_max, y_max = y_max, z_max =
z_max,
270       #         title = 'y-force (N)', type_string ='_Y-force_')
271
272       # # Plot the x (radial) force in 1D
273       # Plot1D(slices_mm = slices, field = x_force, x_max = x_max, y_max = y_max, z_max =
z_max,
274       #         title = 'x-force (N)', type_string ='_X-force_')
275
276
277       # # Plot the z (axial) force for x=0, y = yslice
278       # Plot1D(slices_mm = slices, field = z_force, x_max = x_max, y_max = y_max, z_max =
z_max, title = 'z-force (N)', type_string ='_Z-force_',
279       #         maxValue=None, minValue = None)
280
281
282       return
283
284
285       #   Plot any scalarfield
286       #   Coordiante format for slices_mm = [x,y,z]. Example for a slice parallel to z-
Axis: [0,0,'z']
287   def Plot1D(slices_mm, field, x_max = 0, y_max = 0, z_max = 0,
288              title = 'No Title', type_string ='Not_set', maxValue = None,
289              minValue = None):
290       for i in slices_mm:
291           fig0,ax0 = plt.subplots()
292           #   find out which plane is sliced
293           if i[0] == 'x':     # slice parallel to x-axis, y,z are defined
294               y_mm    = i[1]
295               y_grid  = int(y_mm/wsf)
296               z_mm    = i[2]
297               z_grid  = int(z_mm/wsf)
298               values          = field[z_grid, y_grid, : ]   # values format [z,y,x]
299               x_axis          = np.arange(0, x_max + 1)*wsf
300               title_add       = ', y = ' + str(y_mm) + ' mm, z = ' + str(z_mm) + ' mm'
301               x_axis_label    = 'x (mm)'
302               type_str        =  type_string +  '_y_eq' + str(y_mm) + 'z_eq' + str(z_mm)
303
304           elif i[1] == 'y':     # slice parallel to y-axis, x,z are defined
305               x_mm    = i[0]
306               x_grid  = int(x_mm/wsf)
307               z_mm    = i[2]
308               z_grid  = int(z_mm/wsf)
309               values          = field[z_grid, : , x_grid] # values format [z,y,x]
310               x_axis          = np.arange(0, y_max + 1)*wsf
311               title_add       = ', x = ' + str(x_mm) + ' mm, z = ' + str(z_mm) + ' mm'
312               x_axis_label    = 'y (mm)'
313               type_str        =  type_string +  '_x_eq' + str(x_mm) + 'z_eq' + str(z_mm)
314
315           elif i[2] == 'z':     # slice parallel to z-axis, x,y are defined
316               x_mm    = i[0]
```

```
            x_grid  = int(x_mm/wsf)
            y_mm    = i[1]
            y_grid  = int(y_mm/wsf)
            values          = field[:, y_grid , x_grid] # values format [z,y,x]
            x_axis          = np.arange(0, z_max + 1)*wsf
            title_add       = ', x = ' + str(x_mm) + ' mm, y = ' + str(y_mm) + ' mm'
            x_axis_label    = 'z (mm)'
            type_str        =  type_string +  '_x_eq' + str(x_mm) + 'y_eq' + str(y_mm)


        # ax0.set_xlim( 4, 6)
        if (maxValue != None or minValue != None): plt.ylim(minValue, maxValue)
        ax0.plot(x_axis, values )
        plt.title(title + title_add)
        plt.xlabel(x_axis_label)
        filename = giveDateTime() + type_str
        plt.savefig(checkMakeDir() + filename +'.svg', format = 'svg')
        plt.savefig(checkMakeDir() + filename +'.jpg', format = 'jpg', dpi = 300)
        plt.show()
        saveslice = np.stack([np.array(x_axis), values])
        np.save(checkMakeDir() + giveDateTime() + type_str +  '.npy', saveslice)
    return

# Calculates the Gradient of a 3d numpy array, then the dot product
# Subfunction of CalcDraw()
def DiffAndDot(scalarfield, spacing_i):
    # Calculate the gradient and Scalar product
    z_grad, y_grad, x_grad = np.gradient(scalarfield, spacing_i)
    dotProd = Dot(z_grad, y_grad, x_grad)
    return dotProd

# calculates dotproduct of 3D vector. z_grad etc. are scalarfields
def Dot(z_grad, y_grad, x_grad):
    z_grad_sq = np.square(z_grad)
    y_grad_sq = np.square(y_grad)
    x_grad_sq = np.square(x_grad)

    dotProd = z_grad_sq + y_grad_sq + x_grad_sq
    return dotProd


# Feed with effPot = DiffAndDot(pot, spacing)
# dotproduct has to be the dotproduct of the electric field
# Electrostatic part still missing
def Force(dotproduct, spacing_i, dcpot, charge, RFsmoothing = False, smoothing_factor =
None):
    z_force, y_force, x_force = np.gradient(dotproduct, spacing)
    forces = np.array([z_force, y_force, x_force])
    # Add prefactor
    forces = f_fact * forces

    # DC Force
    z_dc, y_dc, x_dc = np.gradient(dcpot, spacing_i)
    dcfield = -1*np.array([z_dc, y_dc, x_dc])
    dcforce = dcfield * charge

    # Add DC and RF Force
    forces = forces + dcforce

    force_mag = np.sqrt(Dot(forces[0], forces[1], forces[2]))

    #Smooth
    all_forces = np.array([forces[0], forces[1], forces[2], force_mag])
    for number, i in enumerate(all_forces):
        if RFsmoothing == True: all_forces[number] = Smooth(i, smoothing_factor)
    # print('mean of x_force', np.mean(z_force), ' mean of all_force[2] ',
np.mean(all_forces[0]))

    return all_forces[0], all_forces[1], all_forces[2], all_forces[3]



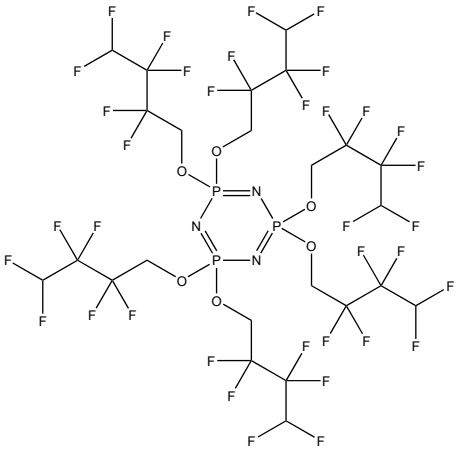
# smoothes numpy 3D array to avoid spikes on sharp geometry changes
def Smooth(field, smoothing_factor):
    mean = field.mean()
    std = field.std()
    # print('mean:', mean, 'std:', std)
```

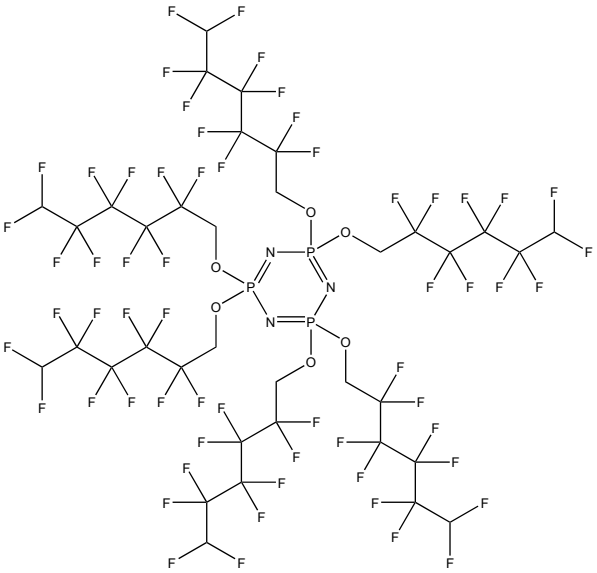
```
392       field[field > (mean + ((10/smoothing_factor)*std))] = (mean + ((10/
smoothing_factor)*std))
393       field[field < (mean - ((10/smoothing_factor)*std))] = (mean - ((10/
smoothing_factor)*std))
394       return field
395
396   # Plots a 2D slice, the last numpy array column is selected of a 3d array, default is x=0
plane
397   # slice_plane in mm, default 0
398   def Plot2D(scalarfield, y_max, z_max, x_max, maxValue, title, fileAppen, minValue = 0,
plane = 'x', slice_plane = 0):
399       fig, ax = plt.subplots()
400       slice_plane = round(slice_plane/wsf) # adapt to wsf
401       print(slice_plane)
402
403       if plane == 'z':
404           plotfield = scalarfield[slice_plane,:,:]
405           ex = (0,(y_max + 1)*wsf,(x_max + 1)*wsf,0)
406           plt.xlabel('x (mm)')
407           plt.ylabel('y (mm)')
408           title = title + '\nz='
409
410       elif plane == 'y':
411           plotfield = scalarfield[:,slice_plane,:]
412           ex = (0,(x_max + 1)*wsf,(z_max + 1)*wsf,0)
413           plt.xlabel('x (mm)')
414           plt.ylabel('z (mm)')
415           title = title + '\ny='
416
417       elif plane == 'x':
418           plotfield = scalarfield[:,:,slice_plane]
419           ex = (0,(y_max + 1)*wsf,(z_max + 1)*wsf,0)
420           plt.xlabel('y (mm)')
421           plt.ylabel('z (mm)')
422           title = title + '\nx='
423
424       im = ax.imshow(plotfield, cmap=plt.cm.jet, vmin = minValue, vmax= maxValue,
425                   extent = ex)
426       plt.title(title + str(round(slice_plane*wsf,1)) + 'mm')
427
428       # plt.xlim( 0,5)
429       # plt.ylim(30,50)
430       # ax.set_xticks(np.arange(0,5, 0.1), minor = True)
431       # ax.set_yticks(np.arange(2,9, 0.1), minor = True)
432       # ax.grid(which='minor', alpha=0.4)
433       fig.colorbar(im)
434       filename = giveDateTime() + fileAppen
435       plt.savefig(checkMakeDir() + filename, format = 'jpg', dpi = 400)
436       plt.show()
437       return
438
439
440   # plots a 3D representation of a 2D array. scalarfield is a 3D array,
441   # fileAppen the filename description
442   def Plot3D(scalarfield, fileAppen, title, y_max, z_max, maxValue = None):
443       Val = scalarfield[:,:,0]
444       z = np.linspace(0, (z_max )*wsf, z_max + 1)
445       y = np.linspace(0, (y_max )*wsf, y_max + 1)
446
447
448       Y, Z = np.meshgrid(y, z) # makes a matrice of coordinates
449
450       # plt.contour(Y, Z, Val, 20, cmap='RdGy')
451       # plt.show()
452
453       # 3d
454       ax = plt.axes(projection='3d')
455       if maxValue != None:
456           Val[Val > maxValue] = np.nan # crop the data to set z limit
457       # ax.plot_surface(Y, Z, Val, rstride=1, cstride=1,
458       #             cmap='gist_ncar', edgecolor='none' )
459
460       ax.plot_surface(Y, Z, Val,
461                           alpha=1,
462                           color = 'dodgerblue',
463                           rstride=1,
464                           cstride=1)
```

```
465       ax.view_init(elev=30, azim=190)
466       ax.set_xticks([])    # makes ticks and grid invisble
467       ax.set_yticks([])
468       # ax.set_zticks([])
469       # ax.set_xlabel('y (mm)')
470       # ax.set_ylabel('z (mm)')
471       # ax.set_xlim3d( 0, 7)
472       ax.set_zlabel(title)
473       plt.tight_layout()
474       filename = giveDateTime() + fileAppen
475       plt.savefig(checkMakeDir() + filename , format = 'jpg', dpi = 500)
476       plt.show()
477       return
478
479
480
481   # Save the parameters to text file - Not the nicest way to do this
482   def saveParameters(filename):
483       with open(filename, 'r') as f:
484           lines = f.readlines()
485           param = lines[36:54]
486           f.close()
487       with open(checkMakeDir() + giveDateTime() + '_param.txt', 'w') as f:
488           for item in param:
489               f.write("%s" % item)
490           f.close()
491       shutil.copyfile(filename,checkMakeDir() + filename) # additional copy of the entire
script
492       return
493
494   # Load and save potentials with this section
495   dc_a_o, dc_b_o, pot_o, x_max_o, y_max_o, z_max_o = readPA(RfPlus =r"srigpa1.patxt",
496                                         RfMinus=r"srigpa2.patxt",
497                                         dctxt_a=r"srigpa3.patxt",
498                                         dctxt_b=None,
499                                         yslice_mm = 1)
500   SavePA(pot_o, dc_a_o, dc_b_o, x_max_o, y_max_o, z_max_o)
501
502   # Draw with this section. Above section can be commented to save time
503   pot_o, dc_a_o, dc_b_o, x_max_o, y_max_o, z_max_o = LoadPA('RfArray.npy', 'DcArray_a.npy',
'DcArray_b.npy', 'dimensions.npy')
504   CalcDraw(pot_o, dc_a_o, dc_b_o, x_max_o, y_max_o, z_max_o, slices = [['x',0.0,1.0],
[0,'y',2.0], [0,0,'z']], RFsmoothing= True, smoothing_factor= 2.5,
505             drawRF=True, drawDC=True)
506   saveParameters('20220714_plot_Potential.py')
```

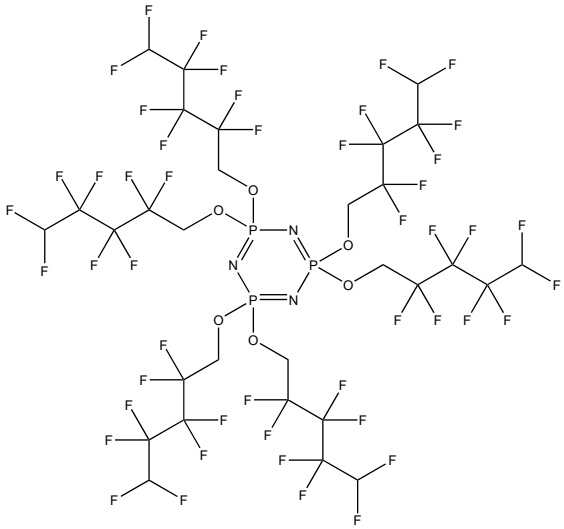
11.6 Ions used for mobility filter simulation

a) 'red', 1222 m/z, K_0 = 0.78 cm²/Vs





c) 'blue', 1822 m/z, K_0 = 0.62 cm²/Vs



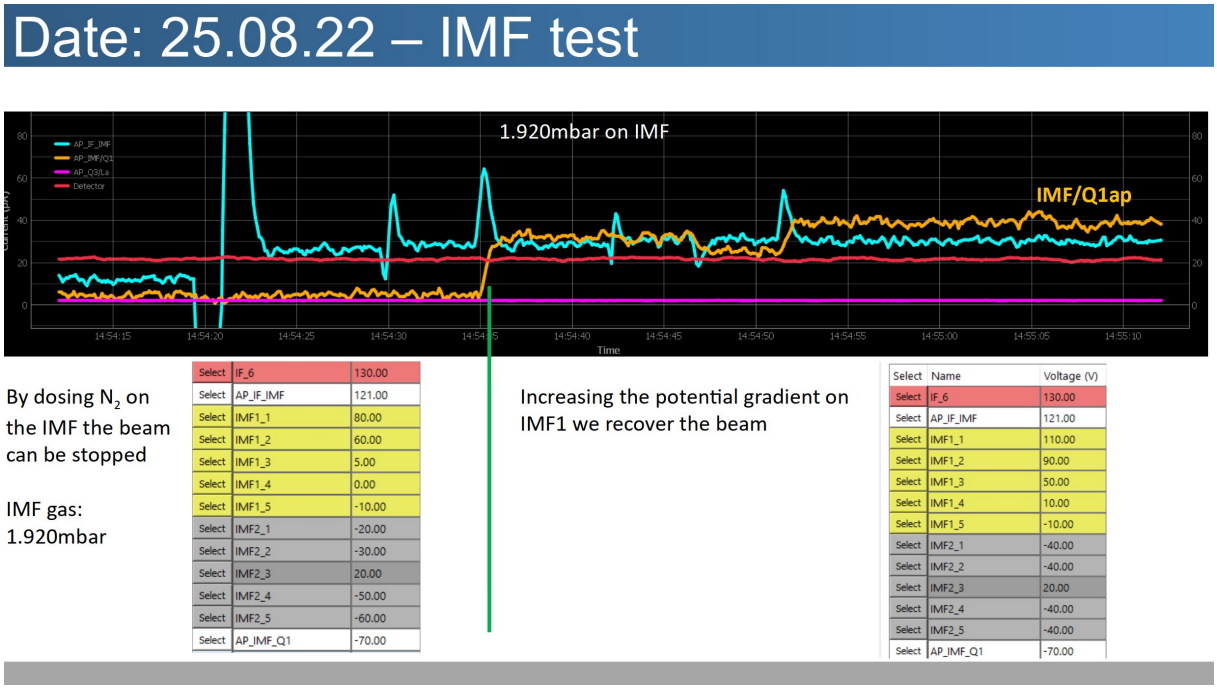
b) 'green', 1522 m/z, K_0 = 0.69 cm²/Vs

Figure 87: Structure formula of three molecules used for the ion mobility filter trajectory simulation. The structures a) red b) green and c) blue show the neutral molecules, not the ions, which have an additional proton.

11.7 Step-by-step manual to optimise the voltages for mobility filtering

- Measure the ion current transmitted through the filter in transport mode (High-pass pumping valve closed, no gas through the gas inlet, low-pass pumping valve partially closed to tune the pressure to the ion. About 1...3 mbar are good for a small ion).
- Set the gas flow and adapt the pressure with the pumping valves.
- Set high positive electric fields supporting ion transport in all sections of the mobility filter, trying to reach a similar ion current as when the mobility filter is operated as an ion guide only.
- Optional steps to optimise potentials and to limit the overall DC drop in the filter:
    - Zones with gas counter flow and transport zones (all but low-pass tunnel section): Lower the electric fields to the point when you see a decrease in current and keep them just above this point.
    - Low-pass tunnel zone: Set a repulsive DC field between the tap at electrode 80 and 115 (Figure 53). Increase the magnitude of the repulsive field to the point when you see a decrease in current and keep it just below this point.
- Now, everything is prepared to activate the mobility filter.
- To set the low-pass cut-off, decrease the electric field (increase of the magnitude) in the low-pass filtering section between the taps at electrode 115 and 122 (Figure 53).
- To set the high-pass cut-off, decrease the electric field (decrease of the magnitude) in the high-pass filtering section between the taps at electrode 22 and 39 (Figure 53).

11.8 Ion mobility filter test



Select	IF_6	130.00
Select	AP_IF_IMF	121.00
Select	IMF1_1	80.00
Select	IMF1_2	60.00
Select	IMF1_3	5.00
Select	IMF1_4	0.00
Select	IMF1_5	-10.00
Select	IMF2_1	-20.00
Select	IMF2_2	-30.00
Select	IMF2_3	20.00
Select	IMF2_4	-50.00
Select	IMF2_5	-60.00
Select	AP_IMF_Q1	-70.00

Select	Name	Voltage (V)
Select	IF_6	130.00
Select	AP_IF_IMF	121.00
Select	IMF1_1	110.00
Select	IMF1_2	90.00
Select	IMF1_3	50.00
Select	IMF1_4	10.00
Select	IMF1_5	-10.00
Select	IMF2_1	-40.00
Select	IMF2_2	-40.00
Select	IMF2_3	20.00
Select	IMF2_4	-40.00
Select	IMF2_5	-40.00
Select	AP_IMF_Q1	-70.00

Figure 88: Extract of the laboratory book of the 'inverted porcupine'. It shows the first test of the high-pass mobility filter. With an increased DC-gradient, the beam can be transmitted against a gas counterflow.